Life–climate interactions on the Archean Earth and exoplanets

Jake Kazu Eager-Nash

Submitted by Jake Kazu Eager-Nash to the University of Exeter as a thesis for the degree of Doctor of Philosophy in Physics, September, 2023.

Abstract

Finding life beyond the Earth remains one of the major drivers of science today. The search for extra-solar life has predominantly been based on Earth-like biosignatures from across Earth's history, such as oxygen and methane. Life on Earth has changed dramatically since the origin of life, with life on the early Earth potentially an important period to understand when looking for life on other planets. In this thesis, I investigate the interaction between life and the environment, with a general focus on life before the advent of oxygenic photosynthesis. Methane is thought to have been an important greenhouse gas during the Archean, although its potential warming has been found to be limited at high concentrations due to its high shortwave absorption. I used the Met Office Unified Model (UM), a general circulation model, to further explore the climatic effect of different Archean methane concentrations. Surface warming peaks at a pressure ratio pCH_4:pCO_2 of approximately 0.1, reaching a maximum of up to 7 K before significant cooling above this ratio. Equator-to-pole temperature differences also tend to increase up to $pCH_4 \leq 300$ Pa, which is driven by a difference in radiative forcing at the equator and poles by methane and a reduction in the latitudinal extend of the Hadley circulation. 3D models are important to fully capture the cooling effect of methane, due to these impacts of the circulation. I then shift the focus to exoplanets. The majority of detected potentially habitable exoplanets orbit stars cooler than the Sun and are therefore irradiated by a stellar spectrum that peaks at longer wavelengths than the spectrum incident on Earth. I present results from a set of simulations of tidally locked terrestrial planets orbiting three different host stars to isolate the effect of the stellar spectra on the simulated climate. Specifically, we perform simulations based on TRAPPIST-1e, adopting an Earth-like atmosphere and using the UM. Whilst holding the planetary parameters constant, including the total stellar flux (900 W/m^2) and orbital period (6.10 Earth days), we compare results between simulations where the stellar spectrum is that of a quiescent TRAPPIST-1, Proxima Centauri, and the Sun. In simulations with cooler host stars, an increased proportion of incident stellar radiation was absorbed directly by the troposphere compared to the surface. This in turn led to an increase in the stability against convection, that is, a reduction in overall cloud

coverage on the dayside (reducing scattering), leading to warmer surface temperatures. The increased direct heating of the troposphere also led to more efficient heat transport from the dayside to the nightside and therefore to a reduced day-night temperature contrast. We inferred that planets with an Earth-like atmosphere orbiting cooler stars had lower dayside cloud coverage, potentially allowing habitable conditions at increased orbital radii, compared to similar planets orbiting hotter stars for a given planetary rotation rate. Finally, after improving our understanding of the Archean and Earth-like planets orbiting M-dwarf planets, I focus on the interaction between the biosphere and the atmosphere for Earth and how this may differ on a planet orbiting an M-dwarf, TRAPPIST-1e, and the possible effect this may have on the detection of life on such a planet. I develop and apply a coupled 1D atmosphere-ocean-ecosystem model to understand how primitive biospheres that exploit free-energy gradients between possible abiotic sources of H_2, CO and O_2 could influence the atmospheric composition of rocky terrestrial exoplanets. I apply this to the Earth at 3.8 Ga and to TRAPPIST-1e. I focus on metabolisms that evolved before the evolution of oxygenic photosynthesis, which consume H_2 and CO and produce potentially detectable levels of CH_4. Oxygen-consuming metabolisms are also considered for TRAPPIST-1e as abiotic oxygen production is predicted. I show that these primitive biospheres can lead to high levels of abiotic oxygen (close to 10%), which is a result of converting an H_2 flux into a biotic CH_4 flux which could stabilise high oxygen scenarios. The inclusion of oxygen-consuming metabolisms could lower oxygen levels to around 10 parts per million and support a productive biosphere at low reductant inputs. I find that CO metabolism is as productive as H_2 metabolisms for a planet orbiting an M-dwarf. Using predicted transmission spectral features from CH_4, CO, O_2/O_3 and CO_2 across the hypothesis space for tectonic reductant input, I show that biotically produced CH_4 may only be detectable at high reductant inputs. CO is also likely to be a dominant feature in transmission spectra for planets orbiting M-dwarfs, which could reduce the confidence in any potential biosignature observations linked to this species. Finally, this thesis covers future work, and some proof of concept experiments that advance the discussed work further.

Contents

List of Figures

List of Tables

Declaration

Chapter 3

This chapter contains developments that were made to both the 3D and 1D models used here. Developments from the 3D model were led by myself. I was involved in co-developing the 1D model, alongside Stuart Daines. Development of the 1D radiative convective model was conducted by a summer student, Tom Boxer, who I lead the supervision of. Similarly development of the reactions rates was conducted by Chadiga Khalek, whom I provided primary supervision. The model development was aided by simulations and testing performed as part of an undergraduate research project, which I co-supervised the following students: James W. McDermott, Peter Andrews, Lucy A. Grain, James Bishop, Aaron A. Rogers and Jack W. G. Smith.

Chapter 4

This chapter is adapted from work published in Eager-Nash et al. (2023)

Chapter 5

This chapter is adapted from work published in Eager-Nash et al. (2020)

Chapter 6

This chapter is adapted from work that has been submitted for publication to Monthly Notices of the Royal Astronomical Society.

Acknowledgements

I would first like to thank my funder, Graham Hill. Without your amazing support, this PhD would not have been possible. I am very grateful that this funding has given me the freedom to investigate the scientific problems I find most interesting. Your generosity will never be forgotten.

Next I would of course like to thank my amazing supervision team. Nathan, you have been such an amazing supervisor and mentor to me. Your dedication to helping people should never be overlooked, and I am inspired by your outlook and how you always challenge your own views. I'm so glad I came across your TED talk all those years ago, I had no idea what I was looking for in a supervisor back then, but I stumbled into the perfect one. Tim, thank you for your endless knowledge on the biogeochemistry of the Earth that you have imparted on me. Thank you for lending me a copy of your book, *Earth System Science: A Very Short Introduction*, which made me fascinated with Gaia and the interaction between life and the environment. Eric, you are a joy to be around – thank you so much for always being there at short notice to help me with all my chemistry problems. Hugo, I really appreciate all of the climate knowledge you have enlightened me with, like correcting my use of subsistence and subsidence. Thank you for welcoming me into your group even though I'm still not sure whether you are officially my supervisor or not! You're humour and personality always light up every meeting.

A special thanks must also go to Stuart, who is always able to solve the most complicated of coding problems with ease and poses the most interesting scientific problems. The EETG group has provided amazing support for me and I would not have achieved as much as I have without the group's kind and supportive nature. In particular, I would like to thank Denis, for always being too selfless in offering your time to help me with science and coding issues - and for being my fitness class partner. Arwen, thank you for being

there during stressful times and sharing your experiences and pictures of kittens and mice, the combination of which would always make me feel better. Thanks also for chatting to me as an undergrad and talking to me about your work, which I always thought was the coolest thing ever and made me want to do similar things.

I am really grateful to the many people that I have met during my PhD both in Exeter and around the world who I am lucky to call friends. Martha, I feel like we have become each others second mothers, I will always feed you and you will always clean my laptop screen. Thank you for some excellent badminton games during the stressful parts of the PhD. Michelle, I am so glad we started at the same time, and that you were the first person I met at in the PhD. I'm so glad we could share every laugh and that you would always be more outraged on my behalf than I was myself. Your passion for positive change is inspiring and I know you are going to change the world.

My PhD experience would not have been the same without the amazing students that I got to supervise. Working with all of the fantastic students helped to drive my research and these interactions have definitely been a highlight of this journey.

I would not be the person I am without the love and support of my family including my brother, Leon, and my parents, John and Shoko, thank you for your hard work, which provided the platform for me to do what I enjoy, and for helping me to fall in love with science. Finally, my wife, Katy. Thank you for proof reading my work and sitting through countless practice presentations. You inspire me every day, with your hard work and determination to do what makes you happy - even when change is so scary. You supported me throughout, keeping the house and our lives in order while I was at my busiest. I would not have finished this PhD with a good work-life balance without you. We have done so much together over the last four years, planning our wedding, and helping each other through tough points in our lives, but it has only reaffirmed that we can do anything together.

Jake Kazu Eager-Nash

Exeter, U.K.

4th December 2023

Chapter 1

Introduction

The question of whether there is life out there in the universe has been posed for as long as human kind has looked into the skies. Planets located outside of the Solar System are known as exoplanets, and since the discovery of the first by Wolszczan and Frail (1992), many thousands have since been discovered. Characterisation of some of these planets has found exotic atmospheres that would have once been scarcely believable. With the capability to characterise the atmospheres of more Earth sized planets approaching in the near future, it is important to understand what inhabited planets may look like, and look beyond the current composition of the Earth's atmosphere.

The Earth has been inhabited for at least 3.7 billion years (Rosing 1999; Hassenkam et al. 2017), with some estimates of life stretching as far back as the formation of the Earth. Thus, the Earth itself provides a diverse range of inhabited states over its history. The Archean, spanning from roughly 4 to 2.5 billion years ago, is the period where life first emerged, with the atmosphere very alien to the one we know today. The atmosphere was oxygen poor, inhospitable to the animals that later evolved, including us. In order to get where we are at now, a series of unlikely and difficult evolutionary steps were required (Watson 2008), which means the majority of inhabited planets could remain in some of these early stages, such as the Archean. Planets with Archean-like life may be most likely to be found and so it is important to better understand both the Archean on Earth and how the Archean may differ for other planets.

As we are most likely to detect life indirectly though observing the atmosphere, it is important to understand how life interacts with the atmosphere, and how the atmospheric circulation of these planets may affect detectability.

This thesis works towards improving our understanding of the Archean Earth, and the interaction of life with the atmosphere prior to the evolution of oxygen photosynthesising organisms. This is considered for the Earth and for exoplanets, with the aim of improving our understanding of what biosignatures may look like on other planets, if they host life that resembles that of the early Earth.

1.1 Structure of the thesis

This thesis is laid out as follows. Chapter 2 introduces our current understanding of the Archean Earth in terms of the atmospheric composition and the timeline of the evolution of life. This chapter then discusses the state of detection and characterisation of terrestrial Earth-like exoplanets and our understanding of biosignatures. Chapter 3 discusses the various modelling types that are important to understand the atmospheres of terrestrial planets that are used in this thesis, which includes general circulation models (GCM) and biogeochemical models of the atmosphere and ocean. Chapter 4 investigates the role of methane on the climate of the Archean Earth using a GCM. Chapter 5 compares the effect of stellar type on the climate of a tidally locked planet. A coupled model of the atmosphere and biosphere is then investigated in Chapter 6, to establish differences in the atmospheric composition of biotic and abiotic configurations of the Earth and a hypothetical inhabited planet orbiting TRAPPIST-1. Finally, Chapter 7 concludes this thesis and presents ideas and proofs of concept for future work.

Chapter 2

Background to Archean Earth and terrestrial exoplanets

In this section, I provide context to the background of the fields of the Archean Earth and terrestrial exoplanets that are advanced in this thesis. A history of the Earth and more specifically the Archean are provided, focusing on conditions and processes for life and the atmosphere. This is followed by a background of the exoplanet field, and the prospects of detecting and characterising the atmospheres of planets with similar properties to the Earth, which with current and near future telescopes is likely to be restricted to planets orbiting M-dwarfs. Together, these provide the context for the rest of this thesis on how connecting these elements is important to finding and interpreting biosignatures on other planets.

2.1 The Earth and the Archean Eon

Since the formation of the Earth, the Earth has had many different habitable environments, with billions of years worth of examples of the interaction between life and the planet (Lenton and Watson 2011; Olson et al. 2018). The evolution of the Earth's atmospheric composition is shown in Figure 2.1. Oxygen is thought to have risen in the atmosphere during two oxidation events at the beginning and end of the Proterozoic to reach the levels found today (Holland 2006; Och and Shields-Zhou 2012). Carbon dioxide is likely

to have steadily declined in response to a warming Sun (Walker et al. 1981), while methane concentrations would have been much higher during the Archean (Zahnle et al. 2019) following the evolution of methanogens in this low oxygen environment (Kharecha et al. 2005; Sauterey et al. 2020). Earth's history thus provides many examples of different habitable worlds with different atmospheric compositions. The first eon of Earth's history is the Hadean.

The Hadean spanned the formation of the Earth through to the start of the Archean at 4.0 Ga. During this period, the moon formed (Thiemens et al. 2019), as did the oceans (Harrison 2009), whilst there was a significant evolution of the atmosphere. The atmospheric affected by outgassing, ingassing (gas being taken up by the mantle) and the addition of volatiles from impacts (Catling and Kasting 2017, Ch. 6). The composition of the Hadean atmosphere is limited due to the lack of a geological record from then. The presence of an ocean could support a carbon cycle that stabilises carbon dioxide and the climate over million year timescales (Krissansen-Totton et al. 2018a). The lack of geological evidence, leads to a lack of estimates for the potential atmospheric composition of the Hadean (Figure 2.1).

The Archean Eon on Earth spanned 4.0-2.5 Ga - approximately a third of the Earth's total history. The Archean preceded the Great Oxidation Event (GOE) and, therefore, had a more reducing atmosphere compared to the present day, with evidence for oxygen being a trace gas (Zahnle et al. 2006), at concentrations less than 600 parts per billion (Gregory et al. 2021). Furthermore, compared to the present day, the Archean likely had higher concentrations of carbon dioxide and methane and potentially a lower surface pressure (Catling and Zahnle 2020). Life was thought to have originated around the start of the Archean (Rosing 1999; Knoll and Nowak 2017), with oxygenic photosynthesis evolving later in the Archean between 3.2 to 2.7 Ga (Catling and Zahnle 2020), which led to the eventual rise in oxygen. The GOE, however, occurred at least a few hundred million years after the evolution of oxygenic photosynthesis, at around 2.4 Ga (Warke et al. 2020).

Improving our understanding of the Archean is important to understand how this period remained warm despite the faint young Sun (described in more detail in Section 2.1.2), as well as how early life may have interacted with and driven changes in at-

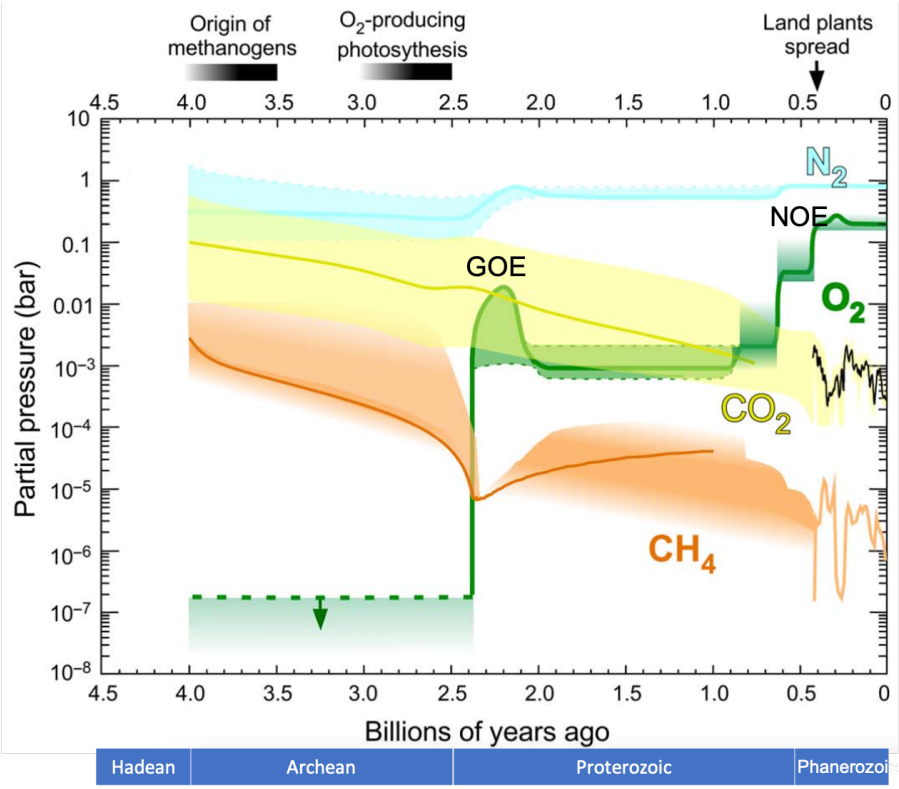

Figure 2.1: Showing the potential atmospheric evolution of key gases from the Archean, through to the present day. The major rises in atmospheric oxygen, termed the great oxidation event (GOE) and the Neoproteozoic oxidation event (NOE), are marked as occurring around 2.4 Ga and 0.6 Ga respectively. Major evolutionary land marks are also included, showing the range where methanogens and oxygenic photosynthesis could have evolved, as well as the spread of land plants around 0.4 Ga. This figure is adapted from Catling and Zahnle (2020).

mospheric composition. The latter of these is an important example of how life may work on other planets, providing additional data points for potential biosignatures. Geological evidence has led to many discoveries about the conditions and potential processes during the Archean. Understanding the Archean provides insight into life during this period and could increase our understanding of what signs of life may look like on other planets.

2.1.1 Evolution of life on Archean Earth

Following the formation of the Earth, it is apparent that life evolved relatively quickly, with geological evidence of life from at least 3.7 Ga (Rosing 1999), with the origin of life potentially occurring much earlier (Knoll and Nowak 2017). Methanogens, methane producing organisms, were believed to be one of the first organisms to have evolved (Battistuzzi et al. 2004; Schopf et al. 2018). Many methanogens are autrotrophic, meaning they produce organic carbon molecules by reducing CO_2. Other examples of autotrophs are plants and other photosynthesisers. Methanogens, however, generate energy to produce biomass, which is stored in adenosine triphosphate (ATP) for use in other reactions, which, for H_2–consuming methanogens takes the form of

$$CO_2 + 4\,H_2 \longrightarrow CH_4 + 2\,H_2O\ (+\ \text{energy}), \tag{R2.1}$$

with the ATP subsequently used to generate biomass, CH_2O, via

$$CO_2 + 2\,H_2\ (+\ \text{energy}) \longrightarrow CH_2O + 2\,H_2O. \tag{R2.2}$$

Measurements of this process have found that for 1 mol of biomass to be produced, around 10 mol of CO_2 are required to be metabolised (Schonheit et al. 1980; Fardeau and Belaich 1986; Morii et al. 1987), via Reaction R2.1. CH_2O in this context represents organic carbon, which represents the mean ratios of carbon, oxygen and hydrogen in organic matter. Other elements including nitrogen and phosphorus are also required in organic mat-

ter in smaller ratios (Redfield 1934). Nitrogen and phosphorus may be limiting factors to producing organic matter, with substantial sources of biologically available nitrogen not clearly established in the Archean (Stüeken et al. 2016). Possible abiotic sources of nitrogen could have been through atmospheric HCN production (Zahnle 1986; Tian et al. 2011) or lightning, before nitrogen fixers evolved. However, prior to the evolution of oxygenic photosynthesis, it is thought that electron donor supply (H_2 in this case) was the limiting factor to primary productivity (Ward et al. 2019). Primary productivity is the rate at which biomass is produced by primary producers.

CO metabolism by autotrophs is also thought to have evolved early in life's history (Ferry 2006; Lessner et al. 2006; Weiss et al. 2016), with a possible metabolism of

$$4\,CO + 2\,H_2O \longrightarrow 2\,CO_2 + CH_3COOH\ (+\ \text{energy}), \tag{R2.3}$$

with this energy is again used to create organic carbon via a pathway similar to Reaction R2.2, via anabolism of CO, such as via

$$2\,CO + H_2O\ (+\ \text{energy}) \longrightarrow CH_2O + CO_2. \tag{R2.4}$$

Heterotrophs, organisms that consume living or dead organic matter, could have evolved following the evolution of autotrophic organisms. These would convert the majority of organic carbon back to CH_4 and CO_2. Examples of these are acetogenic bacteria (fermentors) and acetotrophic methanogens, which would have the following pathway for recycling organic carbon

$$2\,CH_2O \xrightarrow{\text{acetogens}} CH_3COOH \xrightarrow{\text{acetotrophs}} CH_4 + CO_2. \tag{R2.5}$$

These pathways allow for recycling of organic carbon and reduce organic carbon burial. Organic carbon burial is the process of organic carbon or biomass descending to the seabed and forming new sediments.

Oxygenic photosynthesis evolved later in the Archean between 3.2 to 2.7 Ga (Catling and Zahnle 2020), with stromatolites and microbial mats from the time having shown signs of this (Bosak et al. 2009; Flannery and Walter 2012; Riding et al. 2014; Homann et al. 2015). Signs of oxygen production are also present in evidence of oxidative weathering taking place on continents (Planavsky et al. 2014), and trends in sulphur isotopes are suggestive of localised oxygen production (Zerkle et al. 2012; Eickmann et al. 2018). At some point between the evolution of oxygenic photosynthesis and the origin of life, anoxic photosynthesis could have evolved, as the photosyntheitc machinery used by oxygenic photosynthesisers are though to have evolved from these (Hohmann-Marriott and Blankenship 2011; Cardona 2019). Photosynthesisers would have had the capability to use energy from the Sun to create biomass rather than chemical metabolisims, increasing the growth rate of such systems.

2.1.2 Faint Young Sun problem

Solar models suggest that the Sun has not always been as luminous as it is today (Feulner 2012). As discussed in Charnay et al. (2020), as the Sun fuses hydrogen into helium the mean molecular weight of the Sun's core increases. The core then contracts and warms to maintain the balance between the pressure gradient and gravitational forces. This increases the rate of fusion, which causes the photosphere to expand, which increases the area of the emitting surface causing Solar flux to increase with time. The long term evolution can be approximated by the following simplified formula as a function of time, t, from when the Sun entered the main sequence Gough (1981):

$$\frac{L(t)}{L_\odot} = \frac{1}{1 + \frac{2}{5}\left(1 - \frac{t}{t_\odot}\right)}, \tag{2.1}$$

where $L_\odot = 3.85 \times 10^{26}$ W is the modern day solar luminosity, $t_\odot = 4.57 \times 10^9$ yr is the present day time since the Sun entered the main sequence. This simple model provides

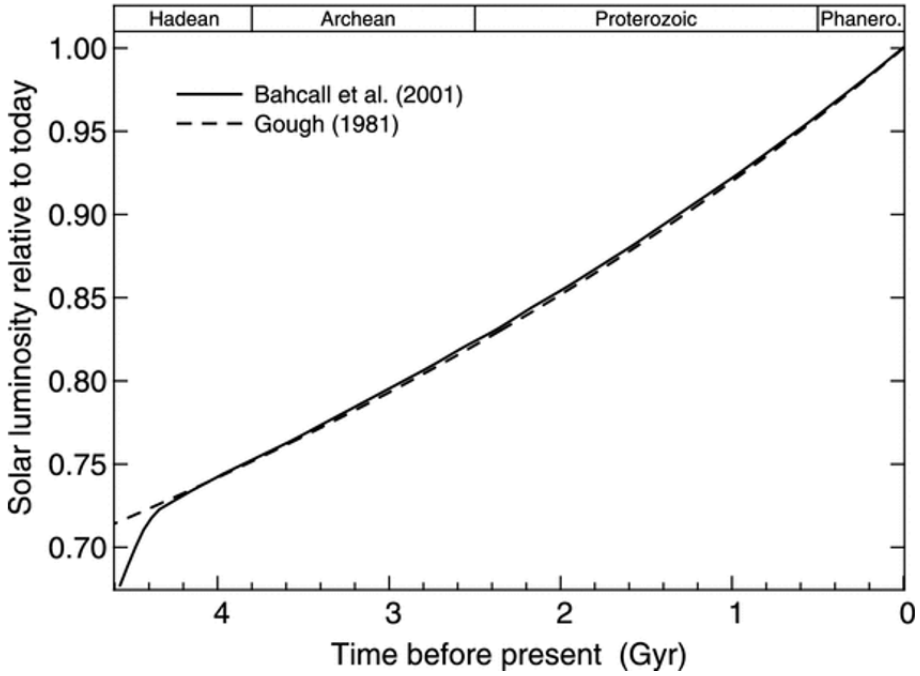

Figure 2.2: Showing the solar luminosity evolution, from a simple model (Reaction 2.1 from Gough (1981) and a more sophisticated solar model (Bahcall et al. 2001)). This Figure is from Feulner (2012).

good agreement with solar models such as Bahcall et al. (2001) from 4.2 Ga to the present day, shown in Figure 2.2. Using Equation 2.1, over the course of the Archean the Solar luminosity would have evolved from 74.1% to 82.0% of the present day value.

Under the present atmospheric composition the Earth would have been globally ice covered (known as a snowball state) prior to ~2.0 Ga (Kasting and Catling 2003). However, there is ample evidence that the Earth was not in a snowball state (for example see Feulner 2012; Charnay et al. 2020). This was termed the faint young Sun (FYS) paradox (Sagan and Mullen 1972), with uncertainty over what kept the early Earth warm. The resolution of the FYS paradox is likely to be due to increased greenhouse gas concentrations during the Archean, particularly carbon dioxide (Charnay et al. 2020), as well as methane.

The resolution to the FYS paradox is a result of a difference in atmospheric composition, with the Archean atmosphere being very different to that of today. In particular, CO_2 and CH_4 were thought to be higher, as shown in Figure 2.1. Reviews by Feulner (2012) and Charnay et al. (2020) discuss this in more detail, however the exact composition of the Archean environment remain unknown. In Section 2.1.3.1 I summarise evidence for differences in the atmospheric composition as well as other differences in conditions that

have been predicted.

2.1.3 Conditions during the Archean

Geological evidence for life and atmospheric composition are key to reconstructing conditions during the Archean, providing a parameter space that can be explored in models. Here, I outline evidence for low O_2 and, potentially, N_2 and higher CO_2 and CH_4 atmospheric abundances, as well as considering differences in cloud properties and the land surface during the Archean.

2.1.3.1 Oxygen - A reduced atmosphere

Possibly the biggest contrast in the atmospheric composition between the present day and the Archean is the molecular oxygen abundance. During the Archean, oxygen was a trace gas and there was no ozone layer. Evidence for this comes from the sulphur, S, record (for detailed discussion see Ono 2017). Sulphur has 4 stable isotopes, ^{32}S, ^{33}S, ^{34}S and ^{36}S, which each have a standard abundance relative to one another. Changes in the relative abundance of these isotopes can be attributed to either mass dependent fractionation (MDF) or mass independent fractionation (MIF). MDF is caused predominantly by changes in the vibrational energies for chemical bonds within a molecule, which are directly related to the mass of the atoms and are associated with processes involving microbes. MIF of isotopes accounts for fractionations that do not follow this relationship. S–MIF is present in the rock record until 2.501 to 2.434 Ga (Warke et al. 2020), after which it disappears.

The S–MIF signals can be generated in the atmosphere via photochemistry in the absence of oxygen and an ozone layer, which absorbs radiation in the region of 180—300 nm, allowing significant UV in this range to enter the troposphere. The photolytic destruction of SO_2, $SO_2 + h\nu \longrightarrow SO + O$, is one pathway that can generate S–MIF, given an availability of photons between 180—220 nm (Farquhar et al. 2000; Farquhar 2001). Following the generation of a S–MIF signal, it must be preserved, and in oxic atmosphere sulphur is deposited as SO_2 or as the sulphate aerosol meaning any S–MIF signal generated is lost with all SO returning to its oxidised form. In reduced atmospheres, atmospheric deposition of sulphur also occurs through the reduced forms HS_2 and S_8, which preserves

S–MIF having formed from the further reduction of SO (Pavlov and Kasting 2002; Ono et al. 2003). 1D photochemical models, discussed in Chapter 3, have been used to constrain surface oxygen concentrations during the Archean to be less than 10^{-5} present atmospheric level (PAL) to be able to generate S–MIF signals (Pavlov and Kasting 2002).

As well as the S–MIF record, further evidence also suggests the Archean was a low oxygen environment. Riverine sediments dating back to the Archean have been found to include minerals such as pyrite, uranite and siderite, which would oxidise, dissolve or rust at higher O_2 levels (Rasmussen and Buick 1999; Johnson et al. 2014).

The disappearance of the S-MIF at around 2.4 Ga in the paleoproterozoic, suggests there was a rise in atmospheric concentrations at this point, which has been termed the Great Oxidation Event (GOE). The mechanism for this rise and controls of atmospheric oxygen are described in Section 2.1.4.1.

Oxygen is an oxidising species, meaning it readily reacts with reduced species through donating electrons. The presence of high levels of oxygen today leads to relatively short lifetimes for reduced species such as methane, which are readily oxidised. In the Archean atmosphere however, the low oxygen content meant species like methane had much longer lifetimes and could have reached higher concentrations, as in Figure 2.1. The Archean is considered a weakly reducing atmosphere, because despite the high prevalence of reducing gases, oxidised species such as CO_2 are still found in high abundance, which would not occur in more reduced atmospheres such as the atmosphere of Titan, which is dominated by N_2 and CH_4 (Niemann et al. 2005).

2.1.3.2 Carbon dioxide

An increased concentration of CO_2 is thought to be key to, at least partially, resolving the FYS problem. Geological evidence suggests that CO_2 concentrations were much higher throughout the Archean compared to the present atmospheric level. Mass balance calculations from CO_2 dissolved in rainwater from weathered soils provide estimates of CO_2 10–50 PAL at 2.69 Ga (Driese et al. 2011) and 7.7–69 PAL at 2.2 Ga (Sheldon 2006). At these levels, other warming processes are also required (Charnay et al. 2020). However, these may be lower limits, as it is assumed that all the CO_2 weathering was 100% efficient (Catling

and Zahnle 2020). Another method using chemical compositions of paleosols predicts CO_2 85-510 PAL at 2.77 Ga, 78-2500 PAL at 2.75 Ga and 160–490 PAL at 2.45 Ga (Kanzaki and Murakami 2015). This study had a weaker dependence of weathering on CO_2 concentrations leading to higher predictions compared to values estimated in Sheldon (2006) and Driese et al. (2011) (Catling and Zahnle 2020).

More recent approaches to constrain CO_2 have come about in the process of explaining the oxidation of fossilised micrometeorites from 2.7 Ga (Tomkins et al. 2016). These suggest a lower limit for atmospheric CO_2 concentration of greater than between 23–70% (Payne et al. 2020; Lehmer et al. 2020; Huang et al. 2021). With N_2 levels similar to the present, the climate at these CO_2 concentrations would be much warmer than the mean surface temperature of the preindisutrial Earth (around 287 K) and upwards of 300 K (Payne et al. 2020). Geological evidence, suggests there may have been glaciations at this time (Ojakangas et al. 2014), which may suggest lower abundances of N_2, and thus a lower surface pressure than today, which is discussed further in Section 2.1.3.4. This is supported by Rimmer et al. (2019), who found that the micrometeorites may be more readily oxidised in atmospheres with lower surface pressures.

2.1.3.3 Methane and larger hydrocarbons

Low levels of atmospheric oxygen increase the atmospheric lifetime of reduced gases such as methane, which would otherwise be readily oxidised to CO_2 in the modern atmosphere. The presence of methanogens and methanotrophs, inferred from the presence of light organic carbon (biological processes preferentially uptake ^{12}C compared to the heavier ^{13}C) suggests that CH_4 was abundant (Stüeken and Buick 2018). Further, modelling work suggests that methane must have been greater than 10 ppmv to allow the formation of S_8 and thus a S—MIF signal (Zahnle et al. 2006). Mass fractionations in Xe isotopes from 3.5 Ga could be explained by hydrogen escape, which would have required at least 1% total hydrogen (Zahnle et al. 2019). With a methanogen biosphere thought to be prevalent at this point, the majority of total hydrogen at the surface would be in the form of methane (Kharecha et al. 2005), providing a methane constraint of >5000 ppmv (Zahnle et al. 2019).

Methane has a secondary impact on the climate through its importance in the forma-

tion of hydrocarbon hazes, similar to those on Titan (Trainer et al. 2006), and it is suggested that there may have been periods during the Archean where a haze layer was present (Domagal-Goldman et al. 2008; Izon et al. 2015). Haze forms when the CH_4:CO_2 ratio exceeds approximately 0.1 (Trainer et al. 2006), with modelling work suggesting that significant haze could lead to global glaciation (Arney et al. 2016). A haze layer could have affected S–MIF records by blocking UV radiation, and evidence from the Neoarchean suggests that the atmosphere may have oscillated between a hazy and haze–free state (Zerkle et al. 2012). However, definitive interpretations from these signals require more work (Catling and Zahnle 2020).

2.1.3.4 Atmospheric surface pressure

An increase in atmospheric N_2 and atmospheric mass can lead to an increase in greenhouse effect through pressure broadening (Goldblatt et al. 2009). However, more recent geological evidence suggests that surface pressures may have been lower than the present day (Som et al. 2012; Som et al. 2016; Rimmer et al. 2019). Fossil raindrops have been used to approximate surface pressure at 2.7 Ga to between 5×10^4 to 1.1×10^5 Pa (Som et al. 2012), although debate remains over the upper limit of this constraint (Kavanagh and Goldblatt 2015). Furthermore, fossilised gas bubbles in lava flows at 2.74 Ga predict a surface pressure of $2.3\pm2.3\times10^4$ Pa (Som et al. 2016). The oxidation of fossilised micrometeorites from 2.7 Ga (Tomkins et al. 2016) can be achieved with a lower surface pressure. A 0.3 bar surface could allow significant amounts of water vapour to reach the stratosphere, which is then dissociated to form molecular oxygen sufficient to oxidise the micrometeorites (Rimmer et al. 2019).

2.1.3.5 Clouds

How clouds will respond to climate change remains a major uncertainty for the modern atmosphere (Gettelman and Sherwood 2016). Clouds are likely to have been different during the Archean as a result of a different solar constant, atmospheric composition and land coverage (Rosing et al. 2010; Goldblatt and Zahnle 2011). Cloud condensation nuclei (CCN), are small aerosol particles that facilitate the condensation of water vapour in the atmosphere and cause cloud droplets to be smaller and prolong the longevity of cloud.

Smaller cloud droplets are more reflective, and increased longevity would increase the amount of cloud. The amount of CCN during the Earth's past could be less than today, with a significant proportion of CCN generated from anthropogenic sources (Bréon et al. 2002). Biological sources are another important factor for generating CCN (Andreae 2007). As there would have been no wildfires, vegetation and likely a lower land fraction, CCN may have been available as only sea salt and sulphate. Sulphate aerosols may also have been considerably lower as algae had yet to evolve, which produce dimethyl sulphide, and subsequently get oxidised in the atmosphere to form sulphate (Rosing et al. 2010).

2.1.3.6 The surface of the Earth

Land fraction remains uncertain for the Archean, with a general consensus that the fraction of continental crust was less than present day (Hawkesworth et al. 2019), with evidence coming from the zircon ($ZrSiO_4$) record (Roberts and Spencer 2015). There is also potential for a larger ocean volume, with depletion of deuterium in the Archean oceans suggesting they were up to 26% more volumous (Pope et al. 2012). The mantle has gradually cooled which has led to an increase in the amount of water that can be stored in the mantle, which could also support more volumous oceans during the Archean (Dong et al. 2021). High mantle temperatures weaken continental crust, which limits mountain building and could have led to much of the continental crust being flooded. This means the land fraction could have been as low as 2-3% until 2.5 Ga (Flament et al. 2008), which is consistent with widespread Archean flooded continents (Arndt 1999).

2.1.3.7 Rotation rate

Tidal forces between the Earth and the moon have caused the Earth's rotation rate to slow (Wahr 1988). The deformation of the Earth by the moon lags slightly behind the gravitational force from the moon, meaning the peak deformation occurs after the moon is directly overhead. As a result, the bulge leads the Earth–Moon axis by a small angle. The Moon's gravitational force acts to pull the bulge back to the Earth–Moon axis, leading to a gradual decrease in the rotation rate (Wahr 1988). The same forces acting between the host star and planet leads to the predicted tidal locking of close orbiting exoplanets around M–dwarf stars (see Section 2.2.3). The Earth may have maintained a constant rotation rate

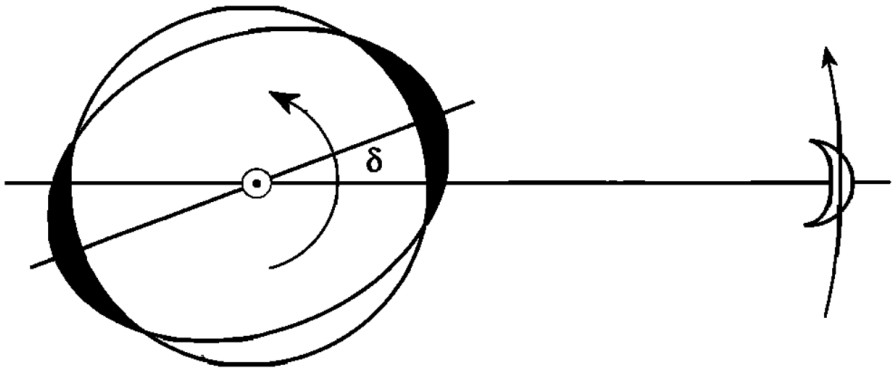

Figure 2.3: A schematic of tidal forces. δ is a small angle by which the bulge of the Earth from tidal forces lags the Earth-Moon axis. Gravitational forces act to attempt to make $\delta = 0$ which acts against the direction of the Earth's rotation, leading the rotation rate to slow over time. This Figure is from Williams (2000).

for a long period of time of a 21 hr orbital period, due to a resonance with the semidiurnal atmospheric thermal tide (Zahnle and Walker 1987; Bartlett and Stevenson 2016), which could have maintained this constant orbital period from around 2 Ga through to 0.6 Ga (Bartlett and Stevenson 2016). Evidence from banded iron formations (sedimentary rock consisting of alternating layers of iron oxide and iron poor silica rock) from 2.45 Ga (Barley et al. 1997) show tide related variability, which could suggest an orbital period of 16 to 19.4 hours (Williams 2000).

2.1.4 Processes during the Archean

As discussed, the geological evidence from the Archean provides us with some constraints on the atmospheric composition and climate. However, evidence for the conditions during the Archean are caused by a range of processes that are now discussed in more detail. Particularly, I focus on elements affecting the atmospheric composition of the Archean.

2.1.4.1 Controls on oxygen

During the Archean, as oxygen fluxes were lower than the fluxes of reduced gases (such as H_2 and CH_4), oxygen entering the atmosphere from abiotic processes or via oxygenic photosynthesis quickly reacts with these reduced species, maintaining low oxygen concentrations. This acted as the major control on oxygen concentrations at the time, such that oxygen concentration remained low for several hundreds of millions of years following the evolution of oxygenic photosynthesis.

Although photosynthesis generates oxygen, the organic carbon it produces is converted back to methane, leaving the overall reaction redox neutral. However, if some fraction of the organic carbon is buried without being oxidised, there is a net source of oxygen to the atmosphere-ocean system (Claire et al. 2006). This organic carbon burial is key to oxidising the Earth. When the total reductant flux from metamorphism and volcanic sources dropped below the flux of organic carbon burial, more oxygen entered the atmosphere compared to reduced species leading to the accumulation of oxygen in the atmosphere, leading to the first major rise in atmospheric oxygen, known as the great oxidation event. Oxygen concentrations remained low in the Archean, despite the evolution of oxygenic photosynthesis during this time.

The rise in oxygen is amplified by the formation of the ozone layer, which shields the oxygen from photochemically driven destruction and allows oxygen to further accumulate in the atmosphere, leading to two distinct regimes (Claire et al. 2006; Goldblatt et al. 2006) – a weakly reducing regime where O_2 is a trace gas, with a volume mixing ratio of less than 6×10^{-7}, and an oxidising atmosphere with an O_2 abundance of greater than 2×10^{-3} (Gregory et al. 2021). These results are obtained from a 1D photochemical model, with these models described in more detail in Chapter 3. The Archean remained in this weakly reducing, low oxygen state for its entirety, as indicated by the many proxies discussed in Section 2.1.3.1.

2.1.4.2 Hydrogen escape

Escape of atmospheres to space is an important process in understanding how the atmosphere evolves over time. Following Catling and Zahnle (2009), atmospheric escape can be split into three main categories: thermal escape, suprathermal escape and impact erosion. Thermal escape is when radiation, usually from the star, heats the atmosphere, leading to molecules escaping, which can be considered through either Jeans' escape, where individual molecules are considered, or hydrodynamic escape, which considers the bulk loss of the atmosphere. Suprathermal escape is when molecules or atoms reach the escape velocity following a chemical or ionic reaction, and impact erosion is the loss of atmosphere following an impact.

I consider the escape of hydrogen as it is the lightest component of the atmosphere and, therefore, the most likely to escape via thermal processes as less energy is required for it to reach escape velocity. The escape of hydrogen is important for the evolution of the atmosphere because it gradually oxidises the atmosphere as reductant is lost to space (Catling and Kasting 2017). A way to understand this is through the case of water. High up in the atmosphere photolysis will split the hydrogen from the oxygen, leaving the hydrogen to escape to space. The oxygen remains in the atmosphere, leading to a gradual irreversible oxidation of the Earth system.

Hydrogen escape on Earth is considered to be diffusion limited. That is to say, it is the upward diffusion of hydrogen through the rest of the atmosphere, which is the limiting step to hydrogen escape. The process of escape itself occurs rapidly once hydrogen reaches the exobase (bottom of the exosphere) (Catling and Kasting 2017). Modelling of this diffusion limited escape is described in Section 3.3.2.1.

2.1.4.3 The carbonate–silicate cycle

Carbon dioxide is regularly emitted into the Earth's atmosphere through outgassing from the mantle. However, carbon dioxide levels have generally tended to decrease over Earth's history. Alongside this decrease, the Solar constant for the Earth has gradually increased due to the Sun's increasing luminosity (see Section 2.1.2). The carbon cycle regulates carbon dioxide concentrations, and thus temperature, over time scales of millions of years to maintain a relatively consistent mean temperature (Walker et al. 1981). As the solar luminosity increases, the surface temperature of the Earth increases, which leads to an increase in evaporation and subsequently an increase in precipitation as well. An increase in precipitation, which contains dissolved CO_2 in the form of carbonic acid, increases the weathering rate of silicate rock. I present equations and discussion from Chapter 11 of Catling and Kasting (2017). The reaction for silicate weathering is:

$$CaSiO_3 + 2\,CO_2 + H_2O \longrightarrow Ca^{2+} + 2\,HCO_3^- + SiO_2, \tag{2.2}$$

where silicate rock is represented as wollastonite ($CaSiO_3$). The products of weathering,

dissolved in water, are transported to the ocean by rivers, where they undergo carbonate precipitation:

$$Ca^{2+} + 2\,HCO_3^- \longrightarrow CaCO_3 + CO_2 + H_2O, \tag{2.3}$$

with the calcium carbonate ($CaCO_3$) going on to form sediments on the seafloor. These sediments are eventually subducted into the mantle, where under high pressure and temperature, silicate rock is reformed:

$$CaCO_3 + SiO_2 \longrightarrow CaSiO_3 + CO_2, \tag{2.4}$$

with gaseous CO_2 making its way back to the surface, where it is eventually outgassed back into the atmosphere. This is known as the silicate weathering feedback and is an important control of temperature over timescales of millions of years.

A similar weathering feedback occurs on the ocean floor, which becomes important when there is little or no land surface on the planet (Krissansen-Totton and Catling 2017). This process is similarly temperature sensitive and likely controlled CO_2 levels (Brady and Gíslason 1997; Coogan and Gillis 2013; Coogan and Dosso 2015). Thus, seafloor weathering was likely a significant carbon sink and control of temperature when the land fraction was lower (Krissansen-Totton and Catling 2017).

2.1.4.4 The solid Earth

Processes involving the solid Earth play an important role in the atmosphere (Lenardic et al. 2016). The oxidation state and composition of the mantle determines the species and fluxes outgassed to the atmosphere (Kasting et al. 1993b; Ortenzi et al. 2020). Further, the tectonic regime of the crust can also affect outgassing rates, topography and the efficiency of the crustal recycling. Here, I provide a brief overview of the effects of these processes.

The oxidation state of the mantle is referred to as the fugacity (Frost 1991), a higher value indicates the mantle is more oxidising. The fugacity of the upper mantle sets the

outgassing rate. A more oxidised mantle may emit more oxidised species, such as H_2O, CO_2 and SO_2, whereas a more reducing mantle may instead emit more H_2, CO and H_2S (Holland 2020). However, the fugacity of the Earth's mantle in the past is uncertain. It is likely that following formation, the mantle was reduced (Wood et al. 2006). However, some geological evidence suggests that the mantle was oxidised to today's levels by the early Archean (e.g. Trail et al. 2011; Nicklas et al. 2018; Armstrong et al. 2019), while a more gradual oxidation is also suggested (Aulbach and Stagno 2016; Nicklas et al. 2019).

It is the subject of debate as to how long plate tectonics have existed on the Earth. Geological evidence suggests that the planet could have had various different regimes over the course of its history and a complete review can be found in Palin and Santosh (2021). Here, I will summarise information relating to the Archean and its possible implications for the atmosphere. Consensus is starting to form that plate tectonics began around 3 to 2.8 Ga (Palin and Santosh 2021), but evidence has been presented for plate tectonics to have started anywhere between 4.2 and 0.85 Ga (Korenaga 2013). The Archean, then, was likely to not be in this regime for at least some fraction of this Eon. Arguments have been made that plate tectonic could have been preceded by a plutonic squishy lid, a regime has small strong plates that are separated by warm and weak regions created by plutonism (Lourenço and Rozel 2023). Venus is believed to be in such a regime and thus a better understanding of the Venusian surface may help to understand the Archean (Harris and Bédard 2014; Davies et al. 2023).

The Early Earth would have had hotter mantle temperatures and low extrusion efficiencies (Lourenço and Rozel 2023). Extrusion efficiency is the fraction of melt that erupts to the surface compared to intrusion to the crust via plutons. These conditions are suitable for a plutonic squishy lid regime, for which outgassing rates could be higher than the present day within a factor of two, assuming a similar extrusion efficiency (Lourenço et al. 2020). Thus although the tectonic regime was likely different in the Archean, outgassing rates may not have been drastically different. The mantle was hotter in the past due to a combination of higher heat production from radioactive decay and residual heat from the Earth's accretion and core formation (Catling and Kasting 2017). This meant that the higher heat flow from the mantle could have led to higher outgassing rates (Sleep and

Zahnle 2001). However, evidence from zircons suggest that heat flow could actually be lower than the present day (Hopkins et al. 2008).

Overall, the state of the solid Earth during the Archean remains uncertain, with uncertainties in the mantle fugacity, tectonic regime and the effect this had on crustal recycling and outgassing rates.

2.1.5 Summary

Developing an understanding of the Archean is important to allow us to understand how early life interacted with the planet. Although the Sun was fainter during the Archean, processes such as silicate weathering and early life could have regulated the early climate, which led to higher concentrations of CO_2 and CH_4. This likely kept the Archean generally free of global glaciations. Our understanding of the Archean will provide insight into interpreting potential biosignatures for exoplanets in the not to distant future, with exoplanets potentially being more likely to support life that resembles the primitive life from then rather than the more complex life that has evolved on the Earth.

2.2 The search for inhabited planets

Any planet that is outside of our Solar System is known as an exoplanet. Following the discovery of the first exoplanet (Wolszczan and Frail 1992) and the first planet to orbit a main sequence star outside of the Solar System (Mayor and Queloz 1995), thousands of exoplanets have been subsequently detected, which includes planets that may be habitable. As Earth is our only data point for inhabited planets, understanding life on Earth in the context of exoplanets may be useful in the search for life outside of the Solar System.

The planets discovered to date cover a larger range of parameter space in terms of their mass and orbital distance from the host star, shown in Figure 2.4. So far, all of the planets found have a shorter orbital period and/or are more massive than the Earth. This is due to current limits in the detectability of Earth sized planets at longer orbital periods, where longer observations and greater instrument sensitivity are required for detecting these planets, discussed further in Section 2.2.1.

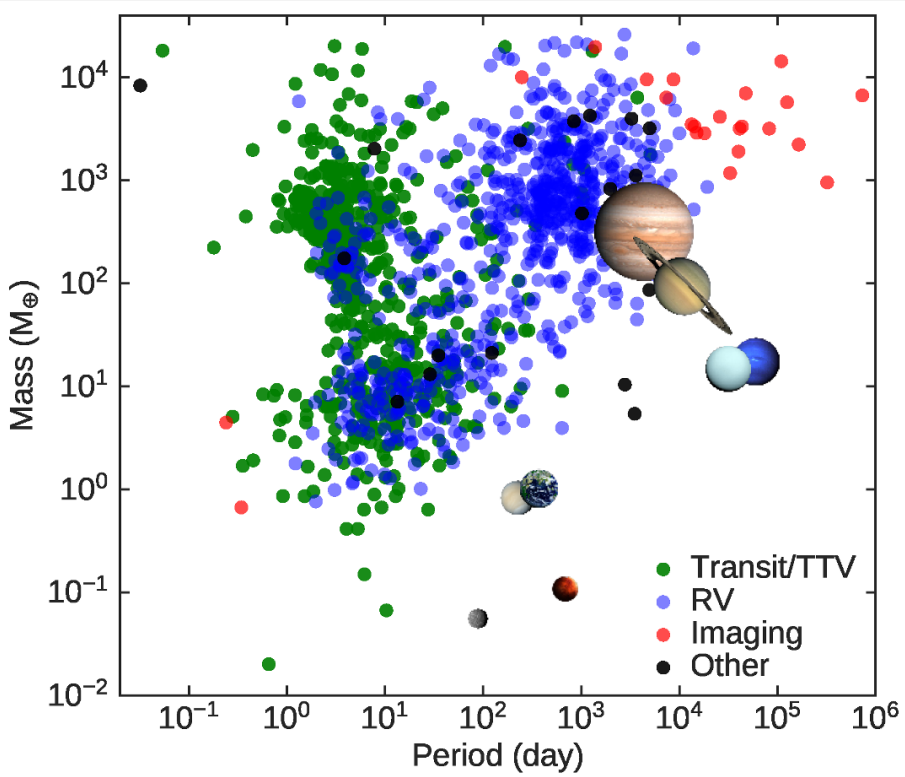

Figure 2.4: Showing the mass, orbital period distribution of discovered exoplanets, with the Solar system planets placed for perspective. Colours represent the different methods that these planets have been detected by. Figure from Adibekyan (2019)

2.2.1 Exoplanet detection

Exoplanets can be detected in a number of ways. Currently, the most prolific methods are the transit and radial velocity methods. The transit method measures the dip in brightness of the host star as the planet transits across the star. From this dip in luminosity the radius of the planet relative to the star can be calculated. Radial velocity measures the velocity of the star along the radial line connecting the observer to the star, caused by the orbit of the host star around the centre of gravity between the planet and star. This is used to constrain the planet's mass. These methods favour short orbit massive planets, with more massive planets having larger transit depths and radial velocities, while shorter orbital periods allow for regular measurements that can build a stronger signal. This led to an initial wave of hot Jupiter's — Jupiter size planets that orbit very close to their host star with very hot atmospheres.

More recently planets with a similar size and that receive a similar stellar flux to the Earth, henceforward referred to as Earth–like planets, have been detected, including Prox-

ima Centauri b (Anglada-Escudé et al. 2016) and the planets in the TRAPPIST-1 system (Gillon et al. 2017). These planets however, orbit stars in the classification of M-dwarfs, which are cooler and smaller than the Sun. The detection of these planets is because of the favourable observing conditions for planets orbiting these stars. Shorter orbital periods provide more repeatable observations in a given period of time and the ratio of radius and mass between the planet and star are larger than Sun-like stars. It is important to understand how orbiting such a star would impact the climate and also potential life on such a planet, given the importance of the Sun to life on Earth.

2.2.2 Atmospheric characterisation

While the detection of atmospheres of Earth–like planets is out of reach of current telescopes, we continue to learn about the atmospheres of larger and hotter planets. The main method for detecting the atmospheres of planets currently comes from transit spectroscopy. Transit spectroscopy allows for three different observations of the planet's atmosphere to be made. First, during a primary eclipse, when the planet passes between the observer and the host star, transmission spectroscopy can be used to determine the thickness of the atmosphere at different wavelengths and thus inferences can be made regarding the atmospheric composition around the terminator of the planet. Alternatively, during a secondary eclipse, when the planet is behind the host star relative to the observer, emission spectroscopy can measure the emergent flux on the dayside. This is achieved by taking the difference of the combined planet and star spectrum just prior to the eclipse and the star only spectrum observed during the secondary eclipse. Finally, as the planet moves between the primary and secondary eclipse, a phase curve can be measured, showing the planetary spectrum at different phases. Transmission spectroscopy measures the transit depth of a planet at different wavelengths. If the atmosphere is more opaque at a given wavelength, the transit depth increases. When measured over a range of wavelengths, a transmission spectra is produced, with atmospheric composition inferred from the position of absorption peaks in the spectra. Emission spectroscopy detects the radiation emitted by the planet directly, from which the atmospheric composition can be inferred. A more detailed discussion can be found in Madhusudhan (2019).

Perhaps the easiest planets to both detect and characterise are Hot Jupiters. These planets, of which we have no comparable planet in the Solar System, are roughly Jupiter sized gas giant planets that orbit very close to their host star, making them very hot, up to 2,200 K — with ultra-hot Jupiters reaching hotter temperatures still (Showman et al. 2020). Phase curves maxima have been found to have the peak offset eastward of the substellar point (Zellem et al. 2014), which was first predicted by climate models due to an equatorial superrotating jet (Showman et al. 2009; Showman and Polvani 2011). Recently, JWST has been used to characterise the atmosphere of WASP-39b, a hot Jupiter planet, which has been found to have a significant CO_2 detection (Ahrer et al. 2023a), as well as Na, H_2O, CO and SO_2 (Alderson et al. 2023; Feinstein et al. 2023; Rustamkulov et al. 2023; Tsai et al. 2023), with minimal amounts of CH_4 (Ahrer et al. 2023b). The presence of SO_2 provides substantial evidence of photochemistry occurring on these planets as part of the oxidation of H_2S to SO_2 (Tsai et al. 2023).

2.2.2.1 Prospects of atmospheric characterisation of Earth-like planets

JWST has began to characterise planets in the TRAPPIST-1 system, finding that the inner most planets TRAPPIST-1b+c are unlikely to have thick atmospheres (Greene et al. 2023; Zieba et al. 2023). Further to this, atmospheric modelling of this data for TRAPPIST-1b+c could not rule out the presence of an atmosphere (Ih et al. 2023; Lincowski et al. 2023). However, JWST is unlikely to be able to resolve detailed spectral features of the TRAPPIST-1 planets that could indicate life, with clouds and hazes potentially limiting observations to CO_2 (Fauchez et al. 2019; Komacek et al. 2020). The next generation of space missions and ground based telescopes are being designed to characterise the atmospheres of potentially habitable and inhabited planets. Examples of these include the European Extremely Large Telescope (E–ELT) (Lopez-Morales et al. 2019), Large Interferometry for Exoplanets (LIFE) mission (Quanz et al. 2022) and the Habitable Worlds Observatory (HWO) (Bolcar et al. 2018). Atmospheric data is likely to continue coming from potentially habitable planets orbiting M-dwarfs, such as the planets in the Trappist-1 system, with future missions designed for characterising the atmospheres of more Earth-like planets. Thus, it is becoming more important to be able to understand any potential atmospheric signals in the context of life.

2.2.3 Earth–like planets orbiting M-dwarfs

I have established that the majority of planets of a similar size and receiving a similar solar flux to the Earth that have been detected to date have been found to orbit cooler and smaller stars compared to the Sun. These host stars, in the class of M–dwarfs, constitute as much as 70% of stars in the Milky Way (Bochanski et al. 2010). Orbiting an M–dwarf leads to an array of differences compared to the Earth and the Sun, which I now discuss in more detail.

For a planet to orbit in the habitable zone (Kasting et al. 1993a) around an M dwarf, it must have a smaller orbital radius (and therefore shorter period) than the orbital radius of Earth. Therefore the planet will experience stronger tidal forces from the host star than the Earth does from the Sun, which is likely to result in the planetary rotation rate and orbital period becoming synchronised; this is known as tidal locking (Pierrehumbert and Hammond 2019). The physics of this is the same as the slowing of the Earth's rotation rate due to the Moon, and to a lesser extent the Sun, which is discussed in Section 2.1.3.7 and schematically represented in Figure 2.3.

2.2.3.1 M-dwarf evolution

M-dwarfs spend more time on the main sequence than hotter stars like the Sun, with the smallest stars, like TRAPPIST-1, living for up to 10 trillion years (Laughlin et al. 1997), 1000 times longer than the lifetime of the Sun. This could provide more time for life to emerge and thrive on these planets (Shields et al. 2016). However in contrast to the faint young Sun on Earth, M-dwarfs luminosity decreases with time. Thus, planets now in the habitable zone of M-dwarfs may have lost their atmosphere earlier, unless the planet migrated inward. This may have led to these planets entering a runaway greenhouse. Provided there was sufficient water vapour, there is a potential for the build up of oxygen from H_2O photolysis and subsequent escape of hydrogen (Luger and Barnes 2015). However, this could be avoided if water was delivered later in the star's evolution following the decrease in luminosity (Ramirez and Kaltenegger 2014).

2.2.3.2 M-dwarf spectra & flaring

M-dwarfs have different stellar spectrum, compared to G-dwarfs. M-dwarf spectra peak at longer wavelengths and have a higher proportion of XUV radiation. Their lower mass means that M-dwarf stars cannot fuse hydrogen as quickly and cannot reach the same temperatures as G-dwarfs, and as such, have lower effective temperatures ranging from 2,450 to 3,850 K (Pecaut and Mamajek 2013). As a result, their spectra peak at longer wavelengths than G dwarfs and thus for the same stellar flux have fewer photons in the photosynthetic range on Earth (400-750nm), which may limit the size of an oxygenic photosynthesis driven biosphere (Lehmer et al. 2018). As well as this, some M-dwarfs have been found to have a higher ratio of far UV radiation (less than 200 nm) to mid and near UV (200-400 nm) compared to that of Sun-like stars (France et al. 2013; Wilson et al. 2021).

Some M-dwarfs have been observed to flare frequently (e.g. Joy and Humason 1949; Hawley and Pettersen 1991). Stellar flares result in a temporary increase in UV radiation by the star. Günther et al. (2020) found that flaring occurs in 30% of mid to late M-dwarfs and 5% of early M-dwarfs, which is significantly higher than other stars (less than 1%). TRAPPIST-1 has been observed to flare, with flares potentially emitting at cooler temperatures than previously observed flares, which could play an important role in the UV emission during the flare (Maas et al. 2022). Frequent flaring could endanger life directly through high UV levels (Tilley et al. 2019), and indirectly through enhancing atmospheric escape (Amaral et al. 2022). Alternatively, flaring could provide important UV fluxes in biogenesis (Rimmer et al. 2018).

2.2.4 Signatures of life

The atmospheres of exoplanets are most likely to provide evidence for life on these worlds, due to detection limits caused by their great distance from the Earth. Life that exists on the planet that interacts with the atmosphere will act to generate a state of chemical disequilibrium, which, if different to what can be generated abiotically, would suggest life is present (Hitchcock and Lovelock 1967). Throughout Earth's history, different chemical disequilibria may have been significant enough to give a clear indication of the presence of life (Krissansen-Totton et al. 2018c). For the Archean, an atmosphere consisting N_2,

CO_2, CH_4 in the presence of liquid water and negligible CO could be the key chemical disequilibrium to suggest inhabitance (Krissansen-Totton et al. 2018c).

Biosignatures can be split into three broad categories, gaseous, surface and temporal, as reviewed in Schwieterman et al. (2018). Gaseous biosignatures are gases in the atmosphere that have either been produced by the biosphere (direct) or gases that are the product of chemical reactions of reactants produced by the biosphere (indirect). For example, oxygen is the product of photosynthesis, while ozone is produced via the photolysis of molecular oxygen in the atmosphere. The surface may also provide a source for bio-signatures through measurement of the reflected or scattered light from the planets surface. An example of this would be the absorption of red light by plants on Earth known as the 'red edge' (Seager et al. 2005).

Gaseous biosignatures can again be split again into types, using the formalism defined in (Seager et al. 2013). Type 1 biosignatures are gases produced directly as biproducts of metabolic reactions that extract energy from chemical gradients, such as methane by methanogens. Type 2 biosignature gasses are byproducts from biomass building, the most prominent example of this would be the creation of molecular oxygen from oxygenic photosynthesis. Finally type 3 biosignature gases are those produced by life that are not type 1 or type 2 signatures that could be produced for a range of functions, such as volatile organic carbons, such as isoprene produced by trees or dimethyl sulphide.

Even if biosignature gases are detected, it is important to see them in their context to determine the likelihood that they are genuine. For this, a probabilistic framework has been proposed by Catling et al. (2018). In this framework four factors are suggested to be considered. Firstly, external parameters, such as properties of the host star, including the star age, and the planet, including the mass and radius, are required to determine the feasibility of habitability. Secondly, internal parameters of the climate and atmospheric composition are required, such as surface temperature and the presence of volcanically emitted gases. Thirdly, potential biosignatures are identified through observations and considered in the context of internal and external factors to determine their plausibility as biosignatures. Finally, false positives of the prospective biosignature gas should be considered to increase the likelihood of a possible biosignature. Many factors could lead

to false positives. Examples of these include: moons contaminating spectra to create a false chemical disequilibria (Rein et al. 2014); or geothermal production of gases such as CH_4 with potential outgassing rates uncertain for other planets (Thompson et al. 2022).

2.2.5 Summary

In this Section, I have introduced exoplanets and methods for detecting them as well as characterising their atmospheres, which, for Earth-like planets, are likely to be restricted to planets orbiting M-dwarfs in the near future. Planet's orbiting M-dwarfs are likely to have many differences compared to the Earth, with the planet likely to be tidally locked, and have a higher chance of experiencing regular flaring. It will be of utmost importance to understand what biosignatures may look like on these planets so that the community is ready to interpret these atmospheres.

2.3 Chapter summary

This Chapter arms us with knowledge of the potential climate and life present during the Archean as well as the processes controlling them. Additionally, this chapter has provided a background to terrestrial exoplanets, their detection and the potential for observing biosignatures. The Archean provides a fascinating alien world that we are still trying to understand. With an atmosphere that was more reducing, which was predominantly driven by non oxygen producing organisms for much of it, this provides an intriguing contrast to the modern Earth. With the next generation of telescopes focusing on the search for biosignatures, it is important to understand how Archean-like biospheres interact with the atmosphere and to determine what biosignatures may be expected. It will also be important to understand how these may change when the planet is orbiting an M-dwarf, as these planets will be the next targets for characterisation. In the next chapter, I discuss modelling techniques that can help us to understand the atmospheric composition and climate of Archean-like worlds.

Chapter 3

Modelling planetary processes over varying temporal and spatial scales

Modelling over different temporal and spacial scales is important to gain a more complete understanding of the role of the interaction between life and its environment. In this Chapter, the modelling tools used in this thesis will be discussed in detail. A hierarchy of models were used to understand processes that affected the Archean Earth. These can also be used to understand analogous planets orbiting M-dwarfs, which may have atmospheres that resemble the Archean that could be tidally locked. Short timescale processes like atmospheric heat transport and radiative heating are required to be modelled using a general circulation model, which allows for understanding of variations across spatial scales and allows for representation of processes such as clouds. For modelling of longer time scales processes, such as the evolution of the atmosphere due to volcanic outgassing and biotic fluxes, we use a 1D photochemical model coupled to an ecosystem model to run simulations on million year time scales.

3.1 Modelling of terrestrial planets

A range of modelling tools are required to understand the atmospheres of terrestrial planets and as well as their potential interaction with life. Here, I overview these different modelling tools.

General circulation models (GCM) have been used for a range of studies of the climate of the Earth's past (Charnay et al. 2020) and exoplanets (Showman et al. 2013). GCMs are climate models that solve the Euler equations for a rotating sphere with thermodynamic terms. GCMs exist for the atmosphere (AGCM) and ocean (OGCM), which can be coupled for an atmosphere-ocean GCM (AOGCM), which are predominantly used for state of the art modelling of modern day climate. This work uses atmosphere only GCMs, to reduce model complexity, with ocean modelling dependant on many poorly constrained factors such as bathymytry (ocean depth) and continental distribution for both Archean Earth and exoplanets. GCMs can include coupled chemistry, which are being applied more and more to understanding the Earth's past and terrestrial exoplanets (Chen et al. 2019; Braam et al. 2022; Cooke et al. 2022; Jaziri et al. 2022; Ridgway et al. 2022).

Photochemical models are important for understanding what the chemical composition of an atmosphere may look like given a set of boundary conditions. They solve the continuity equation

$$\frac{\partial n_i}{\partial t} = P_i - n_i L_i - \nabla \cdot \mathbf{\Phi_i}, \tag{3.1}$$

where n_i is the number density of species i, P_i is the production rate of the species and L_i is the loss rate. $\mathbf{\Phi_i}$ is flux from transport into a region, which in the case of 1D models comes from vertical transport takes the form of $\frac{\partial \Phi_i}{\partial z}$. This creates a set of coupled differential equations, which are solved to find the evolution of the chemical network with time. This is discussed in more detail in Section 3.2.2.

Biological components can be included through chemistry at the planetary surface or in the ocean, which is connected to the atmosphere. Biological models can range from flux based approaches which consider the rate of biological productivity as limited by the availability of the products for metabolism. For pre-oxygenic photosynthesising organisms, the limiting factor is generally assumed to be the availability of electron donors, such as CO or H_2. However, following the evolution of oxygenic photosynthesis, the reactants (CO_2 and H_2O) are much more available and productivity is likely limited by the availability of nitrogen and phosphorus. Alternatively, ecosystems can be modelled us-

ing population models (Sauterey et al. 2020; Nicholson et al. 2022), which require a more detailed understanding of cellular properties and population growth.

Now that I have established the main modelling components that will be used in this thesis for modelling terrestrial planets, I will explain the current state of the art within this modelling framework both for the Archean and terrestrial exoplanet modelling. I will then describe the models that I use in more detail along with developments that I have made to these models for this thesis.

3.1.1 Understanding from modelling of terrestrial planets

I now describe key science from the modelling of terrestrial atmospheres in terms of atmospheric circulation, chemistry and biological models. Initially, I describe modelling work for the Archean, followed by Earth-like exoplanets orbiting M-dwarfs.

3.1.1.1 Archean Earth

The use of GCMs have further aided the resolution of the FYS problem (Charnay et al. 2020). GCMs have been used to show that compared to 1D models, lower amounts of CO_2 are required to maintain global surface temperatures of 15°C, and more importantly, avoid a full glaciation (Charnay et al. 2013; Wolf and Toon 2013). Just 200 mbar and 40 mbar of CO_2 are required to keep the Archean global mean temperatures of 288 K at 3.8 and 2.5 Ga respectively, but when including 0.1 mbar of CH_4 and reduced cloud condensation nuclei, these drop to 30 and 5 mbar of CO_2 respectively, which fall well within the CO_2 constraints of the time (Sheldon 2006; Kanzaki and Murakami 2015). It has also been found that if CO_2 is reduced further, global mean surface temperatures of 248 K are able to retain some surface ice region around the equator (Charnay et al. 2013). Thus, a combination of lower CCN, lower albedo due to lower land coverage, and a realistic treatment of sea ice leads to relatively modest levels of CO_2 required to offset the FYS problem.

Clouds could also play an important role in stabilising climate over Earth's history through changes in low cloud fraction (Goldblatt et al. 2021). In the past, when the solar constant was lower, it was found that low cloud levels reduced the CO_2 concentrations required to maintain a constant surface temperature compared to when cloud levels were

fixed (Goldblatt et al. 2021). This is because low level cloud tends to increase planetary albedo, thus, a reduction in low cloud coverage leads to an albedo decrease.

The use of a coupled ocean has led to findings that salinity could play an important role in keeping the Archean ice free (Olson et al. 2022). Salinity increases the density of seawater, whilst also decreasing the freezing point of water, which may inhibit sea ice formation (Fofonoff and Millard 1983). Alongside this, the low residence times of sodium and chloride ions, 80 and 98 Myr respectively (Emerson and Hedges 2008), means that in the past the salinity of the oceans could have been drastically different. Olson et al. (2022) finds that by increasing ocean salinity by a factor of 2.5, ice coverage reduces by 71 % for the modern Earth, primarily by changing the ocean dynamics.

Photochemical models have been useful in understanding the atmospheric composition of past climates. Photochemical models have predicted an oscillation between haze and haze free states (Zerkle et al. 2012). Arney et al. (2016) found that photochemical hazes only become radiatively significant when CH_4:CO_2 ration exceeds 0.2, below which there is little effect on temperature. Further, when the CH_4:CO_2 ratio increases further, temperatures drop, but this cooling reaches a maximum level as haze acts to shield CH_4 from photolysis and thus prevents further haze production, which could prevent the Earth from a global glaciation. As well as the formation of haze at high CH_4:CO_2 ratios, higher order hydrocarbons form, such as ethane, C_2H_6, which could contribute to warming the Archean.

Photochemical models also allow for developing our understanding of the GOE. Fixed O_2 surface mixing ratio models have been used to predict changes to the O_3 (Kasting and Donahue 1980; Zahnle et al. 2006). Characterisations of the reaction between methane and oxygen from these into a simpler box atmosphere, led to the prediction that oxygen would rise in a relatively quick oxygenation event (Claire et al. 2006; Goldblatt et al. 2006). Gregory et al. (2021) revisitied this problem using a 1D photochemical model with flux based constraints at the surface, which supports prior reduced complexity work predicting this transition. Photochemical models can also be used to predict S-MIF (Zahnle et al. 2006; Claire et al. 2014; Izon et al. 2017) and other fractionations (Gregory 2020), which allow us to better understand the geological record.

GCMs with coupled chemistry have also explored the GOE and the post GOE state. Jaziri et al. (2022) find that temperature is important and O_3 can reach much higher levels at a given O_2 mxixing ratio, suggesting the GOE could be triggered by lowering temperatures. The use of coupled chemistry GCMs have suggested lower O_3 estimates for a given O_2 mixing ratio by a factor of over four as well as lower CH_4 lifetimes (Cooke et al. 2022). This highlights the importance of 3D models when understanding chemistry, which can provide better representations of water vapour and vertical transport, but elements of the 3D models may be oversimplified (Ji et al. 2023).

Modelling of biological fluxes and the impacts on the atmosphere has been considered for the Earth. Kasting et al. (2001) show that once methanogenisis (methane producing organisms) became widespread, CH_4 likely grew to high concentrations in the atmosphere. Small regions of relatively high levels of oxygen were likely present due to the evolution of oxygenic photosynthesis, which could have been consumed alongside CH_4 by methanotrophs via the overall reaction:

$$CH_4 + 2\,O_2 \longrightarrow CO_2 + 2\,H_2O. \tag{R3.6}$$

However, this was found to be unlikely to be able to draw down CH_4 significantly due to oxygen availability limiting productivity. However, Sauterey et al. (2020) found that anaerobic based methanotropy, such as sulphur based methanotropy, should it have evolved significantly after methanogens, could lead to a glaciation due to a rapid drop in CH_4. The greenhouse effect of high amounts of CH_4 may have also led to a decrease in CO_2 due to an increase in silicate weathering, until temperatures reduced again. Following this, Kharecha et al. (2005) looked at similar ecosystems with a photochemical model, where coupling was achieved by finding the intersect between H_2 deposition from the photochemical and ecosystem model. Here, it was found that CH_4 could rise to around 1000 ppmv after the evolution of methanogens, but following the evolution of anoxygenic photosynthesis using H_2, methane levels could drop as organisms could grow quicker and lead to a higher organic carbon burial (Kharecha et al. 2005). Kharecha et al. (2005)

also explore the potential of ecosystems using sulphur and iron as electron donors from anoxygenic photosynthesis, however, they found that the productivity of these biospheres is significantly smaller than the H_2 consuming biospheres. Ozaki et al. (2018) found that biospheres driven by H_2 and Fe using phototrophs could amplify CH_4 concentrations at low H_2 outgassing rates, such that CH_4 abundance is almost constant for any outgassing rate.

Applications of these ecosystem models have begun for exoplanets (Nicholson et al. 2022; Schwieterman et al. 2019). Nicholson et al. (2022) uses a population model to understand nutrient limited biospheres. This is when biosphere's growth is limited by the availability of a nutrient such as H_2 for methanogens. Nicholson et al. (2022) show that when a biosphere is nutrient limited, differing assumptions with regard to the properties of the population, such as the cell death rate or energy requirements, do not affect the CH_4 levels produced by the biosphere, and instead the abiotic processes and the biosphere's ability to exploit it, are more fundamentally important. With CO consuming organisms likely to have evolved relatively early in Earth's history, a common observation from these ecosystem models is that the CO:CH_4 ratio is likely to be small and could be an important sign of life (Schwieterman et al. 2019; Sauterey et al. 2020; Thompson et al. 2022).

3.1.1.2 Earth-like exoplanets orbiting M-dwarfs

In this section, I overview the role of models in improving our understanding on the potential habitability and differences in photochemistry of terrestrial planets orbiting M-Dwarfs. Planets in the habitable zone of these stars are likely to be in or close to a state of tidal locking. I focus on this regime although note that other orbital configurations are possible. Tidally locked exoplanets present a very different regime compared to rapidly rotating planets such as the Earth. One hemisphere remains in constant daytime, while the other in constant night time, which has led to questions being posed of whether these regimes are sustainable due to potentially cold night side temperatures which could lead to the condensation of species such as CO_2 from the atmosphere. The first study of a tidally locked exoplanet using a GCM was by Joshi et al. (1997), who found that tidally locked planets are likely to be able to support atmospheres and potentially liquid water. I now describe the understanding generated from the study of tidally locked planet's with

GCMs.

The circulation of tidally locked exoplanets is important to understand the potential heat and moisture transport from the dayside to the nightside. Hammond and Lewis (2021) show that atmospheric circulation can be decomposed into three components: overturning circulation, stationary waves and the equatorial super-rotating jet. The overturning circulation transports air in a circular motion, upwelling around the sub-stellar point, before being transported towards the poles and the nightside, where they descend (Showman et al. 2013), where this motion generates stationary waves (Sardeshmukh and Hoskins 1988; Showman and Polvani 2010), which then accelerates a superrotating equatorial jet in the direction of planets rotation (eastward). The jet, which forms in the upper troposphere is considered to be superrotating if the speed of the jet is faster than the rotation of the planet below (Showman and Polvani 2010, 2011). Hammond and Lewis (2021) find that overturning circulation is best represented as a flow from the sub stellar point to the anti-stellar point to consider flow both around the equator and across the poles, with this flow dominating the heat transport between the day and night side. A more detailed review of the dynamics of tidally locked circulation can be found in Pierrehumbert and Hammond (2019) and Hammond and Lewis (2021).

Simulations of tidally locked planets often form "eyeball" states (Pierrehumbert 2011), where only a region around the dayside supports an ice free surface. Tidally locked planets could be in danger of water being trapped on the nightside, as if water precipitates onto ice regions here, the ice free region will eventually be depleted of water, unless there is some form ocean transport returning water to the dayside. Modelling of this suggests that it is possible to both lose all water to a nightside ice sheet, but also retain a wet region around the substellar point (Ding and Wordsworth 2020). When water is limited and stellar fluxes are high, another regime could form where the terminator is the only habitable region (Lobo et al. 2023). These regions would likely receive less UV flux, which could be beneficial to life when the host star flares regularly (Ridgway et al. 2022).

Ice and snow albedo is lower for an M-Dwarf spectra (Joshi and Haberle 2012). This has been found to lead to a weaker ice-albedo feedback and subsequently a smaller hysteresis between ice covered and ice free states (Shields et al. 2013). However, when con-

sidering a tidally locked regime as in Checlair et al. (2017), bifurcations between snowball and non-snowball states are not present due to the high stellar irradiance at the substellar point. This result was also maintained in the presence of a dynamic ocean (Checlair et al. 2019). Thus a planet in the habitable zone is unlikely to be in a snowball state (Checlair et al. 2019).

Clouds play an important role in extending the inner edge of the habitable zone (Yang et al. 2013). When solar flux is increased, dayside cloud coverage increases, through increasing evaporation, leading to an increase in the dayside albedo of the planet, which leads to a reduction in temperatures (Yang et al. 2013). However, when convection is resolved by the model using a high horizontal resolution, this effect has found to be smaller due to significantly less low cloud (Sergeev et al. 2021; Lefèvre et al. 2021).

Studies have also been undertaken that focus on the TRAPPIST-1 planets. For TRAPPIST-1 e and f, CO_2 is unlikely to condense on the nightside, provided the atmosphere contains around 1 bar or greater of N_2, however for the planets further out from the star, g and h, have a high chance of CO_2 condensation (Turbet et al. 2018). GCMs can then be used to provide a more accurate prediction of observables such as transmission spectra, which can only detect the atmosphere of the terminator region. Using GCMs with atmospheric mixing ratios generated from a 1D photochemical model, the effects of clouds and hazes were investigated in Fauchez et al. (2019). In this, it was found that CO_2 would be readily detectable, but hazes and clouds would interfere with observations of most other gases when observed with JWST's NIRSpec Prism.

The UM was adapted for tidally locked planets in Mayne et al. (2014b) and applied to exoplanet Proxima Centauri b with a modern Earth like atmosphere in (Boutle et al. 2017). This has provided a platform to look at a range of processes on planets with stellar and planetary parameters of Proxima Centauri and TRAPPIST-1e with modern Earth-like (N_2 dominated) and CO_2 dominated atmospheres. Here, the findings from these are described.

TRAPPIST-1e exists in a bistable regime, which can support a climate with either a single equatorial eastward jet or two mid-latitude eastward jets (Sergeev et al. 2022b).

The double jet regime leads to significantly warmer nightside temperatures, due to a higher rate of transport of warm moist air from the dayside to the nightside (Sergeev et al. 2022b). This bistability can be triggered by a range of model parameters, including convection scheme (Sergeev et al. 2020), however, this behaviour was also found in other GCMs (Turbet et al. 2022; Sergeev et al. 2022a).

Continents have also been found to play a role in the climate. The presence of a continent around the substellar point was found to reduce humidity, which decreased the water vapour greenhouse effect as well as the cloud radiative effect, which, in turn, reduces the effectiveness of redistributing heat to the nightside of the planet (Lewis et al. 2018). The presence of continents may also lead to mineral dust aerosols entering the atmosphere. Boutle et al. (2020) found that on tidally locked planets dust acts to cool the dayside and warm the nightside. A negative feedback could also exist at the inner edge of the habitable zone to prevent water loss due to increased evaporation of oceans leading to an increase in exposed continent, which increases dust content cooling the dayside. However mineral dust may also obscure the detection of biosignatures such as ozone and methane.

Atmospheric chemistry has been explored for tidally locked planets with a modern day atmosphere, focusing on the change in the ozone layer due to the difference in host star and orbital configuration. Yates et al. (2020) found the ozone layer on Proxima Centauri to be thinner due to the reduction in UV radiation emitted by the host star. Braam et al. (2022) show that the strong convection around the sub-stellar point leads to lightning induced nitrogen oxide formation below 20 km, which is advected to the nightside, where it is stored as reservoir species. These studies were conducted under the assumption of a quiescent solar spectrum. When flaring of the host star is considered, ozone levels increase by a factor of 20 (Ridgway et al. 2022), and the increase in ozone following a flare reduces the surface UV flux caused by subsequent flares. This increase the ozone UV shielding of the surface.

The focus of photochemical modelling for planets orbiting M-dwarfs has been on potential biosignatures and false positives, which usually relate to O_2. Differences are generally driven by the difference in the spectrum, particularly in the UV. The proportion

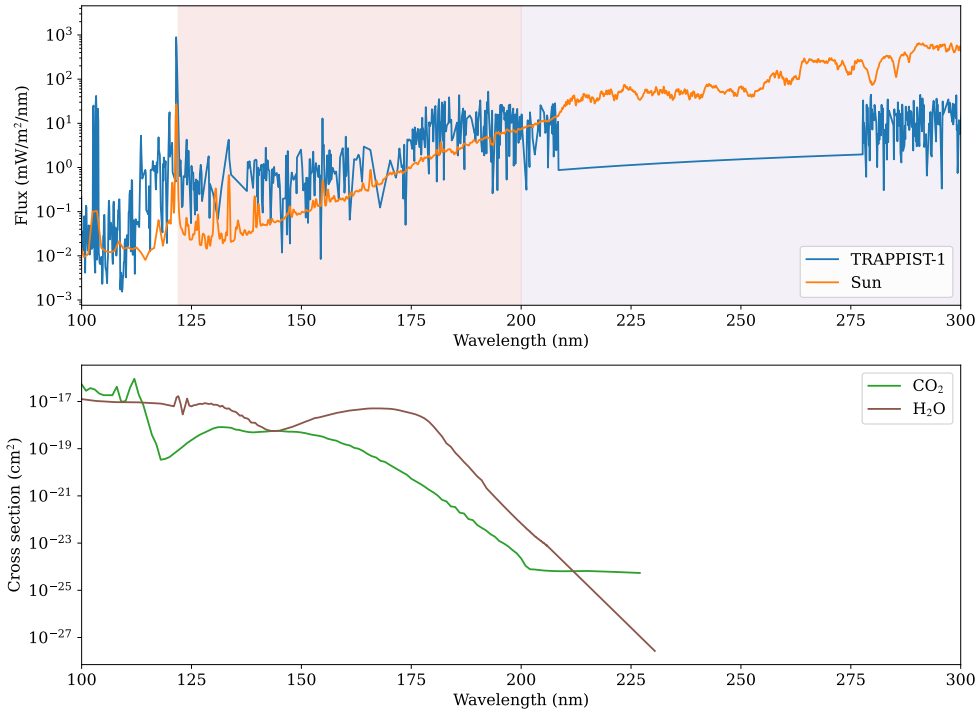

Figure 3.1: Top panel: Shows the TOA flux received by the Earth for the Sun and a scaled version of the TRAPPIST-1 (Wilson et al. 2021) spectrum scaled to the same total flux. The FUV region is shaded red, while the NUV is shaded blue. Data between approximately 210 and 280 nm is from a polynomial fit from the semi-empirical model used in spectra regions with signal to noise ratios too low to measure. Bottom panel: shows the cross sections of CO_2 and H_2O. Although the cross section of CO_2 extends into the NUV, this absorption does not contribute to photolysis.

of flux in the UV is less for M-dwarfs. Figure 3.1 shows a comparison of UV flux by the Sun and TRAPPIST-1.

It has been found that M-dwarfs may be more likely to accumulate significant abiotic O_2 (and CO) in the atmospheres with high concentrations of CO_2 (Tian et al. 2014; Domagal-Goldman et al. 2014; Harman et al. 2015). The mechanism for this is now described following (Harman et al. 2015). CO_2 may undergo photolysis via:

$$CO_2 + h\nu \longrightarrow CO + O, \tag{R3.7}$$

the recombination of the two products is spin forbidden and thus has a very low reaction

rate. Thus O molecules tend to combine with each other to form O_2:

$$O + O + M \longrightarrow O_2 + M, \tag{R3.8}$$

CO and O_2 can be reformed via a catalitic cycle following the photolysis of H_2O:

$$H_2O + h\nu \longrightarrow H + OH, \tag{R3.9}$$

which is followed by

$$CO + OH \longrightarrow CO_2 + H, \tag{R3.10}$$

$$O_2 + H + M \longrightarrow HO_2 + M, \tag{R3.11}$$

$$HO_2 + O \longrightarrow O_2 + OH, \tag{R3.12}$$

which has the net effect of:

$$CO + O \longrightarrow CO_2. \tag{R3.13}$$

The photolysis of CO_2 can only be photolysed by radiation with wavelengths less than 200 nm called far-UV (FUV), while H_2O photolysis goes up to 240nm, which is important for tropospheric OH. The region from 200-400 nm is referred to as the near and mid UV range (NUV), shown in Figure 3.1. Domagal-Goldman et al. (2014) suggest that it is the high levels of FUV that causes O_2 accumulation, while Tian et al. (2014) suggest it is caused by the lower levels of NUV, while (Harman et al. 2015) shows that it is the ratio of these two fluxes that is important, and that treatment of atmospheric redox balance also plays an important role in this process, discussed in Section 3.3.2.2. A source of NO in the atmosphere that can come from lightning, which could eradicate the O_2 false positive, by catalysing the recombination of CO and O (Harman et al. 2018). Ranjan et al. (2020) also found that H_2O cross sections were previously underestimated in the NUV range, which can also increase the H_2O photolysis driven catalytic recombination of CO_2. Hu et al. (2020) went on to show that the inclusion of NO_x reservoir species HO_2NO_2 and N_2O_5 could lead to large abiotic sources of atmospheric O_2. HO_2NO_2 and N_2O_5 act as reservoirs as they are relatively stable and store NO in a form that cannot catalyse CO_2 formation, and would rainout into the oceans. However, it was recently found that this result was due to the model top height being too low, which leads to eroneously high levels of O production at the model top (Ranjan et al. 2023). Thus, it is now thought that abiotic O_2 production from CO_2 containing atmospheres is unlikely to be a potential false positive.

For low oxygen worlds, CH_4 is likely to accumulate to higher levels for a given flux when orbiting an M-dwarf due to a lower photochemical destruction rate (Segura et al. 2005; Schwieterman et al. 2019). Haze is also relatively transparent in the main regions where M-dwarfs emit radiation, so haze is unlikely to have as large a cooling effect compared to the Earth (Arney et al. 2017).

3.1.1.3 Towards model intercomparisons

The growth in modelling of terrestrial exoplanets has led to model intercomparisons (e.g. Yang et al. 2019b). The TRAPPIST Habitable Atmosphere Intercomparison (THAI) project focuses on TRAPPIST-1e, which compared similation from the ExoCAM, LMD-G, ROCKE-3D and the UM (Fauchez et al. 2020). The aim of this was to understand differences between the GCMs and to understand how these may affect the interpretaion of obser-

vations. In these, it was found that TRAPPIST-1e lies at a boundary of two dynamical regimes, with the models falling into either state (Turbet et al. 2022), discussed further in (Sergeev et al. 2022b). The hydrological cycle varied significantly between the models, with the UM producing a strong dayside cloud negative feedback compared to the other models (Sergeev et al. 2022a). Given these differences, the simulated transmission spectra of these models were similar with differences caused by the height of the cloud deck (Fauchez et al. 2022). This initial model intercomparison has paved the way for many more intercomparisions called the Climates Using Interactive Suites of Intercomparisons Nested for Exoplanet Studies (CUISINES), which are important to highlight differences between GCMs and other exoplanet modelling tools. This includes photochemical models in the upcoming Photochemical model Intercomparison for Exoplanet Science (PIE).

3.1.2 Summary

The use of GCMs and single column models have greatly improved our understanding of both the Archean and terrestrial exoplanets. GCMs have shown that lower CO_2 constraints are required for maintaining ice free regions during the Archean and tidally locked exoplanets can be suitable for maintaining habitable conditions. GCMs have also improved our understanding of the atmospheric dynamics of tidally locked planets, and suggest that these atmospheres may be able to maintain long term habitability. However, they are expensive in their simulations time and are not able to capture longer timescale physical processes like the evolution of the atmosphere and the influence of the biosphere. The use of single column photochemical models of Earth-like planets orbiting M-dwarfs have generated debate over whether oxygen may be able to produce large quantities of abiotic oxygen as a result of a different UV spectrum for M-dwarfs compared to the Sun. Meanwhile, photochemical models coupled to preoxygenic photosynthesising biospheres may provide large sources of methane, and can be characterised by a ratio of methane to carbon monoxide. I now discuss the models that will be used going forward in this thesis.

3.2 Modelling tools used in this thesis

I now describe the models used in the remainder of this thesis. Initially, I describe the GCM I use, the Met Office Unified Model (UM), followed by the model of a single column atmosphere model coupled to a single box atmosphere, known as the Platform for Atmosphere, Land, Earth and Ocean (PALEO) modelling framework.

3.2.1 UM

In this work I use the UM, which has been adapted to a range of exoplanet applications and used for a large number of studies covering hot Jupiters (Mayne et al. 2014a; Amundsen et al. 2016; Helling et al. 2016; Mayne et al. 2017; Tremblin et al. 2017; Drummond et al. 2018b; Drummond et al. 2018c; Lines et al. 2018b; Lines et al. 2018a; Lines et al. 2019; Sainsbury-Martinez et al. 2019; Debras et al. 2019; Debras et al. 2020; Drummond et al. 2020), mini-Neptunes/Super Earths (Drummond et al. 2018a; Mayne et al. 2019) and terrestrial planets (Mayne et al. 2014b; Bolmont et al. 2017; Lewis et al. 2018; Fauchez et al. 2020; Yates et al. 2020; Boutle et al. 2020; Joshi et al. 2020; Sergeev et al. 2020). The GCM simulations used in this thesis are based on the Global Atmosphere 7.0 configuration (Walters et al. 2019). The UM has implemented the ENDGame dynamical core, which uses a semi-implicit semi-Lagrangian formulation to solve the non-hydrostatic, fully compressible deep atmosphere equations of motion (Wood et al. 2014). At the top of atmosphere a sponge layer is used to surpress numerical instabilities by damping vertical velocities. The full set of equations for this are:

$$\frac{\partial u}{\partial t} + \frac{u}{r\cos\phi}\frac{\partial u}{\partial \lambda} + \frac{v}{r}\frac{\partial u}{\partial \phi} + w\frac{\partial u}{\partial r} = \frac{uv\tan\phi}{r} - \frac{uw}{r} + fv - f'w - \frac{c_p\theta}{r\cos\phi}\frac{\partial \Pi}{\partial \lambda} + D(u) \quad (3.2)$$

$$\frac{\partial v}{\partial t} + \frac{u}{r\cos\phi}\frac{\partial v}{\partial \lambda} + \frac{v}{r}\frac{\partial v}{\partial \phi} + w\frac{\partial v}{\partial r} = -\frac{u^2\tan\phi}{r} - \frac{vw}{r} - fu - \frac{c_p\theta}{r}\frac{\partial \Pi}{\partial \phi} + D(v), \quad (3.3)$$

$$\frac{\partial w}{\partial t} + \frac{u}{r\cos\phi}\frac{\partial w}{\partial \lambda} + \frac{v}{r}\frac{\partial w}{\partial \phi} + w\frac{\partial w}{\partial r} = \frac{u^2+v^2}{r} + f'u - g(r) - c_p\theta\frac{\partial \Pi}{\partial r}, \tag{3.4}$$

$$\frac{\partial \rho}{\partial t} + \frac{u}{r\cos\phi}\frac{\partial \rho}{\partial \lambda} + \frac{v}{r}\frac{\partial \rho}{\partial \phi} + w\frac{\partial \rho}{\partial r} = -\rho\left[\frac{1}{r\cos\phi}\frac{\partial u}{\partial \lambda} + \frac{1}{r\cos\phi}\frac{\partial\left(v\cos\phi\right)}{\partial \phi} + \frac{1}{r^2}\frac{\partial\left(r^2 w\right)}{\partial r}\right], \tag{3.5}$$

$$\frac{\partial \theta}{\partial t} + \frac{u}{r\cos\phi}\frac{\partial \theta}{\partial \lambda} + w\frac{\partial \theta}{\partial r} = \frac{Q}{\Pi} + D(\theta). \tag{3.6}$$

$$\Pi^{\frac{R^*}{c_p}-1} = \frac{R^*\rho\theta}{P_0}, \tag{3.7}$$

These are the zonal, meridional and vertical momentum equations, the continuity equation, the thermodynamic equation and the equation of state respectively. The coordinate system used here are λ, ϕ, r and t representing longitude, latitude (from equator to poles), radial distance from the centre of the planet and time respectively. The wind components of these spatial coordinates are u, v, w for zonal, meridional and vertical directions respectively and ρ is the density. f and f' are Coriolis parameters that account for the rotation of the planet:

$$f = 2\Omega\sin\phi, \tag{3.8}$$

$$f = 2\Omega\cos\phi, \tag{3.9}$$

where Ω is the rotation rate. c_p is the specific heat capacity at constant pressure, D is the diffusion operator, Q is the heating rate (calculated from the radiative transfer) and R^* is the specific gas constant. θ is the potential temperature, defined as the temperature a parcel of air, at initial temperature T, would be if moved adiabatically from a pressure, P to reference pressure, P_0:

$$\theta = T\left(\frac{P_0}{P}\right)^{\frac{R^*}{c_p}}. \tag{3.10}$$

Π is the Exner pressure, a non-dimensional pressure defined as:

$$\Pi = \left(\frac{P}{P_0}\right)^{\frac{R^*}{c_p}} = \frac{T}{\theta}. \tag{3.11}$$

Finally, $g(r)$ is a height dependant gravity, defined as:

$$g(r) = g_p\left(\frac{R_p}{r}\right)^2, \tag{3.12}$$

where g_p is the surface gravity and R_p is the radius of the planet.

3.2.1.1 SOCRATES

The Suite of Community Radiative Transfer codes based on Edwards and Slingo (1996) (SOCRATES) scheme treats the radiative transfer in the UM, employing a two-stream correlated-k method (Manners et al. 2022). SOCRATES uses spectral files that are created for specific atmospheric compositions and stellar spectra, which treat planetary and stellar radiation separately. These files are input to the GCM and contain all the radiative transfer information, including the solar spectrum, absorbing gases, continua, collision induced absorption and photochemical cross sections and quantum yields. Spectral files treat radiation in bands, with each band designated a dominant and minor contributing species to treat overlapping absorption of gas species (Amundsen et al. 2017). This is called the equivalent extinction method. In this the dominant gas is treated with a full k-distribution, with minor gases treated as gray. The radiation code calculates the heating rates at each point in the atmosphere in Equation 3.6.

3.2.1.2 Model parametrisations

Processes that occur on a scale smaller than the size of the grid boxes are parametrised. Convection uses a mass-flux approach based on Gregory and Rowntree (1990), which has

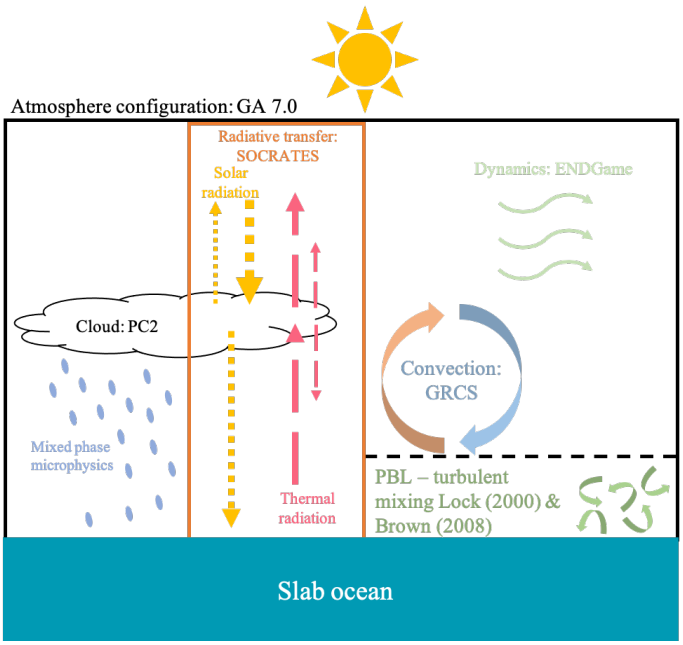

Figure 3.2: Schematic of the different components of the the model. The GA 7.0 atmospheric configuration consists of the ENDGame dynamical core (Wood et al. 2014), the PC2 scheme to treat clouds (Wilson and Ballard 1999; Wilson et al. 2008), microphysics is based on Wilson and Ballard (1999), SOCRATES to treat radiative transfer, the Gregory-Rowntree Convection Scheme (GRCS) (Gregory and Rowntree 1990), with turbulent mixing in the planetary boundary layer (PBL) based on Lock et al. (2000) and Brown et al. (2008). The ocean is treated as a single layer slab with a prescribed mixed layer depth with no horizontal heat transport.

been developed to improve representation of downdrafts and convective momentum flux (Walters et al. 2019). Water clouds are represented by the Prognostic Cloud fraction and Prognostic Condensate (PC2) scheme detailed in Wilson et al. (2008), which is updated to include treatments of cloud erosion and critical relative humidity. The scheme is used to calculate the mixing ratios of water vapour, liquid water and ice, as well as liquid, ice and mixed phase cloud fractions. Precipitation formation is based on Wilson and Ballard (1999) and warm rain, rain formed from liquid droplets, is based on Boutle et al. (2014). Turbulent mixing uses an approach based on Lock et al. (2000) and Brown et al. (2008). A schematic of these components can be found in Figure 3.2.

3.2.2 PALEO

The PALEO modelling framework has been used to look at the evolution of the Earth system over history, including modelling the Great Oxidation event (Daines and Lenton 2016), and the controls of oxygen during the Proterozoic (Daines et al. 2017). This model also has incorporated the Carbon, Oxygen, Phosphorus, Sulphur Evolution (COPSE) model (Lenton et al. 2018a), which models the evolution of the Phanerozoic. This modelling

framework allows for simple coupling between different parts of the Earth system, such as the atmosphere and ocean, however, its atmosphere component was previously limited to a single box model.

The atmosphere module has now been extended to include a vertically resolved photochemical model. The model is based on the atmos model[1], which has a rich history in modelling the Archean and exoplanets (e.g. Haqq-Misra et al. 2008; Harman et al. 2015). Solar flux is split into 750 bins from 117.65 to 1000 nm. This included the adoption of a two stream approach to track stellar radiation for photolysis. Cross sections and quantum yields data are the same as in the atmos repository and include the updated cross sections for H_2O (Ranjan et al. 2020). A list of the photolysis reactions are shown in Table B.1.

The photochemical model solves the 1D continuity equation

$$\frac{\partial n_i}{\partial t} = P_i - n_i L_i - \frac{\partial \Phi_i}{\partial z}, \tag{3.13}$$

where n_i is the number density of species i, P_i is the production rate of the species and L_i is the loss rate. Φ_i is flux from transport into a region, which in the case of 1D models comes from vertical transport, but could more generally include horizontal transport in 3D models. This creates a set of coupled differential equations, which are solved to find the evolution of the chemical network with time. The rates of chemical production and loss are now discussed.

Chemical loss and production is considered through three types of reactions: bimoecular, termolecular and unimolecular (photolysis) reactions, following Jacob (1999) and (Ridgway 2023). Bimolecular reactions involve the reaction of generally two reactants, for example:

$$\mathrm{A} + \mathrm{B} \longrightarrow \mathrm{C} + \mathrm{D}. \tag{R3.14}$$

1. https://github.com/VirtualPlanetaryLaboratory/atmos

The rate of this reaction is

$$-\frac{d}{dt}[\mathrm{A}] = -\frac{d}{dt}[\mathrm{B}] = \frac{d}{dt}[\mathrm{C}] = \frac{d}{dt}[\mathrm{D}] = k[\mathrm{A}][\mathrm{B}], \tag{3.14}$$

$[i]$ is the concentration of species i and k is the rate constant for the reaction. That is to say, the rate at which the reaction occurs depends on the abundance of the reactants and the likelihood of the reaction taking place due to energetic constraints and the collisional cross sections of the molecules, which are subsumed into k.

Termolecular reactions involve a third body, M, which stabilises the products. In the atmosphere, [M] is the number density of the air. For example

$$\mathrm{A} + \mathrm{B} \longrightarrow \mathrm{AB}^* \quad (k_1) \tag{R3.15}$$

where AB^* is an excited state, which can either be stabilised by a third body, removing this energy, or the molecule may split apart again:

$$\mathrm{AB}^* \longrightarrow \mathrm{A} + \mathrm{B} \quad (k_2) \tag{R3.16}$$

$$\mathrm{AB}^* + \mathrm{M} \longrightarrow \mathrm{AB} + \mathrm{M}^* \quad (k_3) \tag{R3.17}$$

$$\mathrm{M}^* \longrightarrow \mathrm{M} + \mathrm{heat} \tag{R3.18}$$

with the overall reaction written as

$$A + B + M \longrightarrow C_2H_6 + M \tag{R3.19}$$

The rate of this reaction, ie the formation of AB is

$$\frac{d}{dt}[AB] = k_3[AB^*][M]. \tag{3.15}$$

The excited complex AB^* has a short lifetime and reacts as soon as it is produced, so we can thus assume that the rate of formation and loss of AB^* from these reactions are equal:

$$k_1[A][B] = k_2[AB^*] + k_3[AB^*][M] \tag{3.16}$$

rearranging this for AB^* and substituting into Equation 3.15

$$-\frac{d}{dt}[A] = -\frac{d}{dt}[B] = \frac{d}{dt}[AB] = \frac{k_1k_3[M]}{k_2 + k_3[M]}[A][B] = k[A][B]. \tag{3.17}$$

The rate constant k for this termolecular reaction can be considered in two limits. First, the low density limit $[M] << k_2/k_3$:

$$k = \frac{k_1k_3}{k_2}[M] = k_0[M] \tag{3.18}$$

where k_0 is referred to as the low-pressure limit rate constant. In the high density limit $[M] >> k_2/k_3$:

$$k = k_1 = k_\infty \tag{3.19}$$

where k_∞ is the high pressure limit rate constant, where k can be rewritten in terms of the high and low pressure rate constants:

$$k = \frac{k_0[M]}{1 + \frac{k_0}{k_\infty}[M]} F. \tag{3.20}$$

Included in this definition is a broadening factor, F, and in this derivations takes the value of unity. However, this is not always the case, and a derivation of this broadening factor comes from Troe (1983), and takes the form

$$F = F_c^{\frac{1}{1+(\log P_r)^2}} \tag{3.21}$$

where F_c is a parameter greater than zero or less than or equal to one, and P_r, known as the reduced pressure is

$$P_r = \frac{k_0}{k_\infty}[\mathrm{M}]. \tag{3.22}$$

This is the general form of termolecular reaction, although some reactions can take just the low or high pressure limit as the rate constant as in Equations 3.18+3.19.

The reaction rate constant of a photolysis reaction, k, is calculated as

$$k = \int_0^\infty Q(\lambda)\sigma(\lambda)F(\lambda)d(\lambda), \tag{3.23}$$

where $Q(\lambda)$ is the quantum yield, $\sigma(\lambda)$ is the cross section of the absorbing species and $F(\lambda)$ is the actinic flux (radiation from the host star), all of which are dependent on wavelength, λ. The quantum yield is the likelihood that a specific photolysis pathway for a species will occur, obtaining a value between zero and one, with the sum of quantum yields at a given wavelength for each pathway of a species not able to exceed one. Cross sections, represent the visibility of the molecule to radiation, with a larger cross section increasing the effective cross section of the molecule leading to a higher chance of photon absorption. The actinic flux is the number of photons crossing the unit horizontal area per unit time (photons $\mathrm{cm}^{-2}\mathrm{s}^{-1}$).

Water vapour in the troposphere is treated using either a constant relative humidity, RH, a pressure, p, dependent parametrisation from Manabe and Wetherald (1967):

$$RH(p) = RH_{\text{surf}} \frac{p/p_{\text{surf}} - 0.02}{1 - 0.02}, \tag{3.24}$$

where the surface relative humidity, RH_{surf}, is a prescribed value, nominally 70%, and p_{surf} is the surface pressure. Above the tropopause, relative humidity can either be restored to a value, assuming condensation, or can be allowed to evolve through production and loss via chemical reactions.

Rainout, or wet deposition, is the process of the removal of species through dissolving into raindrops and subsequent precipitation to the surface. In PALEO, rainout follows the prescription described in (Giorgi and Chameides 1985). As H_2O mixing ratio is prescribed in the troposphere, the change in H_2O flux caused by eddy diffusion is equivalent to the rainout of H_2O. The rainout of every other species can be calculated from this based on their solubility.

Dry deposition is modelled at the lowest atmosphere level, with deposition flux, Φ^{dep} (molecules/cm^2/s) for species i is calculated as

$$\Phi_i^{\text{dep}} = n_i v_i^{\text{dep}}, \tag{3.25}$$

where v^{dep} is the deposition velocity. This represents the free fall of species out of the atmosphere.

Eddy diffusivity models the upward vertical mixing of the atmosphere, and contributes to Φ_i in Equation 3.13, which takes the form

$$\Phi_{\text{eddy}} = -KN \frac{\partial f}{\partial z}, \tag{3.26}$$

where K is the eddy diffusion coefficient, plotted in Figure 3.3. This resembles those used

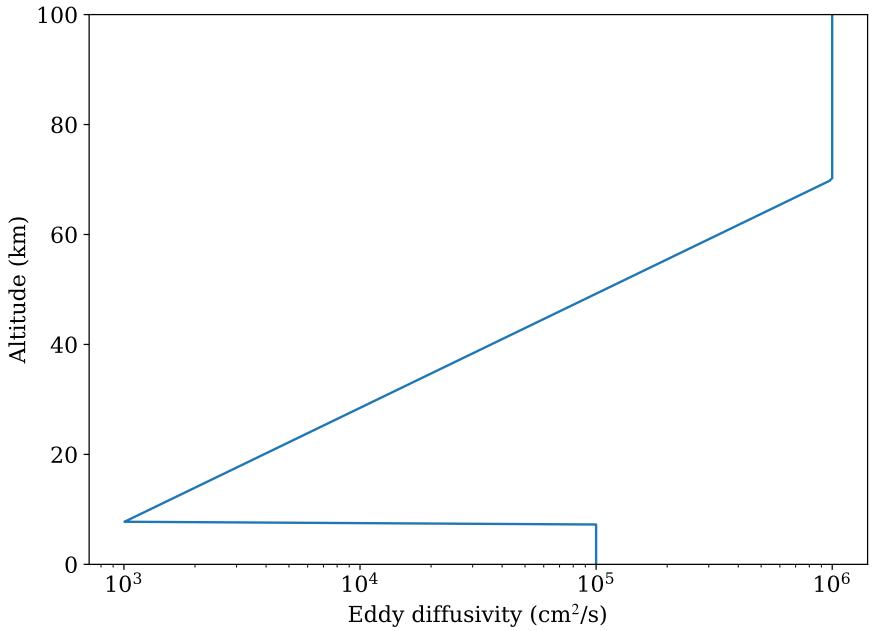

Figure 3.3: Example of an eddy diffusion profile used in PALEO.

in other photochemical models (eg Ranjan et al. 2020).

The surface boundary conditions for a species can be either defined by fluxes or mixing ratios. For example CO_2 can be prescribed a fixed value, which can be assumed given temperatures are likely to be regulated by the silicate weathering feedback. Setting a constant CO_2 means that a full carbon cycle is not required to regulate temperature. Flux boundary conditions are used to simulate gas input to the atmosphere, through processes such as volcanism.

3.3 Development and testing of the modelling framework

I now discuss developments I have made to both the UM and PALEO. The UM was developed for modelling of Archean atmospheres, while I co-developed PALEO to develop the atmosphere and biosphere modeling.

3.3.1 Adaption of UM to Archean

Before my work, the UM had yet to be adapted to the simulate the Archean. In order to do this, two main components were required: the development of the sea-ice albedo cal-

culations, which were initially designed for planets orbiting an M-dwarf star; and testing of the spectral files were required to check their validity at high methane concentrations.

3.3.1.1 Sea-ice albedo

As the idealised version of the UM used for terrestrial exoplanets has been developed without an ocean, the treatment of sea-ice is important to consider. Sea-ice plays an important role as a positive feedback on the Earth. As temperatures decrease due to some perturbation such as a reduction in CO_2, ice cover would increase. Ice has a high albedo for a solar spectra, which leads to more solar radiation reflected back to space, leading to a cooling of the Earth. In the absence of a fully coupled ocean, parametrisations are required to model the sea ice feedback. Initially, a parametrisation was included in the UM based on Joshi and Haberle (2012), for use with planet's orbiting M-Dwarfs. As M-dwarfs have a significantly lower effective temperature compared to the Sun, their stellar flux peaks at longer wavelengths, where the ice and snow albedo is smaller, shown in Figure 3.4.

The sea ice albedo effect is represented by a change in albedo at 271.35 K ($T_{\text{threshold}}$) using the HIRHAM parametrization from Liu et al. (2007), which calculates a temperature dependent sea ice albedo (α_{ice}) as

$$\alpha_{\text{ice}} = \alpha_{\text{max}}(\lambda) - \exp\left(-\frac{T_{\text{threshold}} - T_{\text{surf}}}{2}\right) \times (\alpha_{\text{max}}(\lambda) - \alpha_{\text{sea}}), \tag{3.27}$$

where T_{surf} is the surface temperature and $\alpha_{\text{max}}(\lambda)$ is the maximum sea ice albedo, a function of wavelength, λ. In the initial configuration, which I refer to as maximum albedo, when $\lambda \leq 1.1\,\mu$m $\alpha_{\text{max}} = 0.8$, while bands above $\lambda > 1.1\,\mu$m $\alpha_{\text{max}} = 0.05$.

However, when testing this ice albedo scheme for a preindustrial modern Earth configuration (N_2 dominated 280 ppmv CO_2), ice extended to close to 30° in latitude after 35 years of simulation time, shown in Figure 3.5. This is obviously much further than ice extends on Earth today and suggests that the ice albedo feedback is too sensitive, and the overall albedo is too large.

To resolve this, I tested different fits for albedo, the results for which are shown in Figure 3.6. These fits for albedo are marked on Figure 3.4 and assume a minimum,

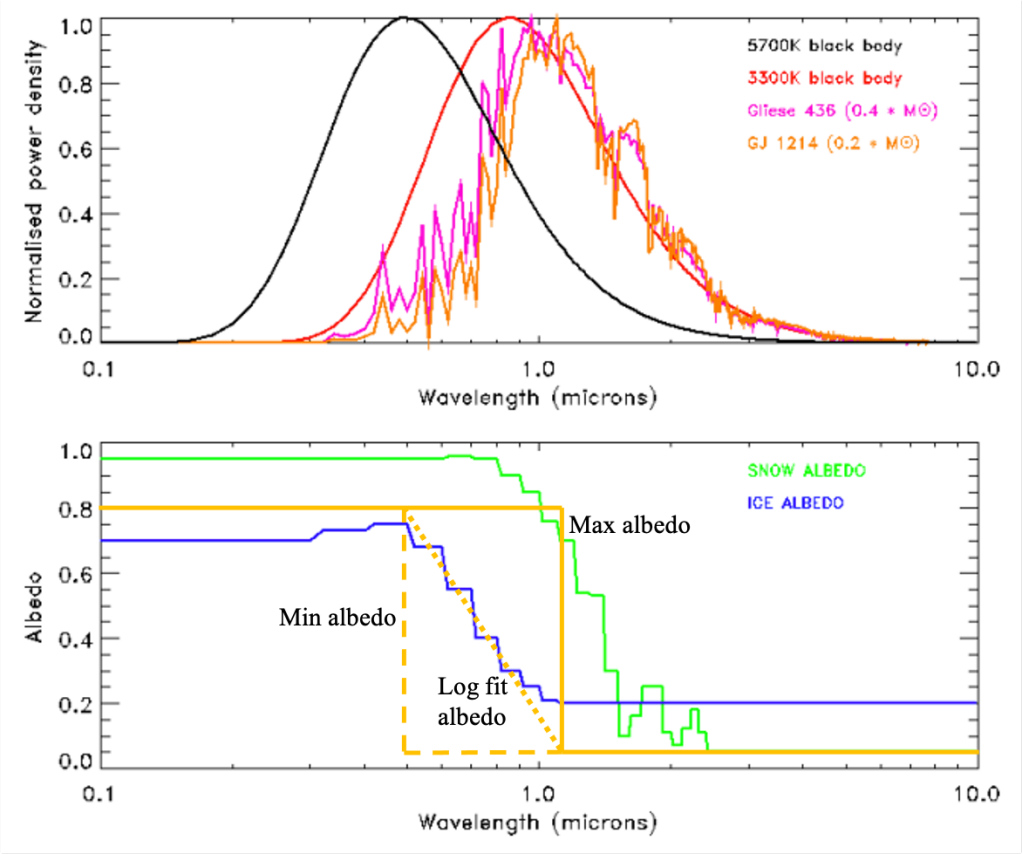

Figure 3.4: Top panel: Showing the normalised flux of black bodies of 5,700 K (approximately Solar) and 3300 K (M-Dwarf effective temperature), as well as the stellar fluxes of two M-dwarfs, Gleise 436 and GJ 1214. Lower panel: shows wavelengths dependence for ice and snow albedo, as well as different fits for albedo tested for the modern Earth. Figure is adapted from Fig. 1 in Joshi and Haberle (2012).

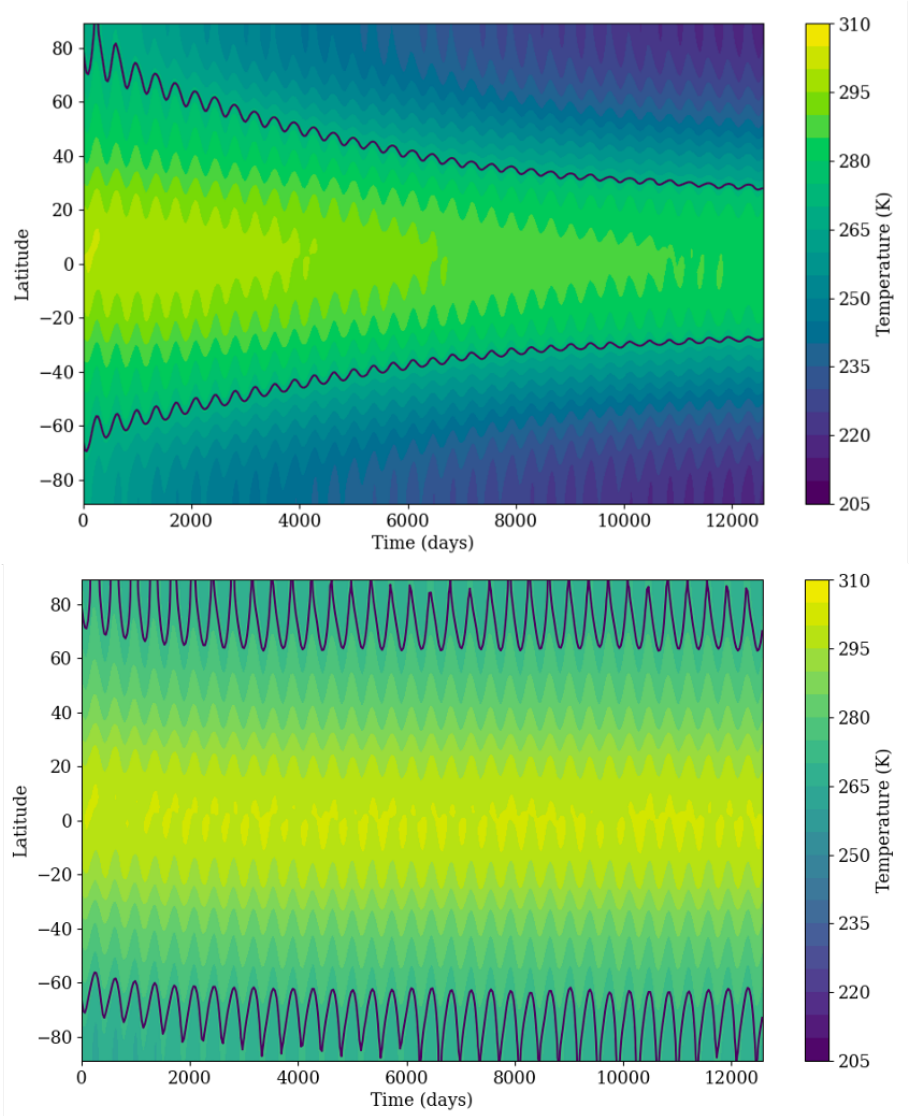

Figure 3.5: Shows the temporal evolution of zonal mean temperature for the previous maximum albedo sea-ice pararmetrisation (A) and the now used minimum albedo sea-ice pararmetrisation (B). The ice boundary (271.35 K) is shown as a black contour.

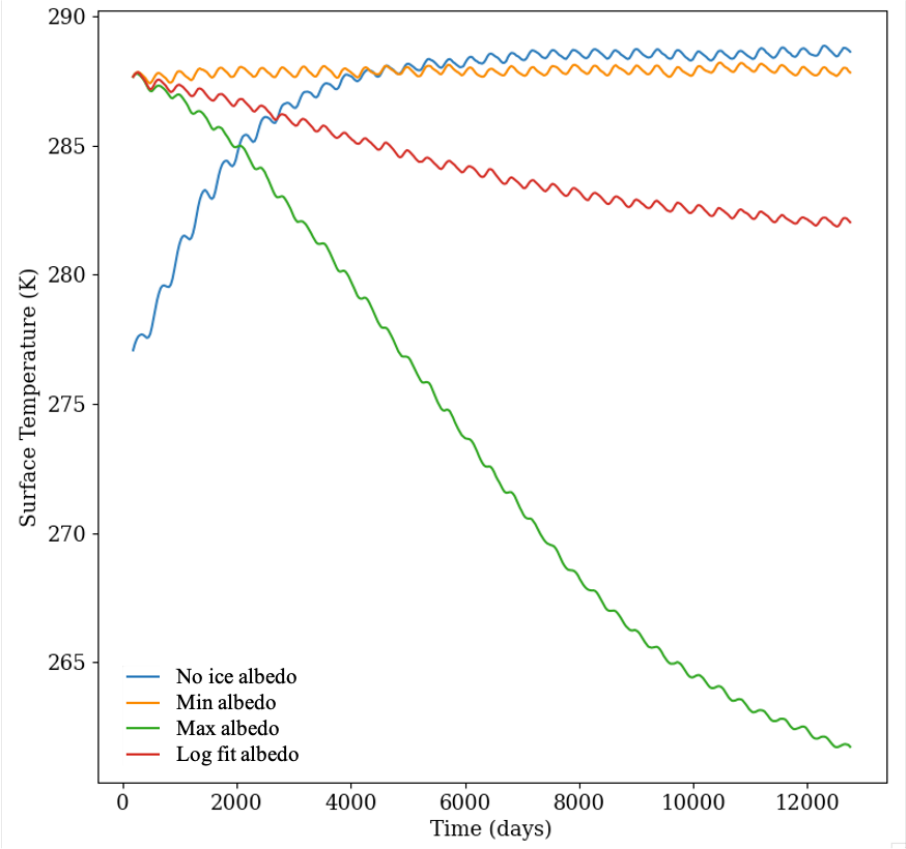

Figure 3.6: Shows the temporal evolution of global mean temperature for the diffeent sea-ice albedo parametrisations. The initial difference is due to different starting conditions for the no ice albedo case compared to the other simulations.

maximum (initial fit used) and log fitted albedo. A case where no change in albedo when temperatures drop below 271.35 K is also shown for reference. The minimum albedo case, sets the drop in albedo from 0.8 to 0.05 at 0.5 μm, while the log fit albedo case uses linear fit to calculate albedo between 0.5 and 1.1 μm over for $\log(\lambda)$. The new log fit still shows temperatures to be lower than the global mean pre-industrial temperatures (approximately 288 K), while the minimum albedo case is closest to the global mean, and is approximately 1° cooler than the case with no change in ice albedo. The sea ice extends to latitudes of approximately 65° (Figure 3.5b) during each hemisphere's winter, which is a reasonable comparison to Earth today, although during the summer, ice retreats too close to the poles.

For this minimum albedo fit, when convolved with the solar flux, our simplified scheme leads to a maximum ice albedo of approximately 0.2. Although this value is somewhat lower that the actual ice albedo (approximately 0.7), the simulations reproduced reasonable ice coverage for the modern Earth, see Figure 3.6. In reality, the scheme setup is

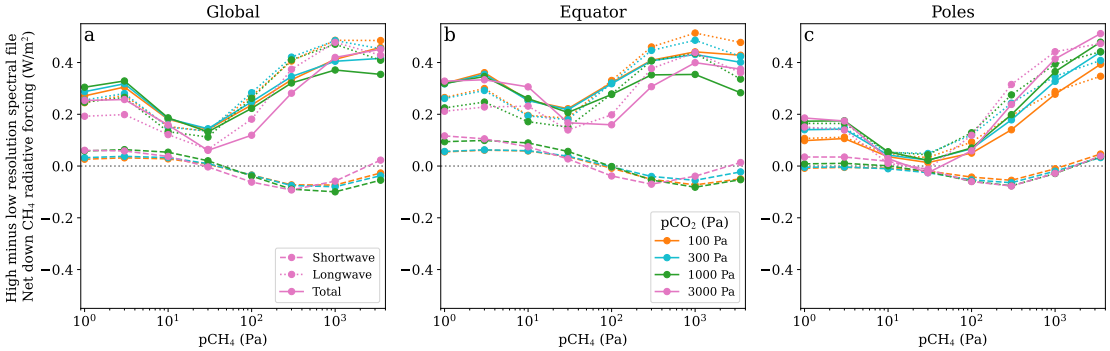

Figure 3.7: (a) shows the high resolution minus the low resolution spectral file global average net down radiative forcing at the tropopause for methane for shortwave (dashed), longwave (dotted) and their sum (solid). (b) and (c) show the same as (a) averaged over 10°S to 10°N as the equator in (b), and poleward of 70°N/S for the polar regions in (c). The high resolution spectral files for thermal and solar radiation are `sp_lw_350_etw_arcc10bar` and `sp_sw_280_etw_arcc10bar_sun_2.9gya` respectively, while the low resolution spectral files are `sp_lw_17_etw_arcc10bar` and `sp_sw_43_etw_arcc10bar_sun_2.9gya` for thermal and solar radiation respectively.

compensating for missing heat transport via the ocean and the lack of a more sophisticated thermodynamic ice scheme, alongside sea ice transport. Simple non-thermodynamic ice schemes like the ones used here have been shown to result in larger climate fluctuations and generally less ice coverage than their thermodynamic counterparts (Poulsen and Jacob 2004). This sea-ice albedo parametrisation is used going forwards for the modelling of the Archean climate.

3.3.1.2 Spectral file validity

In order to use spectral files for a range of Archean conditions, they must be tested against high resolution spectral files to confirm their validity and assumptions in their relatively low spectral resolution. This is particularly important when using spectral files close to their designed limits. Spectral files are designed for specific atmospheric compositions, temperatures and pressures. Outside of these limits the species opacities can change, which could also affect which species is the dominant absorbers in a band. This leads to inaccuracies in the radiative transfer calculations. I test the validity of these spectral files used in Chapter 4 and a higher resolution spectral file treatment with 280 solar radiation bands

(`sp_sw_280_etw_arcc10bar_sun_2.9gya`) and 350 thermal radiation bands (`sp_lw_350_etw_arcc10bar`) to assess the accuracy of our radiative transfer calculation. The results of this are shown in Figure 3.7. Errors in both the shortwave and longwave forc-

ing remain small (around 1 %) compared to the overall methane radiative forcing found in each configuration (see Figure 4.2), and thus the spectral files remain valid up to methane partial pressure of up to 3,500 Pa (3.5%).

3.3.2 PALEO developments

I co-developed the atmosphere module to add and update a range of important processes. Here I describe these processes and their implementation.

3.3.2.1 Molecular diffusion & hydrogen escape

Molecular diffusion is an important process for the upward transport of molecules that are significantly lighter than the mean molecular mass of the atmosphere. Of particular importance to molecular diffusion is molecular and atomic hydrogen. For this, I follow the implementation by Hu et al. (2012), with the molecular diffusion flux, Φ_{MD},

$$\Phi_{MD} = -DN\frac{\partial f}{\partial z} + Dn\left(\frac{1}{H_0} - \frac{1}{H} - \frac{\alpha_T}{T}\frac{dT}{dz}\right), \tag{3.28}$$

where n is the number density of either H or H_2, N is the overall number density of all species, f is the mixing ratio of the species (equal to n/N). D is the molecular diffusion coefficient, while the mean scale height is H_0, and H is the scale height of the species. α_T is the thermal diffusion factor and T is the temperature. The scale height is the change in altitude that would lead to a decrease in pressure by a factor of e, from which hydrostatic balance can be estimated as

$$H = \frac{RT}{\mu g} \tag{3.29}$$

where R is is ideal gas constant, μ is the the molecular mass (mean molecular mass for H and molecular mass of atomic or molecular hydrogen for H_0) and g is the gravitational acceleration.

The molecular diffusion coefficients, D (cm^2/s), from Hu et al. (2012) have a form obtained from gas kinetic theory with parameters derived from experimental data (Mar-

rero and Mason 1972) for atomic and molecular hydrogen in a N_2 dominated atmosphere are

$$D(\mathrm{H}, \mathrm{N_2}) = \frac{4.87 \times 10^{17} \left(\frac{T}{1\,[\mathrm{K}]}\right)^{0.698}}{N}, \tag{3.30}$$

$$D(\mathrm{H_2}, \mathrm{N_2}) = \frac{2.80 \times 10^{17} \left(\frac{T}{1\,[\mathrm{K}]}\right)^{0.740}}{N}, \tag{3.31}$$

and for a CO_2 dominated atmosphere Ranjan et al. (used for benchmarking our model to 2020):

$$D(\mathrm{H}, \mathrm{CO_2}) = \frac{3.87 \times 10^{17} \left(\frac{T}{1\,[\mathrm{K}]}\right)^{0.750}}{N}, \tag{3.32}$$

$$D(\mathrm{H_2}, \mathrm{CO_2}) = \frac{2.15 \times 10^{17} \left(\frac{T}{1\,[\mathrm{K}]}\right)^{0.750}}{N}, \tag{3.33}$$

where N is the number density in units of cm^{-3}.

Hydrogen escape can then be considered as the molecular diffusion at the top most level of the atmosphere, with hydrogen diffusing above this level, leaving the atmosphere top. At a model top of 100 km, H_2 and H are the predominant hydrogen bearing species, as other species are photochemically destroyed, justifying this approximation.

3.3.2.2 Redox balance

Reducing species are willing donators of electrons, while oxidants accept electrons, and reactions involving oxidation and reduction must be conserved, meaning that the net redox state of the reactants must be the same as the products. Following the discussion in Catling and Kasting (2017) Chapter 8, this means that for the atmosphere to be in equilibrium, the net redox input into the atmosphere, must be equal to loss. In atmospheres that

are more reducing, species redox potential is considered in terms of their redox potential relative to H_2. If we consider a hypothetical reaction of H_2 with O_2 to form water:

$$2\,H_2 + O_2 \longrightarrow 2\,H_2O, \tag{3.34}$$

as water is readily available on the surface H_2O can be arbitrarily set to be redox neutral, so that water flowing in and out of the system does not need to be tracked for redox balance. It can then be seen that as it takes 2 molecules of H_2 to reduce O_2, O_2 in terms of redox is -2 H_2 equivalents. The H_2 equivalents of C, N and S, can also be selected such that certain species are redox neutral. For C and S, a H_2 equivalent of +2 make CO_2 and SO_2 a neutral species, while H_2 equivalent of 0 for N makes N_2 neutral. The redox potential can be arbitrarily selected without affecting the results, however this choice makes tracking redox budgets simplest for reducing atmospheres (Kasting and Canfield 2012; Kasting 2013). From this, all species can then be assigned an H_2 equivalent redox state. Following Harman et al. (2015) for redox balance in the atmosphere to be conserved, the following balance must exist:

$$\Phi_{\text{outgas}}(\text{Red}) + \Phi_{\text{dep}}(\text{Ox}) = \Phi_{\text{esc}}(H_2) + \Phi_{\text{dep}}(\text{Red}) \tag{3.35}$$

where $\Phi_{\text{outgas}}(\text{Red})$ is the reductant outgassing through species such as H_2. $\Phi_{\text{esc}}(H_2)$ is the hydrogen escape flux, and $\Phi_{\text{dep}}(\text{Ox})$ and $\Phi_{\text{dep}}(\text{Red})$ is the wet and dry deposition of oxidising and reducing species respectively. While for global redox balance to be conserved, the following flux balance must be satisfied:

$$\begin{aligned}\Phi_{\text{outgas}}(\text{Red}) + \Phi_{\text{OW}} + \Phi_{\text{burial}}(CaSO_4) + \Phi_{\text{burial}}(Fe_3O_4) = \Phi_{\text{esc}}(H_2) + 2\Phi_{\text{burial}}(C_2HO) \\ + 5\Phi_{\text{burial}}(FeS_2)\end{aligned} \tag{3.36}$$

Φ_{OW} is the oxidative weathering of the continents and seafloor (reaction with oxygen), which would be minimal in low oxygen conditions like the Archean. $\Phi_{\text{burial}}(i)$ is the burial

of species i in the sediments, including organic matter, C_2HO. The burial terms are written in terms of their H_2 equivalent redox potential, with reducing fluxes on the left and oxidising fluxes on the right. Harman et al. (2015) make the assumption that on an abiotic planet, Φ_{OW} and $\Phi_{burial}(i)$ are negligible, leaving

$$\Phi_{outgas}(\text{Red}) = \Phi_{esc}(H_2), \tag{3.37}$$

which means that, from Equation 3.35

$$\Phi_{dep}(\text{Ox}) = \Phi_{dep}(\text{Red}), \tag{3.38}$$

meaning that the deposition must be redox neutral. To account for this, as these fluxes are rarely equal, balancing flux of H_2 or O_2 is added back into the atmosphere so that this surface exchange is redox neutral, as shown in Figure 3.8. In a biotic configuration, this is no longer true and organic carbon burial becomes and important flux in Equation 3.36. This is managed by separating the ocean cycling of species that are utilised by the biosphere from the deposition of other species, which is discussed in Section 3.3.2.7.

3.3.2.3 Chemical rates

The chemistry scheme was initially adapted from the atmos code using a similar rate calculator and reaction network in the Virtual Planetary Laboratory open access repository[2]. Initially, the atmos format for reaction rates were implemented, but were adapted to align with the format used in the UM (Drummond et al. 2020; Ridgway et al. 2022) and ATMO (Drummond et al. 2016), based on the JPL specification. For bimolecular reactions the rate coefficient, k, is calculated from the Arrhenius equation

$$k = A\left(\frac{T}{300}\right)^{\alpha} e^{-\beta/T}, \tag{3.39}$$

where A is a pre-exponential factor, T is temperature in kelvins, α determines the

2. https://github.com/VirtualPlanetaryLaboratory/atmos

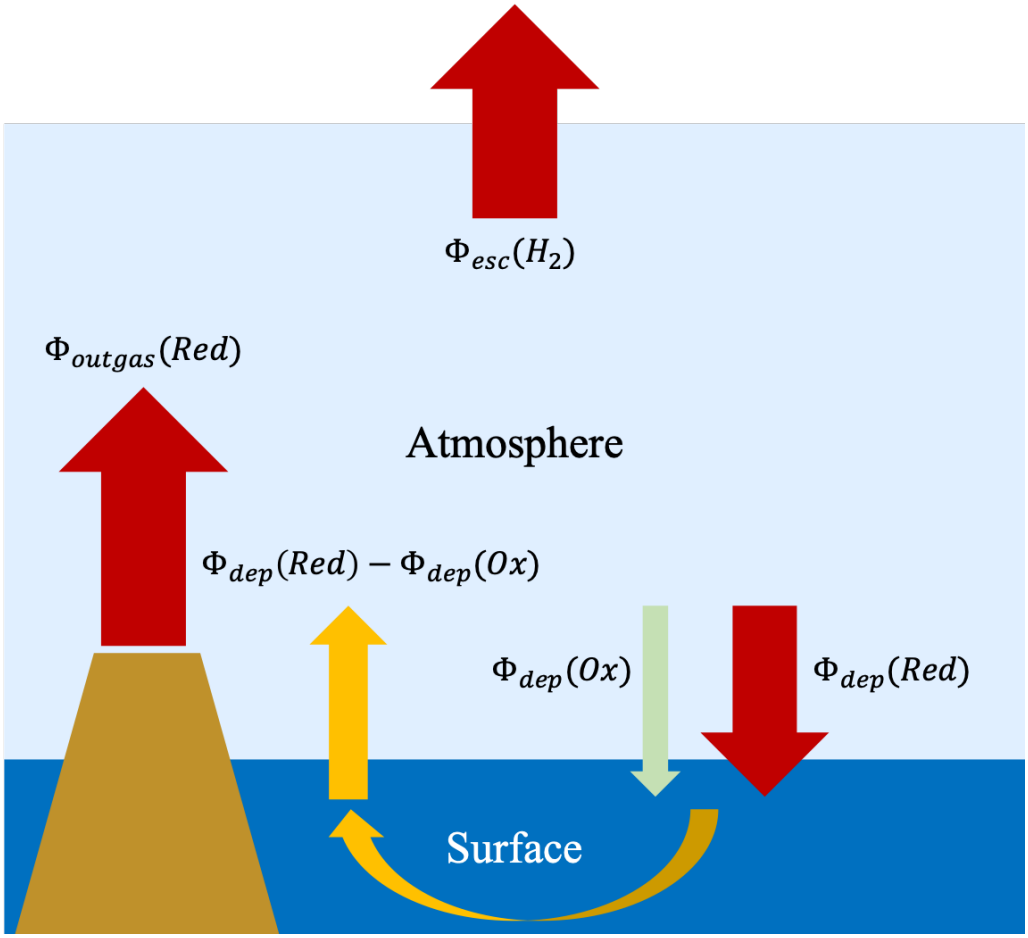

Figure 3.8: Schematic showing atmospheric redox balance. Reductant outgassing is equal to hydrogen escape, while total reductant and oxidant deposition is balanced by an equivalent return flux into the atmosphere to satisfy Equation 3.38.

degree of the temperature dependence for the reaction, β is the activation energy of the reaction divided by the gas constant. The parameters for each of the bimolecular reactions and their sources are listed in Table B.2.

For termolecular reactions, the following definitions are used for k_0 and k_∞

$$k_0 = A_1 \left(\frac{T}{300}\right)^{\alpha_1} e^{-\beta_1/T} \tag{3.40}$$

$$k_\infty = A_2 \left(\frac{T}{300}\right)^{\alpha_2} e^{-\beta_2/T} \tag{3.41}$$

with the terms for these mirroring those of Equation 3.39. The parameters for each of the termolecular reactions and their sources are listed in Table B.3.

3.3.2.4 Chemical network

A new reaction network was acquired from Mark Claire (Gregory et al. 2021), containing reactions for elements C, H, O, N, S for oxidising and reducing atmospheres. Some of these reactions did not follow conventional forms of the rate coefficient for bimolecular or termolecular reactions, which are termed "weird reactions" in the atmos code. These were adapted to conform with the formalism described in Section 3.3.2.3 without changing the rate coefficient. The reactions from this network are in Appendix B. As part of this, weird reactions were converted to formalisms that fit the bimolecular or termolecular form, for which there were six weird reactions

$\mathbf{HO_2 + HO_2 \longrightarrow H_2O_2 + O_2}$ - This reaction is a combination of a bimolecular and termolecular reaction and has been split accordingly. These reactions also both include corrective factors

$$k = 3 \times 10^{-13} [\mathrm{cm}^3/\mathrm{molecules/s}]\, e^{-490[\mathrm{K}]/T}, \tag{3.42}$$

the termolecular has the form of

$$k_0 = 2.1 \times 10^{-33} [\mathrm{cm}^6/\mathrm{molecules}^2/\mathrm{s}]\, e^{920[\mathrm{K}]/T}, \tag{3.43}$$

$$k_\infty = 1 \times 10^{-10} [\mathrm{cm}^3/\mathrm{molecules}/\mathrm{s}], \tag{3.44}$$

with $F_c = 0.6$.

HNO_3 + OH $\longrightarrow$ H_2O + NO_3 - Similar to above, this is another case of a combination of a bimolecular and termolecular reaction and has been split accordingly:

$$k = 2.4 \times 10^{-14} [\mathrm{cm}^3/\mathrm{molecules}/\mathrm{s}]\, e^{460[\mathrm{K}]/T}, \tag{3.45}$$

while the termolecular reaction has the form of

$$k_0 = 6.5 \times 10^{-34} [\mathrm{cm}^6/\mathrm{molecules}^2/\mathrm{s}]\, e^{1335[\mathrm{K}]/T}, \tag{3.46}$$

$$k_\infty = 2.7 \times 10^{-17} [\mathrm{cm}^3/\mathrm{molecules}/\mathrm{s}]\, e^{2199[\mathrm{K}]/T}, \tag{3.47}$$

with $F_c = 1$.

N_2O_5 + M $\longrightarrow$ NO_3 + NO_2 + M - This reaction takes the termolecular form from Atkinson et al. (2004)

$$k_0 = 1.3 \times 10^{-3} [\mathrm{cm}^3/\mathrm{molecules}/\mathrm{s}] \left(\frac{T}{300[\mathrm{K}]}\right)^{-3.5} e^{-11000[\mathrm{K}]/T}, \tag{3.48}$$

$$k_\infty = 9.7 \times 10^{14} [\mathrm{s}^{-1}] \left(\frac{T}{300[\mathrm{K}]}\right)^{0.1} e^{-11080[\mathrm{K}]/T}, \tag{3.49}$$

with $F_c = 0.35$.

HO_2NO_2 + M $\longrightarrow$ HO_2 + NO_2 + M - This reaction takes the termolecular form from (Atkinson et al. 2004)

$$k_0 = 4.1 \times 10^{-5}[\mathrm{cm}^3/\mathrm{molecules/s}]\, e^{-10650[\mathrm{K}]/T}, \tag{3.50}$$

$$k_\infty = 6 \times 10^{15}[\mathrm{s}^{-1}]\, e^{-11170[\mathrm{K}]/T}, \tag{3.51}$$

with $F_c = 0.4$.

SO_3 + H_2O + H_2O $\longrightarrow$ H_2SO_4 + H_2O - This reaction now takes the form of a bimolecular reaction with three reactants from Krasnopolsky (2012):

$$k = 6.9 \times 10^{-14}[\mathrm{cm}^6/\mathrm{molecules}^2/\mathrm{s}] \left(\frac{T}{300[\mathrm{K}]}\right)^1 e^{6540[\mathrm{K}]/T}. \tag{3.52}$$

OH + CO $\longrightarrow$ H + CO_2 - This currently takes the form of a chemical activation reaction (Sander et al. 2011). However, this has not been implemented yet within our network and so is included as a constant rate for a bimolecular reaction as suggested by (Burkholder et al. 2015; Ranjan et al. 2020)

$$k = 1.5 \times 10^{-13}[\mathrm{cm}^3/\mathrm{molecules/s}]. \tag{3.53}$$

HS + CS $\longrightarrow$ CS_2 + H - This reaction follows the same as the above, and is given the same rate equation.

The reducing network was also expanded to include species from the oxidising atmosphere, by including reactions involving NO_3, N_2O_5, HO_2NO_2 and converting the aggregate reaction:

$$HNO_3 + OH \longrightarrow H_2O + NO_2 + O, \tag{R3.20}$$

to

$$HNO_3 + OH \longrightarrow H_2O + NO_3, \tag{R3.21}$$

with the former used as NO_3 was not previously present.

3.3.2.5 Radiative-convective equilibrium models

The radiative transfer code SOCRATES, described in Section 3.2.1.1, has been coupled to PALEO to create a 1D radiative convective model. This setup allows for similar modelling tools to be used between 1D and 3D models, with these the same radiative transfer component. SOCRATES calculates the radiative heating rates from longwave and shortwave heating rates, which evolves the atmospheric temperature to reach a radiative equilibrium. The atmosphere above the tropopause exists in radiative equilibrium, however in the tropopause, radiative equilibrium leaves the atmosphere highly unstable, due to a high temperature gradient near the surface. If a parcel of air in this region moves upwards, it will be less dense than the surrounding air until it reaches a neutral buoyancy, with the parcel releasing energy, to reduce the temperature gradient. This should adjust the temperature structure of the troposphere to a profile that is just stable. This temperature gradient, termed the lapse rate is used to prescribe a convective adjustment, and can either be modelled as a fixed value, e.g. 6 K/km or by the pseudoadiabatic lapse rate, Γ_{ps},

$$\Gamma_{ps} = g \frac{(1 + r_v)\left(1 + \frac{L_v r_v}{RT}\right)}{c_{pd} + r_v c_{pv} + \frac{L_v^2 r_v (\epsilon + r_v)}{RT^2}}, \tag{3.54}$$

which is the dry lapse rate with moisture corrections. r_v is the water vapour mixing ratio,

c_{pd} and c_{pv} are the specific heats at constant pressure of dry air and water vapour. L_v is the latent heat of vaporization of water, R is the dry air gas constant, ϵ =0.62 is the ratio of the gas constants of dry air and water vapour. To be in equilibrium, the top of atmosphere net flux must be zero, and after applying this convective adjustment, the atmosphere is too hot, and the outgoing flux is greater than the incoming flux at the top of atmosphere. Equilibrium is restored by cooling the surface, until the the top of atmosphere is in radiative equilibrium, with the rate of surface temperature change calculated as

$$\frac{dT_{\text{surf}}}{dt} = -\frac{\Delta F_{\text{TOA}}}{C_p}, \tag{3.55}$$

where ΔF_{TOA} is the net outgoing top of atmosphere (TOA) flux (outgoing minus incoming) and C_p is the heat capacity of the surface per unit area.

This component is not currently coupled to the photochemical model, but can be used to generate climate solutions for atmospheric regimes that are explored.

3.3.2.6 Ocean

A single box ocean is used to house a biosphere, which is connected to the atmosphere via an atmosphere–ocean flux. The diffusion of species across the atmosphere–ocean interface is calculated using a stagnant boundary layer model (Liss and Slater 1974), with the exchange of gas dependent on the concentration of these gases through a thin stagnant layer at the ocean surface (thickness of 40 μm Kharecha et al. 2005). Using a similar procedure to Kharecha et al. (2005) the diffusion is determined by a piston velocity (thermal diffusivity of the species divided by the thickness of the stagnant layer) and solubility coefficient. The flux across the ocean-atmosphere boundary for species X, $\Phi(X)$ is then:

$$\Phi(X) = v_p(X) \times (\alpha(X) \times pX - [X]_{aq}) \times C, \tag{3.56}$$

where $v_p(X)$ is the piston velocity, $\alpha(X)$ is the Henry's solubility coefficient, pX is the atmospheric partial pressure at the top of the stagnant layer of species X and $[X]_{aq}$ is the ocean concentration of X at the bottom of the stgnant layer. C is a constant for unit

conversion to obtain a flux in mol/yr.

3.3.2.7 Biosphere

With an atmosphere-ocean flux established, considerations can be made for how species accumulation in the ocean could be utilised by the biosphere. An organism could consume a species to undergo either catabolism (production of energy) or anabolism (production of biomass). For example, consider an H_2 consuming methanogen. Catabolism can take the form of the following reaction, creating energy, which for organisms on Earth, are stored as adenosine triphosphate (ATP), which can then be used as energy for other processes:

$$CO_2 + 4\,H_2 \longrightarrow CH_4 + 2\,H_2O + (\text{energy}). \tag{R3.22}$$

When enough energy is stored it can be used to undergo anabolism:

$$CO_2 + 2\,H_2 + (\text{energy}) \longrightarrow CH_2O + 2\,H_2O. \tag{R3.23}$$

Lab measurements of these organisms have found that they can convert 1 mol of CO_2 into biomass via Reaction R3.23 for every 10 mol of CO_2 they metabolise via Reaction R3.22 (Schonheit et al. 1980; Fardeau and Belaich 1986; Morii et al. 1987). This gives them a growth rate, μ, of approximately $1/10$, eg for 10 mol of CO_2 is consumed in total to fix 1 mol of carbon as biomass. As CO_2 is widely available, H_2 is the limiting factor for this metabolism, and can be drawn down to some concentration, $[X]^{lim}_{aq}$, below which it is energetically unfavourable to draw concentrations down any further, with an overall methane flux, $\Phi_{bio}(CH_4)$ of

$$\Phi_{bio}(\mathrm{CH_4}) = \frac{1}{4} \times (1 - x \cdot \mu) \times ([X]_{aq} - [X]^{lim}_{aq}), \tag{3.57}$$

where x is the burial rate. The burial rate is the fraction of organic carbon that is buried in the sediments, known as organic carbon burial. This fraction may not be 100% if secondary organsims exist that consume the primary organisms (either alive or dead), undergoing a sequence of reactions such as:

$$2\,CH_2O \xrightarrow{\text{acetogens}} CH_3COOH \xrightarrow{\text{acetotrophs}} CH_4 + CO_2. \tag{R3.24}$$

This allows for some fraction of recycling within the ecosystem, which reduces organic carbon burial and therefore increases the CH_4 flux. On Earth, modern organic burial fraction is thought to be around 0.2% (Berner 1982), but in the past, it could have been around 2%, based on measurements in anoxic environments (Arthur et al. 1994).

Following the evolution of anoxygenic photosynthesis, this growth rate could be higher as energy does not need to be created by catabolsim to produce biomass and instead can use energy from photons for anabolism:

$$CO_2 + 2\,H_2 + h\nu \longrightarrow CH_2O + 2\,H_2O. \tag{R3.25}$$

which leads to a growth rate of $\mu = 1$. Without some form of recycling in this case, the majority of consumed H_2 would be buried, providing a significant reductant sink for the global redox budget, as in Equation 3.36. Ignoring other burial fluxes, our global redox balance is then determined by

$$\Phi_{\text{outgas}}(\text{Red}) = \Phi_{\text{esc}}(H_2) + 2\Phi_{\text{burial}}(CH_2O), \tag{3.58}$$

whilst the surface redox from deposition is maintained from Equation 3.38, provided that fluxes across the atmosphere-ocean boundaries are excluded and treated in the context of organic carbon burial.

3.4 Chapter Summary

In this chapter, I have introduced general circulation models, describing their use in resolving the faint young Sun paradox, as well as improving our understanding of the atmospheric circulation on terrestrial exoplanets. I also described the model I used in this thesis, the UM, and developments made to this. I will use this model in Chapters 4+5 in application to the Archean and then to terrestrial exoplanets.

I also introduced single column photochemical models, similarly describing their role in developing our understanding of the Archean and terrestrial exoplanets. I then introduced PALEO, which is a flexible model of the atmosphere and ocean, and described my contributions to developments here to construct a simple general ecosystem model that is used in Chapter 6 to understand the effect of primitive biospheres on the atmospheres of exoplanets.

Chapter 4

Climate of Archean-like Atmospheres

4.1 Introduction

This Chapter investigates the role of methane in the Archean climate using a general circulation model, and its potential to contribute to the faint young Sun paradox. The work from this chapter has been published in Eager-Nash et al. (2023).

Methane (CH_4) is thought to have played an important role as a greenhouse gas in warming the Archean Earth (Haqq-Misra et al. 2008; Catling and Zahnle 2020). The Archean is the geological eon spanning 4.0–2.5 billion years ago (Ga). The Archean was believed to be oxygen poor, with oxygen concentrations less than 3×10^{-6} of the present atmospheric level (PAL) (Gregory et al. 2021), which allowed reduced gases, such as methane, to accumulate in the atmosphere (Catling and Zahnle 2020). Here, I investigate the potential role of methane, and to a lesser extent carbon dioxide (CO_2), on the Archean climate using a three-dimensional general circulation model (GCM), at various carbon dioxide concentrations. The use of a GCM further allows an understanding to be gained of the effect of methane on the global mean climate and the meridional temperature structure.

The Archean could have supported high methane concentrations at various points

in its history (e.g Fig. 5 in Catling and Zahnle 2020). A primitive pre-photosynthetic biosphere would effectively turn reductant (electron donors) from mantle inputs or oxidation of the crust into reduced organic carbon and ultimately methane (e.g. Nicholson et al. 2022). As methane will be photolysed to hydrogen at high altitude, atmospheric methane levels are then determined by the balance between surface net reductant (hence methane) input, and hydrogen escape (Kharecha et al. 2005; Goldblatt et al. 2006; Claire et al. 2006). Kharecha et al. (2005) used a coupled ecosystem-atmosphere model to suggest that the early Archean biosphere could have sustained methane concentrations between 100 to 35,000 ppm (equivalent to 10–3,500 Pa in surface partial pressure for a 10^5 Pa atmosphere). Subsequent evolution of increasingly productive photosynthetic biospheres and ultimately oxygenic photosynthesis could increase methane concentrations as they increase the net reductant input via oxidation of crustal material (Walker 1987, primarily Fe,). This is supported by a depletion in organic carbon-13 in deep water sediments at 2.7 Ga (Eigenbrode and Freeman 2006). After the great oxidation event, the concentration of methane as a minority gas in an oxic atmosphere will be controlled by the balance between primarily biological production and photochemistry, where the net biological flux to the atmosphere will be controlled by ecosystem structure and biogeochemical cycling hence methane oxidation within the surface environment (Daines and Lenton 2016).

Updates to the high-resolution transmission molecular absorption database (HITRAN) have led to work finding that earlier studies have overestimated methane's potential to warm the Archean (Byrne and Goldblatt 2015). Previously, Haqq-Misra et al. (2008) found that methane, ethane and the subsequent formation of longer chain hydrocarbons can provide significant warming. However, updates to HITRAN (Brown et al. 2013; Rothman et al. 2013) show an increase in the shortwave absorption by methane that was previously underestimated, leading to a decrease in tropopause radiative forcing by methane at high concentrations (see discussion in Byrne and Goldblatt 2014). This was found to lead to the greenhouse effect of CH_4 becoming offset by strong shortwave absorption by methane in the atmosphere (Byrne and Goldblatt 2015). Using a 1D radiative convective model (RCM) Byrne and Goldblatt (2015) found that surface warming due to methane is diminished at 100 Pa (0.1% by volume), with shortwave cooling dominating longwave heating above this. Methane shortwave radiative forcing has also been investigated for

the modern Earth (Etminan et al. 2016; Collins et al. 2018; Byrom and Shine 2022). Byrom and Shine (2022) found that methane's warming of the stratosphere by absorption of shortwave radiation can enhance methane longwave radiative forcing.

During the Archean, the Sun's luminosity was 75% to 80% of the present day value (Gough 1981). As discussed in Charnay et al. (2020), as the Sun fuses hydrogen into helium the mean molecular weight of the Sun's core increases. The core then contracts and warms to maintain the balance between the pressure gradient and gravitational forces. This increases the rate of fusion, which causes the Solar flux to increase with time. Under present atmospheric conditions the Earth is predicted to have been globally ice covered (known as a snowball state) prior to ~2.0 Ga (Kasting and Catling 2003). However, there is ample evidence that the Earth was not in a snowball state (for example see Feulner 2012; Charnay et al. 2020). This was termed the faint young Sun (FYS) paradox (Sagan and Mullen 1972), with uncertainty over what kept the early Earth warm. The resolution of the FYS paradox is likely to be due to increased greenhouse gas concentrations during the Archean, particularly carbon dioxide (Charnay et al. 2020) as well as methane.

Geological evidence has been used to predict CO_2 concentrations through the Archean. Mass balance calculations from CO_2 dissolved in rainwater give estimates of CO_2 10–50 PAL (340–1,700 Pa) at 2.7 Ga (Sheldon 2006; Driese et al. 2011), although this may be a lower limit (Catling and Zahnle 2020). Another method using chemical compositions of paleosols predicts CO_2 85-510 PAL (3,000–15,000 Pa) at 2.77 Ga and 78-2500 PAL (2,000–75,000 bar) at 2.75 Ga (Kanzaki and Murakami 2015). A more recent approach using oxidation of fossilised micrometeorites from 2.7 Ga (Tomkins et al. 2016) suggests a lower limit for atmospheric CO_2 of 32% (32,000 Pa) (Huang et al. 2021), although debate remains over these estimates, with a lower surface pressure offering an alternative solution to explain the micrometeorite oxidation (Rimmer et al. 2019).

General Circulation Models (GCMs), which are three-dimensional models attempting to capture the main processes determining the planetary climate, have played an important role in understanding the climate of the Archean (Charnay et al. 2013; Wolf and Toon 2013; Kunze et al. 2014; Le Hir et al. 2014; Charnay et al. 2020). GCMs have been used to show that compared to 1D models, lower amounts of CO_2 are required to main-

tain global surface temperatures of 15°C, and more importantly, avoid a full glaciation (Charnay et al. 2013; Wolf and Toon 2013). Furthermore, the use of GCMs has found that potential reductions in land fraction and albedo during the Archean, as well as a reduction in cloud condensation nuclei may have helped to keep the early Earth warm (Wolf and Toon 2014; Goldblatt et al. 2021). GCMs have also been used to explore the potential for glaciations at the end of the Archean (Teitler et al. 2014), alongside being combined with models of carbon cycling to investigate the plausibility of hot Archean climates (Charnay et al. 2017).

In this chapter I extend the 1D work of Byrne and Goldblatt (2015) by exploring the 3D effects of changing the methane concentration using the Met Office Unified Model (UM) GCM. First, I outline the model configurations used for our Archean-like Earth simulations using the UM in Section 4.2. The results are presented in Section 4.3 where I demonstrate that methane has a maximum potential global warming of up to 7 K. I then go on to show that methane changes the equator-to-pole temperature differences by changing the meridional circulation and the radiative forcing at the poles. In Section 4.4 I discuss the importance of 3D modelling in understanding the meridional circulation, and the possible impact haze may have on the results. Finally, I draw conclusions in Section 4.5 and highlight future avenues for improving on this study.

4.2 Methods

The UM has been used extensively to study the modern Earth (e.g. Walters et al. 2019; Sellar et al. 2019; Andrews et al. 2020; Maher and Earnshaw 2022), and has been adapted to simulate a range of idealised Earth-like planets (e.g. Mayne et al. 2014b; Boutle et al. 2017; Lewis et al. 2018; Yates et al. 2020; Boutle et al. 2020; Sergeev et al. 2020; Eager-Nash et al. 2020; Sergeev et al. 2022b). Here, I apply this model to the Archean, deep in the Earth's past. I use the Global Atmosphere (GA) 7.0 configuration (Walters et al. 2019). Dynamics are calculated using the ENDGame dynamical core (Wood et al. 2014), while convection is treated using a mass-flux approach based on Gregory and Rowntree (1990). Water clouds are treated using the prognostic cloud fraction and prognostic condensate scheme (PC2) (Wilson et al. 2008), which incorporates mixed phase microphysics based on Wilson and

Ballard (1999). Turbulent mixing is based on Lock et al. (2000) and Brown et al. (2008). These schemes are combined and shown as a schematic in Figure 3.2. Simulations have a horizontal resolution of 2.5° in longitude by 2° in latitude, with 38 vertical levels between the surface ($z = 0$ km) and the top-of-atmosphere ($z = 40$ km). The vertical levels are quadratically stretched to enhance the resolution at the surface.

The Suite of Community Radiative Transfer codes based on Edwards and Slingo (SOCRATES) scheme treats the radiative transfer in the UM, employing the correlated-k method (included in schematic in Figure 3.2). Thermal radiation is treated via 17 bands (between 3.3 μm-10 mm), while solar radiation is treated by 43 bands (0.20-20 μm) using the `sp_lw_17_etw_arcc10bar` and `sp_sw_43_etw_arcc10bar_sun_2.9gya` spectral files respectively. These are suitable for atmospheres dominated by a mixture of N_2 and CO_2 (from 1% to 20%), with up to 3.5% CH_4 (tested in Section 3.3.1.2), supporting surface pressures up to 10^6 Pa. These include CO_2 sub-Lorentzian line wings and CO_2 self-broadening. Collision induced absorption is included for: N_2–CH_4, N_2–N_2 and CO_2–CO_2 from HITRAN (Karman et al. 2019), and CH_4–CO_2 from Turbet et al. (2020). Line data are from HITRAN 2012 (Rothman et al. 2013), the same as used in Byrne and Goldblatt (2015). The solar spectrum is taken for a 2.9 Ga Sun spectrum from Claire et al. (2012). Testing of our radiative transfer against higher resolutions for the gas mixtures used here can be found in Section 3.3.1.2 and Figure 3.7, focusing on the CH_4 tropopause radiative forcing.

Methane radiative forcing is calculated at the tropopause. It is the net downward total “all-sky" radiative flux subtracted by the all-sky flux with methane switched off radiatively, which is calculated for the present model configuration without altering the climate state. Similar to the definition from the World Meteorological Organisation (1957), the tropopause is defined as the region above 500 hPa where the lapse rate is less than or equal to 2 K/km for at least two consecutive vertical model levels.

The simulations were configured as an aquaplanet, using a single layer slab homogeneous flat surface as the inner boundary (planet’s surface), which is based on Frierson et al. (2006). It represents an ocean surface with a 50 m mixed layer with a heat capacity of 2.08×10^8 J/K/m^2, with no horizontal heat transport. The emissivity of the surface is fixed at 0.985 (Snyder et al. 1998) and the liquid water surface albedo (α_{sea}) is fixed at 0.07 (Jin

et al. 2004). The assumption of an aquaplanet was made with predictions that the ocean water content may have been larger than today (Dong et al. 2021), and continental coverage was likely lower (Cawood et al. 2013). Although excluding horizontal heat transport in the ocean is inherently inaccurate, the uncertainty in continental coverage and location means that the inclusion of a dynamic ocean will also lead to further inaccuracies that may obfuscate the effects I am exploring in this chapter. I use the developments to the ice scheme discussed in Section 3.3.1.

This Chapter focuses on 2.7 Ga as at this time methane concentrations could have been high, as the evolution of oxygenic photosynthesis may have supported a widespread productive biosphere (indicated by depletion of organic carbon-13 in marine sediments, Eigenbrode and Freeman 2006; Daines and Lenton 2016). This increase in biotic oxygen production is prevented from oxidising the atmosphere by burial of oxidants in the highly insoluble form of iron oxides whilst reductant was added to the atmosphere as methane through recycling of organic carbon (Walker 1987). Hence, there is a net oxidation of the Earth's surface and net reductant input into the atmosphere. Planetary parameters used in our simulations are presented in Table 4.1. The fainter Sun at 2.7 Ga meant that the solar constant was less than the present day. From Gough (1981) (their Equation 1), this can be estimated as 81% of the modern solar constant, S_0, of 1361 W/m^2 (Kopp et al. 2016).

At 2.7 Ga the Earth's rotation rate was believed to be faster than the present Earth. Williams (2000) predict that the rotational period at 2.45 Ga could have been between 16.0 and 19.4 hrs, while Bartlett and Stevenson (2016) (from their Figure 5) suggest a range of between approximately 16.0 to 19.5 hrs at 2.7 Ga depending on the magnitude of the lunar torque at the time. In this Chapter a rotational period of 17 hrs is used, although the exact value over this range has a minimal impact on the overall results presented here. For simplicity, the modern obliquity (see Table 4.1) is used as it is unclear how obliquity could be significantly different to the present day, however, following the choices made by Charnay et al. (2013) and Wolf and Toon (2014), the eccentricity is set to zero.

In these simulations, I vary the methane partial pressures from 1 to 3,500 Pa to cover the range predicted by Kharecha et al. (2005), as well as extending the lower limit in line with Byrne and Goldblatt (2015), to include potential methane concentrations from only

abiotic sources, $pCH_4 \approx 1$ Pa (Kasting 2005). I also include a baseline case, without methane, as a comparison for our simulations with varying atmospheric methane concentrations. The initialised CO_2 surface partial pressure is varied from 100 to 3,000 Pa covering some of the large variation in paleosol constraints (340–75,000 Pa) and use the lower value of 100 Pa to match Byrne and Goldblatt (2015). pCO_2 is varied to cover a range of predicted CO_2 abundances at the time, from 100–3,000 Pa. For pCO_2=10,000 Pa our simulations were significantly warmer than the modern day Earth and the UM becomes unstable for the higher methane concentrations. Therefore, I omitted these cases from this Chapter and used $pCO_2 \leq$3,000 Pa as the upper limit.

These surface partial pressures are the values initialised in the model, while the total surface pressure, and thus individual partial pressures, can evolve from the initialised value. However, the equivalent volume mixing ratios have no spatial or temporal variation. The reason for the choice in using partial pressures is to ensure that the mass of N_2 and CO_2 is kept constant with variations in CH_4 abundance. This is to replicate methane production by the biosphere, adding methane to the atmosphere. Surface pressures range from 1-1.035$\times 10^5$ Pa, which aligns with the upper limit of surface pressures from Som et al. (2012), as well as using similar conditions to Byrne and Goldblatt (2015).

Fixed gas mixing profiles are used in these simulations, with no chemistry included. This assumption is validated by 1D photochemical models, which show that the volume mixing ratio remains relatively constant up to 40 km (top of model in our simulations) for carbon dioxide (e.g. Huang et al. 2021) and methane (e.g. Kharecha et al. 2005; Gregory et al. 2021) at low oxygen concentrations.

Initial simulations with no CH_4 ran for 60 years to allow for atmospheric equilibrium to be reached. Subsequent runs with CH_4 present were initialised from these simulations and ran for another 50 years to reach a new steady state. All the simulations were in steady state by the final 15 years, so this period is used for our analysis. Steady state was deemed to have been reached when the top of atmosphere radiative flux was in balance and the mean global surface temperature was near constant. In this chapter, I refer to equatorial and polar regions. The equatorial region is considered as spanning latitudes of 10° S to 10° N, while the polar regions are 70° S/N to the pole, which are averaged over

Table 4.1: The planetary and orbital parameters used for all planetary configurations, based on a 2.7 Ga Earth. Stellar irradiance is calculated using Gough (1981), based on a modern day solar constant S_0 = 1361 W/m^2 (Kopp et al. 2016). Rotation rate is based on estimates from Williams (2000) and Bartlett and Stevenson (2016). Partial pressures represent the values initialised in the model at the surface.

Parameter	2.7 Ga Archean Earth
Stellar irradiance (W/m^2)	1100.8 (0.809S_0)
Day length (hours)	17.0
Eccentricity	0
Obliquity (°)	23.44
pCO_2 (Pa)	100, 300, 1000, 3,000
pCH_4 (Pa)	0, 1, 3, 10, 30, 100, 300, 1000, 3,500
pN_2+pCO_2 (Pa)	100,000
Surface pressure	pN_2+pCO_2+pCH_4

these regions in figures henceforth. UM output was processed and plotted using Python's IRIS (Met Office 2020), AELOUS (Sergeev and Zamyatina 2022) and Matplotlib (Hunter 2007) packages.

4.2.1 Calculations of heat fluxes in polar and equatorial regions

Here, I outline the method used by Lambert et al. (2011) to understand the net heat transport in and out of regions of the atmosphere. This method was initially designed for use in understanding heat transport by the atmosphere between regions of the atmosphere covering land and ocean. Here, this is applied to the heat transport out of equatorial regions and into polar regions, with the heat flux out of the equatorial region, $\frac{\Delta A_E}{f_E}$, given as:

$$-\frac{\Delta A_E}{f_E} = \Delta N_E - \Delta U_E - \Delta U_{EA}, \tag{4.1}$$

where ΔA_E is the heat transport anomaly between the equatorial region and the rest of the planet. f_E is the equatorial fraction of the global surface (spanning latitudes of 10° S to 10° N, f_E =17.4%). ΔN_E is the net incoming radiation at the top-of-atmosphere, while ΔU_E is the net upward flux at the surface including both turbulent and radiative fluxes. ΔU_{EA} is the rate of heat storage by the atmosphere over the equatorial region, which is approximated by the globally averaged heat uptake by the atmosphere, ΔU_{GA}:

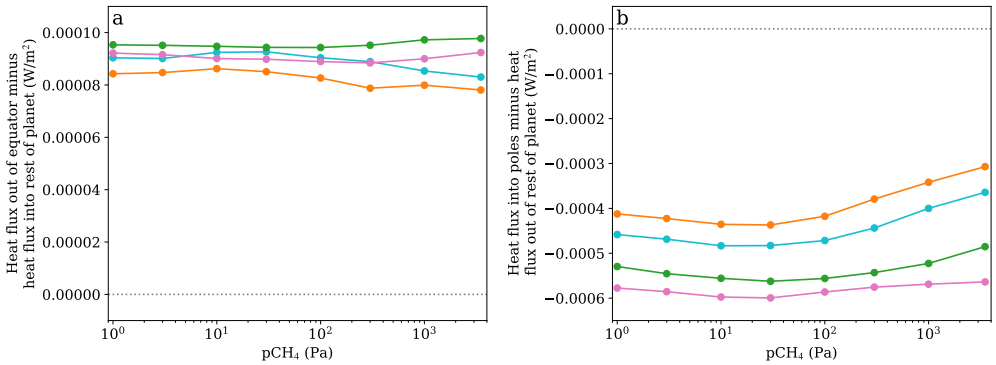

Figure 4.1: (a) shows the difference between the heat flux leaving the equatorial region and the heat flux into the rest of the atmosphere from the equator from Equation 4.1 and Equation 4.3. Similarly (b) shows the difference between the heat flux entering the polar regions and the heat flux from the rest of the atmosphere from Equation 4.4 and Equation 4.5. The equatorial region is considered as spanning latitudes of 10° S to 10° N, while the polar regions are 70° S/N to the pole.

$$\Delta U_{GA} = \Delta N_G - \Delta U_G, \tag{4.2}$$

where the subscript G refers to the global averaged quantities discussed above.

Equivalent expressions can be written for heat flux into the rest of the planet from the equatorial region, as well as the heat flux into the poles and the heat flux from the rest of the atmosphere into the poles:

$$\frac{\Delta A_E}{1 - f_E} = \Delta N_{E'} - \Delta U_{E'} - \Delta U_{E'A}, \tag{4.3}$$

$$\frac{\Delta A_P}{f_P} = \Delta N_P - \Delta U_P - \Delta U_{PA}, \tag{4.4}$$

$$\frac{\Delta A_P}{1 - f_P} = \Delta N_{P'} - \Delta U_{P'} - \Delta U_{P'A}, \tag{4.5}$$

where subscript P represents the polar regions, while E' and P' are the rest of the world excluding the equatorial and polar regions respectively.

This method can be validated by calculating the difference of the heat flux between

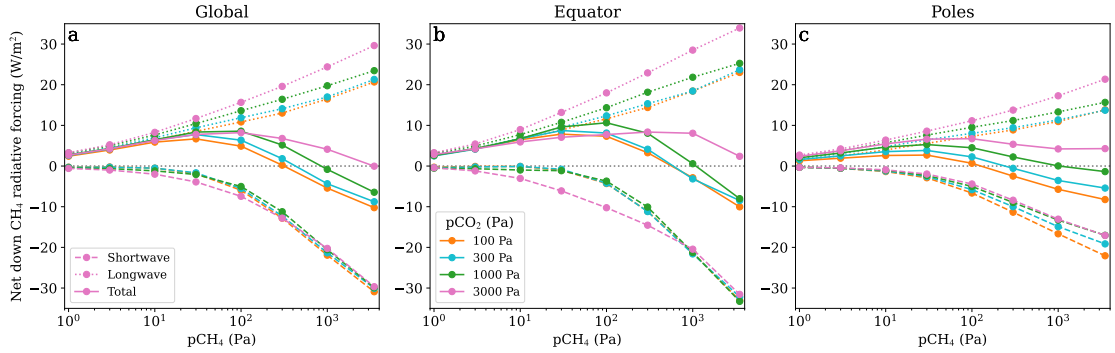

Figure 4.2: (a) shows the global average net down radiative forcing at the tropopause for methane for shortwave (dashed), longwave (dotted) and their sum (solid). (b) and (c) show the same as (a) averaged over 10°S to 10°N as the equator in (b), and poleward of 70°N/S for the polar regions in (c).

the equatorial/polar regions and the rest of the atmosphere. These are shown in Figure 4.1, with the differences more than 1000 times smaller than 1 W/m^2, showing the self consistency of the method and that it is suitable for applying to understanding heat transport between regions of the atmosphere other than just those over land and sea.

4.3 Results

In this section I demonstrate that methane has a maximum potential warming of up to 7 K globally in our Archean-like simulations. Furthermore, I find that the equator-to-pole temperature difference generally increases with pCH_4, which is driven by the difference in methane radiative forcing at the equator and poles and also the decrease in circulation strength driven by upper troposphere heating by methane shortwave absorption.

Methane radiative forcing plays an important role in driving the climate. This is shown for all of our simulations in Figure 4.2. Figure 4.2a shows the global tropopause radiative forcing by methane. As pCH_4 is increased, initially total radiative forcing increases due to an increase in longwave radiative forcing (dotted lines in Figure 4.2a) causing surface temperature to increase. As pCH_4 continues to increase, shortwave radiative forcing becomes more negative (dashed lines in Figure 4.2a) caused by absorption of shortwave radiation, which becomes comparable to the magnitude of longwave radiative forcing and causes methane's total radiative forcing to decrease again, driving a cooling of the surface. Similar to the results found in Byrne and Goldblatt (2014), the shortwave absorption becomes significant for pCH_4>10 Pa, with the total (longwave plus shortwave) methane

radiative forcing similarly having a maximum of approximately 8.5 W/m^2, compared to 9 W/m^2 in Byrne and Goldblatt (2014).

Figure 4.2b,c show the methane radiative forcing for equatorial and polar regions respectively. Equatorial forcing exhibits similar trends to the global average, while polar radiative forcing is of a lower magnitude, with total radiative forcing peaking at smaller pCH_4 compared to the equatorial and global regions. Shortwave forcing is weaker at the poles for pCO_2=3000 Pa compared to the other pCO_2 values, while longwave forcing is stronger, leading to methane radiaitve forcing at the poles plateauing at $pCH_4 \geq 1000$ Pa.

The effects of this change in radiative forcing by methane are now explored for these different cases by examining the difference in climate between these configurations.

4.3.1 Meridional air temperature variation and the Hadley circulation

Increasing pCO_2 in our Archean-like configuration leads to a familiar result in increasing temperatures globally (e.g. Charnay et al. 2013). Figure 4.3 shows a subset of our simulations and reveals that increasing pCO_2 from 100 Pa to 3,000 Pa (comparing left and middle columns) at any pCH_4 leads to the zonal mean air temperatures rising globally in the troposphere, with the polar regions warming more than equatorial regions, shown by the right hand column of Figure 4.3, which shows the increase in air temperature from pCO_2=100 Pa to pCO_2=3,000 Pa. Minimum temperatures decrease due to the stratosphere cooling with increasing pCO_2 due to more efficient cooling of the atmosphere.

Increasing surface pCH_4 from 1 Pa to 3,500 Pa, leads to a smaller change in troposphere air temperatures compared to changing pCO_2, but large increases in stratospheric temperature. Figure 4.3 shows that increasing pCH_4 initially leads to troposphere warming, which peaks between pCH_4 values of 30–300 Pa and increasing pCH_4 further leads to cooling of the troposphere at lower pCO_2 and plateauing at higher pCO_2 (see bottom row of Figure 4.3), which is driven by changes the methane radiative forcing (Figure 4.2a). Increasing pCH_4 also leads to a warming of the stratosphere, and the formation of a stratospheric temperature inversion, visible at $pCH_4 \geq 300$ Pa at pCO_2=100 Pa and pCH_4=3,500 Pa at pCO_2=3,000 Pa in Figure 4.3. The magnitude of the warming can

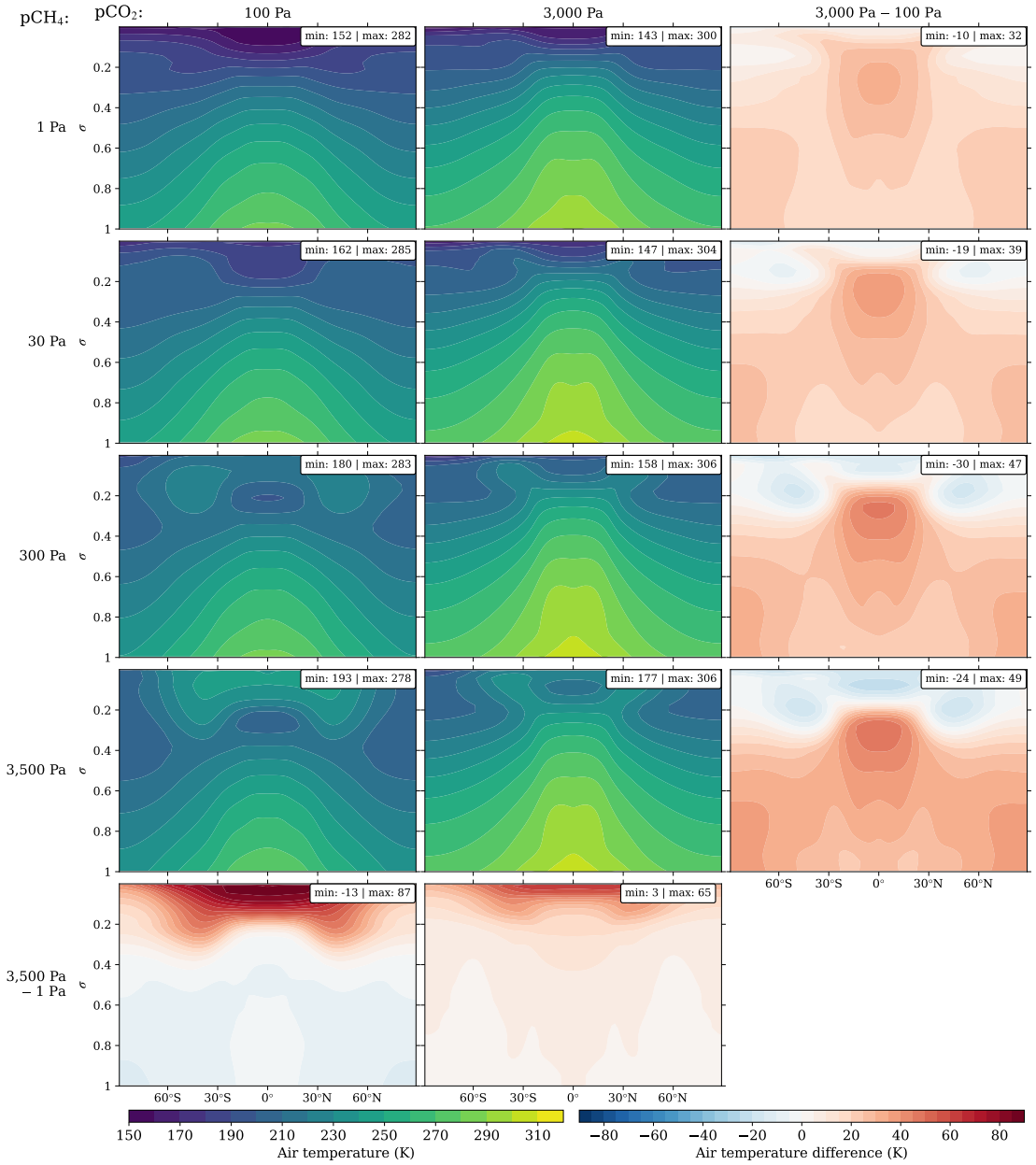

Figure 4.3: Zonal averaged air temperature (colour scale), for increasing surface partial pressures of carbon dioxide from left to right, and methane from top to bottom. The right hand column shows the difference in air temperature between pCO_2=100 Pa and pCO_2=3,000 Pa (the left and middle columns). The bottom row shows the change in air temperature between the pCH_4=1 Pa and pCH_4=3,500 Pa case for a given pCO_2. In both of these cases a positive increase represents an increase in air temperature for the simulation with higher pCH_4/pCO_2. Plotted as latitude vs σ, where σ is the pressure divided by the surface pressure. This is for a subset of the simulations, with the full grid available in A.1 (Figure A.1). The same colour scale is used for the left and middle columns, with maximum and minimum temperatures for each simulation displayed in the top right of each sub figure. The right column and bottom row use a another colour scale that is constant between the subplots. These subplots also displays the maximum/minimum temperature differences in the top right of each sub figure.

by seen in bottom row of Figure 4.3, which shows the change in air temperature between pCH_4=1 Pa and pCH_4=3,500 Pa with the stratosphere warmer by up to 87 K at pCH_4=3,500 Pa and pCO_2=100 Pa. This warming of the stratosphere is caused by the increase in shortwave heating of the upper atmosphere caused by methane (shown by the contours in Figure 4.5). These changes in air temperature show similar trends to those presented in Byrne and Goldblatt (2015). Horizontally averaged pressure-temperature plots for the equator and poles are shown in Figure 4.4.

The Hadley circulation strength is shown in Figure 4.5 in the form of meridional stream functions. The shorter rotational period of the planet used here (17 hour day compared to 24 hour) leads to the Hadley circulation having a reduced latitudinal depth, however there remains only three circulating cells. Additional cells are only expected to form at shorter rotational periods (Kaspi and Showman 2015).

The latitudinal and vertical extent of the Hadley circulation increases when increasing pCO_2 as shown in Figure 4.5 (see Figure A.2 for full grid of simulations). Increasing pCO_2 (left to right) leads to a stronger and deeper Hadley circulation, due to more efficient cooling of the upper tropopause and increasing surface temperatures increasing specific humidity. This is shown by the Hadley cells highlighted by the stream function intensifying, extending in latitudinal breadth and increasing the range of pressures they cover as pCO_2 is increased.

Increasing pCH_4 leads to a decrease in the latitudinal and vertical extent of the Hadley circulation, due to methane's shortwave heating of the upper troposphere for $pCO_2 < 3000$ Pa, while at $pCO_2 = 3000$ Pa the Hadley cell extent remains similar. For $pCO_2 = 100$ Pa, Figure 4.5 shows that at lower values of pCH_4 shortwave heating (black contour lines) predominantly takes place in the lower troposphere, while at higher pCH_4 the shortwave heating is largest in the upper troposphere. This is caused by high pCH_4 values increasing the shortwave absorption of the atmosphere. This results in the upper troposphere being more stable against convection at higher pCH_4, and reduces the tropopause height and subsequently the depth and strength of the Hadley circulation (also see lapse rates for a low pCO_2 and high pCH_4 case and a high pCO_2 and low pCH_4 in Figure 4.6). For $pCO_2 = 3000$ Pa, efficient cooling of the upper troposphere by CO_2 coun-

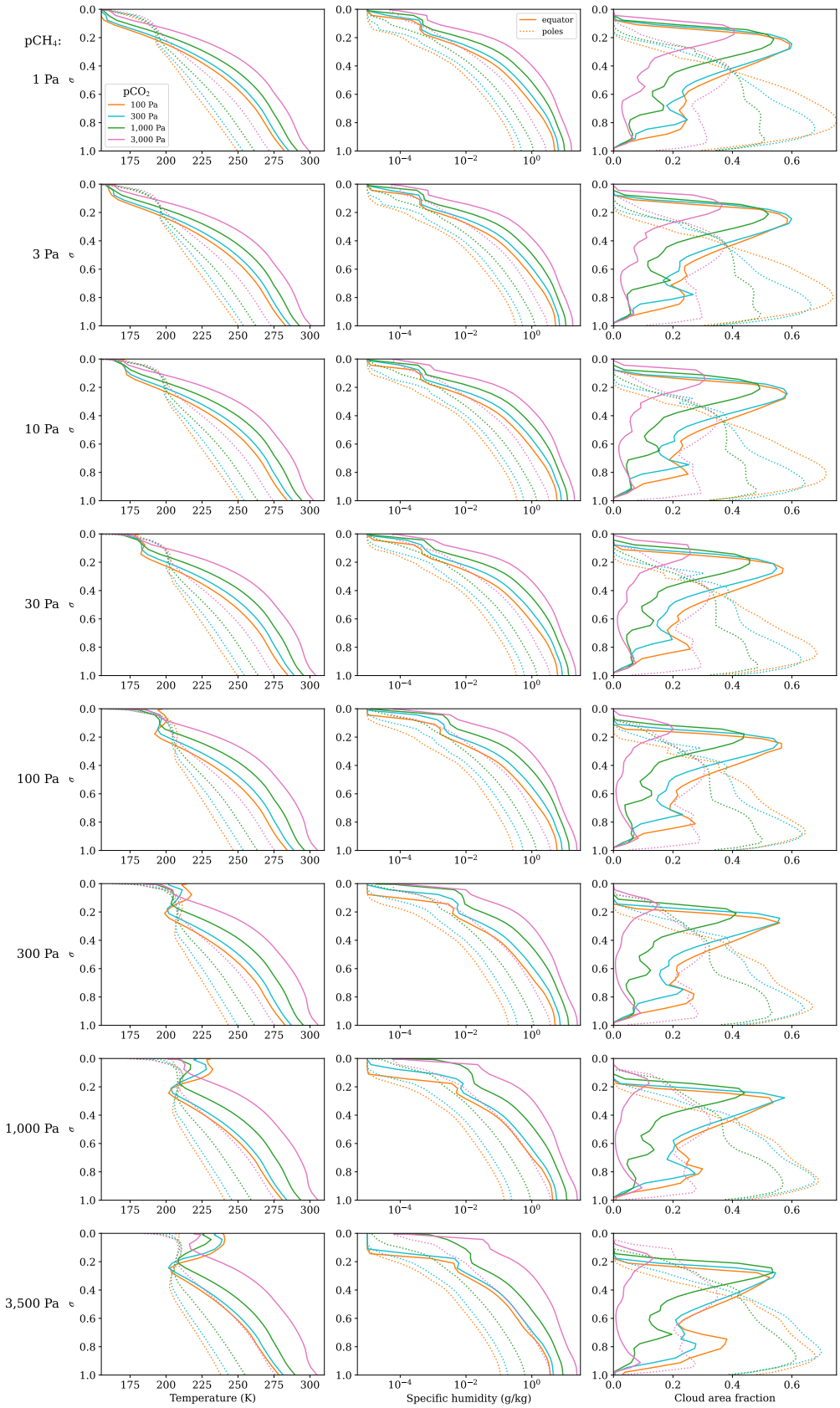

Figure 4.4: Shows horizontally averaged air temperature (left column), specific humidity (middle column) and cloud area fraction (right column) for the equator (solid lines) and poles (dotted lines), for increasing surface partial pressures of methane from top to bottom. The equator is considered as spanning latitudes of 10° S to 10° N, while the poles are 70° S/N to the pole.

teracts methane heating in the stratosphere and upper troposphere (compare warming due to methane in the bottom two panels of Figure 4.3), allowing the vertical extent of the Hadley circulation to remain similar for all pCH_4 values.

4.3.2 The global effect of methane on climate

I now focus on the global effects of changing pCH_4 and pCO_2. In this section I demonstrate that methane has a maximum warming potential on the global mean surface temperature of less than 7 K for $pCO_2 \leq 3{,}000$ Pa for our 2.7 Ga Archean-like aquaplanet configuration (see Figure 4.7b). I compare these results to those of Byrne and Goldblatt (2015) who used a 1D RCM and find that our GCM simulations predict a stronger cooling effect at high methane concentrations.

The global mean surface temperature increase, caused by the addition of methane, is less than 7 K. Figure 4.7a shows the mean surface temperature for our simulated atmospheres without methane, i.e. N_2 and CO_2 only with pCH_4=0, to act as a baseline for simulations where pCH_4>0. The subsequent temperature change from increasing pCH_4 is shown in Figure 4.7b. For our simulations the contribution of methane to the greenhouse effect peaks between pCH_4 values of 30 to 300 Pa, with peak global mean warming ranging from approximately 3.5 K to nearly 7 K as shown in Figure 4.7b. The location and magnitude of the peak in global mean surface temperature is dependent on pCO_2, with the peak occurring at higher pCH_4 and a larger maximum temperature as pCO_2 is increased. Past the peak, increasing pCH_4 leads to the global mean surface temperature decreasing, for which the decrease is largest for the lowest pCO_2, with some simulations for $pCO_2 \leq 1000$ Pa globally cooler than the simulation with no methane at all (below grey dotted line in Figure 4.7b), with global mean surface temperature dropping by up to approximately 8 K at pCH_4= 3500 Pa compared to the maximum methane warming at constant pCO_2 (Figure 4.7b). This peaked response is caused by the balance between methane's longwave warming effect and its shortwave cooling effect, as discussed in Byrne and Goldblatt (2015) and presented here in Figure 4.2a.

Conversely, at the higher pCO_2 amount of 3,000 Pa, the decrease in surface temperature caused by pCH_4=3,500 Pa is minimal. From Figure 4.7c, it can be seen that the

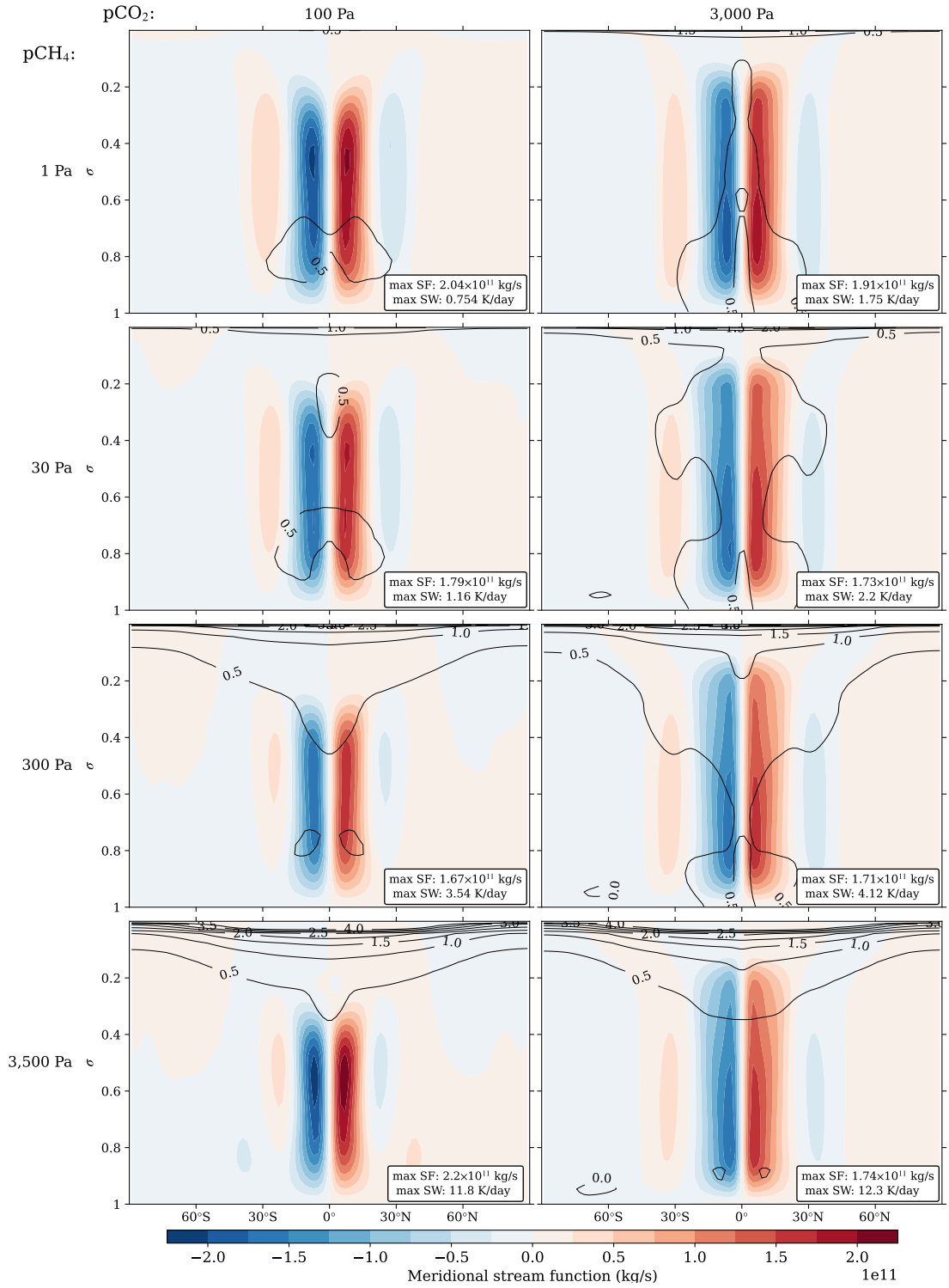

Figure 4.5: Zonal averaged meridional stream functions (colour scale), for increasing surface partial pressures of carbon dioxide from left to right, and methane from top to bottom, in the same format as Figure 4.3, with the full grid available in A.1 (Figure A.2). Positive and negative values represent clockwise and anticlockwise circulation respectively. Contours show the heating of the atmosphere due to shortwave radiation in K/day. The same colour scale is used for each plot, with maximum values for the stream function (SF) and shortwave heating rate (SW) are shown for each simulation in the bottom right of each sub figure.

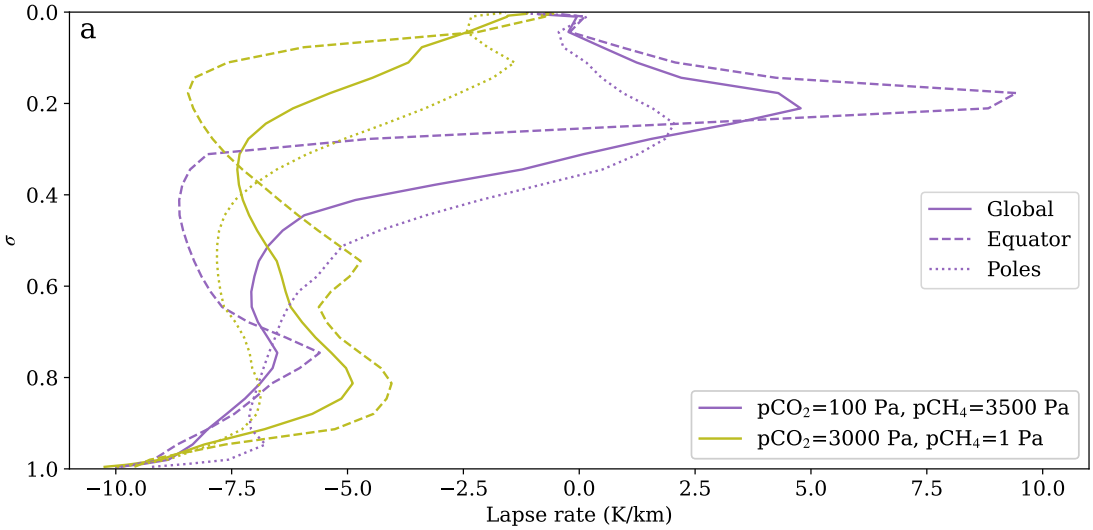

Figure 4.6: Shows lapse rate for the global (solid lines), equatorial (dashed lines) and polar (dotted lines) averages, for pCO_2=100 Pa and pCH_4=3500 Pa (purple) and pCO_2=3000 Pa and pCH_4=1 Pa (green). The equator is considered as spanning latitudes of 10° S to 10° N, while the poles are 70° S/N to the pole.

total water vapour and methane shortwave absorption increases less as pCH_4 increases for pCO_2=3,000 Pa compared to lower values of pCO_2. This is because the warmer climate at pCO_2=3,000 Pa allows for more water vapour in the atmosphere, which reduces the methane shortwave absorption due to overlap in their absorption cross sections in the shortwave. At higher pCO_2, the stratosphere becomes more resistant to the emergence of a stratospheric temperature inversion (see Byrne and Goldblatt (2015), Figure 4.3 and Figure 4.4), and at pCO_2=3,000 Pa, a cold trap only forms much deeper in the atmosphere (see Figure 4.4). This allows water vapour to reach higher abundances higher in the atmosphere, with stratospheric water vapour increasing significantly with pCH_4 for the pCO_2=3,000 Pa case only, shown in Figure 4.7d. This increase in stratospheric water vapour also acts to enhance the greenhouse effect, and leads to only a marginal drop in the global mean surface temperature for pCO_2=3,000 Pa in Figure 4.7b.

Use of a 3D GCM leads to a more significant global cooling at high pCH_4 (see Figure 4.7b) compared to results from a 1D RCM. pCO_2=100 Pa and pCO_2=1000 Pa offer the most comparable configurations to Byrne and Goldblatt (2015), who used CO_2 abundances of 10^{-3} and 10^{-2}. For a CO_2 abundance of 10^{-2}, Byrne and Goldblatt (2015) found a plateau in methane's greenhouse warming with surface temperature remaining constant up to a CH_4 abundance of 10^{-2} from 10^{-3}, compared to a ≈3 K drop in average surface tempera-

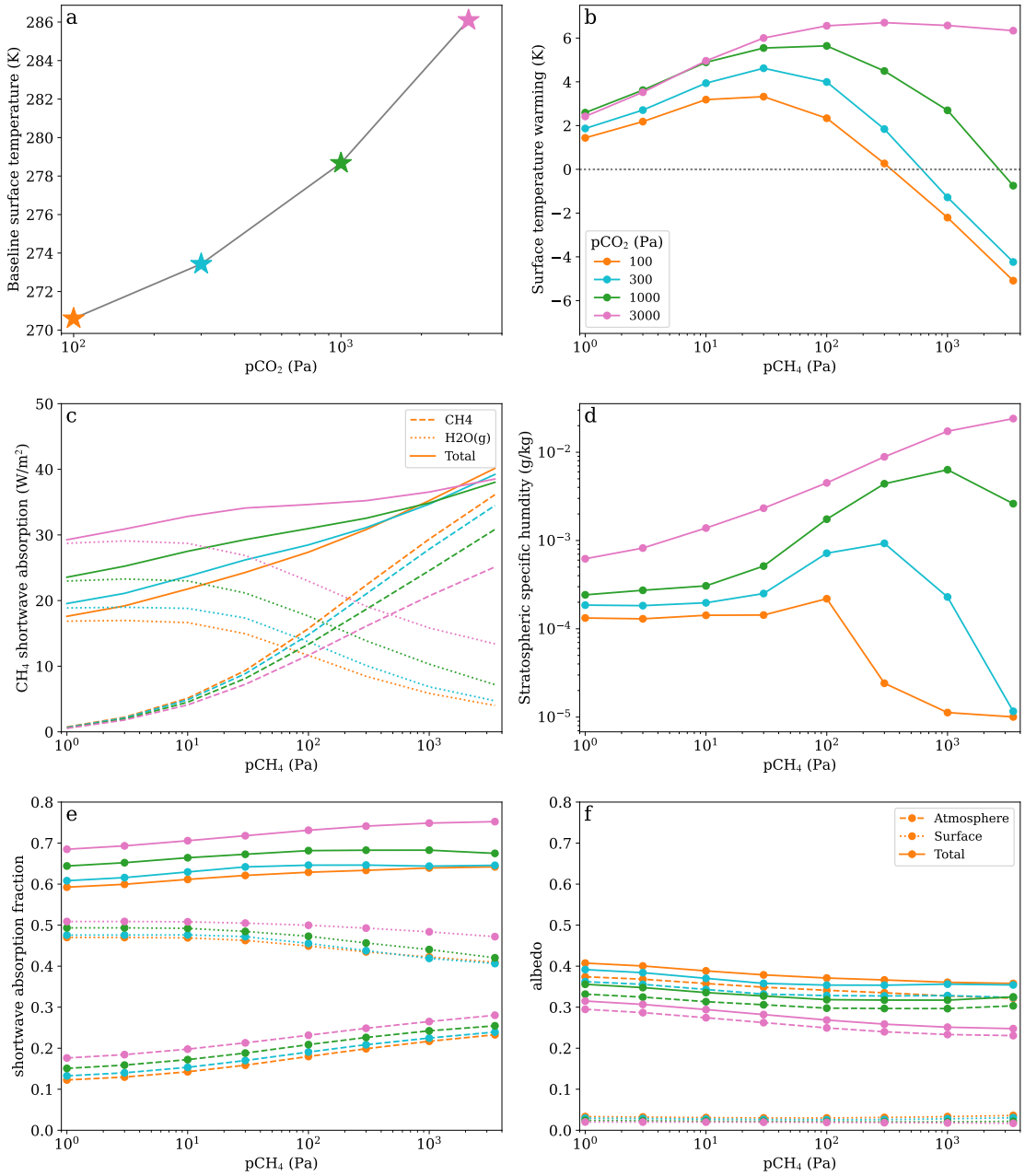

Figure 4.7: (a) shows the global mean surface temperature with respect to the carbon dioxide concentration and assuming pCH_4 is zero, with (b) showing the subsequent change in global mean surface temperature due to the addition of pCH_4 (positive indicates warming). Colours of markers in (a) correspond to the same pCO_2 in (b). Similar plots for near surface specific humidity are shown in Figure 4.8. (c) show the global average atmospheric absorption of shortwave radiation by methane (dashed) and water vapour (dotted) and their sum (solid). (d) shows the specific humidity in the stratosphere at $\sigma = 0.1$. (e) and (f) shows the fractional contribution of atmospheric (dashed), surface (dotted) and total (atmospheric plus surface) to the shortwave radiation budget global mean for shortwave absorption (e) and solar-weighted albedo (f). These were calculated using Donohoe and Battisti (2011), which accounted for atmospheric attenuation of shortwave radiation reflected by the surface.

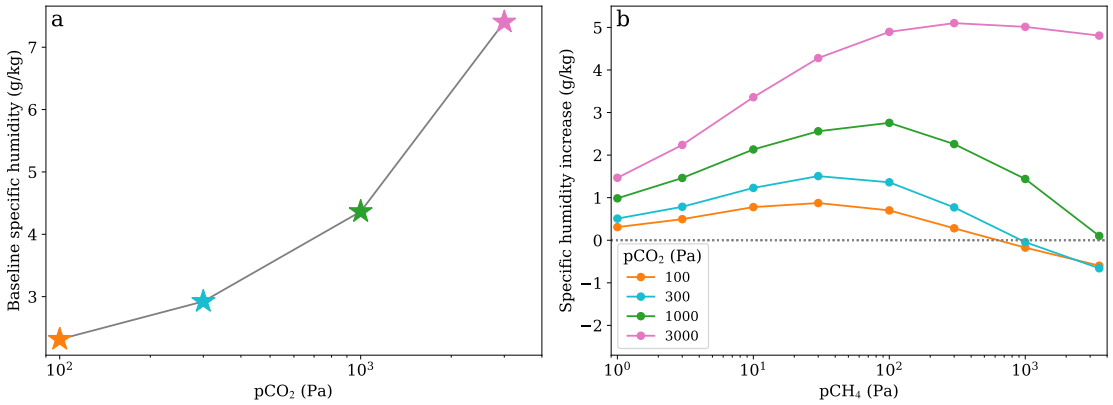

Figure 4.8: Similar to Figure 4.7 (a) shows the global mean near surface (σ = 1.0) specific humidity with respect to the carbon dioxide concentration and assuming pCH_4 is zero, with (b) showing the subsequent change in global mean near surface specific humidity due to the addition of pCH_4 (positive indicates warming). Colours of markers in (a) correspond to the same pCO_2 in (b).

ture from the peak at pCH_4=100 Pa for pCO_2=1000 Pa at pCH_4=1000 Pa (temperature difference for green line between pCH_4=100 Pa to pCH_4=1000 Pa in Figure 4.7b). Similarly for a CO_2 abundance of 10^{-3}, there is a cooling from the peak of ≈1 K in the 1D model compared to ≈5.5 K for pCO_2=100 Pa in our 3D model (temperature difference for orange line between pCH_4=30 Pa to pCH_4=1000 Pa in Figure 4.7b). This increases to ≈8 K when pCH_4=3500 Pa, however methane was not investigated at such levels in Byrne and Goldblatt (2015). These are caused, in part, by the presence of a 3D atmospheric circulation in the GCM, with methane affecting the meridional temperature gradient and Hadley circulation (see Section 4.3.3).

The addition of methane increases atmospheric shortwave absorption (Figure 4.7c) in the upper atmosphere and leads to a reduction in planetary albedo. Figure 4.7e shows this increase in atmospheric absorption of shortwave radiation with pCH_4. This leads to a decrease in surface shortwave absorption and a reduction in total albedo, shown in Figure 4.7f. As discussed in Section 4.3.1 as pCH_4 increases, shortwave heating transitions from predominantly heating the lower troposphere to heating the stratosphere and upper troposphere. This is caused by the increase in shortwave absorption higher in the atmosphere. This is summarised in the schematic in Figure 4.9.

The increase in shortwave absorption by methane higher in the atmosphere leads to a reduction in the water vapour shortwave absorption, shown in Figure 4.7c. This is due

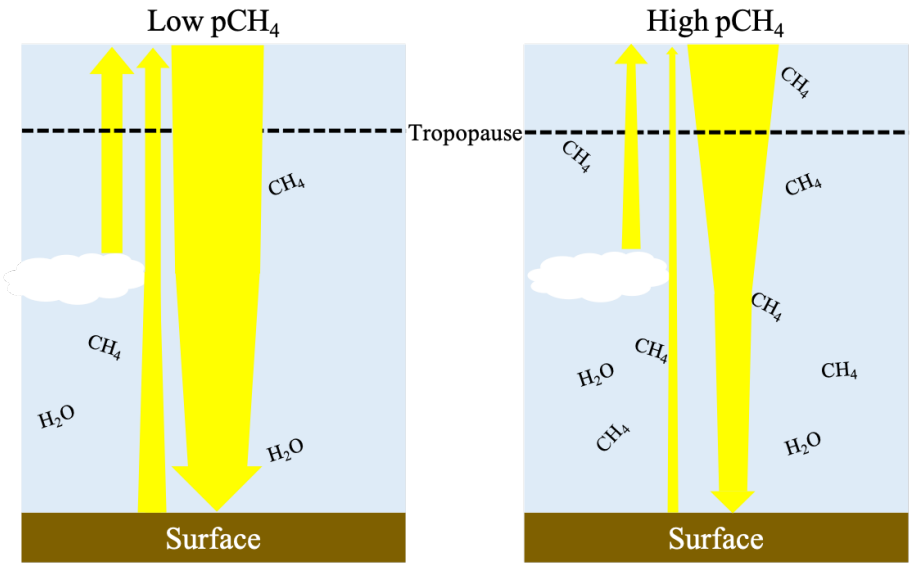

Figure 4.9: Schematic showing how methane affects the vertical distribution of shortwave radiation in the atmosphere for a low (left) and high (right) methane case. Shortwave radiation is represented by yellow arrows. A thinning of the arrow represents a loss of shortwave radiation through absorption in the atmosphere. Upward shortwave radiation represents reflected shortwave radiation from the surface and atmosphere. The tropopause is marked by a dashed line, and for simplicity is placed at the same level in these diagrams.

to spectral overlap between the absorption cross-sections of water vapour and methane in the shortwave (see Figure 6 in Byrne and Goldblatt 2014). Increasing pCH_4 leads to an increase in shortwave radiation absorption high in the atmosphere by methane, where specific humidity is lower in concentration compared to lower in the troposphere (see Figure 4.4). However, the relative contributions to shortwave absorption by methane and water vapour also depends on the temperature, with warmer simulations having a higher specific humidity, leading to shortwave absorption higher in the atmosphere. This explains the greater rates of shortwave heating in the troposphere in Figure 4.5 for pCO_2=3,000 Pa (compared to pCO_2=100 Pa), which is significantly warmer than the other simulations. As a result, these simulations have less shortwave heating by methane at a given pCH_4 (compare magenta and orange dashed lines in Figure 4.7c).

4.3.3 The effect of methane on equator-to-pole temperature gradients

Although the global impacts of methane within our 3D GCM simulations qualitatively match the trends identified in Byrne and Goldblatt (2015), differences are apparent between the 1D and 3D results. In this section I describe the impacts of changing meridional transport across our simulations, which cannot be captured in 1D models. I find that the

equator-to-pole temperature difference tends to increase with pCH_4 initially due to an increase in methane radiative forcing at the equator relative to the poles. As pCH_4 increases further, equator-to-pole temperature differences plateau due to an increase in radiative forcing at the poles and a decrease in efficiency in meridional heat transport.

The equator-to-pole temperature gradient reduces with increasing pCO_2, demonstrated in Figure 4.10a. This is due to an increase in the atmospheric temperature which increases the moist static energy transport (Kaspi and Showman 2015). The meridional stream functions also increases in latitudinal and vertical extent, as shown in Figure 4.5. However, the meridional temperature gradient's response to methane is more complex.

Figure 4.10b shows the increase in equator-to-pole temperature difference as a result of the addition of methane to the simulations. From Figure 4.10b I find that increasing pCH_4 generally causes an increase in equator-to-pole temperature differences for $pCH_4 \leq 300$ Pa, above this the equator-to-pole temperature difference either begins to plateau or decreases. The exact change is dependent on the pCO_2, with the behaviour more extreme for lower pCO_2, but the general trends remain. As well as this the main drivers for the meridional temperature gradients are methane's varying meridional radiative forcing (Figure 4.2b,c) and the effect on the meridional heat transport.

Figure 4.11a shows that for $pCO_2 \leq 1000$ Pa increasing pCH_4 initially leads to an increase in the relative CH_4 tropopause forcing at the equator compared to the pole, which drives an increase in the equator to pole temperature difference. This suggests, that for $pCH_4 \leq 300$ Pa, the equator-to-pole temperature difference in Figure 4.10b is driven by the differences in CH_4 radiative forcing.

The plateau that emerges in the equator-to-pole temerature differences in Figure 4.10b as pCH_4 increases above 300 Pa, can be explained by a balance between a weakening of the meridional heat transport and an increase in methane radiative forcing at the poles relative to the equator. For $pCO_2 \leq 1000$ Pa, as pCH_4 increases above 100 Pa, the difference in the equator-to-pole radiative forcing decreases in Figure 4.11a, with polar forcing approaching equality to the equatorial radiative forcing and eventually exceeding it at $pCH_4 = 3500$ Pa. However the change in equator-to-pole temperature differences over this period shows

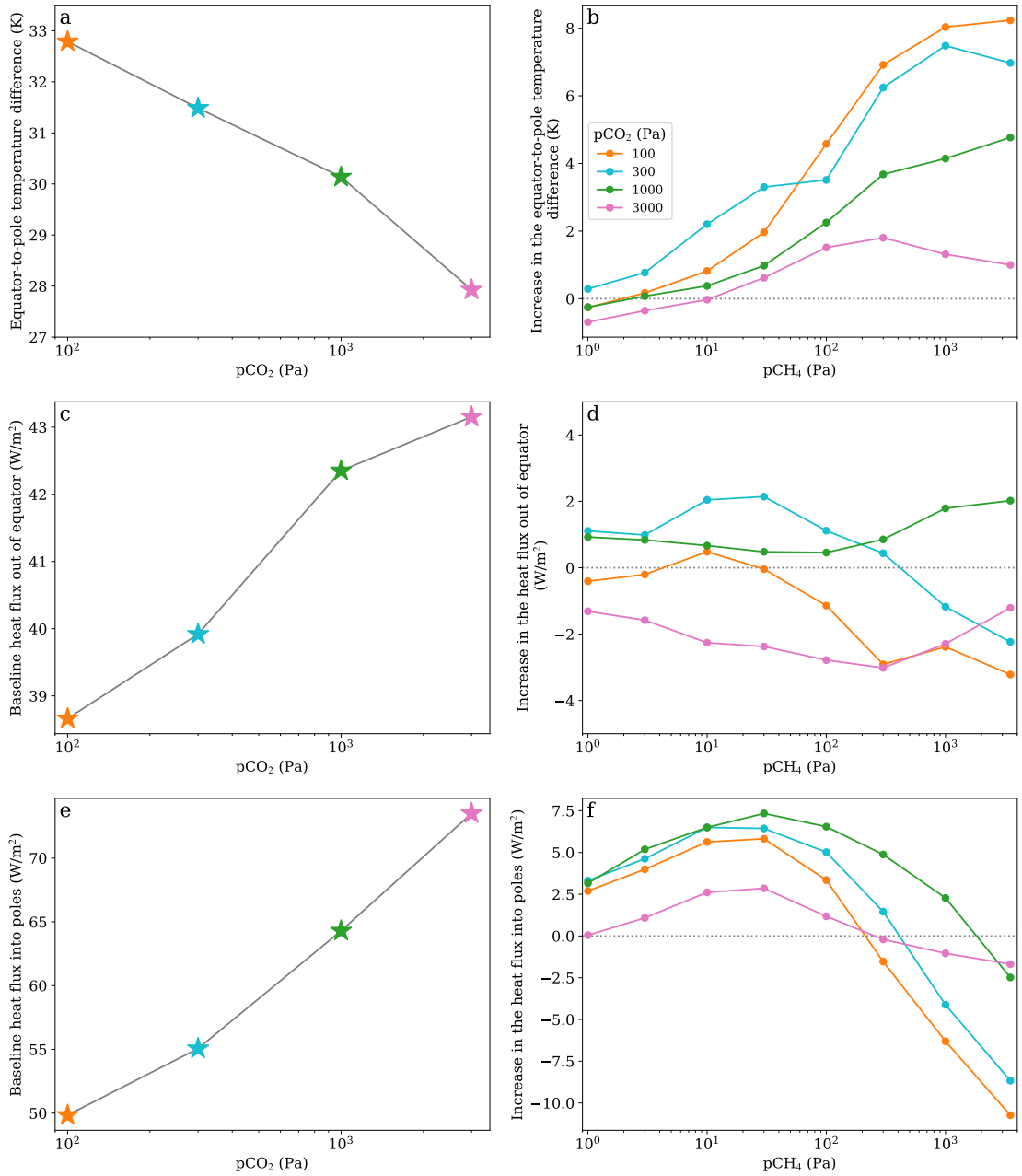

Figure 4.10: (a) shows the average equator-to-pole temperature difference with only carbon dioxide (pCH_4=0), with (b) showing the subsequent increase in equator-to-pole temperature difference due to the addition of methane (positive indicates an increase in the equator-to-pole temperature difference). (c) shows the atmospheric heat flux out of the equatorial region for different pCO_2 with pCH_4=0 (referred to as baseline cases), while (d) shows the increase in the equatorial heat flux from the subsequent addition of methane to (c). (e) shows the atmospheric heat flux into the polar regions for different pCO_2 (with pCH_4=0), while (f) shows the increase in the polar heat flux from the subsequent addition of methane to (e). Calculations for (c)-(f) use methods from Lambert et al. (2011) to calculate atmospheric heat fluxes (see 4.2.1 for more detail). The equatorial region is considered as spanning latitudes of 10° S to 10° N, while the polar regions are 70° S/N to the pole. Colours of data points in (a), (c) and (d) correspond to the same pCO_2 in (b), (d) and (f).

only a small (order of 2 K between 300-3500 Pa) generally increasing trend compared to the large increase in the relative methane radiative forcing between the equator and pole (Figure 4.11a), which would work to decrease the equator-to-pole temperature difference. The minimal change in the equator-to-pole temperature difference is caused by a reduction in the meridional heat transport, which offsets the increase in methane radiative forcing at the poles relative to the equator. Meridional heat transport weakens due to a reduction in the latitudinal extent of the Hadley circulation (Figure 4.5) and a reduction in global mean surface temperature compared to the peak in Figure 4.7b, which would act to increase equator-to-pole temperature differences (see Figure 4.11b). This balance maintains a relatively small change in equator-to-pole temperature differences for $pCH_4 \geq 300$ Pa in Figure 4.10b.

At pCO_2=3,000 Pa, the equator-to-pole temperature difference change is smaller compared to the other case, changing by ≈6 K in total from pCH_4=1 Pa to pCH_4=3,500 Pa. This is partly due to the latitudinal extent of the Hadley circulation in Figure 4.5 remaining similar at pCO_2=3,000 Pa, which may be more important in controlling equator-to-pole temperature difference compared to the change in radiative forcing between the equator and poles. For $pCH_4 \leq 30$ Pa and pCO_2=3,000 Pa relative radiative forcing between the equator and poles remains constant (Figure 4.11a). At pCO_2=3,000 Pa for pCH_4>30 Pa equatorial forcing increases relative to the poles, with the equator-to-pole temperature difference increasing. The reduction in temperature difference between pCH_4=1,000 Pa and pCH_4=3,500 Pa may be partially driven by larger methane radiative forcing at the poles compared to the equator at pCH_4=3,500 Pa.

A reduction in the meridional heat transport with increasing pCH_4 above 30 Pa contributes towards an increase in the equator-to-pole temperature gradient. As discussed in Section 4.3.1 the Hadley circulation reduces in vertical and latitudinal extent when increasing pCH_4 (see Figure 4.5). The effect this has on the atmospheric heat transport for the equatorial and polar regions is shown in Figures 4.10c-f. I used the net flux difference between the surface and top of atmosphere to estimate the flux transported horizontally into a region, as described in Lambert et al. (2011) (see 4.2.1 for more detail), and shown for our simulations in Figures 4.10c-f. The change in heat flux out of the equator is relatively small

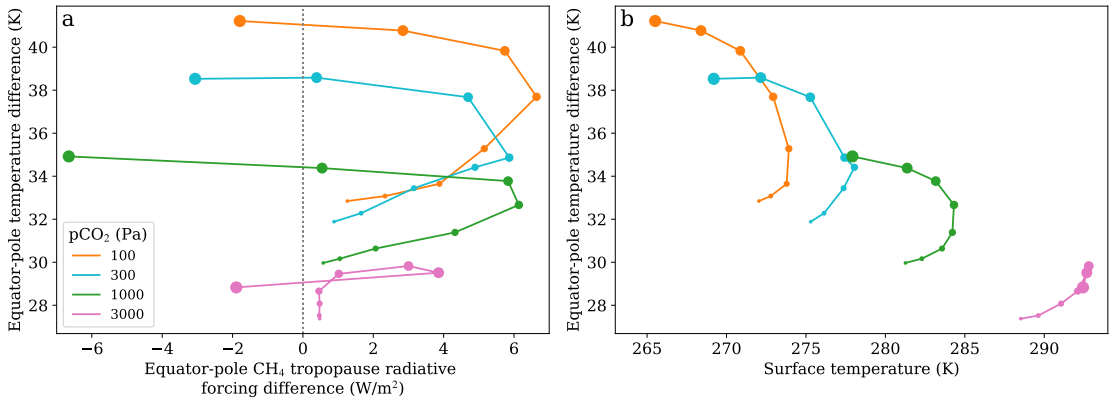

Figure 4.11: (a) Shows the equator-to-pole temperature difference against the difference in equatorial and polar net downward pCH_4 tropopause radiative forcing (positive indicates an increase in radiative forcing at the equator relative to the poles). (b) shows the global mean surface temperature against the equator-to-pole temperature difference. The equatorial region is considered as spanning latitudes of 10° S to 10° N, while the polar regions are 70° S/N to the pole. pCH_4 is represented through the size of the marker (larger maker equivalent to a higher pCH_4) for pCH_4 values of $\{1, 3, 10, 30, 100, 300, 1000, 3500\}$ Pa.

compared to the poles, with changes on order of less than 5% due to changes in methane (by comparing Figure 4.10c and Figure 4.10d). Figure 4.10f shows that as pCH_4 increases, there is an initial increase in heat flux into the poles, which peaks at $pCH_4 \approx 30$ Pa, potentially a result of the warmer global temperatures increasing the energy transported into the poles through moisture. Above $pCH_4 \approx 30$ Pa heat flux into poles reduces again, which is expected from the weakening circulation in Figure 4.5, and a corresponding sharp decrease in polar heat flux can be seen with a corresponding sharp rise in the equator-to-pole temperature difference (shown in Figure 4.10b). The equator-to-pole temperature difference's response to increasing pCH_4 is also dependent on pCO_2, as shown in Figure 4.10b.

The enhanced longwave forcing by methane at higher pCO_2 values in Figure 4.2 is due to an increasing temperature contrast between the surface and upper troposphere. Figure 4.12 shows this change in temperature contrast for the polar regions. The temperature contrast increases with pCO_2, leading to the increased longwave forcing seen in Figure 4.2a-c. In contrast, methane acts to warm the stratosphere and upper troposphere by absorbing solar radiation and thus increasing methane decreases the temperature contrast, shown in Figure 4.12.

For this study clouds play only a secondary effect, and are not, therefore, discussed in detail. Figure 4.13 shows the cloud radiative effect at the tropopause, and although

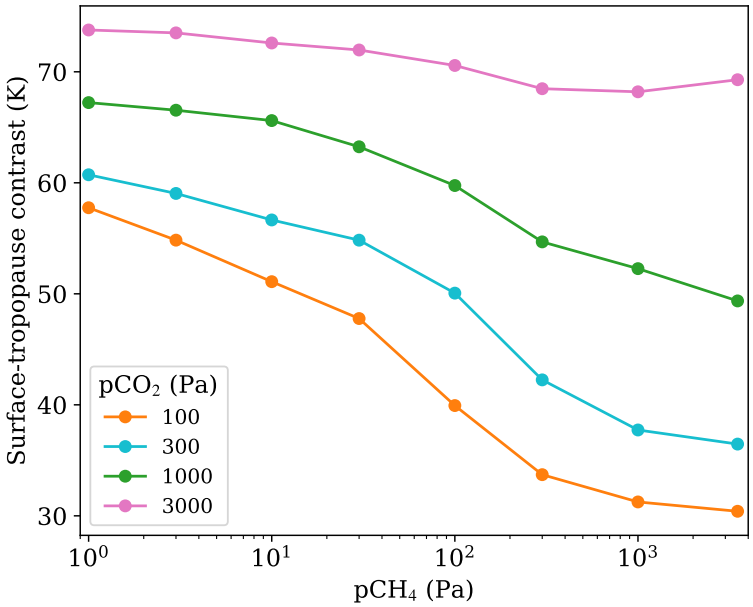

Figure 4.12: Shows the temperature contrast between the surface and atmosphere at σ=0.2 horizontally averaged over the polar regions. The poles span from 70° N/S to the pole. σ=0.2 is used to approximate the tropopause height.

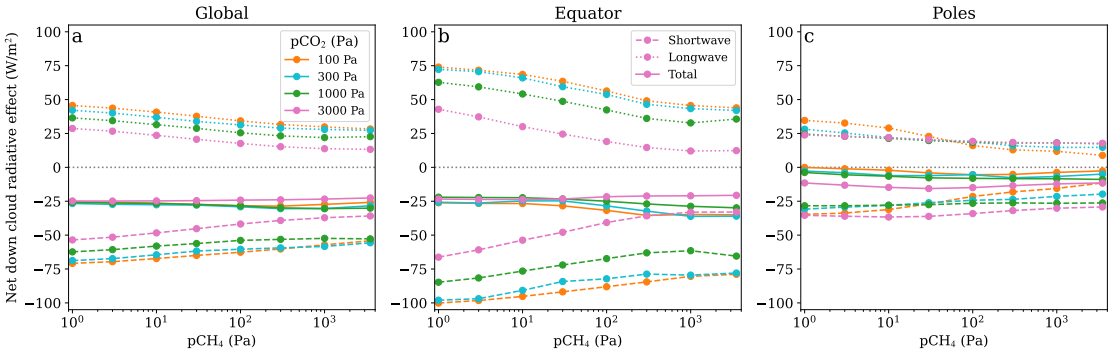

Figure 4.13: (a) shows the global average net down cloud radiative effect at σ=0.2 (approximate location of the tropopause) where σ is the pressure divided by the global mean surface pressure. Cloud radiative effect is shown for shortwave (dashed), longwave (dotted) and their sum (solid). (b) and (c) show the same as (a) averaged over 10°S to 10°N as the equator in (b), and poleward of 70°N/S for the polar regions in (c).

the magnitude of the change in longwave and shortwave cloud radiative effect vary the total cloud radiative effect remains nearly constant. Cloud fractions horizontally averaged pressure-temperature plots for the equator and poles are shown in Figure 4.4. I am currently working on a more in-depth study of the impacts of clouds over this parameter space (see Section 7.2.1).

4.3.4 Methane radiative forcing: albedo dependence

To compare the effect of surface albedo on methane radiative forcing, Figure 4.14 shows a sensitivity test for two surface albedos of 0.07 (case used in this study) and 0.533, which represents a high value for albedo produced by sand in the near infrared. Figure 4.14 shows methane radiative forcing after running the model for one additional timestep from the configurations discussed in the main body of text, hence the slight differences between Figure 4.2 and Figure 4.14a-c. As these are calculated with no evolution of the climate state, there is no change in the longwave radiative forcing between the two cases Figure 4.14g-i, and the change in shortwave methane radiative forcing is zero at the pole due to this region being ice and ice albedo remains unchanged.

Increasing ocean albedo causes the shortwave methane radiative forcing to decrease, however, general trends in radiative forcings discussed in Section 6.5 remain the same. At high pCH_4 global temperatures may increase, leading to a less pronounced decline in temperatures compared to those found in Figure 4.7.

4.4 Discussion

GCMs provide useful insight into the role of methane in the Archean climate, both validating effects found in RCMs and also finding important differences that come from 3D modelling. The initial global warming due to methane is similar between both models, with the models diverging when predicting temperatures for pCH_4:$pCO_2 > 0.1$. In this range GCMs predict large temperature drops, particularly for cooler, lower CO_2 configurations, with temperatures dropping by up to 8 K from the peak temperature.

GCMs are also useful in their ability to investigate the meridional heat distribution,

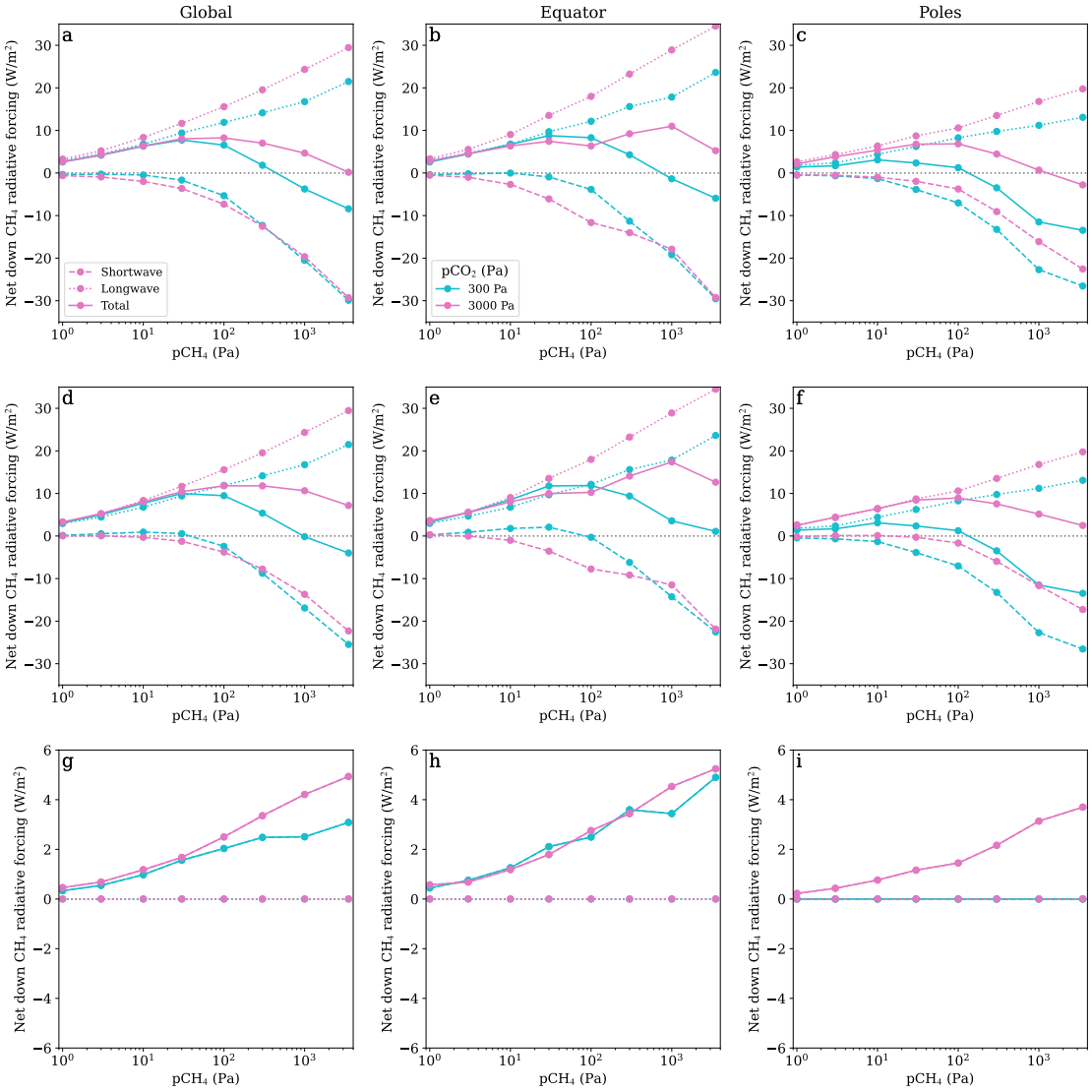

Figure 4.14: (a) shows the global average net down radiative forcing at the tropopause for methane for shortwave (dashed), longwave (dotted) and their sum (solid), for an ocean surface with an albedo of 0.07. (b) and (c) show the same as (a) averaged over 10°S to 10°N as the equator in (b), and poleward of 70°N/S for the polar regions in (c). These are calculated for just one model time step. (d), (e) and (f) shows the same as (a), (b) and (c) respectively, but for an ocean surface albedo of 0.533. (g), (h) and (i) show the difference between a), (b) and (c), and (d), (e) and (f), with a positive value indicating an increase in radiative forcing with the higher albedo of 0.533.

where methane plays three important roles. 1) Differences in equator-to-pole methane radiative forcing: equator dominated for pCH_4:pCO_2 < 0.1, and transitioning to polar dominated above this. 2) Hadley circulation weakens when increasing pCH_4, which reduces meridional heat transport. 3) Atmospheric temperatures affect the moisture held in the atmosphere, so the peaking in temperature at pCH_4:pCO_2 = 0.1 leads to increases in meridional heat transport below this and decreasing heat transport above this when increasing pCH_4. It may be possible to replicate this in a 2 column model (equatorial and polar column) by parameterising these three factors.

Our study supports that the FYS paradox can be resolved based on pCO_2 constraints around 2.7 Ga. Global mean surface temperatures close to the pre-industrial Earth, can be achieved with pCO_2=3000 Pa and pCH_4=0 Pa and pCO_2=1000 Pa and pCH_4≈100 Pa (Figure 4.7a,b). The first of these falls within the range of pCO_2 values constrained by Kanzaki and Murakami (2015) from 2.75 Ga, while the latter composition falls within the constraint of Driese et al. (2011) at 2.7 Ga. The addition of methane to pCO_2=3000 Pa up to pCH_4=3500 Pa would lead to global mean surface temperatures up to 7 K warmer than the pre-industrial Earth, while increasing or decreasing methane from the pCO_2=1000 Pa and pCH_4≈100 Pa configuration would lead to global mean temperatures decreasing. For pCO_2=300 Pa and pCO_2=100 Pa, global mean temperatures could reach up to 278 and 274 K respectively, with optimal methane abundances. In our simulations, these remain ice free, with Wolf and Toon (2013) finding that these concentrations of CO_2 with some CH_4 also avoid being fully glaciated, with at least 50% of the surface remaining ice free. Higher pCO_2 values than 3000 Pa are not necessary for surface pressures around 10^5 Pa, but could be important to warm the Archean Earth if the total surface pressure was lower.

Some studies have suggested that surface pressures may have been lower than the present day. Fossil raindrops have been used to approximate surface pressure at 2.7 Ga to between 5×10^4 to 1.1×10^5 Pa (Som et al. 2012), although debate remains over the upper limit of this constraint (Kavanagh and Goldblatt 2015). Furthermore, fossilised gas bubbles in lava flows at 2.74 Ga predict a surface pressure of $2.3\pm2.3\times10^4$ Pa (Som et al. 2016). The understanding of the effect of methane on the climate at different pressures is thus very important for the Archean. A lower surface pressure and with no thermal inversion at

the tropopause could lead to more stratospheric water vapour, increasing the greenhouse potential at low surface pressures (Kopparapu et al. 2014). Thus the stratospheric temperature inversion created at high methane concentrations could reduce the stratospheric water vapour in this scenario and lead to a larger drop in the mean surface temperature. However, further work is required to understand the full effect of methane at lower surface pressures.

Methane has a secondary impact on the climate through its importance in the formation of hydrocarbon hazes, and it is suggested that there may have been periods during the Archean where a haze layer was present (Domagal-Goldman et al. 2008; Izon et al. 2015). Haze forms when the CH_4:CO_2 ratio exceeds approximately 0.1 (Trainer et al. 2006), and potentially has a cooling effect on climate by up to 20 K (Arney et al. 2016). Arney et al. (2016) found that a thick haze was produced for pCH_4:pCO_2>0.2. For 0.1<pCH_4:pCO_2<0.2 a thin haze is produced that is spectrally indistinguishable from an atmosphere with no haze (Arney et al. 2016). The peak surface temperature in our experiments were found to occur around pCH_4/pCO_2>0.1 so this peak is expected to remain with the presence of haze, and for pCH_4/pCO_2>0.2 hazes form and accelerate cooling further. With global mean surface temperatures for a given pCO_2 tending to peak around pCH_4=0.1×pCO_2, higher methane concentrations are not able to increases global mean surface temperatures further, even without considering the effects of haze.

Byrom and Shine (2022) and Collins et al. (2018) found that surface albedo can affect the shortwave radiative forcing, with higher albedos at wavelengths where methane absorbs strongly leading to an increase in absorption of upward radiation leading to a positive radiative forcing, which can arise from high albedo on land surfaces such as deserts (Byrom and Shine 2022). Land fraction remains uncertain for the Archean (see discussion in Charnay et al. 2020), with a general consensus that the fraction of continental crust was less than present day (Hawkesworth et al. 2019), as well as the potential for a larger ocean volume (Dong et al. 2021), with suggestions land fraction could have been as low as 2-3% until 2.5 Ga (Flament et al. 2008). I test the sensitivity of the tropopause radiative forcing by increasing global ocean albedo to 0.533 Byrom and Shine (value for albedo of quartz sand in near infrared, used in 2022) and run the model for one time step and compare

the radiative forcings, shown in Figure 4.14. Using this extreme value for albedo, I find that the shortwave radiative forcing becomes less negative. However the general trend for radiative forcing remains the same. Thus, for a surface with higher albedo, the decline in global mean surface temperatures is expected to be lower at higher methane values. Further exploration is required to explore the effect of different continent configurations on the methane radiative forcing and the overall effect on climate, with a spectrally dependent surface albedo.

Although methane, across the range investigated in this Chapter, has a relatively small effect on global mean surface temperatures of –6 to +7 K, its abundance has a more significant impact on the meridional heat transport, which could affect the likelihood of the planet entering a snowball state. High methane levels generally increase the equator-to-pole difference by up to 8 K, which combined with a realistic ice-albedo feedback could affect the stability of the temperate state – which in this case refers to a state that is not fully glaciated. However full understanding of this would require consideration of ocean heat transport, continental configuration and a thermodynamic treatment of sea-ice, all of which are beyond the scope of this study, which focuses on the climate differences stemming from methane's radiative effect.

Theoretical opacity data that further fill in missing regions of methane's shortwave absorption up to 833 nm (Yurchenko and Tennyson 2014) and 746 nm (Hargreaves et al. 2020) have also become available that allows for further investigation into the significance of methane's shortwave absorption. However, line lists for methane covering much of the wavelength region covered by the Sun's emission are not yet available, motivating the extension of work generating line lists to cover this missing absorption data.

Potentially habitable planets have now been detected orbiting M-dwarf stars, which are cooler than the Sun. For these exoplanets the shortwave absorption would be stronger due to a larger fraction of the stellar emission coming from the near infrared, for M-dwarfs compared to G-dwarfs like the Sun, where methane has strong absorption. The impacts of missing absorption data, as discussed above, become even more important due to the host star emitting more radiation at longer wavelengths where absorption from greenhouse gases is higher (Eager-Nash et al. 2020). If these planets host life, their early environment

may have resembled that of the Archean Earth, given that a significant fraction of Earth's own 'inhabited' history is represented by this period (Catling and Zahnle 2020). Therefore, these planets could have high concentrations of methane and an even stronger temperature sensitivity to methane abundance due to the interaction of the host star spectrum and the methane rich atmosphere.

4.5 Conclusions

I used the Met Office Unified Model to understand the potential effect of atmospheric CH_4 and CO_2 on the climate of the Archean at 2.7 Ga. A productive biosphere could have led to an atmosphere with pCH_4 ranging from 10–3,500 Pa (Kharecha et al. 2005). I found that the greenhouse effect of methane does not exceed a global average of 7 K for $pCO_2 \leq 3{,}000$ Pa, with the peak temperature occurring for pCH_4 between 30–300 Pa. This peak in temperature shifts to higher pCH_4 for higher values of pCO_2. The peaked effect is due to methane's absorption of shortwave radiation in the stratosphere that reduces heating of the surface, which dominates over the greenhouse effect of methane at higher pCH_4. I confirm results from Byrne and Goldblatt (2015) and extend them to 3D simulations, but also demonstrate that use of a 3D GCM is important to fully capture cooling of the climate at high methane concentrations, due to changes in meridional circulation and methane radiative forcing. Maximum temperatures are reached when the CH_4:CO_2 is approximately 0.1, below the ratio where significant cooling occurs due to the presence of haze (Arney et al. 2016). More work is required to understand the interaction of biogeochemical cycles with the atmospheric composition and potential haze formation.

4.6 Chapter Summary

In this Chapter, I have shown that the role of methane as a greenhouse gas is limited during the Archean, however, could provide a global mean temperature increase of up to 7 K or a radiative forcing of up to 8 W/m^2. However, at high methane concentrations methane has a strong cooling effect by absorbing stellar radiation. This is similar to planets orbiting cooler stars such as M-dwarfs, where more radiation is absorbed directly by the atmosphere, due to the redder spectrum. This is explored in Chapter 5 for tidally locked

planets.

Chapter 5

Comparing the effect of stellar spectra on Tidally locked planets

5.1 Introduction

This Chapter investigates the effect of stellar type on the climate of a tidally locked exoplanet. The work from this chapter has been published in Eager-Nash et al. (2020).

Several potentially habitable terrestrial exoplanets have been detected, including Proxima Centauri b (Anglada-Escudé et al. 2016) and TRAPPIST-1e (Gillon et al. 2017), orbiting M dwarf stars, which are smaller and cooler than the Sun (G dwarf). The change in the host star brightness and temperature leads to two important consequences. Firstly, for a planet to orbit in the habitable zone (Kasting et al. 1993a) around an M dwarf, it must have a smaller orbital radius (and therefore shorter period) than the orbital radius of Earth. Therefore the planet will experience stronger tidal forces from the host star than the Earth does from the Sun, which is likely to result in the planetary rotation rate and orbital period becoming synchronised; this is known as tidal locking (Pierrehumbert and Hammond 2019). Secondly, the amount of stellar radiation incident on the planet peaks at longer wavelengths because the temperature of M dwarfs is lower than that of G dwarfs (e.g. see Joshi and Haberle 2012; Shields et al. 2013; Rushby et al. 2019). Another important difference between G and M dwarfs is the occurrence rates and strength of stellar flares,

and the overall stellar activity, which are both much higher in M dwarfs (e.g. see Howard et al. 2018, for Proxima Centauri). This has important implications for both the atmospheric composition, for example, in terms of stratospheric ozone cycling (Yates et al. 2020), and the habitability of planets orbiting such stars. Initial studies have been performed in 1D (Tilley et al. 2019), but extension to 3D is required given the assumption of tidal locking for planets such as TRAPPIST-1e and Proxima Centauri b, resulting in a permanent dayside and nightside, the latter receiving no direct stellar irradiation. In this work I focus on the differences caused exclusively by the quiescent stellar spectra and reserve inclusion of stellar activity for future work.

The climates of the TRAPPIST-1 planets (Wolf et al. 2017; Turbet et al. 2018; Fauchez et al. 2020) and Proxima Centauri b (Turbet et al. 2016; Boutle et al. 2017; Del Genio et al. 2019; Boutle et al. 2020) have been simulated using different model infrastructures and exploring different facets of the climate system. The vast majority of these simulations reveal a similar dynamical structure of a dominant, coherent, zonal flow or jet that transports heat from the dayside to nightside. However, a direct comparison to isolate the significance of the spectrum of the host star has yet to be performed. The effect of stellar type through differing atmospheric absorption on cloud, convection, and day-night heat and moisture transport are key in determining the impact that the differences in the spectra - between different host stars - will have on the planetary climate.

For terrestrial exoplanets, Yang et al. (2013) demonstrated that clouds produce a negative feedback that extends the inner edge of the habitable zone. As the overall stellar irradiance increases, so does convection, cloud coverage, and consequently, the albedo on the dayside, thus cooling the planet. This is only possible if there is a large water supply on the dayside of the planet (e.g. on an aquaplanet). Yang and Abbot (2014) and Koll and Abbot (2016) employed two-box (dayside and nightside) models to determine what controls the surface temperature. Yang and Abbot (2014), in particular, showed that the nightside of the planet acts as a "radiator fin", allowing outgoing longwave radiation (OLR) to escape from the atmosphere, which cools the planet because of the low level of high-altitude cloud. This is because on the dayside, the water vapour and cloud greenhouse effects reduce the efficiency of the local atmosphere in radiating stellar energy into

space. This energy is instead transported by the atmosphere to the nightside, where there is a strong temperature inversion, and the cloud greenhouse effect is negligible, so that infrared energy is easily emitted into space. Yang and Abbot (2014) showed that when the emissivity of the nightside is increased, the dayside surface temperature decreases significantly, whereas increasing dayside emissivity leads to small increases in temperature.

Boutle et al. (2017) showed that for a simulation of Proxima Centauri b, vigorous convection over the sub-stellar point acted to transport heat and moisture vertically to the altitude of the zonal jet. Recently, Sergeev et al. (2020) have explored the differences obtained when employing various treatments and parametrisations of convection within 3D simulations of a tidally locked terrestrial exoplanet, and performing high-resolution convection-permitting simulations free from such approximated treatments. Sergeev et al. (2020) showed that important differences in the vertical and horizontal transport of heat and moisture exist between coarse-resolution, employing convection parametrisations, and high-resolution simulations with explicit convection. However, these studies have not yet been extended to explore the impact of differing stellar spectra on the behaviour of the convective transport, cloud coverage, and day-night transport.

The impact different stellar spectra have on a planetary climate has been studied for rapidly rotating planets (Shields et al. 2013). Shields et al. (2013) found that when holding the total stellar irradiance received by a planet constant, planets orbiting cooler, redder stars exhibit higher global mean surface temperatures than those orbiting warmer stars. This was due to increased direct absorption of incident stellar radiation by the atmosphere for planets orbiting cooler stars. The stellar spectrum of an M dwarf overlaps considerably more with the absorption features of CO_2 and H_2O than that of a G dwarf, with the former emitting a larger fraction of radiation in the near-infrared (Pierrehumbert 2010). Shields et al. (2013) also found that the H_2O ice albedo feedback (where, as ice forms, more light is reflected from the planetary surface, leading to further cooling and increased ice coverage) was weaker for planets orbiting cooler stars. This is due to the wavelength dependence of the ice albedo, which decreases with wavelength above 0.5 μm, leading to a lower contrast between ice and water (Joshi and Haberle 2012). Shields et al. (2019) took this further to find that a planet orbiting an M dwarf absorbs 12% more incident solar energy than

its G dwarf counterpart for an Earth-like configuration with a 24-hour rotational period. Meanwhile, Yang et al. (2019b) found that an increase in atmospheric absorption of stellar radiation led to an increase in relative humidity at higher altitudes globally, causing a significant decrease in OLR.

In this Chapter, I extend on previous works by investigating the effect that different stellar spectra have on the planetary climate of tidally locked planets with Earth-like atmospheres, focusing on cooler stars around which current, potentially habitable, targets have been detected. I performed simulations using the Met Office 3D climate model, the Unified Model (UM), based on the planetary parameters for TRAPPIST-1e, and a 1 bar N_2 dominated atmosphere with 400 ppm CO_2. Further simulations were performed, replacing the stellar spectrum of TRAPPIST-1 with that of Proxima Centauri and the Sun, holding all other parameters constant, and retaining a tidally locked configuration. Setting a constant rotation rate across our experiments would not be physically consistent with tidally locked planets obeying Kepler's laws. However, the effect of changes in the rotation rate on exoplanet climates has been well studied (e.g. Merlis and Schneider 2010; Haqq-Misra et al. 2018; Penn and Vallis 2018; Komacek and Abbot 2019) and is not our focus here. Additionally, increasing the gravity in a simulation of a given planet leads to a cooling for cases where a dilute, radiatively active condensible (such as water in our configuration) is present (Thomson and Vallis 2019; Yang and Yang 2019). Therefore, as I look to isolate the effect that changing the stellar spectrum has on the planetary climate, a constant top-of-atmosphere (TOA) incident flux, orbital period, atmospheric composition, and planetary mass and radius are used for all of the simulations.

In Section 5.2 I provide an overview of the UM (which has now been employed and detailed in many exoplanet studies) and our specific configurations, followed by presenting our results in Section 5.3. In Section 5.3.1 I investigate the basic climatology of our simulations through the surface temperature and winds. This is followed by investigation of the moisture and cloud coverage in Section 5.3.2, and separation of the radiative, advective, latent, and boundary-layer turbulent contributions to the heating and evaporation or condensation in Section 5.3.3. Finally, in Section 5.4 I present our conclusions and discuss both the limitations of our approach and the potential implications for the habitability

of tidally locked planets with Earth-like atmospheres. I find that planets orbiting cooler stars absorb more shortwave stellar radiation directly in the troposphere, which leads to more efficient zonal circulation and a smaller temperature gradient between the day- and nightside. The increase in the ratio of radiation absorbed by the atmosphere compared to the surface results in a dayside with less vigorous convection, which reduces dayside cloud cover and hence the overall planetary albedo. This results in planets orbiting cooler stars being globally warmer than those orbiting hotter stars. Overall, I find that planets orbiting cooler stars have larger regions on the dayside that can support liquid water, and I infer that such planets likely maintain habitable temperatures out to larger orbital radii (and lower overall incident stellar fluxes) than their counterparts orbiting hotter stars.

5.2 Model setup

In this chapter I use the Met Office general circulation model (GCM), the UM, which has been adapted to a range of exoplanet applications and used for a large number of studies covering hot Jupiters (Mayne et al. 2014a; Amundsen et al. 2016; Helling et al. 2016; Mayne et al. 2017; Tremblin et al. 2017; Drummond et al. 2018b; Drummond et al. 2018c; Lines et al. 2018b; Lines et al. 2018a; Lines et al. 2019; Sainsbury-Martinez et al. 2019; Debras et al. 2019; Debras et al. 2020; Drummond et al. 2020), mini-Neptunes/Super Earths (Drummond et al. 2018a; Mayne et al. 2019) and terrestrial planets (Mayne et al. 2014b; Bolmont et al. 2017; Lewis et al. 2018; Fauchez et al. 2020; Yates et al. 2020; Boutle et al. 2020; Joshi et al. 2020; Sergeev et al. 2020). A similar configuration is followed to that of Boutle et al. (2017) and Lewis et al. (2018), based on the Global Atmosphere 7.0 configuration (Walters et al. 2019). The UM has implemented the ENDGame dynamical core, which uses a semi-implicit semi-Lagrangian formulation to solve the non-hydrostatic, fully compressible deep atmosphere equations of motion (Wood et al. 2014). Processes that occur on a scale smaller than the size of the grid boxes are parametrised. Convection uses a mass-flux approach based on Gregory and Rowntree (1990), water clouds use the PC2 scheme detailed in Wilson et al. (2008), incorporating mixed-phase microphysics based on Wilson and Ballard (1999), and turbulent mixing uses an approach based on Lock et al. (2000) and Brown et al. (2008). The simulations were configured as an aquaplanet, using a single-layer

slab-homogeneous flat surface as the inner boundary (planetary surface), which is based on Frierson et al. (2006). It represents an ocean surface with a 2.4 m mixed layer with a heat capacity of 10^7 J/K/m^2, with no horizontal heat transport. The emissivity of the surface is fixed at 0.985 and the albedo is spectrally dependent and varies with stellar zenith angle, based on Jin et al. (2011). Sea-ice formation is not considered in the model, with the surface remaining as liquid water throughout. The Suite of Community Radiative Transfer codes based on Edwards and Slingo (SOCRATES) scheme treats the radiative transfer in the UM, employing the correlated-k method. SOCRATES has been adapted and tested for a range of exoplanet configurations (e.g. Amundsen et al. 2014; Amundsen et al. 2017), but a configuration is used that is similar to Earth (Walters et al. 2019). Longwave "planetary" radiation is treated via 12 bands (between 3.3 μm-10 mm), while shortwave "stellar" radiation is treated by 29 bands (0.20-20 μm) with the opacity data obtained from the NASA Goddard Institute for Space Studies[1].

As our focus is the effect that different host star emission has on the climate of a planet, input spectra for three different stars are used: TRAPPIST-1, Proxima Centauri, and the Sun. The stellar parameters for these stars are shown in Table 5.1, and their spectra are shown in Figure 5.1 (top), generated using the BT-settl model of theoretical spectra (Rajpurohit et al. 2013). Figure 5.1 (middle) shows the wavelength dependence of the absorption cross section for water vapour (Polyansky et al. 2018) and carbon dioxide (Tashkun and Perevalov 2011). The absorption cross sections were generated using the ExoMol (Tennyson et al. 2016) database, and the ExoCross software (Yurchenko et al. 2018), for an atmospheric pressure and temperature of ~800 hPa and ~230 K, respectively. The solar emission peaks at visible wavelengths, whereas TRAPPIST-1 and Proxima Centauri peak in the infrared, with a larger fraction of the radiation emitted at >1 μm, which is the region where carbon dioxide and, in particular, water vapour begin to absorb. TRAPPIST-1 is the coolest star and emits more radiation at longer wavelengths than Proxima Centauri for a constant total flux. Figure 5.1 (bottom) shows the radiative properties of the cloud. Scattering for both an ice and a liquid-water cloud remains relatively constant across the stellar spectrum, and thus the cloud albedo will remain constant between the simulations

1. From directories sp_sw_dsa_ar and sp_lw_dsa_ar at https://portal.nccs.nasa.gov/GISS_modelE/ROCKE-3D/spectral_files/

for the same cloud distributions. In terms of absorption rates, both ice and liquid-water clouds have global minima at the peak of the solar spectrum at ~0.4 μm, while Proxima Centauri and TRAPPIST-1 peak where cloud absorption rates are about three orders of magnitude higher. It can thus expect that there will be an increased atmospheric absorption by clouds for the cooler stars.

Table 5.1: Stellar parameters for TRAPPIST-1 (Fauchez et al. 2020), Proxima Centauri (Schlaufman and Laughlin 2010), and the Sun as well as the semi-major axis for the planet in our simulations.

Host star	**Effective temperature (K)**	**g (m/s^2)**	**Metallicity (dex)**	**Semi-major axis (AU)**
TRAPPIST-1	2600	1000	0	0.02928
Proxima Centauri	3000	1000	0.3	0.04800
The Sun	5700	274	0.012	1.230

As discussed, in order to isolate the impact of the different stellar spectra, I performed three simulations, all with the planetary parameters of TRAPPIST-1e, taken from Gillon et al. (2017) and Grimm et al. (2018) and shown in Table 5.2. The parameters are consistent with those used recently by Fauchez et al. (2020). The simulations use the input stellar spectra for TRAPPIST-1, Proxima Centauri, and the Sun shown in Figure 5.1; henceforth referred to as T1:T1e, ProC:T1e, and Sun:T1e, respectively. As our primary focus is investigating the effect of different stellar spectra of our three host stars, the total stellar irradiance is fixed. In practice, this required altering the orbital semi-major axis, with the values show in Table 5.1. In reality, the orbital period would increase with semi-major axis according to Kepler's third law, with a commensurate change expected in the rotation rate to retain a tidally locked configuration. However, as changes in the rotation rate lead to well-studied changes in the circulation and climate (Merlis and Schneider 2010; Penn and Vallis 2018), a constant orbital period and angular frequency of rotation are adopted. The simulations were also performed at zero obliquity and eccentricity, consistent with tidal locking. It is important to note that simulations ProC:T1e and Sun:T1e were not designed to represent any particular planet, but solely to investigate the isolated impact of the different stellar spectra.

All simulations used a horizontal resolution of 2.5° in longitude by 2° in latitude, with 38 vertical levels between the surface (z = 0 km) and the TOA (z = 40 km). The

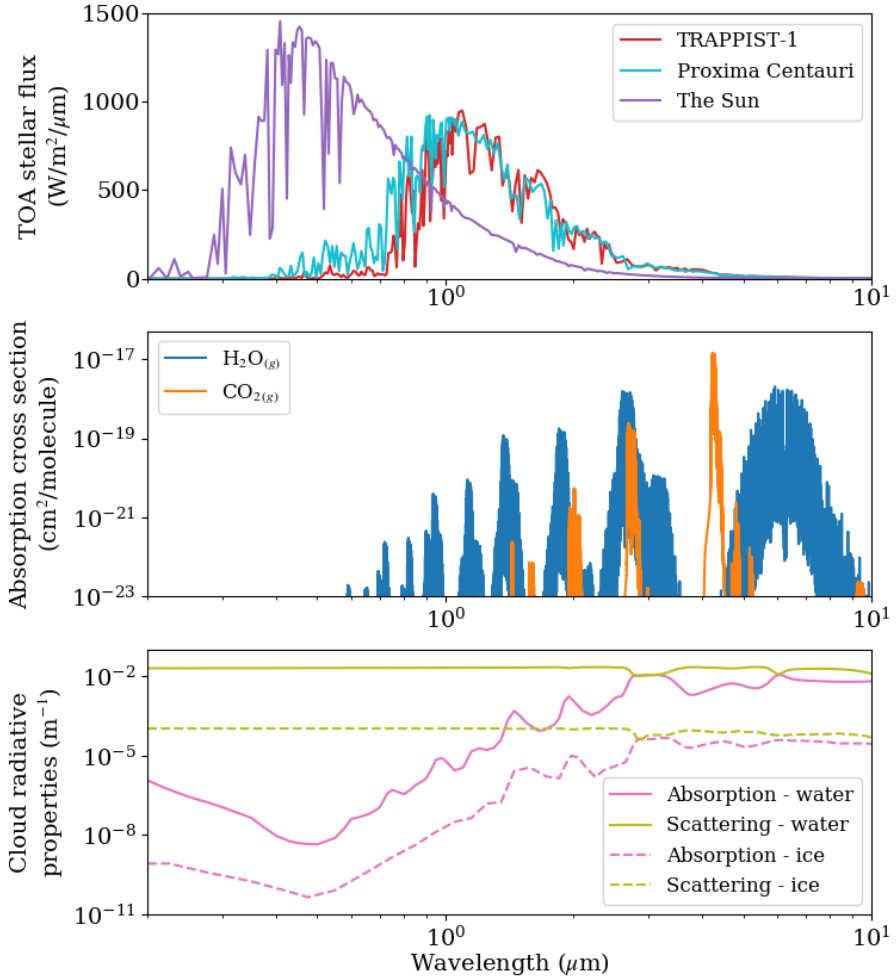

Figure 5.1: Wavelength vs. stellar flux per wavelength (top), received at the TOA for a planet orbiting TRAPPIST-1 (red), Proxima Centauri (cyan), and the Sun (purple), with a fixed total stellar flux of 900 W/m^2. Stellar profiles were created using the BT-settl model grid of theoretical spectra (Rajpurohit et al. 2013) with stellar parameters from Table 5.1. The middle panel shows the absorption cross section per molecule for water vapour (blue) (Polyansky et al. 2018) and carbon dioxide gas (orange) (Tashkun and Perevalov 2011) against wavelength. Absorption cross sections (centre) are for a pressure of ~800 hPa and an air temperature of ~230 K using the ExoMol (Tennyson et al. 2016) database, generated using ExoCross (Yurchenko et al. 2018). Also shown are the cloud absorption (pink) and scattering (green) rates for liquid water (solid) and water ice (dashed). These assume typical cloud droplet radii of 9 μm and 30 μm for a liquid and an ice cloud, respectively.

Table 5.2: Parameters used for all planetary configurations, based on TRAPPIST-1e from Gillon et al. (2017), Grimm et al. (2018) and Fauchez et al. (2020).

Parameter	
Stellar irradiance (W/m^2)	900
Orbital period (Earth days)	6.10
Angular frequency (rad/s)	1.19×10^{-5}
Eccentricity	0
Obliquity (°)	0
Radius (km)	5800
Surface gravity (m/s^2)	9.12

vertical levels were quadratically stretched to enhance the resolution at the surface. All simulations ran for 8000 Earth days, with a time step of 1200 seconds, with equilibrium being reached after 1000 Earth days, as determined through stable global mean surface temperatures and balance of the TOA flux (not shown). The data presented in Section 5.3 are temporal averages from 1000 to 8000 days, and where a vertical coordinate was used, the data were converted from the model height grid into σ, where $\sigma = p/p_s$ and p is the pressure and p_s the surface pressure for that specific model column. The global average surface pressure for all simulations was 1 bar. The sub-stellar point, the point closest to the host star, was located at (0, 0)° and the anti-stellar point, the point farthest from the host star, was located at (0,180)°. Finally, spatial averages are also presented in Section 5.3, where dayside-averaged quantities include data from −90° to 90° in latitude and −90° to 90° in longitude, and nightside-averaged quantities include data from −90° to 90° in latitude and −180° to −90° and 90° to 180° in longitude. Units given in terms of days refer to the duration of an Earth day. UM output was processed and plotted using the Python packages Iris (Met Office 2020) and Matplotlib (Hunter 2007).

5.3 Results

In this section I present results from our three simulations T1:T1e, ProC:T1e, and Sun:T1e. This begins with the basic temperature and wind structure (Section 5.3.1), before I investigate the moisture, cloud coverage, and the subsequent effect on the radiation budget (Section 5.3.2). I conclude with the components contributing to the heat and water vapour budget (Section 5.3.3).

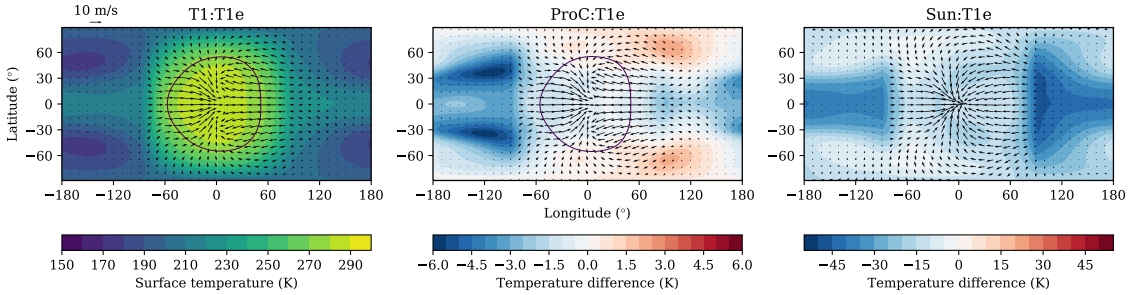

Figure 5.2: Map of the surface temperatures (colour scale) for the T1:T1e simulation (left). The following two plots show the difference in surface temperature from T1:T1e for cases ProC:T1e (middle) and Sun:T1e (right). A negative difference (blue) indicates a cooler surface than T1:T1e. Near-surface (10m) wind vectors (arrows) are also shown in each plot. The sub-stellar point is located at (0°, 0°). A contour (black) is shown for the 273 K surface isotherm, but this temperature is not reached over an extended region for case Sun:T1e. The colour scale for ProC:T1e and Sun:T1e is different. Only the temperature field is subtracted, the winds are the unaltered values for each simulation.

5.3.1 Surface temperature and atmospheric dynamics

A natural metric to describe the basic climatic state is the surface temperature. Figure 5.2 shows the surface temperature variation across latitude and longitude for our three simulations, with the winds at 10m shown as vector arrows. The left panel shows the absolute surface temperature for case T1:T1e, differences are then shown by subtracting the T1:T1e temperature field from either the ProC:T1e or Sun:T1e results as the middle and right panels, respectively. Figure 5.2 shows that as the temperature of the host star increases (left to right), the planetary surface temperature generally decreases. The greatest cooling is seen on the nightside, predominantly at the equator, with some warming in the polar regions of the ProC:T1e case. This suggests that there may be an asymmetry between the changes in the meridional and zonal transport efficiency. The region of the surface above 273 K is enclosed by the black contour in Figure 5.2. These regions are similar in magnitude in cases T1:T1e and ProC:T1e, but case Sun:T1e does not have a substantial region of the planetary surface that may sustain liquid water, and it may be considered less habitable as a result. All simulations have similar near-surface winds, showing a convergence towards the sub-stellar point, because solar forcing gives rise to a region of intense convection, as discussed in Boutle et al. (2017) and Sergeev et al. (2020).

Table 5.3 shows the spatial average dayside, nightside, and global surface temperatures for the three simulations. The values in Table 5.3 confirm that the simulation with the coolest star, T1:T1e, is the warmest, and case Sun:T1e exhibits the coldest temperatures.

The day-night temperature contrast is lowest for simulation T1:T1e, suggesting the most efficient day-night circulation of the three simulations, and case Sun:T1e has the highest contrast and weakest circulation. Cases T1:T1e and ProC:T1e have similar temperatures; T1:T1e is consistently warmer by about 1 K. The small differences in stellar spectra between TRAPPIST-1 and Proxima Centauri (Figure 5.1) may have a small effect on planetary climate, which is only amplified by higher contrasts in effective stellar temperature.

The dominant component of the heat redistribution from the day- to nightside of the planet is the zonal jet (e.g. Lewis et al. 2018). Figure 5.3 shows the longitudinal (and temporally) averaged zonal wind for latitude against σ, shown for simulations T1:T1e (left), ProC:T1e (middle), and Sun:T1e (right). The super-rotating equatorial jet reduces in magnitude as the host star increases in temperature (left to right). As shown by Showman and Polvani (2010) and Showman and Polvani (2011), the zonal jet is accelerated via large-scale wave patterns that are driven by the day-night temperature contrast, and it is further shaped by the vertical and latitudinal heating gradients. Lewis et al. (2018) also showed that changes in the radiative properties of the surface, that is, moving from bare land to ocean, resulted in a change in the temperature structure and thereby in a change in the jet acceleration. Our simulations show an increase in the overall absorption of radiation on the dayside from hotter to cooler stars (see Section 5.3.2). This might be expected to result in a higher day-night temperature contrast for cooler stars, as opposed to the reduction shown in Table 5.3. However, as the absorption is dominated by the atmosphere (as opposed to the surface), this results in a day-night contrast that extends over a wider range of pressures, that is, higher into the atmosphere for cooler stars (see Section 5.3.2). We speculate that this acts to extend the vertical region over which momentum convergence acts to accelerate the jet, and indeed, the jet structure persists over a broader vertical (and meridional) range for the simulations of cooler stars, as shown in Figure 5.3. The vertical component of momentum convergence has been shown to be vital for accelerating super-rotating equatorial flows (Showman and Polvani 2011) in hot Jupiters, and the wave responses in these cases have been studied in detail (Debras et al. 2019; Debras et al. 2020). However, such a detailed study of these simulations for future work, and it is simply note here that the jet is stronger for planets orbiting cooler stars, and the flow acts to transport heat and, critically, moisture zonally around the planet. Planets orbiting cooler stars

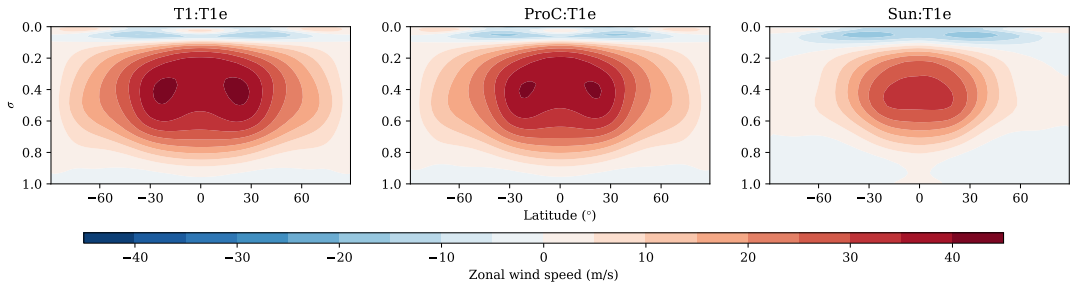

Figure 5.3: Latitude vs. σ (pressure divided by surface pressure), showing the zonal wind speed (colour scale), taken as a longitudinal average for simulations T1:T1e (left), ProC:T1e (middle), and Sun:T1e (right). Positive values for the zonal wind (red) represent eastward flow.

can also have a stronger nightside equatorial return flow near the surface, as shown in Figure 5.2.

Table 5.3: Mean surface temperatures for global, dayside, and nightside, and the temperature contrast (nightside subtracted from dayside) for T1:T1e, ProC:T1e, and Sun:T1e.

Simulation	Temperature (K)			
	Global	Dayside	Nightside	Contrast
T1:T1e	231.2	260.8	201.6	59.2
ProC:T1e	229.8	260.1	199.5	60.6
Sun:T1e	209.4	245.5	173.4	72.1

5.3.2 Moisture and cloud in the atmosphere

Water vapour and cloud play an important role in the radiation budget, particularly in shaping the OLR and in determining the contributions of the atmosphere compared to the planetary surface. Figure 5.4 shows the OLR for our three simulations after subtraction of the longwave surface emission.

All the simulations show the same pattern of dayside OLR originating from colder levels in the atmosphere than the surface, which is due to high-altitude clouds and water vapour. The nightside OLR indicates emission from warmer levels than the surface because of cloud and water vapour around the nightside temperature inversion and the lack of high-altitude cloud. In the rest of this section I investigate the changes in moisture and cloud coverage and use this to understand the changes in radiation emission between the simulations.

Moisture transport from the dayside to the nightside of a tidally locked planet is important because of its effect on the OLR, both directly or through subsequent cloud

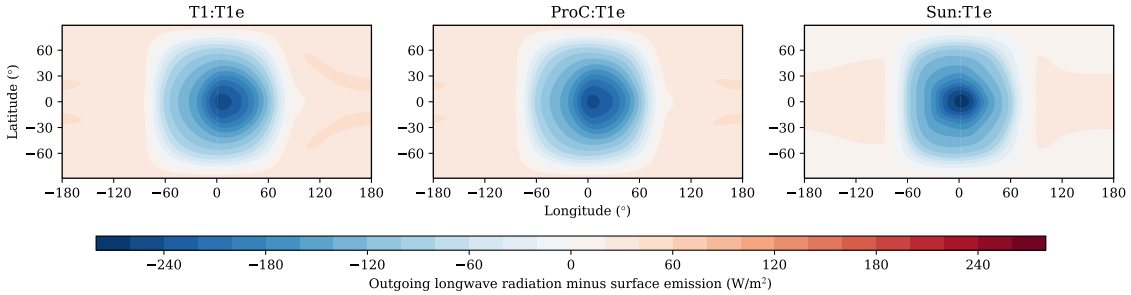

Figure 5.4: Map of the OLR minus the planetary surface emission as a colour scale for simulations T1:T1e (left), ProC:T1e (middle) and Sun:T1e (right). A positive difference (red) indicates an increase in OLR emission relative to the surface. The sub-stellar point is located at (0°, 0°).

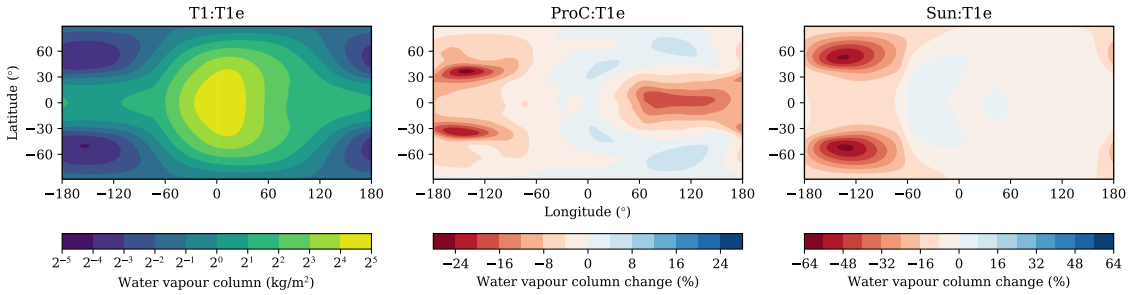

Figure 5.5: Map of the column-integrated water vapour (mass of water per cross-section area, colour scale) for the T1:T1e simulation (left). The following two plots show the change in water-vapour column content for ProC:T1e (middle) and Sun:T1e (right) with the equivalent water-vapour column content of T1:T1e if it were at the same temperature profile as ProC:T1e and Sun:T1e, respectively, at the same relative humidity as T1:T1e. The percentage is calculated from the total water-vapour content of the column. A positive difference (blue) indicates a moister column than the T1:T1e, removing the effect of temperature on moisture from the Clausius-Clapeyron relation. The sub-stellar point is located at (0°, 0°). The scale for ProC:T1e and Sun:T1e is different.

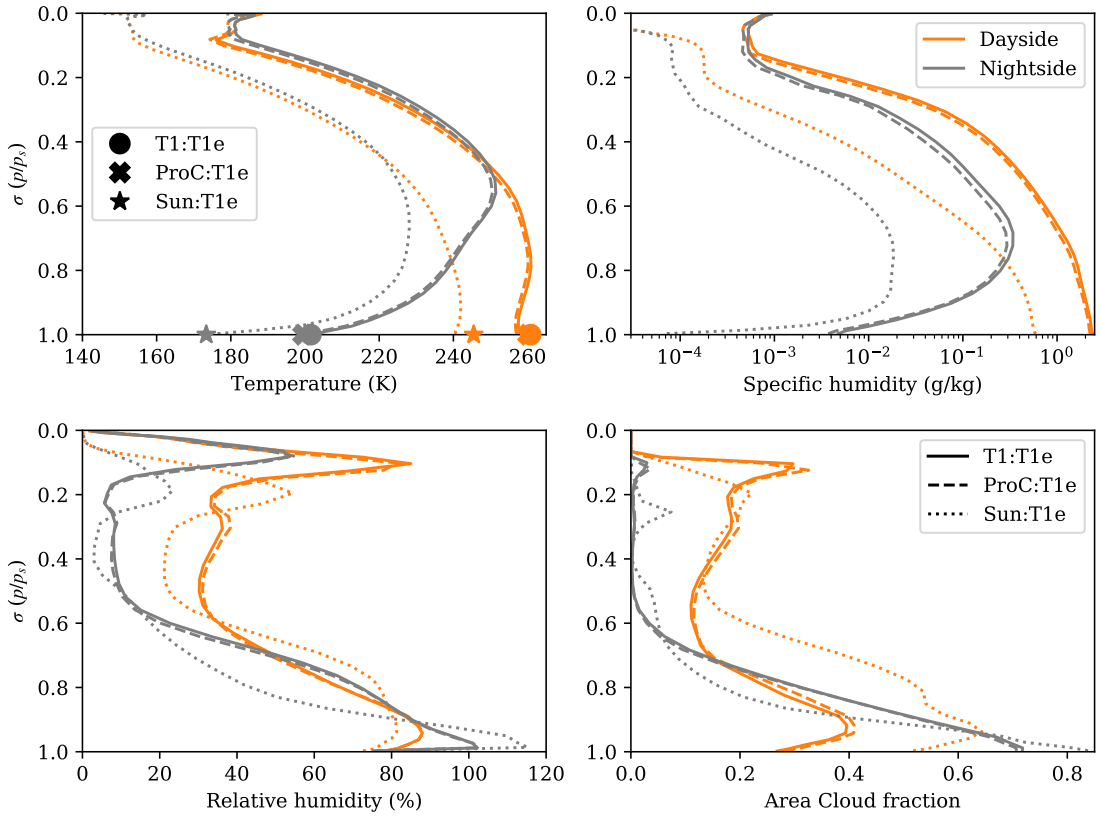

Figure 5.6: Temperature (top left), specific humidity (top right), relative humidity (bottom left), and area cloud fraction (bottom right) horizontally averaged over the dayside (orange) and nightside (grey) hemispheres, plotted against σ (pressure divided by surface pressure). These are shown for all three simulations: T1:T1e (solid line), ProC:T1e (dashed line), and Sun:T1e (dotted line). The left panel also includes the hemisphere-averaged surface temperatures from Table 5.3 as a filled circle for T1:T1e, a filled cross for ProC:T1e, and a filled star for Sun:T1e.

formation (Yang and Abbot 2014). Generally, moisture is transported upward from the surface through convection in the sub-stellar region. This also leads to cloud formation, with the zonal jet transporting moisture (and cloud) horizontally high up in the troposphere. Subsidence and further condensation occur on the nightside (Yang and Abbot 2014; Boutle et al. 2017; Lewis et al. 2018; Sergeev et al. 2020). To explore this for our simulations, Figure 5.5 shows the column-integrated water content as a function of latitude and longitude. The left panel shows the absolute water-vapour column content for simulation T1:T1e, while the middle and right panels show the percentage change in water-vapour column content for simulations ProC:T1e and Sun:T1e after subtraction of an equivalent T1:T1e water-vapour content. However, as the dominant factor in the moisture content variation is due to the temperature change through the Clausius-Clapeyron relation, I attempted to remove this component. To do this, the difference in relative humidity is calculated for cases ProC:T1e and Sun:T1e from the T1:T1e case and integrated the equivalent water column content as a percentage change from cases ProC:T1e and Sun:T1e, respectively. Figure 5.5 shows that as the host star temperature increases (left to right), the nightside of the planets becomes relatively drier, beyond the drying through the Clausius-Clapeyron relation. This means that there is a general decrease in the relative humidity of the atmospheric column, suggesting a decrease in the atmospheric transport observed in the zonal jets in Figure 5.3.

The advection of heat, moisture, and cloud from the dayside results in a nightside temperature inversion (Joshi et al. 2020), leading to the radiator fin effect discussed in Yang and Abbot (2014). The magnitude of this effect depends on the opacity on the nightside, which is determined by the water vapour and cloud content. From Figure 5.5, it is expected that the planets orbiting cooler stars have a stronger water-vapour greenhouse effect on the dayside, but increase the effect of the nightside radiator fin by increasing cloud content and, hence, the OLR. This can be explored further by using vertical profiles of the temperature, moisture content, and cloud fraction from our simulations. Figure 5.6 shows the hemispherically averaged variation with σ of air temperature (top left), specific humidity (top right), relative humidity (bottom left), and area cloud fraction (bottom right). The area cloud fraction is the area within a model grid box that is covered by cloud.

Firstly, Figure 5.6 shows a clear temperature inversion on the nightside of all simulations (top left), linked to the circulation in the free atmosphere and radiative cooling of the surface. Additionally, the day-night temperature difference between the vertical profiles (top left) is also smaller for cases with cooler stars below the inversion, which is consistent with the efficiency of the day-night redistribution, which also increases toward cooler host stars.

On the dayside, with the majority of the atmosphere cooler than the surface (top left of Figure 5.6), greenhouse gases and clouds decrease the OLR relative to surface emission (shown in Figure 5.4). The hemispherically averaged specific humidity is highest at all levels on the dayside and nightside for case T1:T1e and lowest for case Sun:T1e (top right of Figure 5.6). Therefore, a stronger greenhouse effect for simulation T1:T1e is expected. For all simulations, the combination of the temperature inversion, warmer air temperatures, and stronger zonal transport leads to an increased water vapour and a higher OLR relative to the surface on the nightside. T1:T1e is the moistest of our simulations, resulting in the largest increase in OLR due to greenhouse gases, closely followed by ProC:T1e.

The relative humidity (bottom left panel of Figure 5.6) shows an increase at high altitudes, which is both larger in magnitude and higher in the atmosphere for simulations T1:T1e and ProC:T1e than for case Sun:T1e. This effect has previously been noted by Yang et al. (2019b), who demonstrated that the increased high-altitude relative humidity for planets absorbing more shortwave radiation in the atmosphere resulted in an increased water-vapour greenhouse effect and therefore in a reduction in OLR. Table 5.4 shows the TOA radiative effects of water vapour and clouds for all our simulations. The radiative effects of water vapour and clouds were isolated through additional diagnostic radiative transfer calculations, which did not affect the model evolution. One calculation omitted only the water-vapour opacity, and a second calculation (called 'clear-sky') omitted the radiative effects of clouds, both of which can then be compared to the baseline simulation for all cases to provide the values in Table 5.4. For our simulations an increased water-vapour greenhouse effect for planets orbiting cooler stars is also found (as in Yang et al. 2019b), shown in Col. 3 in the top rows of Table 5.4, but a clear and commensurate change in the OLR is absent from Figure 5.4 because the cloud coverage contributes more to the dayside

greenhouse effect, which is shown in Col. 3 in the bottom rows of the same table.

Table 5.4: Hemisphere-averaged TOA radiative effect in the shortwave (dayside only) and longwave (dayside and nightside) for both water vapour (top rows) and cloud (bottom rows), including the net value (sum of three separate terms divided by two) for simulations T1:T1e, ProC:T1e, and Sun:T1e. A positive radiative effect indicates a decrease in outgoing radiation. Parentheses on the longwave TOA radiative effect include the absolute percentages of the averaged TOA outgoing longwave flux for that hemisphere. The effects of the two components are isolated using diagnostic calculations of the radiative transfer omitting their opacities (see text for explanation).

Simulation	**TOA radiative effect (W/m^2)**			
	Shortwave	**Longwave**		**Net**
	Dayside	**Dayside**	**Nightside**	
		Water Vapour		
T1:T1e	+28.7	+9.47 (5.06%)	-21.4 (16.5%)	+8.37
ProC:T1e	+29.1	+8.65 (4.71%)	-21.5 (17.2%)	+8.14
Sun:T1e	+5.39	+0.412 (0.312%)	-15.2 (20.9%)	-4.71
		Cloud		
T1:T1e	-110	+27.0 (14.4%)	-4.58 (3.53%)	-43.8
ProC:T1e	-117	+28.2 (15.3%)	-4.07 (3.25%)	-46.4
Sun:T1e	-189	+40.7 (30.8%)	-0.822 (1.13%)	-74.5

Figure 5.6 also shows that the dayside-averaged cloud coverage (bottom right) is largest for the warmer star, with Sun:T1e having a ~60% larger peak than T1:T1e and ProC:T1e, at around $\sigma = 0.9$. Cloud coverage on the dayside can cool the planet by increasing the TOA albedo. This is demonstrated in Table 5.5, which shows the dayside albedo and total shortwave absorption as fractions of the total TOA incident stellar flux, in particular the second column.

Table 5.5: Dayside shortwave radiation budget hemispherically averaged for the TOA albedo and the dayside shortwave radiation absorption (as a fraction of the total TOA incoming shortwave radiation) for the T1:T1e, ProC:T1e and Sun:T1e simulations. The dayside albedo has been decomposed into an atmospheric and a surface contribution following Donohoe and Battisti (2011). The dayside shortwave radiation absorption is shown for the atmosphere and surface, with the former decomposed into cloud and water-vapour contribution by comparing the baseline model to the calculations where these radiative effects have been omitted (see text for explanation).

Simulation	**Dayside TOA albedo (%)**			**Dayside shortwave absorption (%)**			
	Total	**Atmosphere**	**Surface**	**Atmosphere**	**Cloud**	**Water Vapour**	**Surface**
T1:T1e	28.8	28.0	0.767	43.0	12.2	15.6	28.3
ProC:T1e	30.6	29.8	0.790	41.1	11.0	15.3	28.3
Sun:T1e	54.8	53.6	1.24	11.5	4.38	2.78	33.7

The total albedo increases for hotter stars, see Cols. 2-4 in Table 5.5, partially because the surface albedo increases, but this is predominantly caused by increased cloud coverage, as shown in Col. 2 in the bottom rows of Table 5.4. Table 5.5 shows that the albedo is highest for simulation Sun:T1e and lowest for case T1:T1e, which has the lowest

dayside cloud coverage (clouds are equally reflective in each case, see Figure 5.1). This is the dominant cause for the decrease in surface temperatures in Figure 5.2 and air temperatures; case Sun:T1e is ~15-20 K cooler for all σ on the dayside in Figure 5.6 (top left grey). Cloud also affects the OLR budget, which is shown in Cols. 3 and 4 in the bottom rows of Table 4, which show the cloud radiative effect. On the dayside, cloud increases the longwave radiation retained by the atmosphere, which decreases the OLR. However, this effect is about four times smaller than the shortwave cloud radiative effect, which is the dominant factor in the overall decrease in planetary temperature for hotter stars.

Table 5.6: Hemisphere-averaged OLR budget for the dayside and nightside as a percentage of the non-reflected shortwave radiation absorbed by the planet, shown for simulations T1:T1e, ProC:T1e, and Sun:T1e.

Simulation	**OLR budget (%)**	
	Dayside	**Nightside**
T1:T1e	59.1	40.9
ProC:T1e	59.5	40.5
Sun:T1e	64.5	35.5

On the nightside, the OLR is increased through cloud radiative effects. Near the surface, there is more cloud for simulation Sun:T1e than in the two other cases (Figure 5.6, bottom right). Near-surface cloud has a weaker effect on the cloud radiative effect as the cloud temperature is more similar to that of the surface than are the remaining temperatures below the inversion maxima. Because of the nightside temperature inversion, the atmosphere at $\sigma > 0.2$ for all simulations is warmer than the planetary surface and thus radiates heat into space more efficiently, which increases the cloud radiative effect and cools the planet. Cases T1:T1e and ProC:T1e both have more cloud between $0.6 < \sigma < 0.9$ than case Sun:T1e, which leads to an increase in the nightside OLR relative to the clear-sky case, shown in Col. 4 in the bottom rows of Table 5.4. The radiator fin effect is stronger for planets with more efficient day-night circulation because the nightside cloud and water vapour content is higher. Table 5.6 shows the TOA outgoing radiation budget as the dayside and nightside OLR as a percentage of the non–reflected shortwave radiation. Table 5.6 demonstrates an increase in the proportion of total radiation emitted by the planet coming from the nightside for cooler stars. This might suggest that planets orbiting cooler stars, which have generally a more efficient circulation, are cooler overall. However, our simulations show the reverse, where the cooler host star results in an overall warmer planetary climate, showing that the changes in dayside cloud albedo are

the dominant mechanism (Yang et al. 2013). This is clearly shown in the bottom rows of Table 5.4, where the shortwave dayside cloud radiative effect is strongest and dominates the net cloud radiative effect, which also increases with host star temperature, leading to the strongest planetary cooling.

Table 5.5 shows that the shortwave reflection (albedo) on the dayside is highest for simulation Sun:T1e and lowest for the T1:T1e. The method described by Donohoe and Battisti (2011) was used to determine the atmospheric and surface contributions to the TOA dayside albedo, with the atmosphere as the dominant contribution at ~97.5% for all simulations. The surface contribution has been significantly attenuated by the atmosphere, reducing the surface albedo by ~90% of the actual value for all the simulations. The majority of this atmospheric albedo is produced through cloud scattering, which is the dominant contribution to the TOA shortwave cloud radiative effect compared to cloud absorption (Col. 2 in the bottom rows of Table 5.4). The remaining outgoing radiation budget, emitted as longwave radiation, may be distributed between dayside and nightside emission and is shown in Table 5.6. The proportion of the remaining radiation increases in favour of emission on the dayside for planets orbiting hotter stars, as demonstrated by the increased day-night surface temperature contrast, as shown in Table 5.3. This occurs even with an increase in cloud that suppresses longwave emission on the dayside (Col. 3 in the bottom rows of Table 5.4). The water-vapour greenhouse effect has the opposite effect: it decreases in hotter stars (Col. 3 in the top rows of Table 5.4), but its effect is weaker than that of the cloud.

On the nightside, both cloud and water vapour increase the nightside OLR emission due to the temperature inversion (Col. 4 in Table 5.4), which enhances the radiator fin effect. For water vapour, this effect in terms of the total radiation budget decreases for cooler stars, but when it is compared to the total nightside OLR (parentheses), it increases with host star temperature. For the cloud, this decreases for both interpretations, and their combined effects contribute ~20% of the nightside OLR. The nightside radiator fin effect is thus dominated by the day-night temperature contrast of the surface, rather than the overall cloud or water-vapour structure in the atmosphere, which maintains a similar contribution to the total nightside OLR.

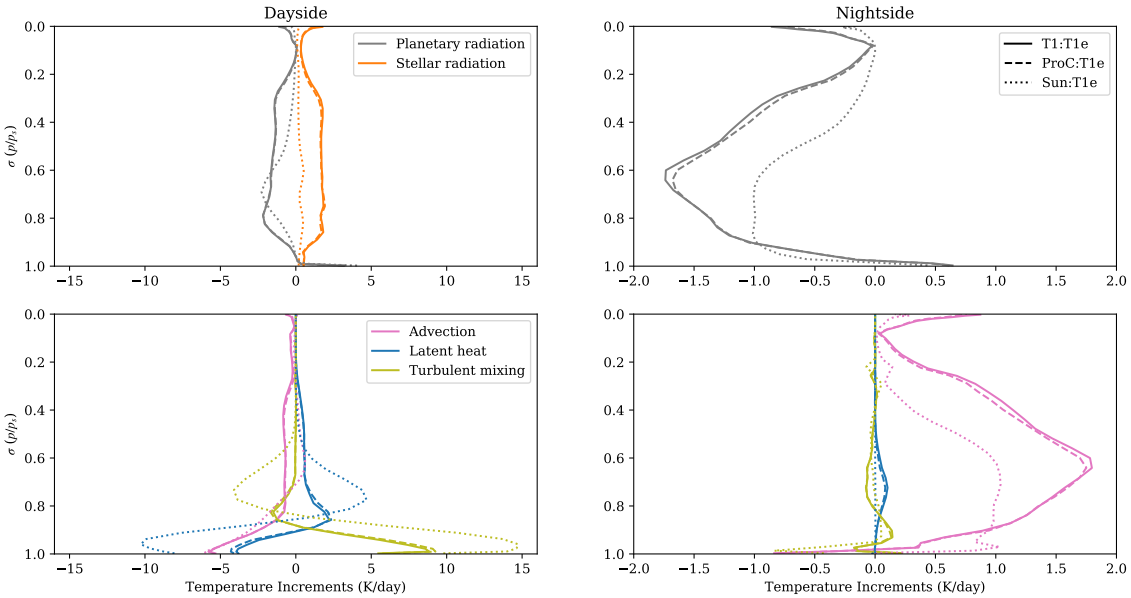

Figure 5.7: The rate of change of temperature or heating profiles, known as temperature increments, plotted against σ (pressure divided by surface pressure) for simulations T1:T1e (solid lines), ProC:T1e (dashed lines), and Sun:T1e (dotted lines) for each component process. The processes shown are atmospheric absorption of stellar radiation (orange, top panels), thermal emission or absorption of planetary radiation (grey, top panels), large-scale circulation, known as advection, (pink, bottom panels), latent heating or cooling of water (blue, bottom panels), and turbulent mixing (green, bottom panels). The day- and nightside hemispherically averaged values are shown in the left and right panels, respectively. The x-axis limits are different between the day- and nightside panels. In equilibrium the net heating is zero.

The global net TOA water-vapour radiative effect (Col. 5 in Table 5.4) is an order of magnitude smaller than the net cloud radiative effect and changes sign between the M dwarf and G dwarf orbiting simulations. Table 5.4 shows that in T1:T1e and ProC:T1e, water vapour has a net warming effect on the global budget, while in case Sun:T1e, water vapour has a net cooling effect. The difference is mainly attributed to the decrease in shortwave absorption (Col. 2 in Table 5.4) for hotter stars, but also to the decrease in water-vapour greenhouse effect stemming from the decrease in moisture in the upper atmosphere on the dayside (Figure 5.6).

5.3.3 Heat and moisture budgets

To further isolate the key or dominant processes, I separated the various contributions to the atmospheric temperature and specific humidity changes. Figure 5.7 shows the hemisphere-averaged heating rates, or temperature increments, as a function of σ for the dayside (left panels) and nightside (right panels). For the dayside radiation (top left panel,

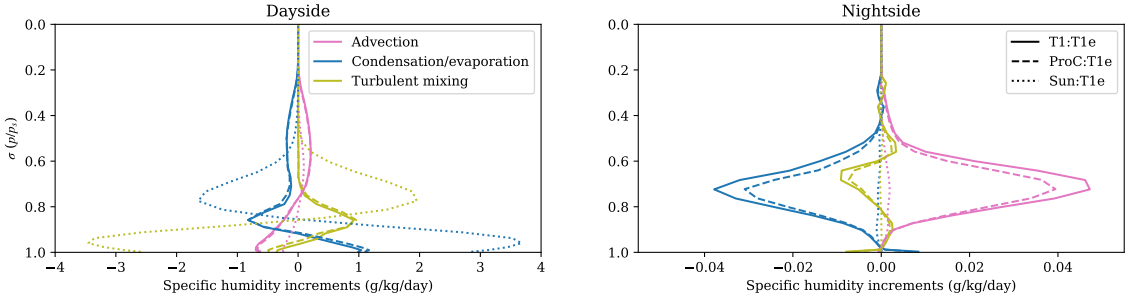

Figure 5.8: The rate of change of the specific humidity, known as specific humidity increments, plotted against σ (pressure divided by surface pressure) for simulations T1:T1e (solid lines), ProC:T1e (dashed lines), and Sun:T1e (dotted lines) for each component process. The processes shown are the large-scale circulation, known as advection, (pink), condensation or evaporation (blue), and turbulent mixing (green). The day- and nightside hemispherically averaged values are shown in the left and right panels, respectively. The x-axis limits are different between the day- and nightside panels. In equilibrium the net heating is zero.

Figure 5.7), direct stellar radiation heats the atmosphere in cases T1:T1e and ProC:T1e, predominantly for $0.2 < \sigma < 0.9$, at ~2 K/day, and the stellar heating of the atmosphere is significantly reduced in case Sun:T1e. For simulations T1:T1e and ProC:T1e, the region where $\sigma < 0.7$ is close to radiative equilibrium (planetary radiation balances stellar radiation), which is not the case for Sun:T1e until much higher in the atmosphere, $\sigma \lesssim 0.3$. The atmospheric absorption of stellar radiation is further quantified in Table 5.5, which shows the dayside atmospheric absorption as a percentage of the incident TOA shortwave radiation. This is nearly four times higher for case T1:T1e than in case Sun:T1e: the T1:T1e atmosphere absorbs 1.9 % more stellar radiation than case ProC:T1e.

The direct heating of the middle to upper troposphere by cooler stars leads to an increase in convective stability in cases T1:T1e and ProC:T1e, reducing the vertical transport of moisture and thus the height and magnitude of the latent heating term on the dayside (bottom left panel, Figure 5.7). This is supported by the dayside cloud coverage shown in Figure 5.6, with case Sun:T1e exhibiting more cloud at $\sigma > 0.5$ than cases T1:T1e and ProC:T1e. As a result of a reduced atmospheric absorption of non-reflected shortwave radiation, case Sun:T1e experiences an increased proportion of (non-reflected) stellar radiation absorbed at the surface on the dayside (Table 5.5, compare Cols. 5 and 8), than the simulations with cooler host stars. This leads to higher turbulent flux heating in the boundary layer, which is balanced by latent cooling from evaporation of precipitation from increased cloud and advective cooling (bottom left panel, Figure 5.7). The shortwave

atmospheric absorption is isolated for both cloud and water vapour in Table 5.5 (Cols. and 7, respectively). Although the effects of both are of a similar order of magnitude for each simulation, for planets orbiting M dwarfs, water vapour contributes more to atmospheric absorption than clouds, while the opposite is true for G dwarfs. The remaining contribution to shortwave atmospheric absorption is carbon dioxide, which is held at a constant concentration in our simulations.

On the nightside (right panels, Figure 5.7), advective heating is balanced by cooling through planetary radiation emission. Advective heating comes from transport of heat from the dayside, producing the temperature inversions seen in Figure 5.6, and is highest for case T1:T1e, which follows from the stronger equatorial jets seen for planets orbiting cooler stars (Figure 5.3). The relatively dry atmosphere on the nightside and the lack of stellar heating at the surface result in low latent heating and boundary layer contributions (bottom right panel, Figure 5.7).

Similarly to the temperature increments, I isolated the contributions from different physical processes to the moisture budget in our simulations. Figure 5.8 shows the rate of change of specific humidity in a similar format as in Figure 5.7. On the dayside (left, Figure 5.8), turbulent mixing transports water vapour from near the surface to the mid-troposphere ($0.5 < \sigma < 0.85$), where it condenses, precipitates, and then evaporates again in the boundary layer ($\sigma > 0.85$). The large-scale transport is strongest for the T1:T1e case, which is shown in the specific humidity increment due to advection. Cool dry air is advected, returning from the nightside near the surface, and moist warm air is transported vertically, reducing moisture near the surface. Simulation T1:T1e has the highest nightside advection of water vapour (right, Figure 5.8), and the lowest is found in case Sun:T1e. On the dayside, advection reduces specific humidity near the surface. The minima for the specific humidity increment due to advection are largest for cases T1:T1e and ProC:T1e, which may be due to a stronger return flow from the nightside. Evaporation, condensation and boundary layer effects occur deeper in the atmosphere for case Sun:T1e than in the remaining simulations, suggesting that convection becomes deeper for hotter host stars. On the nightside (right, Figure 5.8), moist air is transported in by advection from the dayside, where it condenses to form nightside cloud. The cloud forms mainly around σ

= 0.7, where it descends to near the surface, as shown in Figure 5.6, where the cloud area fraction is highest there.

Our results have isolated the effect that different host star spectra have on the simulated planetary climate of a tidally locked terrestrial exoplanet, with a modern-day Earth-like atmosphere. With all else held constant, a planet orbiting a cooler star such as TRAPPIST-1 or Proxima Centauri absorbs more radiation directly in the atmosphere than a planet orbiting the Sun, similar to the results of Shields et al. (2013) for rapidly rotating non-tidally locked planets. Increased atmospheric stellar radiation absorption leads to a decrease in the proportion of radiation that is absorbed by the planetary surface and to an increase in static stability and a decrease in convection, leading to reduced dayside cloud coverage. This decreases the albedo and leads to a warmer planet: simulation T1:T1e is globally 1.4 K and 21.8 K warmer than cases ProC:T1e and Sun:T1e, respectively. The day-night temperature and atmospheric moisture content contrast is also lowest for case T1:T1e.

5.4 Conclusions

I have used the Met Office 3D GCM to compare simulations of the climates of a planet orbiting three different host stars, two of which are M dwarfs known to be orbited by near Earth-sized planets in their habitable zone. The third host star was the Sun, a G dwarf. An Earth-like atmospheric composition and a tidally locked state are assumed. With stellar irradiance and other planetary parameters held constant, planets orbiting cooler stars experience an increased proportion of incident radiation that is absorbed directly by the troposphere compared to the surface. This is due to the increase in the ability of cloud, water vapour, and carbon dioxide to absorb stellar radiation when cooler stars are orbited. This leads to an atmosphere that is more statically stable, reducing dayside convection and thus cloud coverage compared to hotter stars. For these planets orbiting hotter stars, increasing cloud coverage increases the planetary albedo, which decreases the overall proportion of radiation absorbed by the planet, but maintains a lower ratio of atmospheric to planetary surface absorption. The reduction in albedo causes planets orbiting cooler stars to be globally warmer, and atmospheric transport of heat and moisture from the dayside to the nightside is more efficient because the equatorial jets are stronger. This decreases the

ratio of dayside to nightside OLR. I find that the combined contribution of water vapour and cloud to the nightside radiator fin effect is enhanced to a similar degree for all stellar types, contributing ~20% of the nightside OLR for M and G dwarfs. Overall, of planets near the outer edge of the habitable zone that have an Earth-like composition, those orbiting cooler stars may be considered more habitable than similar counterparts orbiting hotter stars because they are likely to have a larger surface region that can support liquid water.

It is important to note that all our simulations adopted the current planetary parameters estimated for TRAPPIST-1e, and the stellar spectrum was varied. The total stellar irradiance was held constant by varying the orbital semi-major axis only between simulations, but a tidally locked configuration was retained. Therefore the two additional simulations irradiated by Proxima Centauri and the Sun were not designed to represent any real planet, and the resulting rotation rate was inconsistent with the orbital period and tidally locked state (as the rotation period should increase with semi-major axis for a tidally locked planet). I have designed the simulations to isolate the impacts of a different host star spectrum on the simulated planetary climates.

Our method, however, has important limitations that must be addressed with additional research that is beyond the scope of this Chapter. As M dwarfs are more active than G dwarfs, and the planet must orbit closer to the host star to intercept similar stellar flux levels, the impact of flares and high-energy radiation must be considered (e.g. see Tilley et al. 2019). Concerted studies in 3D are required to explore the interaction of the stellar activity with the atmosphere, and in particular, the potential impacts on the O_3 distribution, given that tidal locking gives rise to a permanent day- and nightside, the latter never receiving direct stellar radiation. This work has begun for quiescent host stars (Yates et al. 2020), and flaring host stars (Ridgway et al. 2022). Furthermore, the atmospheric composition in our simulations was kept constant in a simplified Earth-like configuration. It is clear from our own Solar System that terrestrial planets can have extremely different compositions. In this Chapter, I focused on the impacts of stellar spectra on climate and potential implications on habitability, therefore I based our work on the only currently known inhabited planet, Earth. However, Earth has sustained life through very different

atmospheric compositions, given the the first evidence of life on Earth is from at least as early as 3.7 Ga (Rosing 1999; Hassenkam et al. 2017).

Potentially important climate processes or mechanisms have also been omitted, such as atmospheric chemistry (e.g. ozone in Yates et al. 2020), land-surface impact (e.g. Lewis et al. 2018), dust (e.g. Boutle et al. 2020), ocean heat transport (e.g. Yang and Abbot 2014; Yang et al. 2019a; Del Genio et al. 2019), and perhaps sea- or land-ice (Rose et al. 2017). In particular, Yang and Abbot (2014) and Del Genio et al. (2019) found that ocean transport also acts to reduce the day-night temperature contrast. Inclusion of ocean heat transport would be expected to decrease our predicted day-night temperature contrasts and day-side convection. However, the ocean transport is sensitive to the configuration of land and ocean (Yang et al. 2019a). Additionally, ice formation may lead to a cooling of all our simulations if it were included, and it might increase the differences between the M dwarf cases and the simulation using the Sun because the ice albedo under G dwarf stellar spectra is higher (Shields et al. 2013). However, as ice formation might well be limited to the nightside, its effect on the overall climate of a tidally locked planet could be weak. The reduction in ice albedo from hotter to cooler host stars suggests that their orbiting planets may be more resistant to entering a "snowball" state (Rushby et al. 2019), which has occurred at least three times for Earth (e.g. Lenton and Watson 2011). Several studies have questioned whether the climate of tidally locked planets can exist in a stable regime and avoid atmospheric collapse (Kasting et al. 2014; Turbet et al. 2018). The reduced day-night temperature contrast found in our simulations irradiated by cooler host stars may aid their atmospheric stability.

The adoption of a fixed Earth-like atmospheric composition also neglects the impact of the stellar irradiation on the long-term evolution of the atmosphere, which is required to determine the likely atmospheric composition. However, this is a difficult and poorly constrained problem (Bolmont et al. 2017; Dong et al. 2018). Finally, the impact of life itself was not considered. The presence of life on terrestrial exoplanets may fundamentally alter the atmospheric composition (Nicholson et al. 2018; Vecchio et al. 2020), as has likely happened throughout Earth's own history (Lenton and Watson 2011; Lenton et al. 2018b).

5.5 Chapter Summary

In this Chapter, I have established the effect that host star has on the climate of tidally locked exoplanets. After considering climate, Chapter 6 will consider how the stellar spectrum affects life and potential biospheres through changes in atmospheric photochemistry.

Chapter 6

Biogeochemical modelling of early biospheres

6.1 Introduction

In this chapter, I investigate the effect of biospheres on the atmospheric composition of TRAPPIST-1e and the Earth at 3.8 Ga. I focus on life prior to the evolution of oxygenic photosynthesis, and particularly focus on how life may affect the atmosphere differently on TRAPPIST-1e. Following this, the potential to observe biosignatures from this ecosystem is investigated for TRAPPIST-1e.

Planets orbiting M-dwarfs provide the most realistic opportunity for detecting biosignatures in the near future through JWST and up and coming telescopes such as the European Extremely Large Telescope. JWST has already been used to determine that TRAPPIST-1b+c are unlikely to have thick atmospheres (Greene et al. 2023; Zieba et al. 2023), but could have surface pressures of up to 10 bar (Ih et al. 2023; Lincowski et al. 2023). In order to detect potential life on these planets, which are orbiting very different host stars to our Sun, it is important to not only study the potential abiotic atmospheres of these planets, but also the potential relationship between life, the atmosphere and the host star (Catling et al. 2018).

Life on other planets may most likely resemble life on the early Earth rather than the modern day. Life was thought to have emerged during the early Archean at the latest by 3.7 Ga (Rosing 1999), with potential for life to have emerged much earlier (Knoll and Nowak 2017). Since then, life on Earth has diversified hugely, undergoing major evolutionary revolutions including the evolution of oxygenic photosynthesis and multi-cellular eukaryotes (Lenton and Watson 2011). The number of evolutionary steps as well as the potential difficulty of some of these that are required to get to higher levels of complexity means that many planets may be limited to more primitive life (Watson 2008). Simple microbial biospheres similar to those that existed during the Archean could be the most common.

The detection of primitive biospheres via their effect on CH_4 and CO has been considered for planets (at least around Sun-like stars), with ecosystems driven by H_2 and CO consumption and are characterised by atmospheres with a low CO:CH_4 ratio (Sauterey et al. 2020; Thompson et al. 2022). Krissansen-Totton et al. (2018c) predicts that biospheres could produce a detectable disequilibrium with an atmosphere composed of CO_2 plus CH_4 in the absence of CO. This may be the most likely source of biosignature detection with current instrumentation (Krissansen-Totton et al. 2018b). A potential additional challenge for the unambiguous identification of biosignatures specific to planets around M-dwarf stars is the accumulation of abiotic CO and possibly O_2. This results from the photolysis of CO_2 by FUV from the M-dwarf spectrum combined with a lower rate of recombination of these species due to lower OH abundances caused by the lower NUV flux emitted by M-dwarfs (Harman et al. 2015). Schwieterman et al. (2019) finds that high levels of CO could accumulate on inhabited M–dwarf orbiting planets. Using GCMs and photochemical models Fauchez et al. (2019), found that clouds and especially hazes could play an important role in blocking the observations of Archean-like atmospheres in large regions of JWST transmission spectra, however CO_2 features are likely to be readily observable on such planets.

A fundamental challenge to identifying a biosignature from atmospheric concentrations of CH_4, CO and O_2 is that all of these gases have both abiotic and biological sources and sinks, and may participate in biogeochemical cycles through the atmosphere-ocean-

surface system. Their concentrations are therefore controlled by the combination of regulatory feedbacks generated by a combination of abiotic and hypothetical biological processes. As argued by Catling et al. (2018), a consistent approach then requires populating a hypothesis space with predictions from exo-Earth system models, applying observational constraints and making full use of available context. Unlike atmosphere-only models, such exo-Earth-system models make explicit the processes and hypotheses they include and facilitate the incorporation of additional constraints and context from multiple sources. This type of model has been applied to the early Earth (Kharecha et al. 2005; Sauterey et al. 2020), however there has yet to be an ecosystem model focusing on the implications of M-dwarfs spectra. Here, I use a newly developed coupled atmosphere-ocean-ecosystem model to show that a H_2 and CO consuming biosphere, which produces CH_4 as a biproduct, leads to an atmosphere with detectable levels of CO_2 and CH_4, but also large signals of CO for a TRAPPIST-1e analogue. I review the abiotic and ecosystem processes considered in Sections 6.2 and 6.3. In Section 6.4, I outline the model components used here, with results from the coupled model and subsequent transmission spectra shown in Section 6.5. In Section 6.6, I discuss the implications of large CO features in our biotic configuration that can lead to ambiguity in a potential biosphere.

6.2 Abiotic background assumptions and processes

I consider a terrestrial planet in the habitable zone of an M-dwarf star, with an Earth-like atmosphere dominated by N_2 and CO_2, with liquid water, noting that this may imply an atypical evolutionary history given the star's extended pre-main sequence phase (Luger and Barnes 2015). In this work, we consider the habitable zone to be the orbital radii at which a planet can maintain some liquid water at the surface (Kasting et al. 1993a). This most likely also requires a functioning recycling of the lithosphere of some kind, in order to cycle CO_2 and generate a silicate weathering feedback.

The atmosphere's total hydrogen content will then be controlled by redox balance, i.e. the balance between net surface reductant input and hydrogen escape, and atmospheric composition by the combination of photochemistry and surface processes.

Outgassing at the planetary surface is uncertain. Modern Earth plate tectonics allow for the efficient cycling of volatiles, which is thought to be important for habitability by controlling CO_2 over geological time scales (Walker et al. 1981). However, the tectonic history of the Earth remains uncertain (e.g. Palin and Santosh 2021; Lourenço and Rozel 2023) and modern plate tectonics may only have evolved as late as 0.85 Ga (Korenaga 2013). During the Archean, the Earth could have been in a stagnant lid state (Solomatov 1995), where the lithosphere is a single lid and there is little surface motion. In these conditions, outgassing rates are thought to be lower (Guimond et al. 2021). Arguments have also been made that plate tectonic could have been preceded by a plutonic squishy lid, a regime that has small strong plates that are separated by warm and weak regions created by plutonism (Lourenço and Rozel 2023), similar to Harris and Bédard (2014) and Davies et al. (2023). Modelling of this regime suggests that outgassing rates could be up to a factor of two higher, assuming a similar extrusion efficiency of the lithosphere to today (Lourenço et al. 2020).

The mix of gases outgassed is affected by the fugacity of the mantle (Kasting et al. 1993b; Guimond et al. 2021). A more reduced mantle will outgas more H_2 and CO and less H_2O and CO_2, while a higher mantle fugacity would lead to the opposite (Guimond et al. 2021). Additional tectonically-driven reduced gases may be produced by serpentinization at mid-ocean ridges (potentially a large source of H_2 and possibly CH_4, with H_2 dominating on modern Earth McCollom and Bach 2009).

The atmospheres of planets orbiting M-dwarfs receive a different stellar spectra compared to the Earth, which has an effect on climate (Shields et al. 2013; Eager-Nash et al. 2020), as well as the atmospheric composition (Harman et al. 2015; Schwieterman et al. 2019; Kozakis et al. 2022). M-dwarfs have a lower proportion of radiation in the ultraviolet range, particularly in the mid and near UV (200-400 nm) (Wunderlich et al. 2020), which is important for photochemistry (Harman et al. 2015). On M-dwarfs, this allows biosignature gases such as CH_4 to be able to be maintained at higher concentration for a given CH_4 outgassing flux due to a lack of OH from water vapour photolysis (Segura et al. 2005; Meadows et al. 2018; Schwieterman et al. 2019).

For lifeless planets, it has been found that O_2 may accumulate to significant levels in

the atmosphere via the photolysis of CO_2, with a slow recombination of oxygen and CO, which is caused by a higher ratio of Far UV (FUV, 110–200 nm) to mid and near UV (200–400 nm) compared to the Sun (Tian et al. 2014; Domagal-Goldman et al. 2014; Harman et al. 2015; Ranjan et al. 2023). This is caused by the lower H_2O photolysis as a result of significantly reduced NUV flux compared to the Sun, which is able to reach close to the surface to photolyse H_2O (Harman et al. 2015). The NUV cross sections for H_2O were found to have been underestimated however, with Ranjan et al. (2020) finding that these increased rates led to higher OH levels, which catalyse the recombination of CO and O to reform CO_2, and removes the possibility of O_2 false positives. NO can be feasibly produced by lightning in the atmosphere and could eradicate the O_2 false positive, by catalysing the recombination of CO and O (Harman et al. 2018). Hu et al. (2020) went on to show that the inclusion of NO_x reservoir species, HO_2NO_2 and N_2O_5, could lead to large abiotic sources of atmospheric O_2. HO_2NO_2 and N_2O_5 act as reservoirs as they are relatively stable and store NO in a form that cannot catalyse CO_2 formation, and would rainout into the oceans. However, it was recently found that this result was due to the model top height being too low (54 km), which leads to erroneously high levels of O production at the model top (Ranjan et al. 2023). Thus, it is now thought that abiotic O_2 production from CO_2 containing atmospheres is unlikely to be a potential false positive.

Although M-dwarfs emit significantly less UV radiation than G-dwarfs, some of these stars can flare regularly (Hawley et al. 2014), which increases UV radiation incident on the planet and significantly impacts atmospheric composition (Chen et al. 2020; Ridgway et al. 2022). For a modern Earth-like atmospheric composition, flaring increases the formation of ozone in the upper atmosphere, which provides additional protection to the planet's surface from the UV radiation from subsequent flares (Ridgway et al. 2022). Taking a temporal average of spectrum of a flaring M-dwarf is found to be a reasonable approximation of the mean chemical composition (Ridgway et al. 2022).

6.3 Ecosystem processes

Methanogens are thought to be one of the first organisms to have been present on Earth (Battistuzzi et al. 2004). Methanogens are methane producing microscopic organisms and

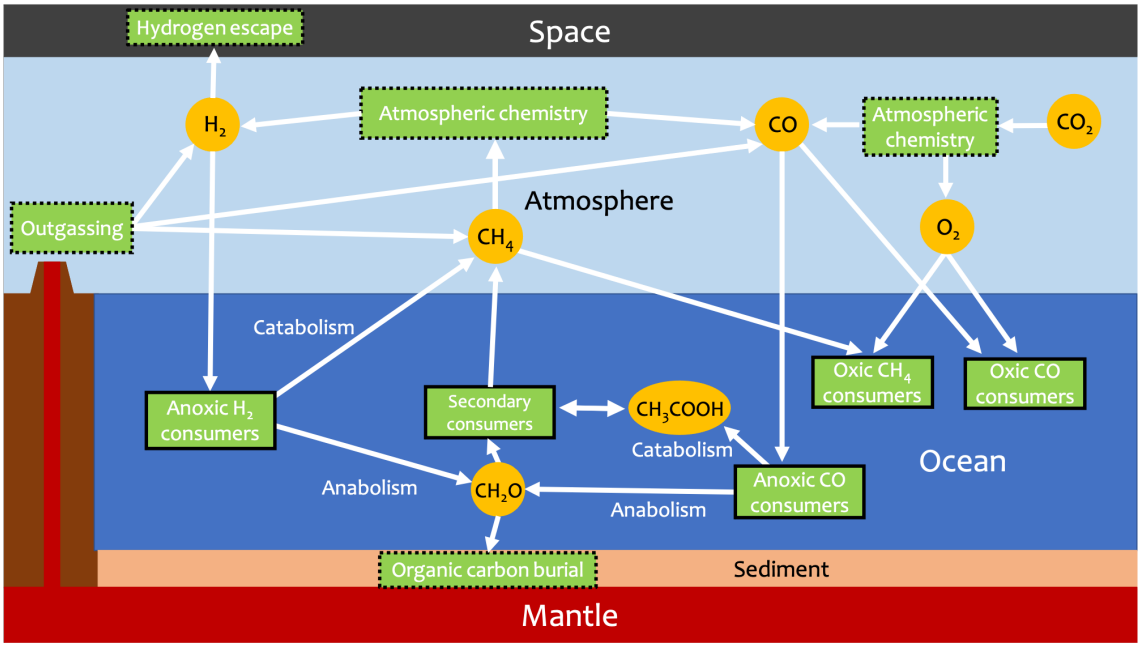

Figure 6.1: Schematic showing the biosphere reaction pathways and an overview of the interaction with the atmosphere captured in our modelling framework. Green boxes show processes, both biotic (dashed outline) and abiotic (solid outline), circles show reservoirs of species and arrows show fluxes between reservoirs via the different processes. Volcanic outgassing drives biospheric productivity by providing electron donors for primary producers. These are used for either catabolism to produce energy and CH_4 as a waste product, with this energy used for biomass production, which is then either recycled by secondary consumers and eventually converted to CH_4 again or the biomass is buried in the sediments.

could have metabolised H_2 from volcanic outgassing. CO–consuming organisms are also thought to have evolved early in Earth's history (Ferry 2006; Lessner et al. 2006; Weiss et al. 2016). These organisms had the potential to impact the composition of the atmosphere by providing a major source of methane (Kharecha et al. 2005), which impacts the climate (Eager-Nash et al. 2023). Models of plausible biospheres on the early Earth, which include methanogens, have been used to investigate possible biological productivity and subsequent atmospheric conditions (Kharecha et al. 2005; Ozaki et al. 2018; Sauterey et al. 2020). Kharecha et al. (2005) found that early methanogenic biospheres could have converted the majority of lower atmospheric hydrogen to methane, producing atmospheres with methane concentrations from 10 to 3,500 ppm, controlled by redox balance between reductant input and hydrogen escape, and with cycling of hydrogen through atmospheric methane photolysis and biosphere methane production. I assume that life on other planets may also utilise available H_2 and CO for metabolism, to understand the effect that these biospheres could have on planets that orbit M-dwarfs.

Conceptually, a biosphere could function as summarised schematically in Figure 6.1, which is the configuration considered in this model. I now describe a modelling framework that follows similar logic to Kharecha et al. (2005), Ozaki et al. (2018), and Sauterey et al. (2020), but is considered in more general terms to apply in an astrobiological context for pre-photosynthetic biospheres exploiting free-energy gradients from available substrates (Nicholson et al. 2022). Organisms use the available H_2 and CO to produce energy (catabolism) via pathways such as:

$$4\,H_2 + CO_2 \longrightarrow 2\,H_2O + CH_4\ (+\ \text{energy}), \tag{6.1}$$

$$4\,CO + 2\,H_2O \longrightarrow 2\,CO_2 + CH_3COOH\ (+\ \text{energy}), \tag{6.2}$$

where this energy can be used for other metabolic processes such as building biomass (anabolism), represented here as CH_2O:

$$2\,H_2 + CO_2\ (+\ \text{energy}) \longrightarrow CH_2O + H_2O, \tag{6.3}$$

$$2\,CO + H_2O\ (+\ \text{energy}) \longrightarrow CH_2O + CO_2. \tag{6.4}$$

The biomass will either descend to the ocean floor once the organism has died and is buried, which contributes a burial of reducing matter and oxidises the Atmosphere-Ocean system. Alternatively, secondary consumers would evolve that consume and recycle this biomass (Kharecha et al. 2005):

$$2\,CH_2O \longrightarrow CH_3COOH \longrightarrow CH_4 + CO_2. \tag{6.5}$$

Some fraction of biomass however is inevitably buried, although this percentage is low on the Earth with estimates of 0.2% in modern oceans (Berner 1982) and could have been 2%

during the past based on studies on anoxic waters (Arthur et al. 1994). The growth rate (relative rate at which Equation 6.1/6.2 occurs compared to Equation 6.3/6.4) is relatively low for this pathway and thus, the biosphere would grow relatively slowly.

On Earth, anoxygenic photosynthesis evolved, which provided energy directly to create biomass rather than from catabolism reactions. I assume that this takes the form of H_2 and CO consuming organisms, which is modelled in the simplified form of

$$2\,H_2 + CO_2 + h\nu \longrightarrow CH_2O + H_2O, \tag{6.6}$$

$$2\,CO + H_2O + h\nu \longrightarrow CH_2O + CO_2. \tag{6.7}$$

As abiotic sources of oxygen have been predicted from CO_2 photolysis, a build up of this would also provide an energy source for catabolism, for example by reaction with CH_4 (known on Earth as methanotrophy Kasting et al. 2001):

$$2\,O_2 + CH_4 \longrightarrow 2\,H_2O + CO_2\ (+\ \text{energy}). \tag{6.8}$$

Other pathways would be possible depending on what reducing species are most readily available, such as CO:

$$O_2 + 2\,CO \longrightarrow 2\,CO_2\ (+\ \text{energy}). \tag{6.9}$$

6.4 Methods

In this chapter, I use the Platform for Atmosphere, Land, Earth and Ocean (PALEO) modelling framework (Daines and Lenton 2016), which is described in more detail in Chapter 3. I use this to study potential abiotic conditions on planets as well biotic conditions with life resembling that on Earth prior to the evolution of oxygenic photosynthesis. I do

Table 6.1: Displays the values used for gravitational field strength at the surface, g and the top of atmosphere Solar constant, S, used in this Chapter for TRAPPIST-1e and the 3.8 Ga Earth. Values are consistent with Fauchez et al. (2020) for TRAPPIST-1e. The Earth solar constant is taken at 3.8 Ga using the formulation in Gough (1981).

Planet	g (m/s^2)	S (W/m^2)
TRAPPIST-1e	9.12	900
3.8 Ga Earth	9.81	1036

this by using a 1D photochemical atmosphere model coupled to a single box ocean that hosts a biosphere. The model conserves redox balance across the atmosphere ocean system. I do these experiments for Earth around 3.8 Ga, when these ecosystems were thought to be present, and TRAPPIST-1e. TRAPPIST-1e is one of several planets in orbit around TRAPPIST-1 (Gillon et al. 2017), which is an ultra cool M-dwarf and the planets in this system are prime targets for atmospheric characterisation. The atmospheric composition and climate solutions for the TRAPPIST-1e simulations are then used to generate synthetic spectra using the Planetary Spectrum Generator (PSG) (Villanueva et al. 2018) to predict the potential detectability of preoxygenic photosyntheic biospheres on TRAPPIST-1e. The components of this model are now described in more detail.

6.4.1 Climate solution

The 1D atmosphere includes a radiative convective model to calculate the climate solution that provides a vertical temperature and humidity profile. This climate state is then used by the photochemical model to calculate chemical rates. For the purpose of this work, these components are not coupled and a typical atmospheric composition is used for each planetary configuration.

Radiative transfer is calculated using the Suite Of Community RAdiative Transfer codes based on Edwards and Slingo (1996) (SOCRATES) (Manners et al. 2022), with a convective adjustment based on Manabe and Strickler (1964), with a pseudo adiabatic lapse rate. Tropospheric water vapour decreases with pressure (Manabe and Wetherald 1967) with a prescribed surface relative humidity of 0.7. Above the tropopause, the water vapour mixing ratio is fixed at the tropopause value. A Solar constant of 75% of the modern value (1036 W/m^2) is used for the 3.8 Ga Earth, based on Gough (1981), while a solar constant of 900 W/m^2 is used for TRAPPIST-1e (Fauchez et al. 2020) (shown in Table 6.1).

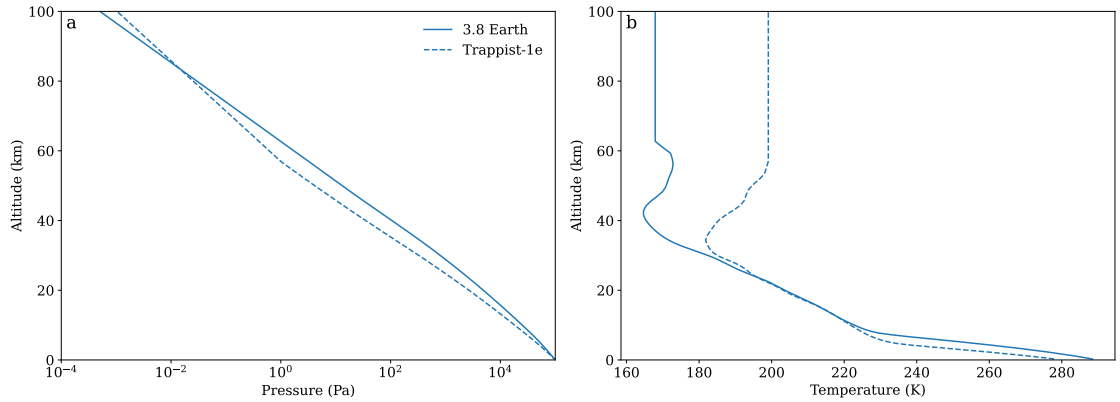

Figure 6.2: Pressure (a) and Temperature (b) profiles used that were generated for TRAPPIST-1e and the 3.8 Ga Earth.

SOCRATES employs the correlated-k method for radiative transfer. Thermal radiation is treated via 17 bands (between 3.3 μm-10 mm), while stellar radiation is treated by 43 bands (0.20-20 μm). These are suitable for atmospheres dominated by a mixture of N_2 and CO_2 (from 1% to 20%), with up to 3.5% CH_4 (see tests in Eager-Nash et al. 2023), supporting surface pressures up to 10^6 Pa. These include CO_2 sub-Lorentzian line wings and CO_2 self-broadening. Collision induced absorption is included for: N_2–CH_4, N_2–N_2 and CO_2–CO_2 from HITRAN (Karman et al. 2019), and CH_4–CO_2 from Turbet et al. (2020). Line data are from HITRAN 2012 (Rothman et al. 2013). The solar spectrum is taken for a 2.9 Ga Sun spectrum from Claire et al. (2012), which has little difference in climate compared to a 3.8 Ga given the same solar constant is used.

The climate for these simulations uses a mean climate state and is used for all simulations for a given planetary configuration of either TRAPPIST-1e or a 3.8 Ga Earth. An atmosphere is imposed with a composition of N_2, CO_2 and CH_4 for a 1 bar atmosphere. CO_2 is fixed at 10% for the Earth case and 20% for TRAPPIST-1e to provide similar surface temperatures (Figure 6.2). Methane is fixed at 0.18%, while N_2 makes up the remaining atmosphere in each case. This is justifiable as long-term modelling including a carbon cycle finds temperatures return to the abiotic steady state (e.g. Sauterey et al. 2020).

6.4.2 Atmosphere-Ocean

The coupled atmosphere-ocean model with a given climate solution solves the continuity equation:

$$\frac{\partial n_i}{\partial t} = P_i - n_i L_i - \frac{\partial \Phi_i}{\partial z}, \tag{6.10}$$

where n_i is the number density of species i, P_i is the production rate of the species and L_i is the loss rate. Φ_i is flux of species i from vertical transport. This is solved for the atmosphere-ocean as a whole with flux across the atmosphere–ocean boundary calculated using a stagnant boundary layer model (Liss and Slater 1974). Simulations were run for 3 to 100 million Earth years to allow the system to reach an equilibrium, which is considered as when the reductant input is equal to reductant output through either hydrogen escape or organic carbon burial. I now describe components of this model in more detail.

6.4.2.1 Photochemistry

Two reaction networks are used, the full network containing reactions with carbon, hydrogen, oxygen, nitrogen and sulphur species and a reduced network containing just carbon, hydrogen and oxygen species. The species in each network are shown in Table 6.2, with the left side of the table showing the species in the reduced network only. The reduced network is used as it converges more readily, while the larger network is used to validate the results of the reduced network. Some species are assumed to be short lived (indicated in Table 6.2), meaning that their chemical lifetime is short enough to assume that the number density can be determined directly from the chemical production and loss rates only. The full network is composed of 399 reactions, compared to 207 in the reduced network, with the network derived from Gregory et al. (2021) and is shown in Appendix B. Reaction rates are calculated as described in Section 3.3.2.3. Solar flux is split into 750 bins from 117.65 to 1000 nm, similar to the ATMOS model (Lincowski et al. 2018; Teal et al. 2022). This included the adoption of a two stream approach to track stellar radiation for photolysis (Teal et al. 2022). Cross sections and quantum yields come from the ATMOS open access repository[1] (Lincowski et al. 2018; Teal et al. 2022) and include the updated cross sections for H_2O (Ranjan et al. 2020). The atmosphere extends to 100km with 200 equally spaced levels. The surface boundary conditions are shown in Table 6.2. As a result of uncertainties in the reductant input, a range of potential values of H_2 volcanic outgassing

1. https://github.com/VirtualPlanetaryLaboratory/atmos

are investigated, $\Phi_{volc}(H_2)$, from 0.1 to 100 Tmol/yr. Fluxes are given in units of Tmol/yr, which are global fluxes equivalent to an Earth sized planet. For the full network, a surface boundary flux of NO and CO is included, which represents the role of lightning (Harman et al. 2018). In the reduced network, both lightning fluxes are excluded as nitrogen chemistry is not included in this network and the CO flux would introduce an additional reductant input, discussed further in Section 6.4.2.4.

Table 6.2: Species list and abiotic surface boundary conditions used in the model, which are either flux based or use a fixed mixing ratio. Species that are short lived are indicated. Dry deposition velocities values are also stated. The CHO network includes species up to the horizontal line in the table.
†CO flux of this value is used for the full network only as part of lightning flux (equal to NO flux). For a sensitivity study in Section 6.5.3.5 a range of abiotic CO fluxes were used from 0.1 to 100 Tmol/yr.

Species	**Short lived**	**Flux (Tmol/yr)**	**Mixing ratio (mol/mol)**	**Dry deposition velocity (cm/s)**
CO_2			0.1	
N_2			0.88	
H_2O				-
CH_4		0.0802		
H_2		0.1–100		
CO		0.16†		
O_3				0.4
O_2				
HO_2				1.0
H_2O_2				0.5
$O(^3P)$				1.0
$O(^1D)$	y			
OH				1.0
HCO				0.1
H_2CO				0.1
H				1.0
CH_3				
$^1CH_2$	y			
$^3CH_2$				

Continued on next page

Table 6.2 – continued from previous page

Species	Short lived	Flux (Tmol/yr)	Mixing ratio (mol/mol)	Dry deposition velocity (cm/s)
CH_3O				0.1
C_2H_6				1×10^{-5}
C_2H_5				
C_2H_4				
CH_3O_2				
C_2H_2				
CH_3CHO				0.1
C				
CH				
CH_2CO				0.1
CH_3CO				0.1
C_2H				
C_2				
C_2H_3				
C_2H_2OH				
C_2H_4OH				
SO_2		0.802		1.0
H_2S		0.0802		
NO		0.16		
CS_2				
CS_2^*	y			
HS				
CS				0.01
HNO_2	y			
HNO_3				0.2
NO_2				3×10^{-3}
N				

Continued on next page

Table 6.2 – continued from previous page

Species	Short lived	Flux (Tmol/yr)	Mixing ratio (mol/mol)	Dry deposition velocity (cm/s)
HNO				1.0
NO_3				
SO				
S				
$^1SO_2$	y			
$^3SO_2$	y			
HSO_3	y			
SO_3				
H_2SO_4				
HSO				1.0
S_2				
OCS				0.01
S_3				
S_4				
S_8				
OCS_2	y			
N_2O_5				
HO_2NO_2				0.2
N_2O				
HCS				

Tropospheric water vapour is fixed and decreases with pressure (Manabe and Wetherald 1967) with a prescribed surface relative humidity of 70 %. Above the tropopause water vapour may evolve from chemical sources and sinks, but when water vapour exceeds a critical relative humidity (10 %), it will condense and rainout.

The species can be deposited at the surface of the atmosphere as a result of either species dissolving into water droplets and subsequently raining out of the atmosphere, or through the particles directly settling from the atmosphere to the surface due to gravity or turbulence, which is known as dry deposition. Rainout follows the prescription described in (Giorgi and Chameides 1985), while dry deposition is modelled at the lowest atmosphere level, with deposition flux, Φ_i^{dep} (molecules/cm^2/s) for species i is calculated as

$$\Phi_i^{\text{dep}} = n_i v_i^{\text{dep}}, \tag{6.11}$$

where v^{dep} is the deposition velocity. This represents the free fall of species out of the atmosphere. Eddy diffusivity models the upward vertical mixing of the atmosphere and is calculated for species i as:

$$\Phi_i^{\text{eddy}} = -KN\frac{\partial}{\partial z}\frac{n_i}{N}, \tag{6.12}$$

where K is the eddy diffusion coefficient plotted in Figure 3.3, N is the total number density of the atmosphere at height z.

Escape and molecular diffusion of molecular and atomic hydrogen follow the procedure outlined in Hu et al. (2012) and Ranjan et al. (2020). I follow the implementation used in Hu et al. (2012), which combines diffusion and escape as linked processes. The escape of atomic and molecular hydrogen is included for an N_2 dominated atmosphere.

The top-of-atmosphere spectra received by the planet used in this work are shown in Figure 6.3. The solar spectrum for 3.8 Ga is generated from Claire et al. (2012), while the quiescent spectrum for TRAPPIST-1 uses the spectrum from Peacock et al. (2019). The mean flaring spectrum is generated using the same approach described in Ridgway et al. (2022) using the TRAPPIST-1 spectrum from the Mega–MUSCLES survey (Wilson et al. 2021).

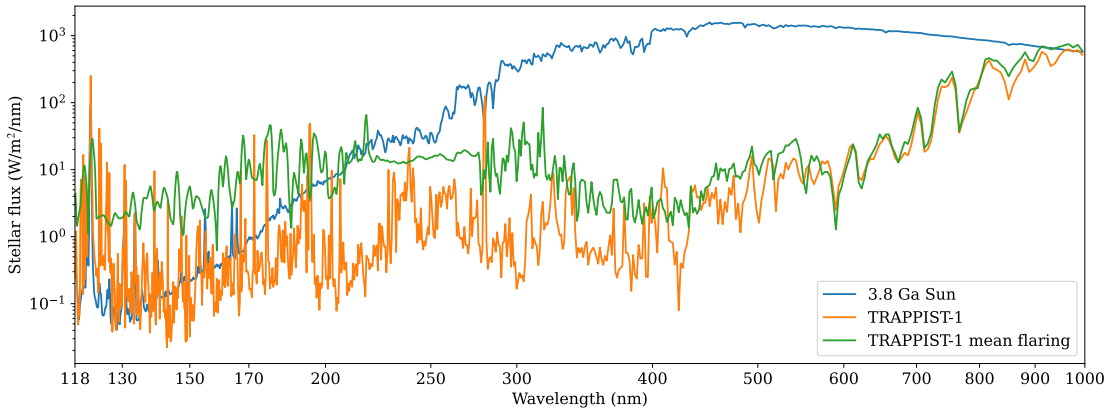

Figure 6.3: Top-of-atmosphere spectra used for Archean Earth at 3.8 Ga and TRAPPIST-1e and a mean flaring TRAPPIST-1 spectrum. The spectra from 3.8 Ga Sun comes from Claire et al. (2012), while the TRAPPIST-1 spectra is from (Peacock et al. 2019). The flaring spectra uses the the spectrum from Wilson et al. (2021) and includes a temporally averaged spectrum which describes a regularly flaring star based on Ridgway et al. (2022).

Table 6.3: Solubility and piston velocity values used within the model.

Species	Solubility (mol/m^3/Pa)	Piston velocity (m/day)
CO_2	1.0×10^{-2}	4.8×10^{-2}
CH_4	1.4378×10^{-5}	4.8
H_2	8.0106×10^{-6}	11.23
CO	1.027×10^{-5}	4.147
O_2	1.2×10^{-5}	4.8

6.4.2.2 Ocean

A single box ocean is connected to the atmosphere, with reservoirs of species connected between the atmosphere and ocean via diffusion. Using a similar procedure to Kharecha et al. (2005) the diffusion is determined by a piston velocity and solubility coefficient, with values given in Table 6.3. The flux across the ocean-atmosphere boundary for species X, $\Phi(X)$ is then:

$$\Phi(X) = v_p(X) \times (\alpha(X) \times pX - [X]_{aq}) \times C, \tag{6.13}$$

where $v_p(X)$ is the piston velocity, $\alpha(X)$ is the Henry's solubility coefficient, pX is the surface partial pressure of X and $[X]_{aq}$ is the ocean concentration of X. C is a constant for unit conversion to obtain a flux in mol/yr.

In the abiotic simulations, the ocean includes a CO sink, following the reaction described in (Harman et al. 2015), taking the form:

$$CO + H_2O \longrightarrow H_2 + CO_2, \tag{6.14}$$

with the rate of removal of CO calculated as τ[CO], where τ is a timescale of removal, with a value of 10^{-4} used here, and [CO] is the concentration of CO.

6.4.2.3 Biosphere

I coupled a simple ocean with a biosphere component to the 1D atmosphere model, which is shown schematically in Figure 6.1. The primary production from this biosphere comes from the consumption of H_2 and CO, which reach the ocean through the diffusion of these species from the atmosphere.

The number of mols of H_2/CO required to produce energy for the biomass pathway can be measured experimentally. For methanogens, it has been measured that 10 mols of CO_2 that are metabolised, 1 mol of CO_2 is coverted to biomass through anabolism (Schonheit et al. 1980; Fardeau and Belaich 1986; Morii et al. 1987). The proportion of the total metabolism by a species in the form of anabolism is termed the growth rate, μ. For the purposes of this work, it is assumed that anoxic H_2 and CO consuming metabolisms have a growth rate of 0.1, while for anoxic photosynthesisers, a growth rate of 1.0 is used as they extract energy directly from the host star to fix carbon. The growth rate has only a minor role in the evolution of the atmosphere, provided the burial fraction is low (Section 6.5.3.3).

Secondary consumers recycle organic carbon back to CH_4. However, this process is not 100% efficient and some fraction of the biomass is buried, which may limit the production of CH_4. The rate of organic carbon burial, x is an unknown parameter, that has thought to have decreased on Earth over its history, with a modern value of 0.2% (Berner 1982). A value of 1% is used in these simulations unless otherwise stated. This value may have been similar to the Archean based on measurements of carbon burial in anoxic waters (Arthur et al. 1994). The sensitivity to various recycling rates is analysed in Section 6.5.3.3, ranging from no recycling to 100% efficient recycling. The growth rate and organic carbon burial rate are not considered for the oxic metabolisms. However, a sensitivity study of the burial rate and growth rate for the other parameters shows that

these only have a minor effect when the burial rate is above 10%, see Section 6.5.3.3.

Following similar treatment in Kharecha et al. (2005) and Ozaki et al. (2018), it is assumed that either H_2 or CO are the limiting factors in primary productivity for anoxic metabolisms. While oxic metabolisms are limited by the availability of O_2 and either CO or CH_4 depending on the metabolism. The primary productivity, in terms of moles of CH_4 equivalent of H_2 or CO consumed by anoxic metabolisms is:

$$\Phi_{\text{bio}} = \frac{1}{4}\tau_{\text{bio}}([X]_{aq} - [X]_{aq}^{lim}), \tag{6.15}$$

where the factor of a quarter comes from the ratio of CH_4 production relative to the consumption of species X (H_2 or CO) and $[X]_{aq}^{lim}$ is the limiting concentration of species X, which the biosphere is unable to draw concentrations below (set here as 4.6×10^{-7} mol/m^3). τ is the timescale for the biological reaction, which is assumed to be 10^4 yr^{-1}. Provide this timescale high enough to reduce ocean concentrations to $[X]_{aq}^{lim}$, which is expected for a global biosphere, this parameter has no effect on the atmospheric configuration. The burial rate is then defined as

$$\Phi_{\text{OCB}} = (1 - x \cdot \mu)\Phi_{\text{bio}}, \tag{6.16}$$

which is dependent on both the growth rater and the burial rate. The CH_4 flux from these metabolisms is then the difference between these two fluxes.

In this work, two ecosystems are predominantly used:

1. Ecosystem 1: preoxygenic anoxic metabolisms only, including anoxic H_2 and CO consumers (Equations 6.1–6.4) and secondary consumers (Equation 6.5)

2. Ecosystem 2: ecosystem 1 plus oxic metabolisms that metabolise O_2 with CH_4 or CO (Equations 6.8+6.9)

6.4.2.4 Global redox balance

In order to conserve redox balance at the surface, the deposition of species at the surface via rain out and dry deposition is balanced by a restoring flux of H_2 in the case a net reducing deposition and O_2 in the case of a net oxidant deposition, following the procedure described in Harman et al. (2015). This excludes species that are coupled to the ocean, such as H_2, CH_4, CO and O_2, which as discussed above, have ocean reservoirs that can undergo biologically or abiotically driven ocean chemistry. In order to maintain consistency in the reductant input for the full network and the reduced network, surface boundary flux of H_2S is included in the surface redox balance discussed above. This ensures that the net reductant input is determined by the H_2 and CH_4 abiotic fluxes only. SO_2 is considered a redox neutral species, so does not affect the redox balance, while the combined lightning fluxes of CO and NO have an equal and opposite redox state, so also do not contribute to the redox balance.

6.4.3 Synthetic spectra

Synthetic spectra were generated using the Planetary Spectrum Generator (PSG) (Villanueva et al. 2018), adopting the parameters of TRAPPIST-1e (Agol et al. 2021). The following species were included to generate the spectrum: O_2, CH_4, N_2, C_2H_6, O_3, CO_2, CO, H, H_2, O, C_2H_2, C_2H_4. From this the differences in transmission spectrum can be investigated between biotic and abiotic configurations to assess the detectability of a potential biosphere of the form modelled here.

6.5 Results

I now present results of abiotic simulations of TRAPPIST-1e, comparing these to similations of the 3.8 Ga Earth, showing the importance of reductant input in abiotic O_2 levels. Following this, I present results from the biotic configurations for TRAPPIST-1e, initially benchmarking the coupled atmosphere ecosystem model against Kharecha et al. (2005) on Earth, and subsequently compare the differences between early Earth biospheres on Earth and on a hypothetical TRAPPIST-1e. Finally, I show transmission spectra for TRAPPIST-1e for a range of both biotic and abiotic configurations.

6.5.1 Abiotic oxygen production

Figure 6.4 shows a comparison of an abiotic configuration of the 3.8 Ga Earth and TRAPPIST-1e, with near surface mixing ratios of key gases as a function of H_2 input. This is shown for the full and reduced network. H_2 is the major hydrogen bearing species and thus its concentration increases with input, balanced by escape and shows a similar trend for both Earth and TRAPPIST-1e. CO is higher in the TRAPPIST-1e case because of CO_2 photolysis and a lack of tropospheric OH from H_2O photolysis to catalyse the recombination of the CO_2 photolysis products (Harman et al. 2015). Near surface O_2 is shown in Figure 6.4b. Reductant input plays an important role in determining abiotic oxygen mixing ratios. At low reductant input, $\Phi_{volc}(H_2) < 10\,\mathrm{Tmol/yr}$, O_2 becomes significantly higher for the TRAPPIST-1e case compared to the Earth analogue. This is because reductant input is lower than O_2 formation from CO_2 photolysis. When reductant input is higher than oxygen production, O_2 returns to levels comparable to the Earth case.

The reduced and full chemical network show similar trends in atmospheric mixing ratio. H_2 and CH_4 remain nearly identical between the two simulations. CO is higher for both TRAPPIST-1e (when $\Phi_{volc}(H_2) > 3.16\,\mathrm{Tmol/yr}$) and the Earth. This is due to the CO flux from lightning in the full network, which is not included in the reduced network. This is not observed at $\Phi_{volc}(H_2) \leq 3.16\,\mathrm{Tmol/yr}$ for TRAPPIST-1e as the CO source from CO_2 photolysis is much larger. O_2 shows very similar trends between the full and reduced network. For TRAPPIST-1e, the O_2 predictions at $\Phi_{volc}(H_2) > 3.16\,\mathrm{Tmol/yr}$ are consistent between both networks. For Earth, abiotic O_2 is higher when the full network is used, which produces values closer to those found in Kasting (1990). The lower values in the reduced network are similar to those quoted in Ranjan et al. (2023). As these O_2 values are very low, differences are likely to be caused by the numerics of the solver.

6.5.2 Benchmarking of atmosphere ecosystem model

I now consider the effects of a biosphere composed of anoxic metabolisms of H_2 and CO. I first compare our model simulations to Kharecha et al. 2005, who implemented a similar ecosystem model. Figure 6.5 shows a comparison to their results for a H_2 and CO consuming biosphere with a 2% organic carbon burial rate. For a hydrogen volcanic flux of

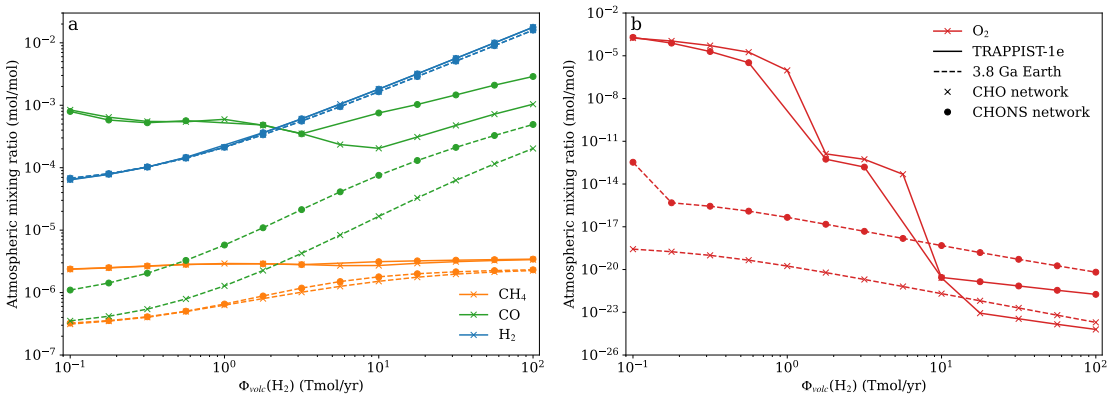

Figure 6.4: Surface mixing ratios for abiotic configurations of TRAPPIST-1e (solid) and the Earth irradiated by a 3.8 Ga Sun (dashed) as a function of H_2 input. The full grid of simulations is shown for the reduced network (crosses), while a subset of the network is plotted as circles.

6.02 Tmol/yr (see Figure 6.5a), the atmospheric profiles of CH_4 are similar up to 70 km, above which our model predicts much lower CH_4 mixing ratios, potentially due to the difference in solar spectrum. The H_2 mixing ratio profile is similar for both cases, while CO is drawn down to lower values near the surface in our model, but reaches higher abundances at the top-of-atmosphere. Top-of-atmosphere differences could be attributed to differences in solar spectrum, with the same plot repeated with the modern Earth spectrum shown as the dotted line in Figure 6.5a. For a larger range flux values, Figure 6.5b shows the surface mixing ratios of H_2 and CH_4, with the latter showing strong agreement with Kharecha et al. (2005). The difference between the full and reduced reaction network are minimal here, with the only difference at low reductant input, where CH_4 concentrations are marginally higher in the full network.

6.5.3 Pre-photosynthetic biospheres on TRAPPIST-1e

I now show the effect of a hypothetical H_2 and CO consuming biosphere on the atmosphere for a planet orbiting TRAPPIST-1, compared to the young Sun. I show results from ecosystem 1 (anoxic H_2 and CO consumers) and subsequently ecosystem 2 (anoxic H_2 and CO consumers and oxic CH_4 and CO consumers) for simulations with high O_2 mixing ratios.

6.5.3.1 Ecosystem 1

Figure 6.6 shows the surface mixing ratios for the biotic configuration with ecosystem 1 (anoxic H_2 and CO consumers only). The TRAPPIST-1e case has CH_4 at higher concen-

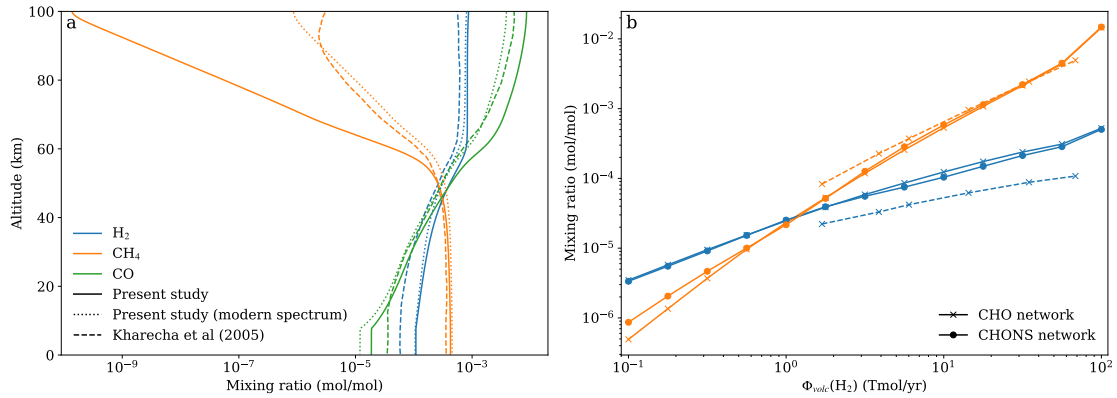

Figure 6.5: Comparison to Kharecha et al. (2005). Data reproduced from Kharecha et al. (2005) (dashed lines), (a) shows a mixing ratio vs altitude for case 2 biosphere in Kharecha et al. (2005), equivalent to their Fig. 7B. This is shown for the 3.8 Ga Solar spectrum (Claire et al. 2012) (solid line) and the modern Solar spectrum (dotted lines) from ATMOS (Teal et al. 2022). (b) shows the near surface mixing ratios of CH_4 and H_2 and Table 2 for their case 3 biosphere. The case 2 and 3 biosphere has a growth rate of 0.1 and 1.0 for H_2 consumers respectively, while the CO consumer growth rate is 0 for both cases. The organic carbon burial rate is 2 %. The CO_2 surface mixing ratio is 2.5 %. Our simulations are shown for the reduced network in (a), while (b) shows the full network (circles) and reduced network (crosses).

trations near the surface compared to the Earth, which is related to the lower OH concentration in the troposphere. The general behaviour of CH_4 is similar for both cases, with CH_4 now the dominant reductant species, and its concentration largely determined by the balance of reductant input with hydrogen escape. The most notable difference however is the relatively high surface oxygen (nearly 10%) at low $\Phi_{\mathrm{volc}}(H_2) < 3.16\,\mathrm{Tmol/yr}$.

The high oxygen state emerges because of a low reductant input compared to the O_2 production from CO_2 photolysis. Here, O_2 concentrations are higher than the reducing species, leading to a change of regime. Figure 6.8 compares the differences between this oxidised state at $\Phi_{\mathrm{volc}}(H_2) = 1.78\,\mathrm{Tmol/yr}$ and the more familiar low oxygen state at $\Phi_{\mathrm{volc}}(H_2) = 3.16\,\mathrm{Tmol/yr}$.

At $\Phi_{\mathrm{volc}}(H_2) \leq 1.78\,\mathrm{Tmol/yr}$, the high levels of O_2 is the product of CO_2 photolysis followed by the combination atomic oxygen:

$$CO_2 + h\nu \longrightarrow CO + O, \tag{6.17}$$

$$O + O + M \longrightarrow O_2 + M. \tag{6.18}$$

When the reductant input is low, the molecular oxygen accumulates faster than it can be

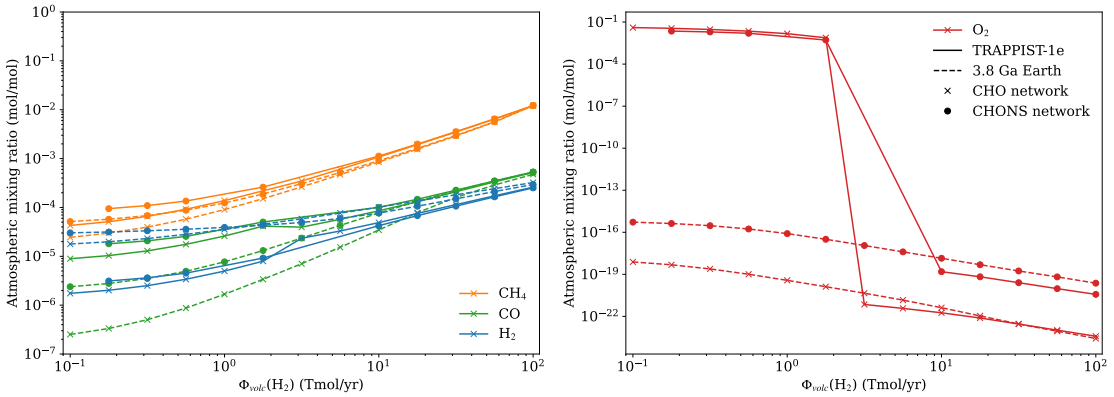

Figure 6.6: Comparison of a hypothetical H_2 and CO consuming ecosystem (ecosystem 1) on Earth (solid lines) compared to TRAPPIST-1e (dashed lines). (a) and (b) show near surface mixing ratios for key gases. The full grid of simulations is shown for the reduced network (crosses), while a subset of the network is plotted as circles.

reduced by the reductant input, leading to an accumulation of O_2 and O_3 (dotted lines in Figure 6.8b). This O_3 shields the tropospheric UV flux (at $\Phi_{\text{volc}}(H_2) = 1\,\text{Tmol/yr}$) and reduces the photolysis of H_2O via:

$$H_2O + h\nu \longrightarrow OH + H, \tag{6.19}$$

which further reduces the loss mechanisms for oxygen as well as CO and CH_4. The high levels of oxygen in the atmosphere lead to low levels of H_2, causing the low methanogen productivity at these fluxes with acetogens contributing the largest methane flux, shown in Figure 6.7. The biologically driven production of CH_4, which makes this the major reducing hydrogen bearing species in the atmosphere rather than H_2 in the abiotic case also allows O_2 to rise to higher levels, with CH_4 oxidised by OH, which is less abundant in this regime, rather than by oxygen directly (Figure 6.8), allowing both species to remain at relatively high concentrations.

When $\Phi_{\text{volc}}(H_2) \geq 3.16\,\text{Tmol/yr}$, the reductant input is large enough to significantly reduce the O_2 concentration to levels seen in the Earth case. The subsequent lack of O_3 no longer shields the troposphere from UV radiation, increasing H_2O photolysis in this region. Increased OH leads to lower CO and CH_4 abundances. The reduction of oxygen down to levels that are comparable to the Earth case allows for a higher H_2 abundance, which consequently leads to an increase in H_2 consumption, which becomes the dominant

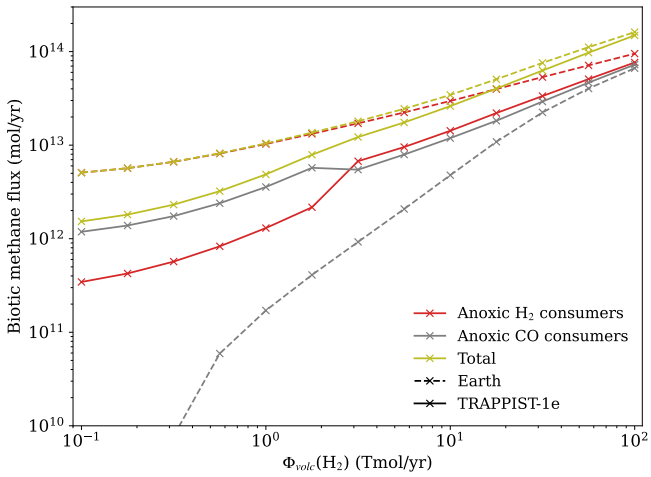

Figure 6.7: Shows the methane production rate from ecosystem 1 for the 3.8 Ga Earth (dashed) and TRAPPIST-1e (solid) case. The methane production rate is split between anoxic H_2 (red) and CO (grey) consumers. the total of these is also shown (green) This plot used simulations with the reduced network.

source of biological methane production over CO consumption (Figure 6.7).

The biotic production of CH_4 allows O_2 to accumulate to higher mixing ratios than the abiotic case. This is because the oxidation of CH_4 depends on the presence of OH from water photolysis, which is produced at a lower rate on planets orbiting M-dwarfs and the rate is reduced further when an ozone layer forms (Figure 6.8b-d). This allows O_2 and CH_4 to exist at higher concentrations simultaneously. This behaviour has similarly been found in modelling of the great oxidation event on Earth (Pavlov and Kasting 2002; Gregory et al. 2021), but for our TRAPPIST-1e configuration the abundance of O_2 and CH_4 are much closer, being only an order of magnitude different ($\approx 10^{-3}$ and $\approx 10^{-4}$ respectively).

At low hydrogen input, the CH_4 flux is a factor of two smaller on TRAPPIST-1e compared to the Earth, see Figure 6.7. This is partly due to the oxygenated nature of the atmosphere that is reducing the H_2 available for biotic consumption. When surface oxygen levels reduce at higher hydrogen inputs, the H_2 consumers overtake CO consumers in their productivity, and resembles the Earth case again. The productivity of CO consumers is consistently higher for the TRAPPIST-1e case compared to the Earth due to the higher CO abundance. The lower CH_4 flux is in contrast to the higher CH_4 abundance, but can be explained by the lower rate of CH_4 destruction in the troposphere due to the lower amount of OH from H_2O photolysis (Segura et al. 2005).

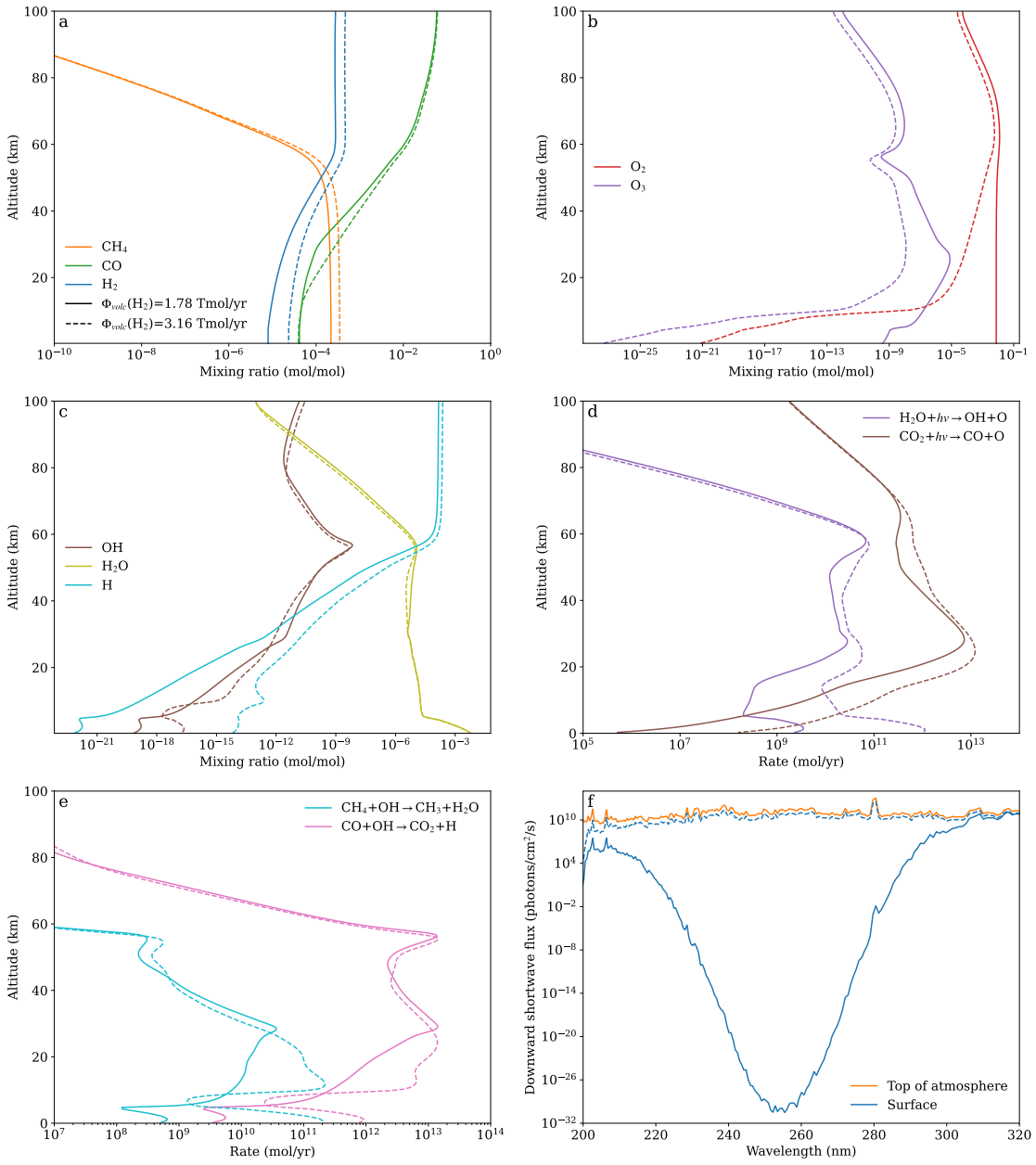

Figure 6.8: Showing the differences between the low oxygen state at$\Phi_{\text{volc}}(H_2)$ = 1.78 Tmol/yr (solid lines) and the high oxygen scenario at $\Phi_{\text{volc}}(H_2)$ = 3.16 Tmol/yr (dash-dotted lines). (a), (b) and (c) show gas mixing ratios, while (d) and (e) show reaction rates. (f) shows the downward shortwave flux at the top of atmosphere (TOA) and the surface.

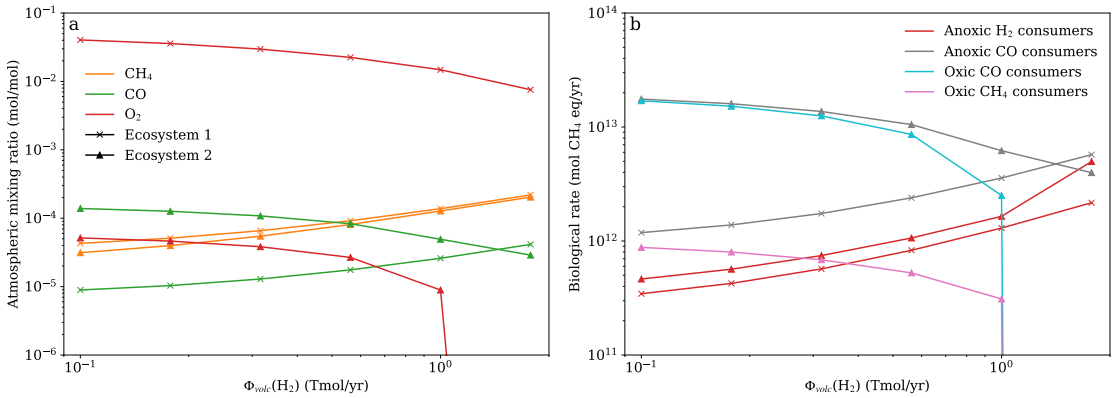

Figure 6.9: Comparison between ecosystem 1 and 2 at low reductant inputs, which produced high oxygen concentrations. (a) shows the near surface mixing ratios for key gases for ecosystem 1 (crosses) and ecosystem 2 (triangles). (b) shows the rate of biological reactions from ecosystem 2 in units of moles of CH_4 equivalent. Above $\Phi_{volc}(H_2)$= 1.78 Tmol/yr, the O_2 concentration drops and oxic metabolisms can no longer function, thus becomes identical to ecosystem 1 and is not shown.

The full and the reduced reaction network, both show very similar predictions for the atmospheric composition. This is shown in Figure 6.6. Most significantly, the high O_2 state is reproduced with both configurations. As I have now shown that the reduced and full network show very similar results for the abiotic configurations, the reproduction of Kharecha et al. (2005) and for ecosystem 1 for TRAPPIST-1e and the Earth. Moving forward, only the reduced network is used.

6.5.3.2 Ecosystem 2

The presence of high abundances of O_2 provides an energy source for potential ecosystems. The effect of including oxic CH_4 and CO consumers (Equations 6.8+6.9) alongside the metabolisms in Ecosystem 1 (Ecosystem 2) is shown in Figure 6.9 for $\Phi_{volc}(H_2) \leq$ 1.78 Tmol/yr. Figure 6.9a shows that O_2 concentrations could be drawn down to near surface mixing ratios of the order 10^{-5}, whilst also drawing down CH_4 concentrations slightly. However, CO is found to rise by up to an order of magnitude (Figure 6.9a and Figure 6.10a). In this ecosystem, the anoxic and oxic CO consumers dominate the biological productivity, as the oxic CH_4 and anoxic H_2 consumer productivity is low, shown in Figure 6.9b. The productivity of anoxic CO consumers is higher than in ecosystem 1 due to the increased atmospheric CO concentration (Figure 6.9a).

The rise of atmospheric CO is a result of an increase in the photolysis rate of CO_2,

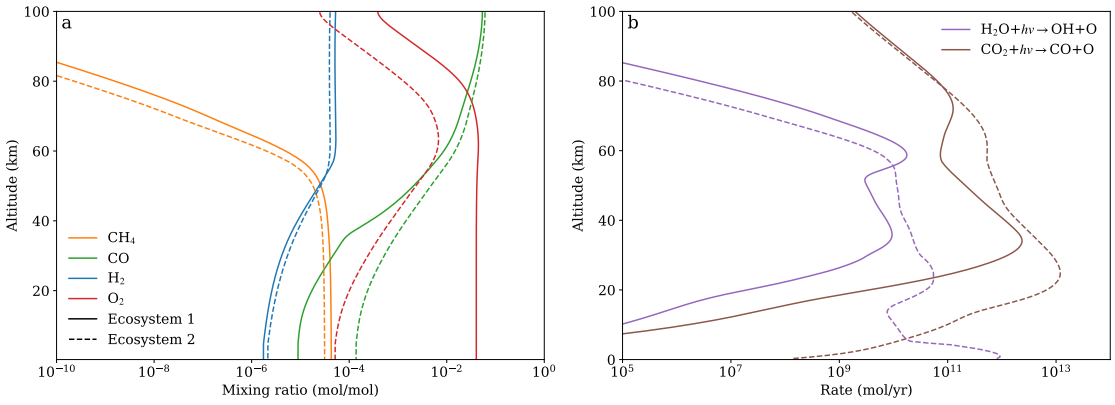

Figure 6.10: Shows a comparison between the atmospheric composition (a) and photolysis rates (b) produced by ecosystem 1 (solid) and ecosystem 2 (dashed) when hydrogen input is 0.1 Tmol/yr.

caused by the reduction in O_2 and thus O_3 abundance, shown in Figure 6.10b at $\Phi_{volc}(H_2) = 0.1$ Tmol/yr. The reduction in O_2 also leads to an increase in the production of tropospheric OH, which contributes to the lower CH_4 abundance in Ecosystem 2.

6.5.3.3 Anoxygenic photosynthesis and carbon burial

I now consider the potential impacts of anoxygenic photosynthesis compared to ecosystems that obtain energy through catabolism. That is to say that the growth rate becomes 100%, as opposed to the 10% that was assumed previously. To consider the effects of this, I investigate the change in growth rate alongside the sensitivity to the rate of organic carbon burial. I find that anoxygenic photosynthesis using H_2 and CO is unlikely to lead to significant changes in the atmospheric composition unless the organic carbon burial rate is low.

Ecosystems with low growth rates, such as prephotosynthetic biospheres are relatively unaffected by the fraction of biomass that is buried. For a growth rate, μ of 0.1, a change in CH_4 mixing ratio is observed from ≈0.001 for a low burial fraction down to ≈0.0004 when all organic carbon is buried (Figure 6.11a), with the CH_4 mixing ratio only dropping noticeably below 0.001 mol/mol when the burial fraction is greater than 0.1. This relatively small change is due to the fact that CH_4 is produced via catabolic reactions for 90% of the H_2 or CO that is consumed, while the burial fraction affects what happens to just the remaining 10%. Increasing the burial rate also has the effect of decreasing the biospheres productivity, shown in Figure 6.11b. This is because as the organic carbon burial

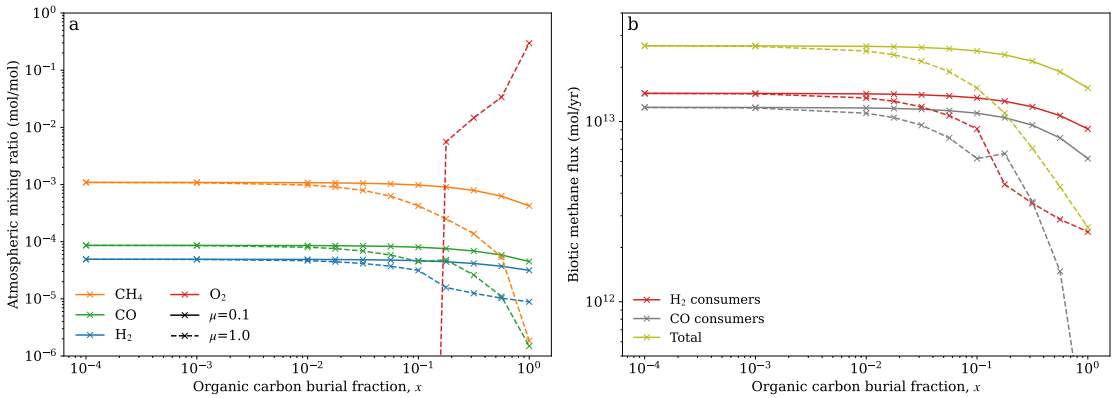

Figure 6.11: Comparing the effects of H_2 organic carbon burial rates and growth efficiencies for a H_2 and CO consuming biosphere. (a) shows the change in near-surface composition vs burial fraction for H_2, CH_4, CO and O_2, while (b) shows the change in biosphere productivity of H_2 and CO consuming organisms. $\mu = 1.0$ (solid lines) represent a growth rate equivalent to a phototrophic primary production, while the lower growth rate of $\mu = 0.1$ (dashed lines) represents a biosphere that produces energy from catabolic reactions instead of using light.

fraction increases, less CH_4 is returning to the atmosphere, and thus less CH_4 is recycled back to H_2 and CO, where it can be consumed by the biosphere again.

In contrast to this, ecosystems with high growth rates, such as via anoxygenic photosynthesis are more sensitive to the organic carbon burial fraction. At low organic carbon burial fractions ($\lessapprox 0.01$), the atmospheric composition is indistinguishable between low and high growth rates, which was also found in Earth like configurations (Kharecha et al. 2005). As organic carbon burial fraction continues to decrease beyond 0.01, atmospheric CH_4 drops faster in the low growth rate case. This is because when the growth rate is higher, CH_4 is produced entirely by secondary consumers, rather than through catabolism processes, and the burial rate effectively determines how efficient secondary consumers are at recycling biomass. Thus, efficient recycling of organic carbon by secondary organisms is required to produce CH_4 levels that are distinguishable from abiotic configurations (compare Figure 6.11a to Figure 6.4).

For photosynthetic anoxic biospheres, if the organic carbon burial fraction is high, high oxygen scenarios become more likely. For $\Phi_{volc}(H_2) = 10\,\text{Tmol/yr}$, a burial fraction of greater than 0.1, can lead to high oxygen states. This is because of the large burial of reductant material and the significantly lower reducing power of the atmosphere from the low CH_4 production, alongside a H_2 consumption from the biosphere.

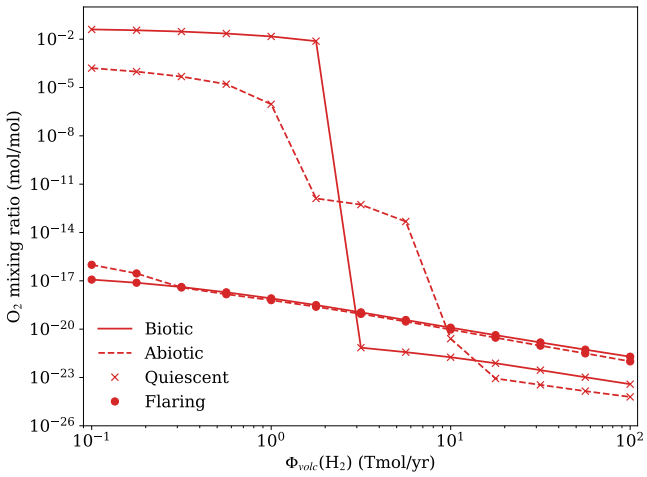

Figure 6.12: Shows the near surface O_2 mixing ratio, for biotic and abiotic configurations for a quiescent and mean flaring spectrum of TRAPPIST-1.

6.5.3.4 Flaring

Flaring has the potential to prevent the O_2 build up found at low $\Phi_{volc}(H_2)$ in the quiescent state. Using a mean flaring spectrum, shown in Figure 6.3, the surface mixing ratios for key gases are shown in Figure 6.12. The change in spectrum due to flaring could be sufficient to prevent O_2 accumulating to values of greater than 1%, seen in the quiescent state. The increased FUV flux due to flaring prevents O_2 and importantly O_3 accumulation, which maintains a weakly reducing atmosphere.

6.5.3.5 Carbon monoxide outgassing

As volcanic input can vary depending on the carbon-to-hydrogen ratio in the mantle, I test the sensitivity of the atmosphere to CO and H_2 outgassing. Instead of volcanic flux from H_2, this is replaced with an equivalent CO flux, which is found to have a minor effect on the atmospheric composition. Figure 6.13a shows the surface mixing ratios from the key components of the atmosphere. Generally the atmospheric composition is the same for a given CO or H_2 flux, particularly for CH_4, while H_2 and CO are similar, apart from at higher volcanic outgassing fluxes where small differences emerge. Figure 6.13b shows the biotic methane flux associated with these different outgassed gases, which generally show the same trend for both CO and H_2 consumers, with H_2 consumer productivity marginally higher when H_2 is outgassed compared to CO, and vice versa for CO consumer productivity.

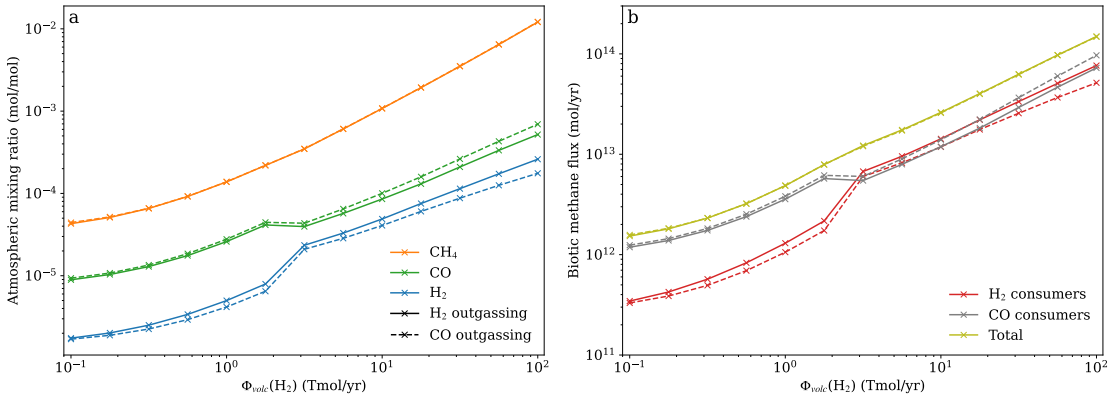

Figure 6.13: Comparing the effects of H_2 outgassing (solid lines) with an equivalent CO outgassing. (a) shows the change in near surface composition vs the hydrogen outgassing rate for H_2, CH_4 and CO, while (b) shows the productivity of H_2 and CO consuming organisms.

6.5.4 Detectability of pre-photosynthetic biospheres on TRAPPIST-1e

Finally, I consider the detectability of potential preoxygenic-photosynthesising biospheres for a planet like TRAPPIST-1e. Abiotic and biotic configurations are now presented from PSG.

Biologically produced CH_4 shows strong signatures at high reductant input, but at low reductant input both the CH_4 and O_2/O_3 signatures are weak. The transmission spectra for abiotic, and biotic ecosystem 1 and 2 configurations are shown in Figure 6.14 for a range of $\Phi_{volc}(H_2)$. Both CO and CO_2 show strong features across all transmission spectra, while CH_4 shows obvious signals only for the biotic configurations, which are most visible at $\Phi_{volc}(H_2)$ $\leq$=100 Tmol/yr. Thus planets may need to have high outgassing rates for these biospheres to be detectable. The strongest O_3 feature is masked by CO_2 at 9.4 microns, although is most visible for ecosystem 1 when the reductant input is lowest. The inclusion of oxygen photosynthesizers leads to this ozone feature being very difficult to distinguish from CO_2.

6.6 Discussion

In the simulations discussed in this chapter, biospheres that consume H_2 and CO producing CH_4 as a waste product have the potential to be observed. Signatures for CH_4 are present when the reductant input is greater than 10 Tmol/yr, which were absent in

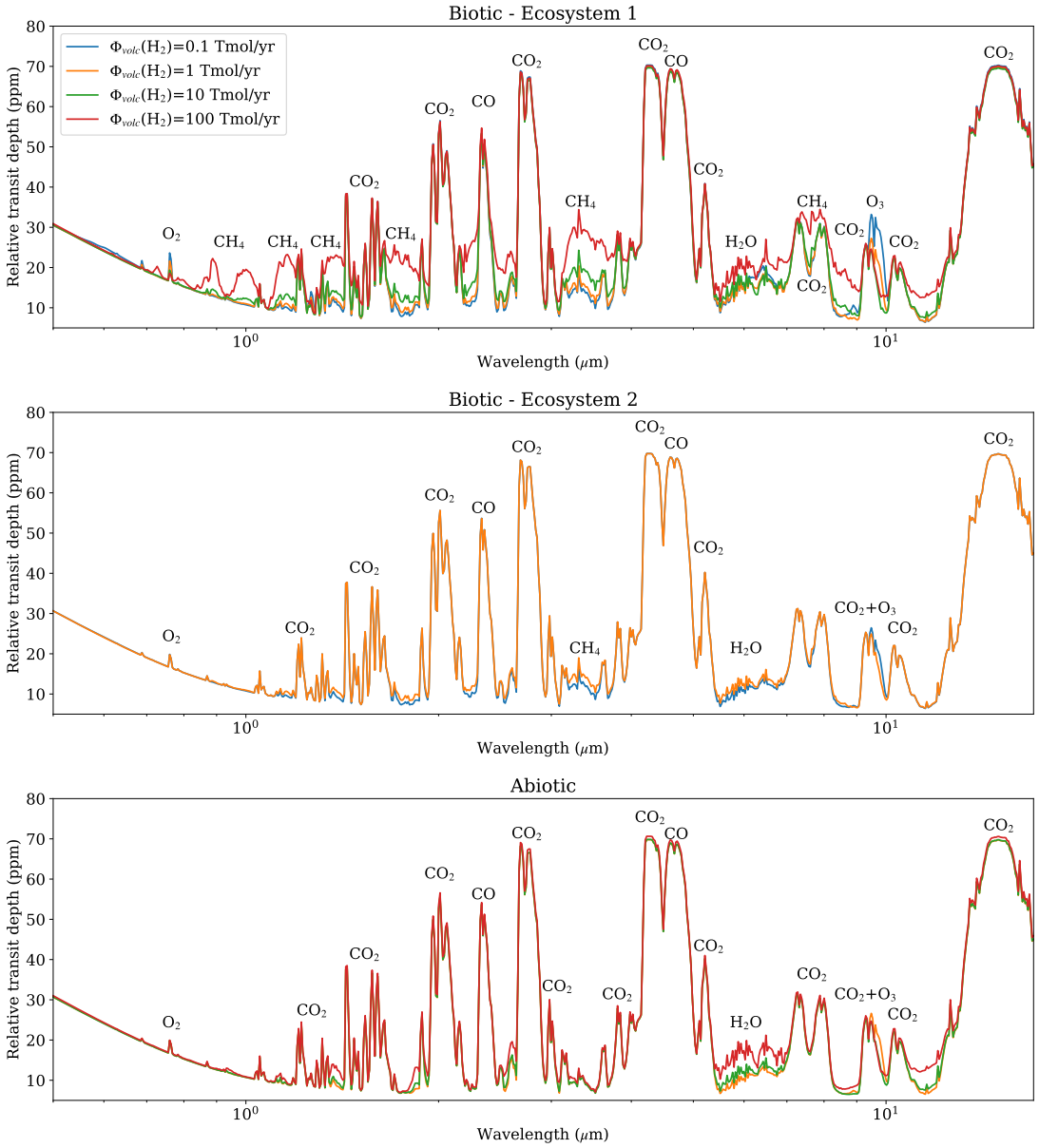

Figure 6.14: Transmission spectra for biotic and abiotic configurations used here for TRAPPIST-1e with stellar spectra that is quiescent and a mean flaring spectra. Transmission spectra is generated using PSG Villanueva et al. (2018), with features labelled with the species causing them.

abiotic cases (see Figure 6.14). As well as this, strong features of CO_2 as well as signs of water vapour are seen in all cases. This could be sufficient to suggest a biosphere with Krissansen-Totton et al. (2018c) finding that this mix could provide a chemical disequilibrium strong enough to suggest the presence of life.

This work revisits the consideration that CO is an antibiosignature for M–dwarf orbiting planets. I find that ecosystems that consume CO can lead to atmospheres with high levels of CO, one to two orders of magnitude higher on TRAPPIST-1e compared to the Earth. This is caused by the lower OH production rate on M–dwarf planets. Further, I find strong CO features in transmission spectra, despite the presence of CO consuming organisms. This may lead to some ambiguity as to whether this would be a definitively indicative biosphere (Thompson et al. 2022). Our results do support the conclusions from Schwieterman et al. (2019) that CO does not necessarily represent an anti-biosignature and can accumulate to high concentrations on inhabited planets for M–dwarf orbiting planets.

As our transmission spectra is generated using a 1D model only without haze, the effects of clouds and hazes have not been considered in the detectability. The presence of cloud may affect transmission spectra as discussed in Fauchez et al. (2019), which may mask some features around 20ppm. This may mean that if TRAPPIST-1e had a lower reductant input, the detection of methane may not be possible, while a flux of greater than 1 Tmol/yr would provide stronger signals. Similarly, a thin haze layer may be present in the highest H2 outgassing rate, which may clear many features below 3 microns (Fauchez et al. 2019). However features of CH_4 beyond 3 μm may be detectable, but only when H_2 outgassing is high, $\Phi_{\text{volc}}(H_2) > 10\,\text{Tmol/yr}$.

Segura et al. (2005) predicted that CH_4 concentrations would be higher if biological fluxes were the same compared to Earth due to a lower rate of photochemical destruction. However, I find biological methane flux is lower due to the atmosphere's slower recycling of CH_4 back to biologically consumable substrates for the TRAPPIST-1e configuration in the troposphere, leading to similar CH_4 abundances between Earth and TRAPPIST-1e. Similarly, I find weaker CH_4 peaks compared to Fauchez et al. (2019). This may be because in this work, CH_4 photolysis was found to peak deeper in the atmosphere meaning methane drops off substantially from around 50 km, compared to above 80 km in Fauchez

et al. (2019).

The generation of high oxygen states by anoxygenic biospheres is likely to be affected by the CO_2 concentration. While a relatively low CO_2 abundance of 10% is used here, higher CO_2 levels could see high levels of O_2 persisting for higher reductant inputs.

The oxidising regime that emerges at these low H_2 input levels in ecosystem 1, with only anoxic H_2 and CO consumers may also be missing important processes. At these levels of 10%, processes such as oxidative weathering are likely to be important (Daines et al. 2017). More work is required to establish the plausibility of the states with high levels of oxygen found here due to different surface compositions.

The configuration used here effectively assumes a well mixed rapidly rotating planet. These planets are likely to be tidally locked however, and either increasing the spatial resolution of 1D photochemical models to include day, night and terminator regions with appropriate mixing parametrisations or coupled chemistry-GCM are required to better constrain the detectability of these biospheres.

6.7 Conclusion

I use a coupled biosphere-atmosphere model to investigate the potential biosignatures from a H_2 and CO consuming biosphere, which produces CH_4 as a waste product. I find that TRAPPIST-1e under a low reductant input with a CH_4 producing biosphere may produce relatively high levels of surface O_2 of close to 0.1 mol/mol, which is not seen in the Earth case. This is due to CH_4 and O_2 being able to coexist to relatively high levels on M-dwarfs due to a lack of OH. In this high oxygen scenario, ozone may be detectable at 9.4 microns, although this is difficult due to the presence of CO_2. The inclusion of oxygen consuming organisms, could reduce these oxygen levels to around 10^{-5} mol/mol. At higher reductant inputs, oxygen abundance decreases and strong features of CH_4 along with CO_2 may provide a robust biosignature. I also show that CO is likely to be present in high quantities, even with a CO consuming organisms. The use of a mean flaring profile removes the high oxygen states shown, however further work is required to understand how a time dependent flaring spectrum may affect the results observed. I have shown that

anoxygenic photosynthesisers are unlikely to affect the atmospheric composition significantly compared to a prephotosyntheic biospheres, unless the recycling efficiency of secondary producers is low, where atmospheric CH_4 becomes very low. These results show that simple biosphere models with consistent ocean fluxes are important in determining atmospheric composition for understanding the potential role of life on the atmospheric composition of exoplanets.

6.8 Chapter Summary

In this Chapter, I have shown that the host star can have a significant effect on the atmospheric composition of a planet with a biosphere. For a planet like TRAPPIST-1e orbiting an M-dwarf, when the reductant outgassing rate is low, a methane producing anoxic biosphere could lead to high concentrations of O_2, due to photochemically driven oxygen production, which is stabilised at higher mixing ratios due to the biotic conversion of H_2 and CO to CH_4. I show that biospheres that utilise this O_2 could lead to more productive biospheres than an Earth analogue, and produce high levels of CO. Next, I conclude my overall science findings from this thesis and discuss avenues for future work.

Chapter 7

Conclusions & Future work

7.1 Conclusion

This thesis has focused on improving our understanding of the Archean, and the application of this to exoplanets. I have used a climate model to improve our understanding of the potential Archean climate, as well as the atmospheric processes on tidally locked exoplanets. I have also used a single column coupled atmosphere-biosphere model to understand the interaction between life and the environment. This has been applied to the early Earth and to Trappist-1e, which can be treated as indicative to other Earth like planets orbiting M-dwarfs.

Chapter 2 provides an overview of our understanding of the Archean in terms of atmospheric composition and the solid Earth, as well as the current state of exoplanet detection, atmospheric characterisation and the search for life. Particular interest is placed on the Archean because this is when life originated on Earth. Life on exoplanets may, then, be more likely to be similar to this period compared to the modern Earth, where many complex evolutionary processes occurred to get to this stage. I explain why geological evidence suggests that the Archean atmosphere was more reducing than today, with significantly less O_2. Alongside this, carbon dioxide concentrations were likely higher than the present day. This is required to offset the lower luminosity of the Sun relative to today, whilst maintaining a planetary surface that is not completely ice covered. Carbon dioxide

is the main candidate for this as the concentrations of this gas are controlled on geological timescales through a negative feedback with temperature, known as the silicate weathering feedback. Meanwhile, the characterisation of the atmosphere of exoplanets that are Earth-like are likely to be limited to planets orbiting M-dwarfs due to current observational constraints. In this context, Earth-like refers to planets that receive a similar stellar flux and are a similar size to the Earth. However, due to the great distance of these exoplanet targets from Earth, observations of their atmospheres through transit spectroscopy are our best opportunity to potentially observe biosignatures. Observations of atmospheric disequilibrium may provide the best evidence for biosignatures, such as the coexistence of methane, water vapour and carbon dioxide in the atmosphere, accompanied by relatively low levels of carbon monoxide. This would likely provide the greatest evidence for life if the early Archean Earth was observed as an exoplanet.

In Chapter 3, I introduce a range of modelling techniques that can be used to understand the atmospheres of planets. General circulation models (GCM) allow for understanding of atmospheric processes with high spatial resolution, such as atmospheric circulation and clouds. These have developed our understanding of the Archean and terrestrial exoplanets, for example by finding that lower carbon dioxide concentrations are required to keep the Archean ice free, compared to simulations in 1D models (Charnay et al. 2020). Photochemical models are important for constraining the abundances of species in the atmosphere. These have been used to understand the formation of haze (Arney et al. 2016), as well as abiotic oxygen production on exoplanets (Harman et al. 2018; Ranjan et al. 2023). Models of biospheres, which effectively provide chemistry at the ocean/surface of the planet, can be used in conjuncture with photochemical models to understand the role of life on the atmosphere. These have been used to predict the effect of various metabolisms on the atmospheric composition and climate of the early Earth. In this work, I used both a general circulation model to investigate the climate and atmospheric circulation on terrestrial planets, as well as a coupled photochemical-ecosystem model of preoxygenic photosynthetic biospheres to investigate the interaction between life and the atmosphere. This Chapter describes the developments that were made to the models to carry out the work in the subsequent chapters.

The work in Chapter 4 investigates the role of methane in the climate of the Archean. Methane is produced as a waste product by methanogens (methane producing organisms), and as such, large quantities of methane are predicted to have been present in the atmosphere during the Archean. Using a GCM, I investigated the effect of a range of potential methane concentrations on the climate of the Archean. I found that methane can provide a radiative forcing of up to 8.5 W/m^2. Above this maximum value, radiative forcing decreases because methane's shortwave absorption increases to the point that it is greater than the longwave forcing. This leads to global mean surface temperatures peaking at a methane to carbon dioxide ratio of 0.1, and methane being able to warm the Archean by up to 7 K compared to simulations with no methane. Methane also affects the meridional circulation, with higher methane concentrations leading to an increase in the equator to pole temperature gradient, due to a combination of a change in atmospheric circulation and the relative methane radiative forcing at the equator compared to the poles.

After investigating the Archean, Chapter 5 switches focus to understanding the climate of terrestrial exoplanets. I used a similar modelling configuration to Chapter 4 to understand the effect of stellar type on the climate of tidally locked exoplanets. Understanding the climate of these planets is important for understanding their potential habitability, as well as highlighting the contrasts between these planets and our the Earth. In this chapter, the stellar spectrum of a hypothetical TRAPPIST-1e was changed to have a spectrum of TRAPPIST-1, Proxima Centauri and the Sun, keeping all other parameters constant. I find that more radiation is absorbed directly by the atmosphere when irradiated by an M-dwarf compared to a G-dwarf. This leads to lower cloud coverage as the atmosphere is more stable against convection, leading to less upwelling air from the surface. As a result of the lower cloud coverage, the global mean surface temperature is warmer due to a lower cloud albedo, with the surface temperature on the nightside of the planet increasing the most, partly due to the increased efficiency of transport of energy from the day to nightside as the atmosphere is heated directly by stellar radiation.

Following the increased understanding of atmospheric processes on both the Archean Earth and M-dwarf orbiting exoplanets, Chapter 6 investigates the potential interaction between life and the atmosphere in both of these cases. Specifically, in this work I inves-

tigate the role of preoxygenic photosynthetic organisms on the atmospheric composition. This includes H_2 and CO consuming organisms that produce CH_4 as a waste product. I found that this biosphere on TRAPPIST-1e may be less productive than an equivalent biosphere on Earth, but the atmospheric methane mixing ratio is higher. This is because CH_4 is more photo-chemically stable in the atmosphere, due to a lower photolysis rate of H_2O on TRAPPIST-1e. We also find, that at low reductant inputs, the conversion of H_2 and CO to CH_4 may lead to oxygen accumulating in the atmosphere of TRAPPIST-1e. This may lead to a niche for oxygen consuming organisms, which could dramatically increase the productivity of such a biosphere. We test this, by including oxygen metabolisers that can consume O_2 alongside either CO or CH_4. We find that the organism consuming O_2 and CO, can drastically increase the productivity of the biosphere, which can decrease oxygen levels down to around 10^{-5} mol/mol, but also leads to an increase in CO mixing ratios. I find that the evolution of anoxygenic photosynthesis is unlikely to alter the atmospheric composition, unless the recycling efficiency of organic matter by secondary consumers is low. This is equivalent to saying that the organic carbon burial fraction of less than $\approx 5\,\%$ would be required to maintain similar atmospheric compositions between photosynthetic and non-photynthetic biospheres. To observe these primitive biospheres, transmission spectroscopy in the region 0.5 to 17 μm, a detection of methane and carbon dioxide may provide the most likely biosignature, although strong signatures of carbon monoxide would also be expected for planets orbiting M-dwarfs, even with the evolution of CO consuming organisms.

7.2 Future Work

The work from this thesis has opened up avenues for future work in increasing both our understanding of the Archean Earth and the applications this can have on exoplanets.

7.2.1 Archean clouds

Following Eager-Nash et al. (2023), a further study can be conducted on the change in cloud under different CO_2 and CH_4 conditions, shown in Figure 7.1. This shows the low, medium and high cloud amount versus the global mean temperature for the data from the

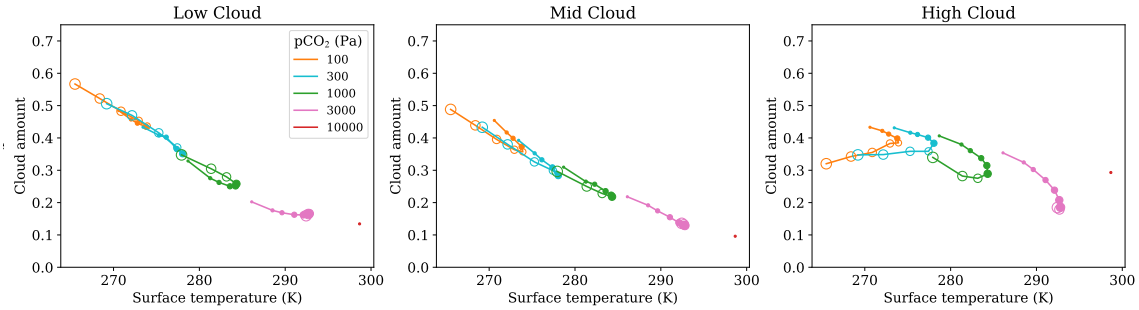

Figure 7.1: Showing the relationship between global mean surface temperature and the low, mid and high cloud amount in simulations with varying levels of CO_2 and CH_4.

simulations in Chapter 4. Low and medium cloud amount has a clear negative correlation with global mean surface temperature, which is primarily driven by varying CO_2 and CH_4 concentrations. The relationship between high cloud amount and temperature is less obvious, with a negative correlation appearing for low CH_4 simulations, while high CH_4 tends to decrease the high cloud amount, whilst also leading to a decrease in temperature.

Understanding the role of cloud is important as a secondary effect for climate, with Goldblatt et al. (2021) showing that cloud could reduce the amount of CO_2 required to maintain a constant mean surface temperature over Earth's history. Reduced low cloud leads to a reduction in the planetary albedo, which generally leads to cooling, with Figure 7.1a showing that the reducing low cloud with temperature could be amplifying the greenhouse effects of CO_2 and CH_4. Meanwhile high cloud is important for its greenhouse effect, thus a lowering of high cloud leads to a lower greenhouse contribution of cloud. These results could provide a valuable understanding of clouds over a large parameter space for the Archean.

7.2.2 The role of methane on a tidally locked planet

Following up from Eager-Nash et al. (2020) and Eager-Nash et al. (2023), one can consider the role of methane on a tidally locked planet. From Eager-Nash et al. (2023), we learnt that at high concentrations, methane becomes a strong absorber on near infrared radiation, while Eager-Nash et al. (2020) shows that the higher proportion of radiation in the infrared of M-dwarfs leads to warmer climates. An exploration of the effect of methane on a tidally locked planet orbiting an M-dwarf would be an obvious next step.

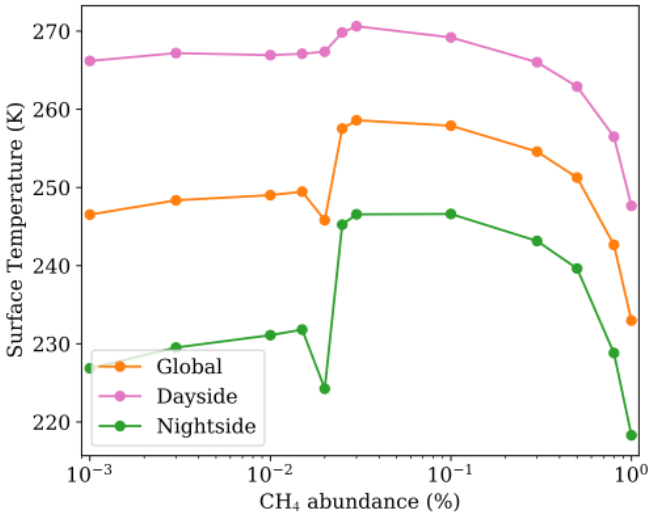

Figure 7.2: mean surface temperature due to change in methane abundance for global, dayside and nightside for TRAPPIST-1e with 3% carbon dioxide atmosphere.

Figure 7.2 shows a proof of concept study of this, for a 3% CO_2 atmosphere with CH_4 ranging from 0.001% to 1%. Two key observations can be made here, with methane's strong absorption of stellar radiation leading to a drop in temperatures on the order of 20 K, which is 2 to 3 times the drop in global temperatures seen in the Archean Earth case in Chapter 4. Secondly, an interesting transition occurs between 0.015% and 0.03%, where the global mean temperature drops and then rapidly increases as CH_4 concentration is increased. This is predominantly caused by a change in the nightside temperature (green line in Figure 7.2), and appears to be caused by a change in the circulation in this regime, as described in Sergeev et al. (2022b). A more detailed investigation into this behaviour is important, to understand the potential of methane producing life to potentially cause quite drastic changes in the climate.

7.2.3 3D chemistry of Archean-like worlds

A key next step in this work is to bring together modelling of general circulation models and photochemical models to coupled chemistry climate modelling of Archean like planets. Investigating this will be particularly important for tidally locked planets, where there is a constant dayside where photochemistry can occur and nightside with no photochemistry. Observations from transmission spectroscopy are able to detect the atmospheric composition of the terminator region only, and so understanding what this region may

look like is important.

Coupled chemistry climate modelling of Archean like planets, could be readily achieved following this work, by using the chemical network developed and predicted surface fluxes in the coupled chemistry climate model developed in Ridgway et al. (2022).

The Appendices

Appendix A

Climate of the Archean-like Atmospheres

A.1 Additional figures

Here, we figures of the full grid of similations from Chapter 4. Figure A.1 and Figure A.2 shows the same information as Figure 4.3 and Figure 4.5 respectively, but for the full grid of simulations.

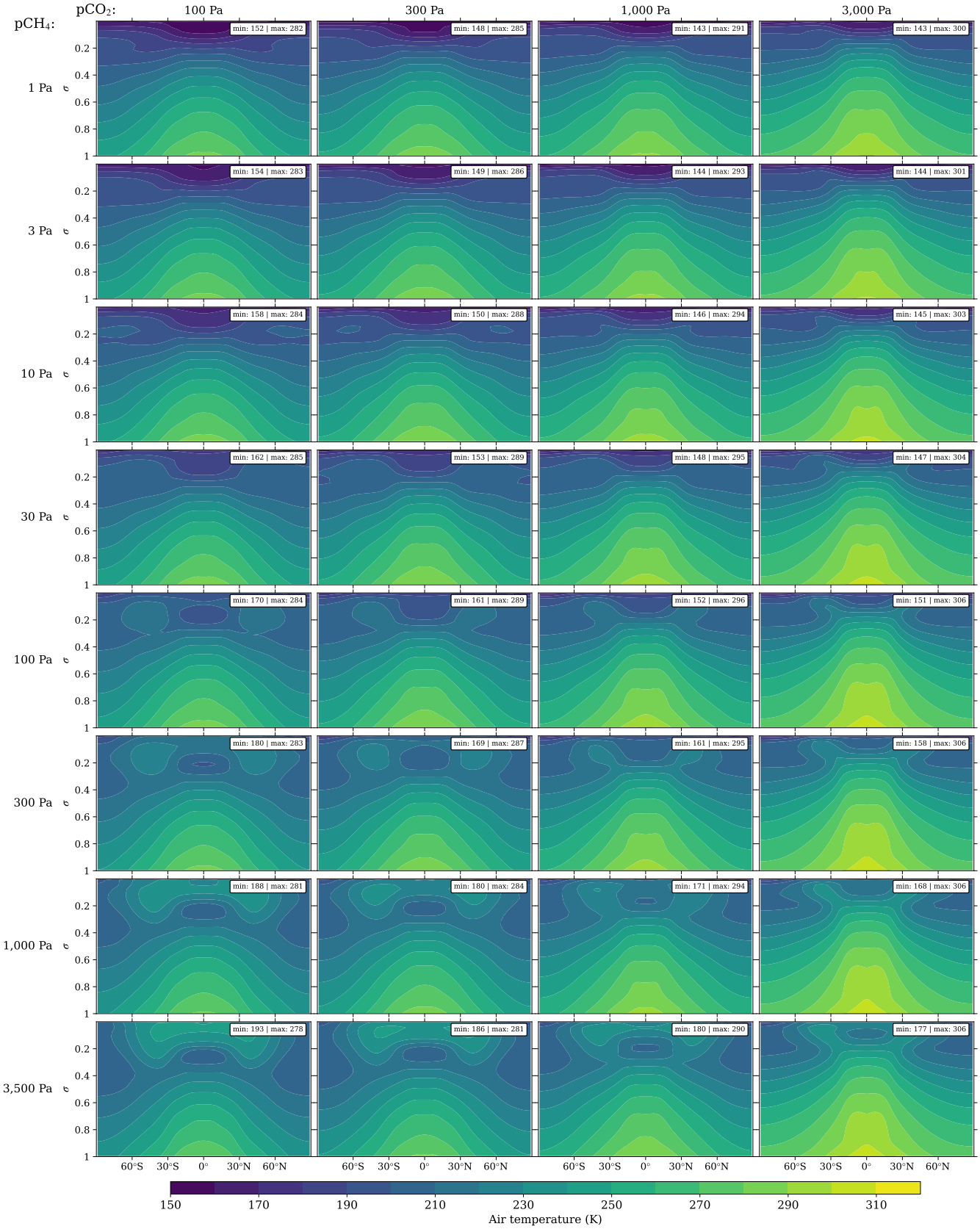

Figure A.1: Zonal averaged air temperature (colour scale), for increasing surface partial pressures of carbon dioxide from left to right, and methane from top to bottom. Plotted as latitude vs σ, where σ is the pressure divided by the global mean surface pressure. The same colour scale is used for each plot, with maximum and minimum temperatures for each simulation displayed in the top right of each sub figure.

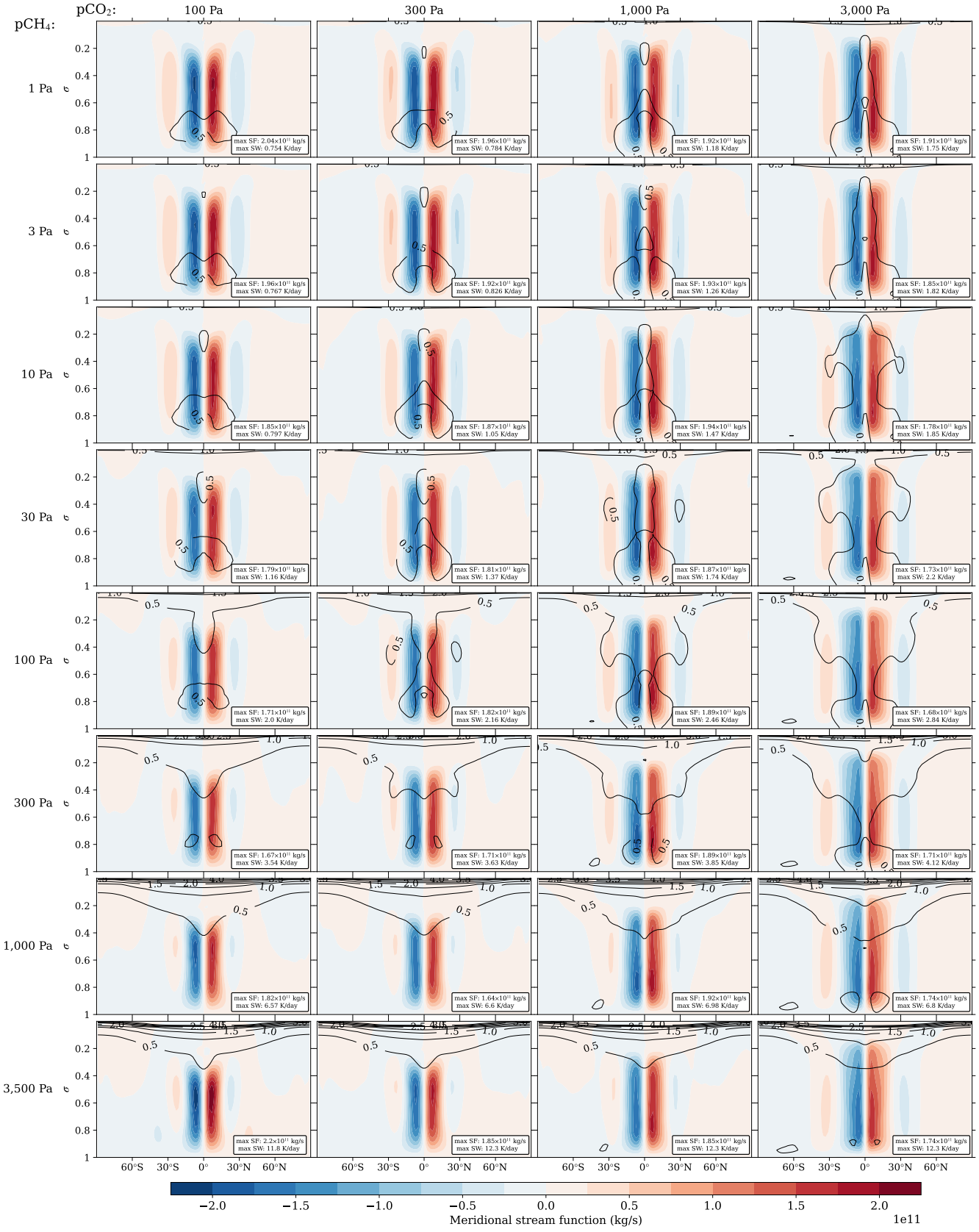

Figure A.2: Zonal averaged meridional stream functions (colour scale), for increasing surface partial pressures of carbon dioxide from left to right, and methane from top to bottom. Positive and negative values represent clockwise and anticlockwise circulation respectively. Contours show the heating of the atmosphere due to shortwave radiation in K/day. The same colour scale is used for each plot, with maximum values for the stream function (SF) and shortwave heating rate (SW) are shown for each simulation in the bottom right of each sub figure.

Appendix B

Chemical network

Table B.1: Photolysis reactions used in this network, with reactants (R) and products (P), with cross section and quantum yields from the open access ATMOS model (Teal et al. 2022). The horizontal line within the table shows the cutoff for the CHO network described in Chapter 6.

R1	R2	P1	P2	P3	BR	Source
O_2	$h\nu$	$O(^3P)$	$O(^1D)$	-		
O_2	$h\nu$	$O(^3P)$	$O(^3P)$	-		
H_2O	$h\nu$	H	OH	-		
H_2O	$h\nu$	H_2	$O(^1D)$	-		
H_2O	$h\nu$	H	H	$O(^3P)$		
O_3	$h\nu$	O_2	$O(^1D)$	-		
O_3	$h\nu$	O_2	$O(^3P)$	-		
H_2O_2	$h\nu$	OH	OH	-		
H_2O_2	$h\nu$	H	HO_2	-		
CO_2	$h\nu$	CO	$O(^3P)$	-		
CO_2	$h\nu$	CO	$O(^1D)$	-		
H_2CO	$h\nu$	H_2	CO	-		
H_2CO	$h\nu$	HCO	H	-		
HO_2	$h\nu$	OH	$O(^3P)$	-		
HO_2	$h\nu$	OH	$O(^1D)$	-		
CH_4	$h\nu$	$^1CH_2$	H_2	-		

Continued on next page

Table B.1 – continued from previous page

R1	R2	P1	P2	P3	BR	Source
CH_4	$h\nu$	CH_3	H	-		
CH_4	$h\nu$	$^3CH_2$	H	H		
C_2H_6	$h\nu$	$^3CH_2$	$^3CH_2$	H_2		
C_2H_6	$h\nu$	CH_4	$^1CH_2$	-		
C_2H_6	$h\nu$	C_2H_2	H_2	H_2		
C_2H_6	$h\nu$	C_2H_4	H	H		
C_2H_6	$h\nu$	C_2H_4	H_2	-		
C_2H_6	$h\nu$	CH_3	CH_3	-		
CH	$h\nu$	C	H	-		
CH_2CO	$h\nu$	$^3CH_2$	CO	-		
C_2H_2	$h\nu$	C2H	H	-		
C_2H_2	$h\nu$	C2	H_2	-		
C_2H_4	$h\nu$	C_2H_2	H_2	-		
C_2H_4	$h\nu$	C_2H_2	H	H		
CH_3CHO	$h\nu$	CH_3	HCO	-		
CH_3CHO	$h\nu$	CH_4	CO	-		
HNO_2	$h\nu$	NO	OH	-		
HNO_3	$h\nu$	NO_2	OH	-		
NO	$h\nu$	N	$O(^3P)$	-		
NO_2	$h\nu$	NO	$O(^3P)$	-		
SO	$h\nu$	S	$O(^3P)$	-		
H_2S	$h\nu$	HS	H	-		
SO_2	$h\nu$	SO	$O(^3P)$	-		
SO_2	$h\nu$	$^1SO_2$	-	-		
SO_2	$h\nu$	$^3SO_2$	-	-		
S_2	$h\nu$	S	S	-		
S_4	$h\nu$	S_2	S_2	-		
S_3	$h\nu$	S_2	S	-		

Continued on next page

Table B.1 – continued from previous page

R1	R2	P1	P2	P3	BR	Source
SO_3	$h\nu$	SO_2	$O(^3P)$	-		
HSO	$h\nu$	HS	$O(^3P)$	-		
OCS	$h\nu$	CO	S	-		
HO_2NO_2	$h\nu$	HO_2	NO_2	-		
HO_2NO_2	$h\nu$	OH	NO_3	-		
N_2O_5	$h\nu$	NO_3	NO_2	-		
N_2O_5	$h\nu$	NO_3	NO	$O(^3P)$		
NO_3	$h\nu$	NO	O_2	-		
NO_3	$h\nu$	NO_2	$O(^3P)$	-		
N_2O	$h\nu$	N_2	$O(^1D)$	-		
CS_2	$h\nu$	CS	S	-		
CS_2	$h\nu$	CS_2^*	-	-		

Table B.2: Bimolecular reactions used in this network. Reactions sourced from the Kinetic Database for Astrochemistry (KIDA) are from https://kida.astrochem-tools.org/. The horizontal line within the table shows the cutoff for the CHO network described in Chapter 6.

R1	R2	R3	P1	P2	P3	A	α	β (K)	Source
$O(^1D)$	H_2O	-	OH	OH	-	1.63e-10	0.000	-60	Burkholder et al. (2019)
$O(^1D)$	H_2	-	OH	H	-	1.20e-10	0.000	0	Burkholder et al. (2019)
H_2	$O(^3P)$	-	OH	H	-	3.44e-13	2.670	3160	Baulch et al. (1992)
OH	H_2	-	H_2O	H	-	2.80e-12	0.000	1800	Burkholder et al. (2019)
H	O_3	-	OH	O_2	-	1.40e-10	0.000	470	Burkholder et al. (2019)
H	HO_2	-	H_2	O_2	-	6.90e-12	0.000	0	Burkholder et al. (2019)
H	HO_2	-	$O(^3P)$	H_2O	-	1.60e-12	0.000	0	Burkholder et al. (2019)
H	HO_2	-	OH	OH	-	7.20e-11	0.000	0	Burkholder et al. (2019)
$O(^3P)$	OH	-	O_2	H	-	1.80e-11	0.000	-180	Burkholder et al. (2019)
OH	HO_2	-	H_2O	O_2	-	4.80e-11	0.000	-250	Burkholder et al. (2019)
OH	O_3	-	HO_2	O_2	-	1.70e-12	0.000	940	Burkholder et al. (2019)
$O(^3P)$	HO_2	-	OH	O_2	-	3.00e-11	0.000	-200	Burkholder et al. (2019)
HO_2	O_3	-	OH	O_2	O_2	1.00e-14	0.000	490	Burkholder et al. (2019)
HO_2	HO_2	-	H_2O_2	O_2	-	3.00e-13	0.000	-460	Burkholder et al. (2019)
OH	H_2O_2	-	H_2O	HO_2	-	1.80e-12	0.000	0	Burkholder et al. (2019)

Continued on next page

Table B.2 – continued from previous page

R1	R2	R3	P1	P2	P3	A	α	β (K)	Source
$O(^3P)$	O_3	-	O_2	O_2	-	8.00e-12	0.000	2060	Burkholder et al. (2019)
OH	OH	-	H_2O	$O(^3P)$	-	1.80e-12	0.000	0	Burkholder et al. (2019)
$O(^1D)$	N_2	-	$O(^3P)$	N_2	-	2.15e-11	0.000	-110	Burkholder et al. (2019)
$O(^1D)$	O_2	-	$O(^3P)$	O_2	-	3.30e-11	0.000	-55	Burkholder et al. (2019)
OH	CO	-	H	CO_2	-	1.50e-13	0.000	0	Burkholder et al. (2015)
H	HCO	-	H_2	CO	-	1.83e-10	0.000	0	KIDA
HCO	HCO	-	H_2CO	CO	-	4.48e-11	0.000	0	KIDA
OH	HCO	-	H_2O	CO	-	1.80e-10	0.000	0	KIDA
$O(^3P)$	HCO	-	H	CO_2	-	5.00e-11	0.000	0	KIDA
$O(^3P)$	HCO	-	OH	CO	-	5.00e-11	0.000	0	KIDA
HCO	$h\nu$	-	H	CO	-	1.00e-02	0.000	0	Pinto et al. (1980)
H_2CO	H	-	H_2	HCO	-	2.16e-12	1.620	1090	KIDA
HCO	O_2	-	CO	HO_2	-	5.20e-12	0.000	0	Burkholder et al. (2015)
OH	H_2CO	-	H_2O	HCO	-	5.50e-12	0.000	-125	Burkholder et al. (2015)
H_2CO	$O(^3P)$	-	HCO	OH	-	3.40e-11	0.000	1600	Burkholder et al. (2015)
$O(^3P)$	H_2O_2	-	OH	HO_2	-	1.40e-12	0.000	2000	Burkholder et al. (2019)

Continued on next page

Table B.2 – continued from previous page

R1	R2	R3	P1	P2	P3	A	α	β (K)	Source
OH	CH_4	-	CH_3	H_2O	-	2.45e-12	0.000	1775	Burkholder et al. (2015)
$O(^1D)$	CH_4	-	CH_3	OH	-	1.66e-10	0.000	0	Burkholder et al. (2015)
$O(^1D)$	CH_4	-	H_2CO	H_2	-	8.75e-12	0.000	0	Burkholder et al. (2015)
$^1CH_2$	CH_4	-	CH_3	CH_3	-	3.60e-11	0.000	0	Zahnle et al. (2006))
$^1CH_2$	O_2	-	H	CO	OH	2.05e-11	0.000	750	Baulch et al. (1994)
$^1CH_2$	O_2	-	H_2	CO_2	-	2.05e-11	0.000	750	Baulch et al. (1994)
$^1CH_2$	N_2	-	$^3CH_2$	N_2	-	1.00e-11	0.000	0	KIDA
$^3CH_2$	H_2	-	CH_3	H	-	5.00e-15	0.000	0	Tsang and Hampson (1986)
$^3CH_2$	CH_4	-	CH_3	CH_3	-	7.13e-12	0.000	5050	KIDA
$^3CH_2$	O_2	-	HCO	OH	-	4.10e-11	0.000	750	Zahnle et al. (2006)
CH_3	O_2	-	H_2CO	OH	-	3.00e-16	0.000	0	Burkholder et al. (2015)
CH_3	$O(^3P)$	-	H_2CO	H	-	1.10e-10	0.000	0	Burkholder et al. (2015)
CH_3	O_3	-	CH_3O	O_2	-	5.40e-12	0.000	220	Burkholder et al. (2015)
CH_3	OH	-	CH_3O	H	-	1.20e-12	0.000	2760	KIDA
CH_3	$h\nu$	-	$^3CH_2$	H	-	1.00e-05	0.000	0	Zahnle et al. (2006)
CH_3	HCO	-	CH_4	CO	-	9.30e-11	0.000	0	Krasnoperov et al. (2005)

Continued on next page

Table B.2 – continued from previous page

R1	R2	R3	P1	P2	P3	A	α	β (K)	Source
CH_3	H_2CO	-	CH_4	HCO	-	1.12e-14	3.360	2170	KIDA
CH_4	$O(^3P)$	-	CH_3	OH	-	8.41e-12	1.560	4280	KIDA
$^1CH_2$	H_2	-	CH_3	H	-	1.20e-10	0.000	0	KIDA
$^1CH_2$	H_2	-	$^3CH_2$	H_2	-	1.26e-11	0.000	0	KIDA
$^1CH_2$	CO_2	-	H_2CO	CO	-	1.00e-12	0.000	0	Zahnle (1986)
$^3CH_2$	$O(^3P)$	-	CO	H	H	2.04e-10	0.000	270	KIDA
$^3CH_2$	CO_2	-	H_2CO	CO	-	3.90e-14	0.000	0	Tsang and Hampson (1986)
OH	C_2H_6	-	H_2O	C_2H_5	-	7.66e-12	0.000	1020	Burkholder et al. (2015)
C_2H_6	$O(^3P)$	-	C_2H_5	OH	-	8.63e-12	1.500	2920	KIDA
C_2H_6	$O(^1D)$	-	OH	C_2H_5	-	3.40e-11	0.000	0	Dillon et al. (2007)
C_2H_6	$O(^1D)$	-	H_2O	C_2H_4	-	1.02e-10	0.000	0	Dillon et al. (2007)
C_2H_6	$O(^1D)$	-	CH_3	CH_3O	-	2.04e-10	0.000	0	Dillon et al. (2007)
C_2H_5	HCO	-	C_2H_6	CO	-	7.21e-11	0.000	0	Baggott et al. (1987)
CO	$O(^1D)$	-	CO	$O(^3P)$	-	4.70e-11	0.000	-63	Davidson et al. (1978)
C_2H_5	H	-	CH_3	CH_3	-	6.00e-11	0.000	0	Baulch et al. (1992)
C_2H_5	$O(^3P)$	-	CH_3	HCO	H	3.00e-11	0.000	0	Tsang and Hampson (1986)

Continued on next page

Table B.2 – continued from previous page

R1	R2	R3	P1	P2	P3	A	α	β (K)	Source
C_2H_5	OH	-	CH_3	HCO	H_2	4.00e-11	0.000	0	Zahnle et al. (2006)
CH_3O_2	H	-	CH_3O	OH	-	1.60e-10	0.000	0	Tsang and Hampson (1986)
CH_3O_2	$O(^3P)$	-	CH_3O	O_2	-	8.30e-11	0.000	0	Herron (1988)
HCO	$^3CH_2$	-	CH_3	CO	-	3.00e-11	0.000	0	Tsang and Hampson (1986)
CH_3O	CO	-	CH_3	CO_2	-	2.60e-11	0.000	5940	KIDA
$^3CH_2$	$O(^3P)$	-	CO	H_2	-	1.36e-10	0.000	270	KIDA
CH_3	OH	-	H_2CO	H_2	-	5.30e-15	0.000	2530	KIDA
C_2H_5	O_2	-	C_2H_4	HO_2	-	1.00e-14	0.000	0	Burkholder et al. (2015)
C_2H_5	H	-	C_2H_4	H_2	-	3.00e-12	0.000	0	KIDA
C_2H_5	$O(^3P)$	-	H_2CO	CH_3	-	2.67e-11	0.000	0	KIDA
C_2H_5	$O(^3P)$	-	CH_3CHO	H	-	1.33e-10	0.000	0	KIDA
C_2H_5	OH	-	CH_3CHO	H_2	-	1.00e-10	0.000	0	KIDA
C_2H_5	OH	-	C_2H_4	H_2O	-	4.00e-11	0.000	0	KIDA
C	OH	-	CO	H	-	1.15e-10	-0.340	0	KIDA
C	O_2	-	CO	$O(^3P)$	-	4.90e-11	-0.320	0	KIDA
CH	H	-	C	H_2	-	1.24e-10	0.260	0	KIDA

Continued on next page

Table B.2 – continued from previous page

R1	R2	R3	P1	P2	P3	A	α	β (K)	Source
CH	$O(^3P)$	-	CO	H	-	6.60e-11	0.000	0	Baulch et al. (2005)
CH	H_2	-	$^3CH_2$	H	-	2.90e-10	0.000	1670	Baulch et al. (2005)
CH	O_2	-	CO	OH	-	8.30e-11	0.000	0	Lichtin et al. (1984)
CH	CO_2	-	HCO	CO	-	5.71e-12	0.000	345	Baulch et al. (1992)
$^3CH_2$	$O(^3P)$	-	H	HCO	-	3.40e-12	0.000	270	KIDA
$^3CH_2$	H	-	CH	H_2	-	2.00e-10	0.000	0	Baulch et al. (2005)
CH_2CO	H	-	CH_3	CO	-	6.89e-12	0.885	1430	Baulch et al. (2005)
CH_2CO	$O(^3P)$	-	H_2CO	CO	-	3.80e-12	0.000	680	Baulch et al. (1992)
CH_2CO	$^3CH_2$	-	C_2H_4	CO	-	2.90e-10	0.000	0	Canosa-mas et al. (1984)
CH_3CO	H	-	H_2	CH_2CO	-	1.92e-11	0.000	0	KIDA
CH_3CO	H	-	HCO	CH_3	-	1.03e-11	0.000	0	KIDA
CH_3CO	$O(^3P)$	-	CO_2	CH_3	-	2.63e-10	0.000	0	Baulch et al. (2005)
CH_3CO	$O(^3P)$	-	OH	CH_2CO	-	8.75e-11	0.000	0	Baulch et al. (2005)
CH_3CO	OH	-	H_2O	CH_2CO	-	2.01e-11	0.000	0	Tsang and Hampson (1986)
CH_3CO	CH_3	-	C_2H_6	CO	-	5.40e-11	0.000	0	Adachi et al. (1981)
CH_3CO	CH_3	-	CH_4	CH_2CO	-	1.00e-11	0.000	0	Hassinen et al. (1990)

Continued on next page

Table B.2 – continued from previous page

R1	R2	R3	P1	P2	P3	A	α	β (K)	Source
CH_3CO	$^3CH_2$	-	CH_3	CH_2CO	-	3.00e-11	0.000	0	Tsang and Hampson (1986)
CH_3CO	C_2H	-	C_2H_2	CH_2CO	-	3.00e-11	0.000	0	Tsang and Hampson (1986)
CH_3CO	HCO	-	CO	CH_3CHO	-	1.50e-11	0.000	0	Tsang and Hampson (1986)
$^3CH_2$	$^3CH_2$	-	C_2H_2	H_2	-	2.00e-11	0.000	400	Baulch et al. (1992)
$^3CH_2$	$^3CH_2$	-	C_2H_2	H	H	1.80e-10	0.000	400	Baulch et al. (1992)
C_2H	$^1CH_2$	-	CH	C_2H_2	-	3.00e-11	0.000	0	Tsang and Hampson (1986)
C_2H	$^3CH_2$	-	CH	C_2H_2	-	3.00e-11	0.000	0	Tsang and Hampson (1986)
C_2H	O_2	-	CO	CO	H	3.00e-11	0.000	0	KIDA
C_2H	$O(^3P)$	-	CO	CH	-	2.41e-11	0.000	230	Devriendt and Peeters (1997)
C_2H	H_2	-	C_2H_2	H	-	1.95e-14	2.320	4	Baulch et al. (2005)
C_2H	CH_4	-	C_2H_2	CH_3	-	7.67e-12	0.940	328	Baulch et al. (2005)
C_2H	C_2H_5	-	C_2H_2	C_2H_4	-	3.00e-12	0.000	0	Tsang and Hampson (1986)
C_2	H_2	-	C_2H	H	-	1.77e-10	0.000	1469	Kasting (1990)
C_2	CH_4	-	C_2H	CH_3	-	5.05e-11	0.000	297	Kasting (1990)
C_2	$O(^3P)$	-	C	CO	-	5.00e-11	0.000	0	Kasting (1990)
C_2	O_2	-	CO	CO	-	1.50e-11	0.000	550	Kasting (1990)

Continued on next page

Table B.2 – continued from previous page

R1	R2	R3	P1	P2	P3	A	α	β (K)	Source
$^3CH_2$	CH_3	-	C_2H_4	H	-	7.00e-11	0.000	0	Kasting (1990)
$^3CH_2$	C_2H_3	-	CH_3	C_2H_2	-	3.00e-11	0.000	0	Kasting (1990)
C_2H_3	H	-	C_2H_2	H_2	-	3.30e-11	0.000	0	Kasting (1990)
C_2H_3	H_2	-	C_2H_4	H	-	2.60e-13	0.000	2646	Kasting (1990)
C_2H_3	CH_4	-	C_2H_4	CH_3	-	2.40e-14	4.020	2754	Kasting (1990)
C_2H_3	C_2H_6	-	C_2H_4	C_2H_5	-	3.00e-13	0.000	5170	Kasting (1990)
C_2H_4	OH	-	H_2CO	CH_3	-	2.20e-12	0.000	-385	Kasting (1990)
C_2H_4	$O(^3P)$	-	HCO	CH_3	-	5.50e-12	0.000	565	Kasting (1990)
C_2H	C_2H_6	-	C_2H_2	C_2H_5	-	5.10e-11	0.000	76	KIDA
CH	CH_4	-	C_2H_4	H	-	6.66e-11	-0.400	0	Thiesemann et al. (1997)
$^3CH_2$	C_2H_5	-	CH_3	C_2H_4	-	3.00e-11	0.000	0	Tsang and Hampson (1986)
$O(^3P)$	C_2H_2	-	$^3CH_2$	CO	-	3.00e-11	0.000	1600	Burkholder et al. (2015)
C_2H_3	$O(^3P)$	-	CH_2CO	H	-	5.50e-11	0.000	0	Kasting (1990)
C_2H_3	OH	-	C_2H_2	H_2O	-	8.30e-12	0.000	0	Kasting (1990)
C_2H_3	CH_3	-	C_2H_2	CH_4	-	3.40e-11	0.000	0	Kasting (1990)
C_2H_3	C_2H_3	-	C_2H_4	C_2H_2	-	2.40e-11	0.000	0	Kasting (1990)

Continued on next page

Table B.2 – continued from previous page

R1	R2	R3	P1	P2	P3	A	α	β (K)	Source
C_2H_3	C_2H_5	-	C_2H_4	C_2H_4	-	3.00e-12	0.000	0	Kasting (1990)
C_2H_5	C_2H_3	-	C_2H_6	C_2H_2	-	6.00e-12	0.000	0	Kasting (1990)
C_2H_5	C_2H_5	-	C_2H_6	C_2H_4	-	2.30e-12	0.000	0	Kasting (1990)
C_2H_2	OH	-	CH_2CO	H	-	1.00e-13	0.000	0	Kasting (1990)
C_2H_2OH	H	-	H_2O	C_2H_2	-	5.00e-11	0.000	0	Kasting (1990)
C_2H_2OH	H	-	H_2	CH_2CO	-	3.30e-11	0.000	2000	Kasting (1990)
C_2H_2OH	$O(^3P)$	-	OH	CH_2CO	-	3.30e-11	0.000	2000	Kasting (1990)
C_2H_2OH	OH	-	H_2O	CH_2CO	-	1.70e-11	0.000	1000	Kasting (1990)
C_2H_4OH	H	-	H_2O	C_2H_4	-	5.00e-11	0.000	0	Kasting (1990)
C_2H_4OH	H	-	H_2	CH_3CHO	-	3.30e-11	0.000	2000	Kasting (1990)
C_2H_4OH	$O(^3P)$	-	OH	CH_3CHO	-	3.30e-11	0.000	2000	Kasting (1990)
C_2H_4OH	OH	-	H_2O	CH_3CHO	-	1.70e-11	0.000	1000	Kasting (1990)
CH_3CHO	H	-	CH_3CO	H_2	-	2.80e-11	0.000	1540	Kasting (1990)
$O(^3P)$	CH_3CHO	-	CH_3CO	OH	-	1.80e-11	0.000	1100	Burkholder et al. (2015)
OH	CH_3CHO	-	CH_3CO	H_2O	-	4.63e-12	0.000	-350	Burkholder et al. (2015)
CH_3CHO	CH_3	-	CH_3CO	CH_4	-	2.80e-11	0.000	1540	Kasting (1990)

Continued on next page

Table B.2 – continued from previous page

R1	R2	R3	P1	P2	P3	A	α	β (K)	Source
C_2H_5	CH_3	-	C_2H_4	CH_4	-	1.50e-12	0.000	0	Kasting (1990)
C_2H	HCO	-	CO	C_2H_2	-	1.00e-10	0.000	0	Tsang and Hampson (1986)
$O(^3P)$	CH_3	-	H_2CO	H	-	1.10e-10	0.000	0	Burkholder et al. (2019)
$O(^1D)$	CO_2	-	$O(^3P)$	CO_2	-	7.50e-11	0.000	-115	Burkholder et al. (2019)
CH_3O_2	O_3	-	CH_3O	O_2	O_2	2.90e-16	0.000	1000	Burkholder et al. (2015)
C_2H_4OH	O_2	-	CH_3CHO	HO_2	-	6.30e-14	0.000	550	Burkholder et al. (2015)
$O(^1D)$	O_3	-	O_2	O_2	-	1.20e-10	0.000	0	Burkholder et al. (2019)
$O(^1D)$	O_3	-	O_2	$O(^3P)$	$O(^3P)$	1.20e-10	0.000	0	Burkholder et al. (2019)
HS	CS	-	CS_2	H	-	1.50e-13	0.000	0	Burkholder et al. (2015)
CH_3	HNO	-	CH_4	NO	-	1.85e-11	0.600	176	Choi and Lin (2005)
N	O_2	-	NO	$O(^3P)$	-	3.30e-12	0.000	3150	Burkholder et al. (2019)
N	O_3	-	NO	O_2	-	0.00e+00	0.000	0	Burkholder et al. (2015)
N	OH	-	NO	H	-	5.00e-11	0.000	6	KIDA
N	NO	-	N_2	$O(^3P)$	-	2.10e-11	0.000	-100	Burkholder et al. (2019)
NO	O_3	-	NO_2	O_2	-	3.00e-12	0.000	1500	Burkholder et al. (2019)
HO_2	NO	-	NO_2	OH	-	3.44e-12	0.000	-260	Burkholder et al. (2019)

Continued on next page

Table B.2 – continued from previous page

R1	R2	R3	P1	P2	P3	A	α	β (K)	Source
$O(^3P)$	NO_2	-	NO	O_2	-	5.30e-12	0.000	-200	Burkholder et al. (2019)
H	NO_2	-	OH	NO	-	1.35e-10	0.000	0	Burkholder et al. (2019)
HCO	NO	-	HNO	CO	-	1.35e-11	0.000	0	Dammeier et al. (2007)
HNO	$h\nu$	-	NO	H	-	1.70e-03	0.000	0	Dammeier et al. (2007)
H	HNO	-	H_2	NO	-	3.01e-11	0.000	500	Tsang and Herron (1991)
$O(^3P)$	HNO	-	OH	NO	-	3.80e-11	-0.080	0	KIDA
OH	HNO	-	H_2O	NO	-	8.00e-11	0.000	500	Tsang and Herron (1991)
OH	HNO_2	-	H_2O	NO_2	-	3.00e-12	0.000	-250	Burkholder et al. (2019)
C_2H_5	HNO	-	C_2H_6	NO	-	1.60e-12	0.000	1000	Zahnle (1986)
HNO_3	OH	-	H_2O	NO_3	-	2.40e-14	0.000	-460	Burkholder et al. (2015)
N	HO_2	-	NO	OH	-	2.20e-11	0.000	0	Brune et al. (1983)
HO_2	NO_2	-	HNO_2	O_2	-	5.00e-16	0.000	0	Burkholder et al. (2015)
SO	O_2	-	SO_2	$O(^3P)$	-	1.60e-13	0.000	2280	Burkholder et al. (2015)
SO	HO_2	-	SO_2	OH	-	2.80e-11	0.000	0	Kasting (1990)
OH	SO	-	H	SO_2	-	2.70e-11	0.000	-335	Burkholder et al. (2015)
SO_3	H_2O	H_2O	H_2SO_4	H_2O	-	6.90e-14	1.000	-6540	Krasnopolsky (2012)

Continued on next page

Table B.2 – continued from previous page

R1	R2	R3	P1	P2	P3	A	α	β (K)	Source
HSO_3	O_2	-	HO_2	SO_3	-	1.30e-12	0.000	330	Burkholder et al. (2015)
HSO_3	OH	-	H_2O	SO_3	-	1.00e-11	0.000	0	Kasting (1990)
HSO_3	H	-	H_2	SO_3	-	1.00e-11	0.000	0	Kasting (1990)
HSO_3	$O(^3P)$	-	OH	SO_3	-	1.00e-11	0.000	0	Kasting (1990)
OH	H_2S	-	HS	H_2O	-	6.10e-12	0.000	75	Burkholder et al. (2015)
H_2S	H	-	H_2	HS	-	3.66e-12	1.940	455	Peng et al. (1999)
$O(^3P)$	H_2S	-	OH	HS	-	9.20e-12	0.000	1800	Burkholder et al. (2015)
$O(^3P)$	HS	-	SO	H	-	7.00e-11	0.000	0	Burkholder et al. (2015)
HS	O_2	-	OH	SO	-	4.00e-19	0.000	0	Burkholder et al. (2015)
HS	HO_2	-	HSO	OH	-	1.00e-11	0.000	0	Stachnik and Molina (1987)
HS	HS	-	H_2S	S	-	1.50e-11	0.000	0	Schofield (1973); Tiee et al. (1981)
HS	HS	-	H_2	S_2	-	5.00e-14	0.000	0	Schofield (1973); Tiee et al. (1981)
HS	HCO	-	H_2S	CO	-	5.00e-11	0.000	0	Kasting (1990)
HS	H	-	H_2	S	-	2.00e-11	0.000	0	Tiee et al. (1981)
HS	S	-	H	S_2	-	5.00e-12	0.000	0	Nicholas et al. (1979)
S	O_2	-	SO	$O(^3P)$	-	1.60e-12	0.000	-100	Burkholder et al. (2015)

Continued on next page

Table B.2 – continued from previous page

R1	R2	R3	P1	P2	P3	A	α	β (K)	Source
OH	S	-	H	SO	-	6.60e-11	0.000	0	Burkholder et al. (2015)
S	HCO	-	H	OCS	-	8.00e-11	0.000	0	Loison et al. (2012)
S	HCO	-	HS	CO	-	4.00e-11	0.000	0	Loison et al. (2012)
S	HO_2	-	HS	O_2	-	5.00e-12	0.000	0	Kasting (1990)
S	HO_2	-	SO	OH	-	5.00e-12	0.000	0	Kasting (1990)
S_2	$O(^3P)$	-	S	SO	-	1.66e-11	0.000	0	Singleton and Cvetanović (1988)
HS	H_2CO	-	H_2S	HCO	-	1.70e-11	0.000	800	Harman et al. (2015)
$^1SO_2$	M	-	$^3SO_2$	-	-	1.00e-12	0.000	0	Turco et al. (1982)
$^1SO_2$	M	-	SO_2	-	-	1.00e-11	0.000	0	Turco et al. (1982)
$^1SO_2$	$h\nu$	-	$^3SO_2$	-	-	1.50e+03	0.000	0	Turco et al. (1982)
$^1SO_2$	$h\nu$	-	SO_2	-	-	2.20e+04	0.000	0	Turco et al. (1982)
$^3SO_2$	O_2	-	SO_3	$O(^3P)$	-	1.00e-16	0.000	0	Turco et al. (1982)
$^1SO_2$	O_2	-	SO_3	$O(^3P)$	-	1.00e-16	0.000	0	Toon et al. (1987)
$^1SO_2$	SO_2	-	SO_3	SO	-	4.00e-12	0.000	0	Turco et al. (1982)
$^3SO_2$	M	-	SO_2	-	-	1.50e-13	0.000	0	Turco et al. (1982)
$^3SO_2$	$h\nu$	-	SO_2	-	-	1.13e+03	0.000	0	Turco et al. (1982)

Continued on next page

Table B.2 – continued from previous page

R1	R2	R3	P1	P2	P3	A	α	β (K)	Source
$^3SO_2$	SO_2	-	SO_3	SO	-	7.00e-14	0.000	0	Turco et al. (1982)
SO	NO_2	-	SO_2	NO	-	1.40e-11	0.000	0	Burkholder et al. (2015)
SO	O_3	-	SO_2	O_2	-	3.40e-12	0.000	1100	Burkholder et al. (2015)
HO_2	SO_2	-	SO_3	OH	-	1.00e-18	0.000	0	Burkholder et al. (2015)
HS	O_3	-	HSO	O_2	-	9.00e-12	0.000	280	Burkholder et al. (2019)
HS	NO_2	-	HSO	NO	-	2.90e-11	0.000	-250	Burkholder et al. (2015)
S	O_3	-	SO	O_2	-	1.20e-11	0.000	0	Burkholder et al. (2015)
SO	SO	-	SO_2	S	-	2.00e-15	0.000	0	Chung et al. (1975); Martinez and Herron (1983)
SO_3	SO	-	SO_2	SO_2	-	2.00e-15	0.000	0	Chung et al. (1975)
S	CO_2	-	SO	CO	-	1.00e-20	0.000	0	Yung and Demore (1982)
HCO	SO	-	HSO	CO	-	5.20e-12	0.000	0	Assumed equal to HCO + O_2 → HO_2 + CO
HSO	NO	-	HNO	SO	-	1.00e-15	0.000	0	Burkholder et al. (2019)
HSO	OH	-	H_2O	SO	-	4.80e-11	0.000	-250	Assumed same as OH + HO_2 → H_2O + O_2
HSO	H	-	S	H_2O	-	1.60e-12	0.000	0	Assumed same as H + HO_2 → $O(^3P)$+ H_2O
HSO	H	-	HS	OH	-	7.20e-11	0.000	0	Assumed same as H + HO_2 → OH + OH
HSO	H	-	H_2	SO	-	6.90e-12	0.000	0	Assumed same as H + HO_2 → H_2 + O_2

Continued on next page

Table B.2 – continued from previous page

R1	R2	R3	P1	P2	P3	A	α	β (K)	Source
HSO	HS	-	H_2S	SO	-	3.00e-11	0.000	0	Zahnle et al. (2006)
HSO	$O(^3P)$	-	OH	SO	-	3.00e-11	0.000	-200	Assumed same as $O(^3P)$+ $HO_2 \rightarrow$ OH + O_2
HSO	S	-	HS	SO	-	3.00e-11	0.000	0	Kasting (1990)
H	OCS	-	CO	HS	-	9.07e-12	0.000	1940	Lee et al. (1977)
HS	CO	-	OCS	H	-	4.15e-14	0.000	7660	Kurbanov and Mamedov (1995)
$O(^1D)$	OCS	-	CO	SO	-	3.00e-10	0.000	0	Gauthier and Snelling (1975)
$O(^3P)$	OCS	-	CO	SO	-	2.10e-11	0.000	2200	Burkholder et al. (2015)
$O(^3P)$	OCS	-	S	CO_2	-	8.33e-11	0.000	5530	Singleton and Cvetanović (1988)
OCS	S	-	CO	S_2	-	1.90e-14	3.970	580	Lu et al. (2006)
OH	OCS	-	CO_2	HS	-	7.20e-14	0.000	1070	Burkholder et al. (2015)
HO_2	H_2S	-	H_2O	HSO	-	3.00e-15	0.000	0	Burkholder et al. (2015)
OCS_2	S	-	OCS	S_2	-	5.00e-12	0.000	0	Basco and Pearson (1967)
S_3	$O(^3P)$	-	S_2	SO	-	1.00e-16	0.000	0	Assumed equal to rate for S_2 + $O(^3P)\rightarrow$ S + SO
S_4	$O(^3P)$	-	S_3	SO	-	1.00e-16	0.000	0	Assumed equal to rate for S_2 + $O(^3P)\rightarrow$ S + SO
OCS_2	CO	-	OCS	OCS	-	3.00e-12	0.000	0	Zahnle et al. (2006)
CH_3O_2	NO	-	CH_3O	NO_2	-	2.80e-12	0.000	-300	Burkholder et al. (2015)

Continued on next page

Table B.2 – continued from previous page

R1	R2	R3	P1	P2	P3	A	α	β (K)	Source
NO	CH_3O	-	HNO	H_2CO	-	2.30e-12	-0.700	0	IUPAC
CH_3O	NO_2	-	H_2CO	HNO_2	-	1.10e-11	0.000	1200	Burkholder et al. (2015)
$O(^3P)$	HNO_3	-	OH	NO_3	-	3.00e-17	0.000	0	Burkholder et al. (2015)
$O(^3P)$	N_2O_5	-	NO_2	NO_2	O_2	3.00e-16	0.000	0	Burkholder et al. (2015)
NO_2	NO_3	-	NO	NO_2	O_2	4.35e-14	0.000	1335	Burkholder et al. (2019)
NO_2	O_3	-	NO_3	O_2	-	1.20e-13	0.000	2450	Burkholder et al. (2019)
NO_3	NO_3	-	NO_2	NO_2	O_2	8.50e-13	0.000	2450	Burkholder et al. (2019)
$O(^3P)$	HO_2NO_2	-	OH	NO_2	O_2	7.80e-11	0.000	3400	Burkholder et al. (2015)
OH	HO_2NO_2	-	H_2O	NO_2	O_2	4.50e-13	0.000	-610	Burkholder et al. (2019)
$O(^3P)$	NO_3	-	O_2	NO_2	-	1.30e-11	0.000	0	Burkholder et al. (2019)
HO_2	NO_3	-	OH	NO_2	O_2	3.50e-12	0.000	0	Burkholder et al. (2019)
NO	NO_3	-	NO_2	NO_2	-	1.70e-11	0.000	-125	Burkholder et al. (2019)
OH	NO_3	-	HO_2	NO_2	-	2.00e-11	0.000	0	Burkholder et al. (2019)
N	NO_2	-	N_2O	$O(^3P)$	-	5.80e-12	0.000	-220	Burkholder et al. (2019)
$O(^1D)$	N_2O	-	N_2	O_2	-	4.64e-11	0.000	-20	Burkholder et al. (2019)
$O(^1D)$	N_2O	-	NO	NO	-	7.26e-11	0.000	-20	Burkholder et al. (2019)

Continued on next page

Table B.2 – continued from previous page

R1	R2	R3	P1	P2	P3	A	α	β (K)	Source
CS	O_2	-	OCS	$O(^3P)$	-	2.75e-19	0.000	0	Burkholder et al. (2015)
CS	O_2	-	CO	SO	-	1.45e-20	0.000	0	Burkholder et al. (2015)
CS	O_3	-	OCS	O_2	-	3.00e-16	0.000	0	Burkholder et al. (2015)
CS_2	$O(^3P)$	-	CS	SO	-	2.88e-11	0.000	650	Burkholder et al. (2015)
CS_2	$O(^3P)$	-	CO	S_2	-	6.60e-13	0.000	650	Burkholder et al. (2015)
CS_2	$O(^3P)$	-	OCS	S	-	2.64e-12	0.000	650	Burkholder et al. (2015)
OH	CS_2	-	HS	OCS	-	2.00e-15	0.000	0	Burkholder et al. (2015)
CS_2^*	M	-	CS_2	M	-	2.50e-11	0.000	0	Wine et al. (1981); Toon et al. (1987)
CS_2^*	O_2	-	CS	SO_2	-	1.00e-12	0.000	0	Wine et al. (1981); Toon et al. (1987)
CS_2^*	CS_2	-	CS	CS	S_2	1.00e-12	0.000	0	Domagal-Goldman et al. (2011)
CS_2	SO	-	OCS	S_2	-	1.60e-13	0.000	2280	Assumed same as SO + O_2
$O(^3P)$	CS	-	CO	S	-	2.70e-10	0.000	760	Burkholder et al. (2015)
H	HCS	-	H_2	CS	-	1.83e-10	0.000	0	Assumed same as H + HCO → H_2 + CO
S	HCS	-	H	CS_2	-	5.00e-11	0.000	0	Assumed same as $O(^3P)$+ HCO → H + O_2
S	HCS	-	HS	CS	-	5.00e-11	0.000	0	Assumed same as $O(^3P)$+ HCO → OH + CO
$^1CH_2$	S_2	-	H	CS	HS	2.05e-11	0.000	750	Assumed same as $^1CH_2$ + O_2 → H + CO + OH

Continued on next page

Table B.2 – continued from previous page

R1	R2	R3	P1	P2	P3	A	α	β (K)	Source
$^1CH_2$	S_2	-	H_2	CS_2	-	2.05e-11	0.000	750	Assumed same as $^1CH_2 + O_2 \rightarrow H_2 + CO_2$
$^3CH_2$	S_2	-	HCS	HS	-	4.10e-11	0.000	750	Assumed same as $^3CH_2 + O_2 \rightarrow HCO + OH$
CH_3	HCS	-	CH_4	CS	-	9.30e-11	0.000	0	Assumed same as CH3 + HCO → CH4 + CO
$^3CH_2$	S	-	CS	H_2	-	9.86e-11	0.000	270	Assumed same as $^3CH_2 + O(^3P) \rightarrow$ CO + H2
$^3CH_2$	S	-	H	HCS	-	3.40e-12	0.000	270	Assumed same as $^3CH_2 + O(^3P) \rightarrow$ H + HCO
$^3CH_2$	S	-	CS	H	H	2.38e-10	0.000	270	Assumed same as $^3CH_2 + O(^3P) \rightarrow$ CO + H + H
HS	HCS	-	H_2S	CS	-	5.00e-11	0.000	0	Assumed same as HS + HCO → H_2S + CO
C	HS	-	CS	H	-	2.00e-10	0.000	0	KIDA
C	S_2	-	CS	S	-	4.90e-11	-0.320	0	Assumed same as $C + O_2 \rightarrow CO + O(^3P)$
CH	S	-	CS	H	-	6.60e-11	0.000	0	Assumed same as $CH + O(^3P) \rightarrow$ CO + H
CH	S_2	-	CS	HS	-	8.30e-11	0.000	0	Assumed same as $CH + O_2 \rightarrow CO + OH$
CH	CS_2	-	HCS	CS	-	3.49e-10	0.000	40	Zabarnick et al. (1989)
OCS	CH	-	H	CO	CS	1.99e-10	0.000	-190	Zabarnick et al. (1989)
C_2	S	-	C	CS	-	5.00e-11	0.000	0	Kasting (1990)
C_2	S_2	-	CS	CS	-	1.50e-11	0.000	550	Kasting (1990)
$O(^1D)$	SO_2	-	$O(^3P)$	SO_2	-	5.28e-11	0.000	0	Burkholder et al. (2019)

Continued on next page

Table B.2 – continued from previous page

R1	R2	R3	P1	P2	P3	A	α	β (K)	Source
$O(^1D)$	SO_2	-	SO	O_2	-	1.67e-10	0.000	0	Burkholder et al. (2019)
HS	H_2O_2	-	H_2S	HO_2	-	5.00e-15	0.000	0	Burkholder et al. (2019)
HSO	O_2	-	HS	O_3	-	2.00e-17	0.000	0	Burkholder et al. (2019)
HSO	O_3	-	HS	O_2	O_2	1.00e-13	0.000	0	Burkholder et al. (2019)
CS	NO_2	-	OCS	NO	-	7.60e-17	0.000	0	Burkholder et al. (2015)
N_2O_5	H_2O	-	HNO_3	HNO_3	-	2.00e-21	0.000	0	Burkholder et al. (2019)
SO	HO_2	-	HSO	O_2	-	2.80e-11	0.000	0	Harman et al. (2015)
HSO	NO_2	-	HNO	SO	-	1.00e-15	0.000	0	Harman et al. (2015)

Table B.3: Termolecular reactions used in this network. Reactions sourced from the Kinetic Database for Astrochemistry (KIDA) are from https://kida.astrochem-tools.org/ and those sourced from the International Union of Pure and Applied Chemistry (IUPAC) are obtained from https://iupac-aeris.ipsl.fr/. The horizontal line within the table shows the cutoff for the CHO network described in Chapter 6.

R1	R2	P1	P2	A_1	α_1	β_1 (K)	A_2	α_2	β_2 (K)	F_c	Source
H	O_2	HO_2	-	5.30e-32	-1.800	0	9.50e-11	0.400	0	0.600	Burkholder et al. (2019)
HO_2	HO_2	H_2O_2	O_2	2.10e-33	0.000	-920	1.00e-10	0.000	0	0.600	Burkholder et al. (2019)
O(3P)	O(3P)	O_2	-	9.46e-34	0.000	-485	1.00e-10	0.000	0	0.600	Campbell and Gray (1973)
O(3P)	O_2	O_3	-	6.10e-34	-2.400	0	1.00e-10	0.000	0	0.600	Burkholder et al. (2019)
CO	O(3P)	CO_2	-	6.51e-33	0.000	2188	1.00e-10	0.000	0	0.600	Slanger et al. (1972)
H	CO	HCO	-	5.29e-34	0.000	373	1.00e-10	0.000	0	0.600	KIDA
H	H	H_2	-	8.85e-33	-0.600	0	1.00e-10	0.000	0	0.600	Baulch et al. (1992)
H	OH	H_2O	-	6.78e-31	-2.000	0	1.00e-10	0.000	0	0.600	KIDA
OH	OH	H_2O_2	-	6.90e-31	-1.000	0	2.60e-11	0.000	0	0.600	Burkholder et al. (2019)
CH_3	CH_3	C_2H_6	-	1.13e-25	-3.750	494	7.42e-11	-0.690	88	0.600	KIDA
CH_3	H	CH_4	-	2.63e-28	-2.980	635	3.50e-10	0.000	0	1.000	KIDA
CH_3	O_2	CH_3O_2	-	4.00e-31	-3.600	0	1.20e-12	1.100	0	0.600	Burkholder et al. (2015)
C_2H_5	H	C_2H_6	-	6.11e-28	-2.000	1040	1.66e-10	0.000	0	1.000	KIDA
C	H_2	$^3CH_2$	-	7.00e-32	0.000	0	2.06e-11	0.000	55	1.000	KIDA
CH	H_2	CH_3	-	5.11e-30	-1.600	0	2.00e-10	0.150	0	0.798	Baulch et al. (2005)
$^3CH_2$	H	CH_3	-	3.10e-30	0.000	-457	1.50e-10	0.000	0	0.600	Gladstone et al. (1996)
$^3CH_2$	CO	CH2CO	-	1.00e-28	0.000	0	1.00e-15	0.000	0	0.600	Yung et al. (1984)

Continued on next page

Table B.3 – continued from previous page

R1	R2	P1	P2	A_1	α_1	β_1 (K)	A_2	α_2	β_2 (K)	F_c	Source
CH_3	CO	CH_3CO	-	5.90e-36	0.000	0	1.24e-13	1.050	2850	0.600	Baulch et al. (2005)
C_2H	H	C_2H_2	-	2.64e-26	-3.100	721	3.00e-10	0.000	0	1.000	Tsang and Hampson (1986)
C_2H_2	H	C_2H_3	-	2.60e-31	0.000	0	3.80e-11	0.000	1374	0.600	Kasting (1990)
C_2H_4	H	C_2H_5	-	2.15e-29	0.000	349	4.95e-11	0.000	1051	0.600	Kasting (1990)
OH	C_2H_2	C_2H_2OH	-	5.50e-30	0.000	0	8.30e-13	2.000	0	0.600	Burkholder et al. (2015)
OH	C_2H_4	C_2H_4OH	-	1.10e-28	-3.500	0	8.40e-12	-1.750	0	0.600	Burkholder et al. (2015)
H	NO	HNO	-	1.34e-31	-1.320	370	2.44e-10	-0.410	0	0.600	Tsang and Herron (1991)
N	N	N_2	-	4.10e-34	0.000	0	1.00e-10	0.000	0	0.600	KIDA
O(3P)	NO	NO_2	-	9.10e-32	-1.500	0	3.00e-11	0.000	0	0.600	Burkholder et al. (2019)
OH	NO	HNO_2	-	7.10e-31	-2.600	0	3.60e-11	-0.100	0	0.600	Burkholder et al. (2019)
OH	NO_2	HNO_3	-	1.80e-30	-3.000	0	2.80e-11	0.000	0	0.600	Burkholder et al. (2019)
HNO_3	OH	H_2O	NO_3	6.50e-34	0.000	-1335	2.70e-17	0.000	-2199	1.000	Burkholder et al. (2015)
SO	O(3P)	SO_2	-	5.10e-31	0.000	0	5.31e-11	0.000	0	0.600	Singleton and Cvetanović (1988)
OH	SO_2	HSO3	-	3.30e-31	-4.300	0	1.60e-12	0.000	0	0.600	Burkholder et al. (2015)
O(3P)	SO_2	SO_3	-	1.80e-33	2.000	0	4.20e-14	1.800	0	0.600	Burkholder et al. (2015)
S	S	S_2	-	1.00e-33	0.000	-206	2.26e-14	0.000	-415	0.600	Du et al. (2008); Babikov et al. (2017)
S	S_2	S_3	-	1.65e-33	0.000	-144	1.38e-14	0.000	-450	0.600	Du et al. (2011)
S_2	S_2	S_4	-	2.50e-30	0.000	0	5.00e-11	0.000	0	0.600	Langford and Oldershaw (1972)
S	S_3	S_4	-	1.65e-33	0.000	-144	1.38e-14	0.000	-450	0.600	Assumed equal to S +S_2 → S_3

Continued on next page

Table B.3 – continued from previous page

R1	R2	P1	P2	A_1	α_1	β_1 (K)	A_2	α_2	β_2 (K)	F_c	Source
S_4	S_4	S_8	-	2.50e-30	0.000	0	5.00e-11	0.000	0	0.600	Assumed equal to $S_2 + S_2 \rightarrow S_4$
H	SO	HSO	-	4.40e-32	-1.300	0	7.50e-11	0.200	0	0.600	Assumed equal to $H + O_2 + M \rightarrow HO_2 + M$
CO	S	OCS	-	6.51e-33	0.000	2188	1.00e-10	0.000	0	0.600	Assumed equal to O(3P)+ $CO + M \rightarrow CO_2$
OCS	S	OCS_2	-	9.72e-25	-6.980	6046	3.50e-11	-8.220	4206	0.600	Lu et al. (2006)
NO_2	NO_3	N_2O_5	-	2.40e-30	-3.000	0	1.60e-12	0.100	0	0.600	Burkholder et al. (2019)
N_2O_5	-	NO_3	NO_2	1.30e-03	-3.500	11000	9.70e+14	0.100	11080	0.350	IUPAC
HO_2	NO_2	HO_2NO_2	-	1.90e-31	-3.400	0	4.00e-12	-0.300	0	0.600	Burkholder et al. (2019)
HO_2NO_2	-	HO_2	NO_2	4.10e-05	0.000	10650	6.00e+15	0.000	11170	0.400	IUPAC
O(3P)	NO_2	NO_3	-	3.40e-31	-1.600	0	2.30e-11	-0.200	0	0.600	Burkholder et al. (2019)
O(1D)	N_2	N_2O	-	2.80e-36	-0.900	0	1.00e-10	0.000	0	0.600	Burkholder et al. (2019)
CS2	S	CS	S_2	7.40e-31	0.000	0	2.20e-12	0.000	0	0.600	Gao and Marshall (2011)
H	CS	HCS	-	5.29e-34	0.000	373	1.00e-10	0.000	0	0.600	Assumed same as $H + CO \rightarrow HCO$

Bibliography

Adachi, Hiroyuki, N. Basco, and D. G. L. James. 1981. 'The acetyl radicals CH3 CO· and CD3 CO· studied by flash photolysis and kinetic spectroscopy.' *International Journal of Chemical Kinetics* 13, no. 12 (December): 1251–1276.

Adibekyan, Vardan. 2019. 'Heavy Metal Rules. I. Exoplanet Incidence and Metallicity.' *Geosciences* 9, no. 3 (February): 105.

Agol, Eric, Caroline Dorn, Simon L. Grimm, et al. 2021. 'Refining the Transit-timing and Photometric Analysis of TRAPPIST-1: Masses, Radii, Densities, Dynamics, and Ephemerides.' *The Planetary Science Journal* 2, no. 1 (February): 1.

Ahrer, Eva-Maria, Lili Alderson, Natalie M. Batalha, et al. 2023a. 'Identification of carbon dioxide in an exoplanet atmosphere.' *Nature* 614, no. 7949 (February): 649–652.

Ahrer, Eva-Maria, Kevin B. Stevenson, Megan Mansfield, et al. 2023b. 'Early Release Science of the exoplanet WASP-39b with JWST NIRCam.' *Nature* 614, no. 7949 (February): 653–658.

Alderson, Lili, Hannah R. Wakeford, Munazza K. Alam, et al. 2023. 'Early Release Science of the exoplanet WASP-39b with JWST NIRSpec G395H.' *Nature* 614, no. 7949 (February): 664–669.

Amaral, Laura N. R. do, Rory Barnes, Antígona Segura, and Rodrigo Luger. 2022. 'The Contribution of M-dwarf Flares to the Thermal Escape of Potentially Habitable Planet Atmospheres.' *The Astrophysical Journal* 928, no. 1 (March): 12.

Amundsen, David S, Isabelle Baraffe, Pascal Tremblin, et al. 2014. 'Accuracy tests of radiation schemes used in hot Jupiter global circulation models.' *Astronomy & Astrophysics* 564 (April): A59.

Amundsen, David S, Pascal Tremblin, James Manners, Isabelle Baraffe, and Nathan J Mayne. 2017. 'Treatment of overlapping gaseous absorption with the correlated-k method in hot Jupiter and brown dwarf atmosphere models.' *Astronomy & Astrophysics* 598 (February): A97.

Amundsen, David S., Nathan J. Mayne, Isabelle Baraffe, et al. 2016. 'The UK Met Office global circulation model with a sophisticated radiation scheme applied to the hot Jupiter HD 209458b.' *Astronomy & Astrophysics* 595 (November): A36.

Andreae, Meinrat O. 2007. 'Aerosols Before Pollution.' *Science* 315, no. 5808 (January): 50–51.

Andrews, Martin B., Jeff K. Ridley, Richard A. Wood, et al. 2020. 'Historical Simulations With HadGEM3-GC3.1 for CMIP6.' *Journal of Advances in Modeling Earth Systems* 12, no. 6 (June).

Anglada-Escudé, G, P J Amado, J Barnes, et al. 2016. 'A terrestrial planet candidate in a temperate orbit around Proxima Centauri.' *Nature* 536 (7617): 437–440.

Armstrong, Katherine, Daniel J. Frost, Catherine A. McCammon, David C. Rubie, and Tiziana Boffa Ballaran. 2019. 'Deep magma ocean formation set the oxidation state of Earth's mantle.' *Science* 365, no. 6456 (August): 903–906.

Arndt, N. 1999. 'Why was flood volcanism on submerged continental platforms so common in the Precambrian?' *Precambrian Research* 97, nos. 3-4 (September): 155–164.

Arney, Giada, Shawn D. Domagal-Goldman, Victoria S. Meadows, et al. 2016. 'The Pale Orange Dot: The Spectrum and Habitability of Hazy Archean Earth.' *Astrobiology* 16, no. 11 (November): 873–899.

Arney, Giada N., Victoria S. Meadows, Shawn D. Domagal-Goldman, et al. 2017. 'Pale Orange Dots: The Impact of Organic Haze on the Habitability and Detectability of Earthlike Exoplanets.' *The Astrophysical Journal* 836, no. 1 (February): 49.

Arthur, Michael A., Walter E. Dean, Eric D. Neff, et al. 1994. 'Varve calibrated records of carbonate and organic carbon accumulation over the last 2000 years in the Black Sea.' *Global Biogeochemical Cycles* 8, no. 2 (June): 195–217.

Atkinson, R., D. L. Baulch, R. A. Cox, et al. 2004. 'Evaluated kinetic and photochemical data for atmospheric chemistry: Volume I - gas phase reactions of Ox, HOx, NOx and SOx species.' *Atmospheric Chemistry and Physics* 4, no. 6 (September): 1461–1738.

Aulbach, Sonja, and Vincenzo Stagno. 2016. 'Evidence for a reducing Archean ambient mantle and its effects on the carbon cycle.' *Geology* 44, no. 9 (September): 751–754.

Babikov, Dmitri, Alexander Semenov, and Alexander Teplukhin. 2017. 'One possible source of mass-independent fractionation of sulfur isotopes in the Archean atmosphere of Earth.' *Geochimica et Cosmochimica Acta* 204 (May): 388–406.

Baggott, J. E., H. M. Frey, P. D. Lightfoot, and R. Walsh. 1987. 'Reactions of the formyl radical with alkyl radicals.' *The Journal of Physical Chemistry* 91, no. 12 (June): 3386–3393.

Bahcall, John N., M. H. Pinsonneault, and Sarbani Basu. 2001. 'Solar Models: Current Epoch and Time Dependences, Neutrinos, and Helioseismological Properties.' *The Astrophysical Journal* 555, no. 2 (July): 990–1012.

Barley, M. E., A. L. Pickard, and P. J. Sylvester. 1997. 'Emplacement of a large igneous province as a possible cause of banded iron formation 2.45 billion years ago.' *Nature* 385, no. 6611 (January): 55–58.

Bartlett, Benjamin C, and David J Stevenson. 2016. 'Analysis of a Precambrian resonance-stabilized day length.' *Geophysical Research Letters* 43 (11): 5716–5724.

Basco, N., and A. E. Pearson. 1967. 'Reactions of sulphur atoms in presence of carbon disulphide, carbonyl sulphide and nitric oxide.' *Transactions of the Faraday Society* 63:2684.

Battistuzzi, Fabia U, Andreia Feijao, and S Blair Hedges. 2004. 'A genomic timescale of prokaryote evolution: insights into the origin of methanogenesis, phototrophy, and the colonization of land.' *BMC Evolutionary Biology* 4 (1): 44.

Baulch, D. L., C. T. Bowman, C. J. Cobos, et al. 2005. 'Evaluated Kinetic Data for Combustion Modeling: Supplement II.' *Journal of Physical and Chemical Reference Data* 34, no. 3 (September): 757–1397.

Baulch, D. L., C. J. Cobos, R. A. Cox, et al. 1992. 'Evaluated Kinetic Data for Combustion Modelling.' *Journal of Physical and Chemical Reference Data* 21, no. 3 (May): 411.

Baulch, D. L., C. J. Cobos, R. A. Cox, et al. 1994. 'Evaluated Kinetic Data for Combustion Modeling. Supplement I.' *Journal of Physical and Chemical Reference Data* 23, no. 6 (November): 847–848.

Berner, R. A. 1982. 'Burial of organic carbon and pyrite sulfur in the modern ocean; its geochemical and environmental significance.' *American Journal of Science* 282, no. 4 (April): 451–473.

Bochanski, John J., Suzanne L. Hawley, Kevin R. Covey, et al. 2010. 'THE LUMINOSITY AND MASS FUNCTIONS OF LOW-MASS STARS IN THE GALACTIC DISK. II. THE FIELD.' *The Astronomical Journal* 139, no. 6 (June): 2679–2699.

Bolcar, Matthew R., Jason E. Hylan, Julie A. Crooke, et al. 2018. 'The large UV/optical/infrared surveyor (LUVOIR): decadal mission study update.' In *Space Telescopes and Instrumentation 2018: Optical, Infrared, and Millimeter Wave*, edited by Howard A. MacEwen, Makenzie Lystrup, Giovanni G. Fazio, et al., 23. SPIE, July.

Bolmont, E., F. Selsis, J. E. Owen, et al. 2017. 'Water loss from terrestrial planets orbiting ultracool dwarfs: implications for the planets of TRAPPIST-1.' *Monthly Notices of the Royal Astronomical Society* 464, no. 3 (January): 3728–3741.

Bosak, Tanja, Biqing Liang, Min Sub Sim, and Alexander P. Petroff. 2009. 'Morphological record of oxygenic photosynthesis in conical stromatolites.' *Proceedings of the National Academy of Sciences* 106, no. 27 (July): 10939–10943.

Boutle, I. A., J. E. J. Eyre, and A. P. Lock. 2014. 'Seamless Stratocumulus Simulation across the Turbulent Gray Zone.' *Monthly Weather Review* 142, no. 4 (April): 1655–1668.

Boutle, I. A., N. J. Mayne, B Drummond, et al. 2017. 'Exploring the climate of Proxima B with the Met Office Unified Model.' *Astronomy & Astrophysics* 601 (May): A120.

Boutle, Ian A., Manoj Joshi, F. Hugo Lambert, et al. 2020. 'Mineral dust increases the habitability of terrestrial planets but confounds biomarker detection.' *Nature Communications* 11, no. 1 (June): 2731.

Braam, Marrick, Paul I Palmer, Leen Decin, et al. 2022. 'Lightning-induced chemistry on tidally-locked Earth-like exoplanets.' *Monthly Notices of the Royal Astronomical Society* 517, no. 2 (October): 2383–2402.

Brady, Patrick V., and Sigurdur R. Gíslason. 1997. 'Seafloor weathering controls on atmospheric CO2 and global climate.' *Geochimica et Cosmochimica Acta* 61, no. 5 (March): 965–973.

Bréon, Francois-Marie, Didier Tanré, and Sylvia Generoso. 2002. 'Aerosol Effect on Cloud Droplet Size Monitored from Satellite.' *Science* 295, no. 5556 (February): 834–838.

Brown, A. R., R. J. Beare, J. M. Edwards, et al. 2008. 'Upgrades to the Boundary-Layer Scheme in the Met Office Numerical Weather Prediction Model.' *Boundary-Layer Meteorology* 128, no. 1 (July): 117–132.

Brown, L R, K Sung, D C Benner, et al. 2013. 'Methane line parameters in the HITRAN2012 database.' *Journal of Quantitative Spectroscopy and Radiative Transfer* 130:201–219.

Brune, W. H., James J. Schwab, and J. G. Anderson. 1983. 'Laser magnetic resonance, resonance fluorescence, resonance absorption studies of the reaction kinetics of atomic oxygen + hydroxyl .fwdarw. atomic hydrogen + molecular oxygen, atomic oxygen + perhydroxyl .fwdarw. hydroxyl + molecular oxygen, atomic nitrogen + hydroxyl .fwdarw. atomic hydrogen + nitric oxide, atomic nitrogen + perhydroxyl .fwdarw. products at 300 K between 1 and 5 torr.' *The Journal of Physical Chemistry* 87, no. 22 (October): 4503–4514.

Burkholder, J. B., S. P. Sander, J. Abbatt, et al. 2015. *"Chemical Kinetics and Photochemical Data for Use in Atmospheric Studies, Evaluation No. 18," JPL Publication 15-10.* Technical report. Pasadena: Jet Propulsion Laboratory.

Burkholder, J. B., S. P. Sander, J. Abbatt, et al. 2019. *Chemical Kinetics and Photochemical Data for Use in Atmospheric Studies, Evaluation No. 19.* Technical report. Pasadena: Jet Propulsion Laboratory.

Byrne, B, and C Goldblatt. 2014. 'Radiative forcings for 28 potential Archean greenhouse gases.' *Climate of the Past* 10 (5): 1779–1801.

———. 2015. 'Diminished greenhouse warming from Archean methane due to solar absorption lines.' *Climate of the Past* 11 (3): 559–570.

Byrom, R E, and K P Shine. 2022. 'Methane's Solar Radiative Forcing.' *Geophysical Research Letters* n/a (n/a): e2022GL098270.

Campbell, I.M., and C.N. Gray. 1973. 'Rate constants for O(3P) recombination and association with N(4S).' *Chemical Physics Letters* 18, no. 4 (February): 607–609.

Canosa-mas, C. E., H. M. Frey, and R. Walsh. 1984. 'Studies of methylene chemistry by pulsed laser-induced decomposition of ketene. Part 1.—Ketene in the presence of noble gases.' *J. Chem. Soc., Faraday Trans. 2* 80 (5): 561–578.

Cardona, Tanai. 2019. 'Thinking twice about the evolution of photosynthesis.' *Open Biology* 9, no. 3 (March).

Catling, David C., and James F. Kasting. 2017. *Atmospheric Evolution on Inhabited and Lifeless Worlds.* Cambridge University Press, January.

Catling, David C., Joshua Krissansen-Totton, Nancy Y. Kiang, et al. 2018. 'Exoplanet Biosignatures: A Framework for Their Assessment.' *Astrobiology* 18, no. 6 (June): 709–738.

Catling, David C., and Kevin J. Zahnle. 2009. 'The Planetary Air Leak.' *Scientific American* 300, no. 5 (May): 36–43.

———. 2020. 'The Archean atmosphere.' *Science Advances* 6, no. 9 (February).

Cawood, P A, C J Hawkesworth, and B Dhuime. 2013. 'The continental record and the generation of continental crust.' *GSA Bulletin* 125, nos. 1-2 (April): 14–32.

Charnay, B, F Forget, R Wordsworth, et al. 2013. 'Exploring the faint young Sun problem and the possible climates of the Archean Earth with a 3-D GCM.' *Journal of Geophysical Research: Atmospheres* 118 (18): 410–414.

Charnay, Benjamin, Guillaume Le Hir, Frédéric Fluteau, François Forget, and David C Catling. 2017. 'A warm or a cold early Earth? New insights from a 3-D climate-carbon model.' *Earth and Planetary Science Letters* 474:97–109.

Charnay, Benjamin, Eric T Wolf, Bernard Marty, and François Forget. 2020. 'Is the Faint Young Sun Problem for Earth Solved?' *Space Science Reviews* 216 (5): 90.

Checlair, Jade, Kristen Menou, and Dorian S. Abbot. 2017. 'No Snowball on Habitable Tidally Locked Planets.' *The Astrophysical Journal* 845, no. 2 (August): 132.

Checlair, Jade H., Stephanie L. Olson, Malte F. Jansen, and Dorian S. Abbot. 2019. 'No Snowball on Habitable Tidally Locked Planets with a Dynamic Ocean.' *The Astrophysical Journal* 884, no. 2 (October): L46.

Chen, Howard, Eric T. Wolf, Zhuchang Zhan, and Daniel E. Horton. 2019. 'Habitability and Spectroscopic Observability of Warm M-dwarf Exoplanets Evaluated with a 3D Chemistry-Climate Model.' *The Astrophysical Journal* 886, no. 1 (November): 16.

Chen, Howard, Zhuchang Zhan, Allison Youngblood, et al. 2020. 'Persistence of flare-driven atmospheric chemistry on rocky habitable zone worlds.' *Nature Astronomy* 5, no. 3 (December): 298–310.

Choi, Y. M., and M. C. Lin. 2005. 'Kinetics and mechanisms for reactions of HNO with CH3 and C6H5 studied by quantum-chemical and statistical-theory calculations.' *International Journal of Chemical Kinetics* 37, no. 5 (May): 261–274.

Chung, Kuenja, Jack G. Calvert, and Jan W. Bottenheim. 1975. 'The photochemistry of sulfur dioxide excited within its first allowed band (3130A) and the "forbidden" band (3700-4000A).' *International Journal of Chemical Kinetics* 7, no. 2 (March): 161–182.

Claire, M. W., D. C. Catling, and K. J. Zahnle. 2006. 'Biogeochemical modelling of the rise in atmospheric oxygen.' *Geobiology* 4, no. 4 (December): 239–269.

Claire, Mark W., James F. Kasting, Shawn D. Domagal-Goldman, et al. 2014. 'Modeling the signature of sulfur mass-independent fractionation produced in the Archean atmosphere.' *Geochimica et Cosmochimica Acta* 141 (September): 365–380.

Claire, Mark W., John Sheets, Martin Cohen, et al. 2012. 'THE EVOLUTION OF SOLAR FLUX FROM 0.1 nm TO 160 μm: QUANTITATIVE ESTIMATES FOR PLANETARY STUDIES.' *The Astrophysical Journal* 757, no. 1 (September): 95.

Collins, William D, Daniel R Feldman, Chaincy Kuo, and Newton H Nguyen. 2018. 'Large regional shortwave forcing by anthropogenic methane informed by Jovian observations.' *Science Advances* 4 (9): eaas9593.

Coogan, Laurence A., and Stan E. Dosso. 2015. 'Alteration of ocean crust provides a strong temperature dependent feedback on the geological carbon cycle and is a primary driver of the Sr-isotopic composition of seawater.' *Earth and Planetary Science Letters* 415 (April): 38–46.

Coogan, Laurence A., and Kathryn M. Gillis. 2013. 'Evidence that low-temperature oceanic hydrothermal systems play an important role in the silicate-carbonate weathering cycle and long-term climate regulation.' *Geochemistry, Geophysics, Geosystems* 14, no. 6 (June): 1771–1786.

Cooke, G. J., D. R. Marsh, C. Walsh, B. Black, and J.-F. Lamarque. 2022. 'A revised lower estimate of ozone columns during Earth's oxygenated history.' *Royal Society Open Science* 9, no. 1 (January).

Daines, Stuart J., and Timothy M. Lenton. 2016. 'The effect of widespread early aerobic marine ecosystems on methane cycling and the Great Oxidation.' *Earth and Planetary Science Letters* 434 (January): 42–51.

Daines, Stuart J., Benjamin J. W. Mills, and Timothy M. Lenton. 2017. 'Atmospheric oxygen regulation at low Proterozoic levels by incomplete oxidative weathering of sedimentary organic carbon.' *Nature Communications* 8, no. 1 (February): 14379.

Dammeier, J., M. Colberg, and G. Friedrichs. 2007. 'Wide temperature range (T = 295 K and 770–1305 K) study of the kinetics of the reactions HCO + NO and HCO + NO2 using frequency modulation spectroscopy.' *Physical Chemistry Chemical Physics* 9 (31): 4177.

Davidson, J. A., H. I. Schiff, Terry J. Brown, and Carleton J. Howard. 1978. 'Temperature dependence of the deactivation of O(1D) by CO from 113–333 K.' *The Journal of Chemical Physics* 69, no. 3 (August): 1216–1217.

Davies, Hannah S., João C. Duarte, and Mattias Green. 2023. 'Hadean and Archean (4600–2500 Ma).' In *A Journey Through Tides*, 133–141. Elsevier.

Debras, F, N Mayne, I Baraffe, T Goffrey, and J Thuburn. 2019. 'Eigenvectors, Circulation, and Linear Instabilities for Planetary Science in 3 Dimensions (ECLIPS3D).' *Astronomy & Astrophysics* 631 (November): A36.

Debras, F, N Mayne, I Baraffe, et al. 2020. 'Acceleration of superrotation in simulated hot Jupiter atmospheres.' *Astronomy & Astrophysics* 633 (January): A2.

Del Genio, A D, M J Way, D S Amundsen, et al. 2019. 'Habitable Climate Scenarios for Proxima Centauri b with a Dynamic Ocean.' *Astrobiology* 19 (1): 99–125.

Devriendt, Katia, and Jozef Peeters. 1997. 'Direct Identification of the C2H(X2Σ+) + O(3P) → CH(A2Δ) + CO Reaction as the Source of the CH(A2Δ→X 2Π) Chemiluminescence in C2H2/O/H Atomic Flames.' *The Journal of Physical Chemistry A* 101, no. 14 (April): 2546–2551.

Dillon, Terry J., Abraham Horowitz, and John N. Crowley. 2007. 'Absolute rate coefficients for the reactions of O(1D) with a series of n-alkanes.' *Chemical Physics Letters* 443, nos. 1-3 (July): 12–16.

Ding, Feng, and Robin D. Wordsworth. 2020. 'Stabilization of Dayside Surface Liquid Water via Tropopause Cold Trapping on Arid Slowly Rotating Tidally Locked Planets.' *The Astrophysical Journal* 891, no. 1 (March): L18.

Domagal-Goldman, Shawn D, James F Kasting, David T Johnston, and James Farquhar. 2008. 'Organic haze, glaciations and multiple sulfur isotopes in the Mid-Archean Era.' *Earth and Planetary Science Letters* 269 (1): 29–40.

Domagal-Goldman, Shawn D., Victoria S. Meadows, Mark W. Claire, and James F. Kasting. 2011. 'Using Biogenic Sulfur Gases as Remotely Detectable Biosignatures on Anoxic Planets.' *Astrobiology* 11, no. 5 (June): 419–441.

Domagal-Goldman, Shawn D., Antígona Segura, Mark W. Claire, Tyler D. Robinson, and Victoria S. Meadows. 2014. 'ABIOTIC OZONE AND OXYGEN IN ATMOSPHERES SIMILAR TO PREBIOTIC EARTH.' *The Astrophysical Journal* 792, no. 2 (August): 90.

Dong, Chuanfei, Meng Jin, Manasvi Lingam, et al. 2018. 'Atmospheric escape from the TRAPPIST-1 planets and implications for habitability.' *Proceedings of the National Academy of Sciences* 115, no. 2 (January): 260–265.

Dong, Junjie, Rebecca A Fischer, Lars P Stixrude, and Carolina R Lithgow-Bertelloni. 2021. 'Constraining the Volume of Earth's Early Oceans With a Temperature-Dependent Mantle Water Storage Capacity Model.' *AGU Advances* 2 (1): e2020AV000323.

Donohoe, Aaron, and David S. Battisti. 2011. 'Atmospheric and Surface Contributions to Planetary Albedo.' *Journal of Climate* 24, no. 16 (August): 4402–4418.

Driese, Steven G, Mark A Jirsa, Minghua Ren, et al. 2011. 'Neoarchean paleoweathering of tonalite and metabasalt: Implications for reconstructions of 2.69Ga early terrestrial ecosystems and paleoatmospheric chemistry' [in English (US)]. *Precambrian Research* 189, nos. 1-2 (August): 1–17.

Drummond, B, N. J. Mayne, I Baraffe, et al. 2018a. 'The effect of metallicity on the atmospheres of exoplanets with fully coupled 3D hydrodynamics, equilibrium chemistry, and radiative transfer.' *Astronomy & Astrophysics* 612 (May): A105.

Drummond, B, N. J. Mayne, J Manners, et al. 2018b. 'Observable Signatures of Wind-driven Chemistry with a Fully Consistent Three-dimensional Radiative Hydrodynamics Model of HD 209458b.' *Astrophysical Journal* 855 (March): L31.

Drummond, B., P. Tremblin, I. Baraffe, et al. 2016. 'The effects of consistent chemical kinetics calculations on the pressure-temperature profiles and emission spectra of hot Jupiters.' *Astronomy & Astrophysics* 594 (October): A69.

Drummond, Benjamin, Eric Hébrard, Nathan J. Mayne, et al. 2020. 'Implications of three-dimensional chemical transport in hot Jupiter atmospheres: Results from a consistently coupled chemistry-radiation-hydrodynamics model.' *Astronomy & Astrophysics* 636:A68.

Drummond, Benjamin, Nathan J Mayne, James Manners, et al. 2018c. 'The 3D Thermal, Dynamical, and Chemical Structure of the Atmosphere of HD 189733b: Implications of Wind-driven Chemistry for the Emission Phase Curve.' *Astrophysical Journal* 869, no. 1 (December): 28.

Du, Shiyu, Joseph S. Francisco, Benjamin C. Shepler, and Kirk A. Peterson. 2008. 'Determination of the rate constant for sulfur recombination by quasiclassical trajectory calculations.' *The Journal of Chemical Physics* 128, no. 20 (May).

Du, Shiyu, Timothy C. Germann, Joseph S. Francisco, et al. 2011. 'The kinetics study of the S + S2 $\rightarrow$ S3 reaction by the chaperone mechanism.' *The Journal of Chemical Physics* 134, no. 15 (April).

Eager-Nash, Jake K., David J. Reichelt, Nathan J. Mayne, et al. 2020. 'Implications of different stellar spectra for the climate of tidally locked Earth-like exoplanets.' *Astronomy & Astrophysics* 639 (July): A99.

Eager-Nash, J. K., N. J. Mayne, A. E. Nicholson, et al. 2023. '3D Climate Simulations of the Archean Find That Methane has a Strong Cooling Effect at High Concentrations.' *Journal of Geophysical Research: Atmospheres* 128, no. 6 (March).

Edwards, J. M., and A. Slingo. 1996. 'Studies with a flexible new radiation code. I: Choosing a configuration for a large-scale model.' *Quarterly Journal of the Royal Meteorological Society* 122, no. 531 (April): 689–719.

Eickmann, Benjamin, Axel Hofmann, Martin Wille, et al. 2018. 'Isotopic evidence for oxygenated Mesoarchaean shallow oceans.' *Nature Geoscience* 11, no. 2 (February): 133–138.

Eigenbrode, Jennifer L, and Katherine H Freeman. 2006. 'Late Archean rise of aerobic microbial ecosystems.' *Proceedings of the National Academy of Sciences* 103 (43): 15759–15764.

Emerson, Steven, and John Hedges. 2008. *Chemical Oceanography and the Marine Carbon Cycle.* Cambridge University Press, April.

Etminan, M, G Myhre, E J Highwood, and K P Shine. 2016. 'Radiative forcing of carbon dioxide, methane, and nitrous oxide: A significant revision of the methane radiative forcing.' *Geophysical Research Letters* 43 (24): 612–614.

Fardeau, Marie-Laure, and Jean-Pierre Belaich. 1986. 'Energetics of the growth of Methanococcus thermolithotrophicus.' *Archives of Microbiology* 144, no. 4 (May): 381–385.

Farquhar, James, Huiming Bao, and Mark Thiemens. 2000. 'Atmospheric Influence of Earth's Earliest Sulfur Cycle.' *Science* 289, no. 5480 (August): 756–758.

Farquhar, Robert W. 2001. 'Introduction.' *The Journal of the Astronautical Sciences* 49, no. 1 (March): 1–9.

Fauchez, T, M Turbet, E T Wolf, et al. 2020. 'TRAPPIST-1 Habitable Atmosphere Intercomparison (THAI). Motivations and protocol.' *Geosci. Model Dev.* 13:707–716.

Fauchez, Thomas J, Martin Turbet, Geronimo L Villanueva, et al. 2019. 'Impact of Clouds and Hazes on the Simulated JWST Transmission Spectra of Habitable Zone Planets in the TRAPPIST-1 System.' *The Astrophysical Journal* 887, no. 2 (December): 194.

Fauchez, Thomas J., Geronimo L. Villanueva, Denis E. Sergeev, et al. 2022. 'The TRAPPIST-1 Habitable Atmosphere Intercomparison (THAI). III. Simulated Observables—the Return of the Spectrum.' *The Planetary Science Journal* 3, no. 9 (September): 213.

Feinstein, Adina D., Michael Radica, Luis Welbanks, et al. 2023. 'Early Release Science of the exoplanet WASP-39b with JWST NIRISS.' *Nature* 614, no. 7949 (February): 670–675.

Ferry, J. G. 2006. 'The Stepwise Evolution of Early Life Driven by Energy Conservation.' *Molecular Biology and Evolution* 23, no. 6 (March): 1286–1292.

Feulner, Georg. 2012. 'The faint young Sun problem.' *Reviews of Geophysics* 50 (2).

Flament, Nicolas, Nicolas Coltice, and Patrice F Rey. 2008. 'A case for late-Archaean continental emergence from thermal evolution models and hypsometry.' *Earth and Planetary Science Letters* 275 (3): 326–336.

Flannery, D. T., and M. R. Walter. 2012. 'Archean tufted microbial mats and the Great Oxidation Event: new insights into an ancient problem.' *Australian Journal of Earth Sciences* 59, no. 1 (February): 1–11.

Fofonoff, N.P., and R.C. Millard. 1983. 'Algorithms for the computation of fundamental properties of seawater.' Paris.

France, Kevin, Cynthia S. Froning, Jeffrey L. Linsky, et al. 2013. 'THE ULTRAVIOLET RADIATION ENVIRONMENT AROUND M DWARF EXOPLANET HOST STARS.' *The Astrophysical Journal* 763, no. 2 (January): 149.

Frierson, Dargan M. W., Isaac M. Held, and Pablo Zurita-Gotor. 2006. 'A Gray-Radiation Aquaplanet Moist GCM. Part I: Static Stability and Eddy Scale.' *Journal of the Atmospheric Sciences* 63, no. 10 (October): 2548–2566.

Frost, B. Ronald. 1991. 'Chapter 1.INTRODUCTION TO OXYGEN FUGACITY AND ITS PETROLOGIC IMPORTANCE.' In *Oxide Minerals,* 1–10. De Gruyter, December.

Gao, Yide, and Paul Marshall. 2011. 'An experimental and computational study of the reaction of ground-state sulfur atoms with carbon disulfide.' *The Journal of Chemical Physics* 135, no. 14 (October).

Gauthier, Michel J.E., and David R. Snelling. 1975. 'La photolyse de l'ozone a 253.7 nm: Desactivation de O(1D) et de O2(1Σ)par les gaz de l'atmosphere.' *Journal of Photochemistry* 4, nos. 1-2 (January): 27–50.

Gettelman, A., and S. C. Sherwood. 2016. 'Processes Responsible for Cloud Feedback.' *Current Climate Change Reports* 2, no. 4 (December): 179–189.

Gillon, M, A H M J Triaud, B Demory, et al. 2017. 'Seven temperate terrestrial planets around the nearby ultracool dwarf star TRAPPIST-1.' *Nature* 542 (7642): 456–460.

Giorgi, F., and W. L. Chameides. 1985. 'The rainout parameterization in a photochemical model.' *Journal of Geophysical Research: Atmospheres* 90, no. D5 (August): 7872–7880.

Gladstone, G.Randall, Mark Allen, and Y.L. Yung. 1996. 'Hydrocarbon Photochemistry in the Upper Atmosphere of Jupiter.' *Icarus* 119, no. 1 (January): 1–52.

Goldblatt, C., and K. J. Zahnle. 2011. 'Clouds and the Faint Young Sun Paradox.' *Climate of the Past* 7, no. 1 (March): 203–220.

Goldblatt, Colin, Mark W Claire, Timothy M Lenton, et al. 2009. 'Nitrogen-enhanced greenhouse warming on early Earth.' *Nature Geoscience* 2 (12): 891–896.

Goldblatt, Colin, Timothy M Lenton, and Andrew J Watson. 2006. 'Bistability of atmospheric oxygen and the Great Oxidation.' *Nature* 443 (7112): 683–686.

Goldblatt, Colin, Victoria L McDonald, and Kelly E McCusker. 2021. 'Earth's long-term climate stabilized by clouds.' *Nature Geoscience* 14 (3): 143–150.

Gough, D O. 1981. 'Solar interior structure and luminosity variations.' *Solar Physics* 74 (1): 21–34.

Greene, Thomas P., Taylor J. Bell, Elsa Ducrot, et al. 2023. 'Thermal emission from the Earth-sized exoplanet TRAPPIST-1 b using JWST.' *Nature* 618, no. 7963 (June): 39–42.

Gregory, B S, M W Claire, and S Rugheimer. 2021. 'Photochemical modelling of atmospheric oxygen levels confirms two stable states.' *Earth and Planetary Science Letters* 561:116818.

Gregory, B. S. 2020. 'Development of a 1-D oxygen isotope photochemical model and its application to atmospheric O2.' PhD diss., University of St Andrews.

Gregory, D., and P. R. Rowntree. 1990. 'A Mass Flux Convection Scheme with Representation of Cloud Ensemble Characteristics and Stability-Dependent Closure.' *Monthly Weather Review* 118, no. 7 (July): 1483–1506.

Grimm, S L, B Demory, M Gillon, et al. 2018. 'The nature of the TRAPPIST-1 exoplanets.' *A&A* 613:A68.

Guimond, Claire Marie, Lena Noack, Gianluigi Ortenzi, and Frank Sohl. 2021. 'Low volcanic outgassing rates for a stagnant lid Archean earth with graphite-saturated magmas.' *Physics of the Earth and Planetary Interiors* 320 (November): 106788.

Günther, Maximilian N., Zhuchang Zhan, Sara Seager, et al. 2020. 'Stellar Flares from the First TESS Data Release: Exploring a New Sample of M Dwarfs.' *The Astronomical Journal* 159, no. 2 (January): 60.

Hammond, Mark, and Neil T. Lewis. 2021. 'The rotational and divergent components of atmospheric circulation on tidally locked planets.' *Proceedings of the National Academy of Sciences* 118, no. 13 (March).

Haqq-Misra, J, E. T. Wolf, M Joshi, X Zhang, and R. K. Kopparapu. 2018. 'Demarcating Circulation Regimes of Synchronously Rotating Terrestrial Planets within the Habitable Zone.' *The Astrophysical Journal* 852, no. 2 (January): 67.

Haqq-Misra, Jacob D, Shawn D Domagal-Goldman, Patrick J Kasting, and James F Kasting. 2008. 'A Revised, Hazy Methane Greenhouse for the Archean Earth.' *Astrobiology* 8 (6): 1127–1137.

Hargreaves, Robert J, Iouli E Gordon, Michael Rey, et al. 2020. 'An Accurate, Extensive, and Practical Line List of Methane for the HITEMP Database.' *The Astrophysical Journal* 247, no. 2 (April): 55.

Harman, C. E., R. Felton, R. Hu, et al. 2018. 'Abiotic O2 Levels on Planets around F, G, K, and M Stars: Effects of Lightning-produced Catalysts in Eliminating Oxygen False Positives.' *The Astrophysical Journal* 866, no. 1 (October): 56.

Harman, C. E., E. W. Schwieterman, J. C. Schottelkotte, and J. F. Kasting. 2015. 'ABIOTIC O ₂ LEVELS ON PLANETS AROUND F, G, K, AND M STARS: POSSIBLE FALSE POSITIVES FOR LIFE?' *The Astrophysical Journal* 812, no. 2 (October): 137.

Harris, Lyal B, and Jean H Bédard. 2014. 'Crustal Evolution and Deformation in a Non-Plate-Tectonic Archaean Earth: Comparisons with Venus,' 215–291. Springer, Dordrecht.

Harrison, T. Mark. 2009. 'The Hadean Crust: Evidence from >4 Ga Zircons.' *Annual Review of Earth and Planetary Sciences* 37, no. 1 (May): 479–505.

Hassenkam, T, M P Andersson, K N Dalby, D M A Mackenzie, and M T Rosing. 2017. 'Elements of Eoarchean life trapped in mineral inclusions.' *Nature* 548 (7665): 78–81.

Hassinen, Eero, Kaarlo Kalliorinne, and Jouko Koskikallio. 1990. 'Kinetics of reactions between methyl and acetyl radicals in gas phase produced by flash photolysis of acetic anhydride.' *International Journal of Chemical Kinetics* 22, no. 7 (July): 741–745.

Hawkesworth, Chris, Peter A Cawood, and Bruno Dhuime. 2019. 'Rates of generation and growth of the continental crust.' *Geoscience Frontiers* 10 (1): 165–173.

Hawley, Suzanne L., James R. A. Davenport, Adam F. Kowalski, et al. 2014. 'KEPLER FLARES. I. ACTIVE AND INACTIVE M DWARFS.' *The Astrophysical Journal* 797, no. 2 (December): 121.

Hawley, Suzanne L., and Bjorn R. Pettersen. 1991. 'The great flare of 1985 April 12 on AD Leonis.' *The Astrophysical Journal* 378 (September): 725.

Helling, Ch., G Lee, I Dobbs-Dixon, et al. 2016. 'The mineral clouds on HD 209458b and HD 189733b.' *Monthly Notices of the Royal Astronomical Society* 460, no. 1 (July): 855–883.

Herron, John T. 1988. 'Evaluated Chemical Kinetic Data for the Reactions of Atomic Oxygen O(3P) with Saturated Organic Compounds in the Gas Phase.' *Journal of Physical and Chemical Reference Data* 17, no. 3 (July): 967–1026.

Hitchcock, Dian R., and James E. Lovelock. 1967. 'Life detection by atmospheric analysis.' *Icarus* 7, nos. 1-3 (January): 149–159.

Hohmann-Marriott, Martin F., and Robert E. Blankenship. 2011. 'Evolution of Photosynthesis.' *Annual Review of Plant Biology* 62, no. 1 (June): 515–548.

Holland, Heinrich D. 2006. 'The oxygenation of the atmosphere and oceans.' *Philosophical Transactions of the Royal Society B: Biological Sciences* 361, no. 1470 (June): 903–915.

Holland, HEINRICH D. 2020. *The Chemical Evolution of the Atmosphere and Oceans.* Princeton University Press, October.

Homann, Martin, Christoph Heubeck, Alessandro Airo, and Michael M. Tice. 2015. 'Morphological adaptations of 3.22 Ga-old tufted microbial mats to Archean coastal habitats (Moodies Group, Barberton Greenstone Belt, South Africa).' *Precambrian Research* 266 (September): 47–64.

Hopkins, Michelle, T. Mark Harrison, and Craig E. Manning. 2008. 'Low heat flow inferred from 4Gyr zircons suggests Hadean plate boundary interactions.' *Nature* 456, no. 7221 (November): 493–496.

Howard, Ward S, Matt A Tilley, Hank Corbett, et al. 2018. 'The First Naked-eye Superflare Detected from Proxima Centauri.' *Astrophysical Journal* 860, no. 2 (June): L30.

Hu, Renyu, Luke Peterson, and Eric T. Wolf. 2020. 'O2 - and CO-rich Atmospheres for Potentially Habitable Environments on TRAPPIST-1 Planets.' *The Astrophysical Journal* 888, no. 2 (January): 122.

Hu, Renyu, Sara Seager, and William Bains. 2012. 'PHOTOCHEMISTRY IN TERRESTRIAL EXOPLANET ATMOSPHERES. I. PHOTOCHEMISTRY MODEL AND BENCHMARK CASES.' *The Astrophysical Journal* 761, no. 2 (December): 166.

Huang, G., J.K. Eager, N.J. Mayne, et al. 2021. 'CO2 and O2 oxidized 2.7 Ga micrometeorites in two stages suggesting a >32% CO2 atmosphere.' *Precambrian Research* 366 (November): 106423.

Hunter, John D. 2007. 'Matplotlib: A 2D Graphics Environment.' *Computing in Science & Engineering* 9 (3): 90–95.

Ih, Jegug, Eliza M.-R. Kempton, Emily A. Whittaker, and Madeline Lessard. 2023. 'Constraining the Thickness of TRAPPIST-1 b's Atmosphere from Its JWST Secondary Eclipse Observation at 15 μm.' *The Astrophysical Journal Letters* 952, no. 1 (July): L4.

Izon, Gareth, Aubrey L Zerkle, Iadviga Zhelezinskaia, et al. 2015. 'Multiple oscillations in Neoarchaean atmospheric chemistry.' *Earth and Planetary Science Letters* 431:264–273.

Izon, Gareth, Aubrey L. Zerkle, Kenneth H. Williford, et al. 2017. 'Biological regulation of atmospheric chemistry en route to planetary oxygenation.' *Proceedings of the National Academy of Sciences* 114, no. 13 (March).

Jacob, D. J. 1999. *Introduction to Atmospheric Chemistry.* Princeton University Press.

Jaziri, Adam Yassin, Benjamin Charnay, Franck Selsis, Jérémy Leconte, and Franck Lefèvre. 2022. 'Dynamics of the Great Oxidation Event from a 3D photochemical–climate model.' *Climate of the Past* 18, no. 10 (October): 2421–2447.

Ji, A., J. F. Kasting, G. J. Cooke, D. R. Marsh, and K. Tsigaridis. 2023. 'Comparison between ozone column depths and methane lifetimes computed by one- and three-dimensional models at different atmospheric O ₂ levels.' *Royal Society Open Science* 10, no. 5 (May).

Jin, Zhonghai, Thomas P Charlock, William L Smith Jr., and Ken Rutledge. 2004. 'A parameterization of ocean surface albedo.' *Geophysical Research Letters* 31 (22).

Jin, Zhonghai, Yanli Qiao, Yingjian Wang, Yonghua Fang, and Weining Yi. 2011. 'A new parameterization of spectral and broadband ocean surface albedo.' *Opt. Express* 19, no. 27 (December): 26429–26443.

Johnson, Jena E., Aya Gerpheide, Michael P. Lamb, and Woodward W. Fischer. 2014. 'O2 constraints from Paleoproterozoic detrital pyrite and uraninite.' *Geological Society of America Bulletin* 126, nos. 5-6 (May): 813–830.

Joshi, M M, A D Elvidge, R Wordsworth, and D Sergeev. 2020. 'Earth's Polar Night Boundary Layer as an Analog for Dark Side Inversions on Synchronously Rotating Terrestrial Exoplanets.' *Astrophysical Journal* 892, no. 2 (April): L33.

Joshi, M M, and R M Haberle. 2012. 'Suppression of the Water Ice and Snow Albedo Feedback on Planets Orbiting Red Dwarf Stars and the Subsequent Widening of the Habitable Zone.' *Astrobiology* 12 (1): 3–8.

Joshi, M.M., R.M. Haberle, and R.T. Reynolds. 1997. 'Simulations of the Atmospheres of Synchronously Rotating Terrestrial Planets Orbiting M Dwarfs: Conditions for Atmospheric Collapse and the Implications for Habitability.' *Icarus* 129, no. 2 (October): 450–465.

Joy, A. H., and M. L. Humason. 1949. 'Observations of the Faint Dwarf Star L 726-8.' *Publications of the Astronomical Society of the Pacific* 61 (June): 133.

Kanzaki, Yoshiki, and Takashi Murakami. 2015. 'Estimates of atmospheric CO_2 in the Neoarchean-Paleoproterozoic from paleosols.' *Geochimica et Cosmochimica Acta* 159 (June): 190–219.

Karman, Tijs, Iouli E. Gordon, Ad van der Avoird, et al. 2019. 'Update of the HITRAN collision-induced absorption section.' *Icarus* 328 (August): 160–175.

Kaspi, Yohai, and Adam P. Showman. 2015. 'ATMOSPHERIC DYNAMICS OF TERRESTRIAL EXOPLANETS OVER A WIDE RANGE OF ORBITAL AND ATMOSPHERIC PARAMETERS.' *The Astrophysical Journal* 804, no. 1 (May): 60.

Kasting, J F, D P Whitmire, and R T Reynolds. 1993a. 'Habitable Zones around Main Sequence Stars.' 101, no. 1 (January): 108–128.

Kasting, J. F., and T. M. Donahue. 1980. 'The evolution of atmospheric ozone.' *Journal of Geophysical Research* 85 (C6): 3255.

Kasting, James F. 2005. 'Methane and climate during the Precambrian era.' *Precambrian Research* 137 (3): 119–129.

Kasting, James F, and David Catling. 2003. 'Evolution of a Habitable Planet.' *Annual Review of Astronomy and Astrophysics* 41 (1): 429–463.

Kasting, James F, Ravikumar Kopparapu, Ramses M Ramirez, and Chester E Harman. 2014. 'Remote life-detection criteria, habitable zone boundaries, and the frequency of Earth-like planets around M and late K stars.' *Proceedings of the National Academy of Sciences* 111 (35): 12641–12646.

Kasting, James F. 1990. 'Bolide impacts and the oxidation state of carbon in the Earth's early atmosphere.' *Origins of Life and Evolution of the Biosphere* 20, nos. 3-4 (May): 199–231.

———. 2013. 'What caused the rise of atmospheric O2?' *Chemical Geology* 362 (December): 13–25.

Kasting, James F., and Donald E. Canfield. 2012. 'The Global Oxygen Cycle.' In *Fundamentals of Geobiology*, 93–104. Wiley, April.

Kasting, James F., David H. Eggler, and Stuart P. Raeburn. 1993b. 'Mantle Redox Evolution and the Oxidation State of the Archean Atmosphere.' *The Journal of Geology* 101, no. 2 (March): 245–257.

Kasting, James F., Alexander A. Pavlov, and Janet L. Siefert. 2001. 'A Coupled Ecosystem-Climate Model for Predicting the Methane Concentration in the Archean Atmosphere.' *Origins of Life and Evolution of the Biosphere* 31 (3): 271–285.

Kavanagh, Lucas, and Colin Goldblatt. 2015. 'Using raindrops to constrain past atmospheric density.' *Earth and Planetary Science Letters* 413:51–58.

Kharecha, P., J. Kasting, and J. Siefert. 2005. 'A coupled atmosphere-ecosystem model of the early Archean Earth.' *Geobiology* 3, no. 2 (April): 53–76.

Knoll, Andrew H., and Martin A. Nowak. 2017. 'The timetable of evolution.' *Science Advances* 3, no. 5 (May).

Koll, Daniel D. B., and Dorian S. Abbot. 2016. 'TEMPERATURE STRUCTURE AND ATMOSPHERIC CIRCULATION OF DRY TIDALLY LOCKED ROCKY EXOPLANETS.' *The Astrophysical Journal* 825, no. 2 (July): 99.

Komacek, T D, and D S Abbot. 2019. 'The Atmospheric Circulation and Climate of Terrestrial Planets Orbiting Sun-like and M Dwarf Stars over a Broad Range of Planetary Parameters.' *Astrophysical Journal* 871, no. 2 (February): 245.

Komacek, Thaddeus D., Thomas J. Fauchez, Eric T. Wolf, and Dorian S. Abbot. 2020. 'Clouds will Likely Prevent the Detection of Water Vapor in JWST Transmission Spectra of Terrestrial Exoplanets.' *The Astrophysical Journal* 888, no. 2 (January): L20.

Kopp, G, N Krivova, C J Wu, and J Lean. 2016. 'The Impact of the Revised Sunspot Record on Solar Irradiance Reconstructions.' *Solar Physics* 291 (9): 2951–2965.

Kopparapu, Ravi Kumar, Ramses M. Ramirez, James SchottelKotte, et al. 2014. 'HABITABLE ZONES AROUND MAIN-SEQUENCE STARS: DEPENDENCE ON PLANETARY MASS.' *The Astrophysical Journal* 787, no. 2 (May): L29.

Korenaga, Jun. 2013. 'Initiation and Evolution of Plate Tectonics on Earth: Theories and Observations.' *Annual Review of Earth and Planetary Sciences* 41, no. 1 (May): 117–151.

Kozakis, Thea, João M. Mendonça, and Lars A. Buchhave. 2022. 'Is ozone a reliable proxy for molecular oxygen?' *Astronomy & Astrophysics* 665 (September): A156.

Krasnoperov, L.N., E.N. Chesnokov, H. Stark, and A.R. Ravishankara. 2005. 'Elementary reactions of formyl (HCO) radical studied by laser photolysis—transient absorption spectroscopy.' *Proceedings of the Combustion Institute* 30, no. 1 (January): 935–943.

Krasnopolsky, Vladimir A. 2012. 'A photochemical model for the Venus atmosphere at 47–112km.' *Icarus* 218, no. 1 (March): 230–246.

Krissansen-Totton, Joshua, Giada N. Arney, and David C. Catling. 2018a. 'Constraining the climate and ocean pH of the early Earth with a geological carbon cycle model.' *Proceedings of the National Academy of Sciences* 115, no. 16 (April): 4105–4110.

Krissansen-Totton, Joshua, and David C. Catling. 2017. 'Constraining climate sensitivity and continental versus seafloor weathering using an inverse geological carbon cycle model.' *Nature Communications* 8, no. 1 (May): 15423.

Krissansen-Totton, Joshua, Ryan Garland, Patrick Irwin, and David C. Catling. 2018b. 'Detectability of Biosignatures in Anoxic Atmospheres with the James Webb Space Telescope : A TRAPPIST-1e Case Study.' *The Astronomical Journal* 156, no. 3 (August): 114.

Krissansen-Totton, Joshua, Stephanie Olson, and David C. Catling. 2018c. 'Disequilibrium biosignatures over Earth history and implications for detecting exoplanet life.' *Science Advances* 4, no. 1 (January).

Kunze, M, M Godolt, U Langematz, et al. 2014. 'Investigating the early Earth faint young Sun problem with a general circulation model.' *Planetary and Space Science* 98:77–92.

Kurbanov, M A, and Kh F Mamedov. 1995. 'The role of the reaction CO + SH yields COS + H in hydrogen formation in the course of interaction between CO and H2S.' *Kinetics and Catalysis* 36.

Lambert, F Hugo, Mark J Webb, and Manoj M Joshi. 2011. 'The Relationship between Land–Ocean Surface Temperature Contrast and Radiative Forcing.' *Journal of Climate* (Boston MA, USA) 24 (13): 3239–3256.

Langford, R. B., and G. A. Oldershaw. 1972. 'Flash photolysis of H2S.' *Journal of the Chemical Society, Faraday Transactions 1: Physical Chemistry in Condensed Phases* 68 (0): 1550.

Laughlin, Gregory, Peter Bodenheimer, and Fred C. Adams. 1997. 'The End of the Main Sequence.' *The Astrophysical Journal* 482, no. 1 (June): 420–432.

Le Hir, G, Y Teitler, F Fluteau, Y Donnadieu, and P Philippot. 2014. 'The faint young Sun problem revisited with a 3-D climate–carbon model – Part 1.' *Climate of the Past* 10 (2): 697–713.

Lee, J. H., L. J. Stief, and R. B. Timmons. 1977. 'Absolute rate parameters for the reaction of atomic hydrogen with carbonyl sulfide and ethylene episulfide.' *The Journal of Chemical Physics* 67, no. 4 (August): 1705–1709.

Lefèvre, Maxence, Martin Turbet, and Raymond Pierrehumbert. 2021. '3D Convection-resolving Model of Temperate, Tidally Locked Exoplanets.' *The Astrophysical Journal* 913, no. 2 (June): 101.

Lehmer, O. R., D. C. Catling, R. Buick, D. E. Brownlee, and S. Newport. 2020. 'Atmospheric CO2 levels from 2.7 billion years ago inferred from micrometeorite oxidation.' *Science Advances* 6, no. 4 (January).

Lehmer, Owen R., David C. Catling, Mary N. Parenteau, and Tori M. Hoehler. 2018. 'The Productivity of Oxygenic Photosynthesis around Cool, M Dwarf Stars.' *The Astrophysical Journal* 859, no. 2 (June): 171.

Lenardic, A., A. M. Jellinek, B. Foley, C. O'Neill, and W. B. Moore. 2016. 'Climate-tectonic coupling: Variations in the mean, variations about the mean, and variations in mode.' *Journal of Geophysical Research: Planets* 121, no. 10 (October): 1831–1864.

Lenton, Tim, and Andrew Watson. 2011. *Revolutions that made the Earth.* Oxford University Press, January.

Lenton, Timothy M, Stuart J Daines, and Benjamin J W Mills. 2018a. 'COPSE reloaded: An improved model of biogeochemical cycling over Phanerozoic time.' *Earth-Science Reviews* 178:1–28.

Lenton, Timothy M., Stuart J. Daines, James G. Dyke, et al. 2018b. 'Selection for Gaia across Multiple Scales.' *Trends in Ecology & Evolution* 33, no. 8 (August): 633–645.

Lessner, Daniel J., Lingyun Li, Qingbo Li, et al. 2006. 'An unconventional pathway for reduction of CO2 to methane in CO-grown Methanosarcina acetivorans revealed by proteomics.' *Proceedings of the National Academy of Sciences* 103, no. 47 (November): 17921–17926.

Lewis, N. T., F. H. Lambert, I. A. Boutle, et al. 2018. 'The Influence of a Substellar Continent on the Climate of a Tidally Locked Exoplanet.' *Astrophysical Journal* 854 (February): 171.

Lichtin, D.A., M.R. Berman, and M.C. Lin. 1984. 'NH(A3Π → X3Σ) Chemiluminescence from the CH(X2 Π) + NO reaction.' *Chemical Physics Letters* 108, no. 1 (June): 18–24.

Lincowski, A. P., V. S. Meadows, S. Zieba, et al. 2023. 'Potential Atmospheric Compositions of TRAPPIST-1 c constrained by JWST/MIRI Observations at 15 um.' *The Astrophysical Journal Letters.*

Lincowski, Andrew P., Victoria S. Meadows, David Crisp, et al. 2018. 'Evolved Climates and Observational Discriminants for the TRAPPIST-1 Planetary System.' *The Astrophysical Journal* 867, no. 1 (November): 76.

Lines, S, J Manners, N. J. Mayne, et al. 2018a. 'Exonephology: transmission spectra from a 3D simulated cloudy atmosphere of HD 209458b.' *Monthly Notices of the Royal Astronomical Society* 481 (November): 194–205.

Lines, S, N J Mayne, J Manners, et al. 2019. 'Overcast on Osiris: 3D radiative-hydrodynamical simulations of a cloudy hot Jupiter using the parametrized, phase-equilibrium cloud formation code EddySed.' *Monthly Notices of the Royal Astronomical Society* 488, no. 1 (April): 1332–1355.

Lines, S, N. J. Mayne, I. A. Boutle, et al. 2018b. 'Simulating the cloudy atmospheres of HD 209458 b and HD 189733 b with the 3D Met Office Unified Model.' *Astronomy & Astrophysics* 615 (July): A97.

Liss, P. S., and P. G. Slater. 1974. 'Flux of Gases across the Air-Sea Interface.' *Nature* 247, no. 5438 (January): 181–184.

Liu, Jiping, Zhanhai Zhang, Jun Inoue, and Radley M Horton. 2007. 'Evaluation of snow/ice albedo parameterizations and their impacts on sea ice simulations.' *International Journal of Climatology* 27 (1): 81–91.

Lobo, Ana H., Aomawa L. Shields, Igor Z. Palubski, and Eric Wolf. 2023. 'Terminator Habitability: The Case for Limited Water Availability on M-dwarf Planets.' *The Astrophysical Journal* 945, no. 2 (March): 161.

Lock, A. P., A. R. Brown, M. R. Bush, G. M. Martin, and R. N. B. Smith. 2000. 'A New Boundary Layer Mixing Scheme. Part I: Scheme Description and Single-Column Model Tests.' *Monthly Weather Review* 128, no. 9 (September): 3187–3199.

Loison, Jean-Christophe, Philippe Halvick, Astrid Bergeat, Kevin M. Hickson, and Valentine Wakelam. 2012. 'Review of OCS gas-phase reactions in dark cloud chemical models.' *Monthly Notices of the Royal Astronomical Society* 421, no. 2 (April): 1476–1484.

Lopez-Morales, Mercedes, Thayne Currie, Johanna Teske, et al. 2019. 'Detecting Earth-like Biosignatures on Rocky Exoplanets around Nearby Stars with Ground-based Extremely Large Telescopes.' *Bulletin of the AAS* 51, no. 3 (May).

Lourenço, Diogo L., and Antoine B. Rozel. 2023. 'The Past and the Future of Plate Tectonics and Other Tectonic Regimes.' In *Dynamics of Plate Tectonics and Mantle Convection*, 181–196. Elsevier.

Lourenço, Diogo L., Antoine B. Rozel, Maxim D. Ballmer, and Paul J. Tackley. 2020. 'Plutonic-Squishy Lid: A New Global Tectonic Regime Generated by Intrusive Magmatism on Earth-Like Planets.' *Geochemistry, Geophysics, Geosystems* 21, no. 4 (April).

Lu, Chih-Wei, Yu-Jong Wu, Yuan-Pern Lee, R. S. Zhu, and M. C. Lin. 2006. 'Experimental and theoretical investigation of rate coefficients of the reaction S(P3)+OCS in the temperature range of 298–985K.' *The Journal of Chemical Physics* 125, no. 16 (October).

Luger, R., and R. Barnes. 2015. 'Extreme Water Loss and Abiotic O2 Buildup on Planets Throughout the Habitable Zones of M Dwarfs.' *Astrobiology* 15, no. 2 (February): 119–143.

Maas, A. J., E. Ilin, M. Oshagh, et al. 2022. 'Lower-than-expected flare temperatures for TRAPPIST-1.' *Astronomy & Astrophysics* 668 (December): A111.

Madhusudhan, Nikku. 2019. 'Exoplanetary Atmospheres: Key Insights, Challenges, and Prospects.' *Annual Review of Astronomy and Astrophysics* 57, no. 1 (August): 617–663.

Maher, P, and P Earnshaw. 2022. 'The Flexible Modelling Framework for the Met Office Unified Model (Flex-UM, using UM 12.0 release).' *Geoscientific Model Development* 15 (3): 1177–1194.

Manabe, Syukuro, and Robert F. Strickler. 1964. 'Thermal Equilibrium of the Atmosphere with a Convective Adjustment.' *Journal of the Atmospheric Sciences* 21, no. 4 (July): 361–385.

Manabe, Syukuro, and Richard T. Wetherald. 1967. 'Thermal Equilibrium of the Atmosphere with a Given Distribution of Relative Humidity.' *Journal of the Atmospheric Sciences* 24, no. 3 (May): 241–259.

Manners, J., J. M. Edwards, P. Hill, and J.-C. Thelen. 2022. *SOCRATES (Suite Of Community RAdiative Transfer Codes Based on Edwards and Slingo) Technical Guide.*

Marrero, T. R., and E. A. Mason. 1972. 'Gaseous Diffusion Coefficients.' *Journal of Physical and Chemical Reference Data* 1, no. 1 (January): 3–118.

Martinez, Richard I., and John T. Herron. 1983. 'Methyl thiirane: Kinetic gas-phase titration of sulfur atoms in SX OY systems.' *International Journal of Chemical Kinetics* 15, no. 11 (November): 1127–1132.

Mayne, N. J., I Baraffe, D. M. Acreman, et al. 2014a. 'The unified model, a fully-compressible, non-hydrostatic, deep atmosphere global circulation model, applied to hot Jupiters. ENDGame for a HD 209458b test case.' *Astronomy & Astrophysics* 561 (January): A1.

Mayne, N. J., I Baraffe, D. M. Acreman, et al. 2014b. 'Using the UM dynamical cores to reproduce idealised 3-D flows.' *Geoscientific Model Development* 7 (December): 3059–3087.

Mayne, N. J., F Debras, I Baraffe, et al. 2017. 'Results from a set of three-dimensional numerical experiments of a hot Jupiter atmosphere.' *Astronomy & Astrophysics* 604 (August): A79.

Mayne, N. J., B Drummond, F Debras, et al. 2019. 'The Limits of the Primitive Equations of Dynamics for Warm, Slowly Rotating Small Neptunes and Super Earths.' *Astrophysical Journal* 871, no. 1 (January): 56.

Mayor, Michel, and Didier Queloz. 1995. 'A Jupiter-mass companion to a solar-type star.' *Nature* 378, no. 6555 (November): 355–359.

McCollom, Thomas M., and Wolfgang Bach. 2009. 'Thermodynamic constraints on hydrogen generation during serpentinization of ultramafic rocks.' *Geochimica et Cosmochimica Acta* 73, no. 3 (February): 856–875.

Meadows, Victoria S., Giada N. Arney, Edward W. Schwieterman, et al. 2018. 'The Habitability of Proxima Centauri b: Environmental States and Observational Discriminants.' *Astrobiology* 18, no. 2 (February): 133–189.

Merlis, Timothy M, and Tapio Schneider. 2010. 'Atmospheric Dynamics of Earth-Like Tidally Locked Aquaplanets.' *Journal of Advances in Modeling Earth Systems* 2 (4).

Met Office. 2020. *Iris: A Python library for analysing and visualising meteorological and oceanographic data sets.*

Morii, Hiroyuki, Yosuke Koga, and Shiro Nagai. 1987. 'Energetic analysis of the growth of Methanobrevibacter arboriphilus A2 in hydrogen-limited continuous cultures.' *Biotechnology and Bioengineering* 29, no. 3 (February): 310–315.

Nicholas, John E., Christopher A. Amodio, and Michael J. Baker. 1979. 'Kinetics and mechanism of the decomposition of H2S, CH3SH and (CH3)2S in a radio-frequency pulse discharge.' *Journal of the Chemical Society, Faraday Transactions 1: Physical Chemistry in Condensed Phases* 75 (0): 1868.

Nicholson, A E, S J Daines, N J Mayne, et al. 2022. 'Predicting biosignatures for nutrient-limited biospheres.' *Monthly Notices of the Royal Astronomical Society* 517, no. 1 (October): 222–239.

Nicholson, Arwen E, David M Wilkinson, Hywel T P Williams, and Timothy M Lenton. 2018. 'Gaian bottlenecks and planetary habitability maintained by evolving model biospheres: the ExoGaia model.' *Monthly Notices of the Royal Astronomical Society* 477, no. 1 (June): 727–740.

Nicklas, Robert W., Igor S. Puchtel, and Richard D. Ash. 2018. 'Redox state of the Archean mantle: Evidence from V partitioning in 3.5–2.4Ga komatiites.' *Geochimica et Cosmochimica Acta* 222 (February): 447–466.

Nicklas, Robert W., Igor S. Puchtel, Richard D. Ash, et al. 2019. 'Secular mantle oxidation across the Archean-Proterozoic boundary: Evidence from V partitioning in komatiites and picrites.' *Geochimica et Cosmochimica Acta* 250 (April): 49–75.

Niemann, H. B., S. K. Atreya, S. J. Bauer, et al. 2005. 'The abundances of constituents of Titan's atmosphere from the GCMS instrument on the Huygens probe.' *Nature* 438, no. 7069 (December): 779–784.

Och, Lawrence M., and Graham A. Shields-Zhou. 2012. 'The Neoproterozoic oxygenation event: Environmental perturbations and biogeochemical cycling.' *Earth-Science Reviews* 110, nos. 1-4 (January): 26–57.

Ojakangas, R. W., R. Srinivasan, V. S. Hegde, S. M. Chandrakant, and S. V. Srikantia. 2014. 'The Talya Conglomerate: an Archean (2.7 Ga) Glaciomarine Formation, Western Dharwar Craton, Southern India.' *Current Science* 106 (3): 387–396.

Olson, Stephanie, Malte F. Jansen, Dorian S. Abbot, Itay Halevy, and Colin Goldblatt. 2022. 'The Effect of Ocean Salinity on Climate and Its Implications for Earth's Habitability.' *Geophysical Research Letters* 49, no. 10 (May).

Olson, Stephanie L., Edward W. Schwieterman, Christopher T. Reinhard, and Timothy W. Lyons. 2018. 'Earth: Atmospheric Evolution of a Habitable Planet.' In *Handbook of Exoplanets*, 2817–2853. Cham: Springer International Publishing.

Ono, Shuhei. 2017. 'Photochemistry of Sulfur Dioxide and the Origin of Mass-Independent Isotope Fractionation in Earth's Atmosphere.' *Annual Review of Earth and Planetary Sciences* 45, no. 1 (August): 301–329.

Ono, Shuhei, Jennifer L. Eigenbrode, Alexander A. Pavlov, et al. 2003. 'New insights into Archean sulfur cycle from mass-independent sulfur isotope records from the Hamersley Basin, Australia.' *Earth and Planetary Science Letters* 213, nos. 1-2 (August): 15–30.

Ortenzi, G., L. Noack, F. Sohl, et al. 2020. 'Mantle redox state drives outgassing chemistry and atmospheric composition of rocky planets.' *Scientific Reports* 10, no. 1 (July): 10907.

Ozaki, Kazumi, Eiichi Tajika, Peng K. Hong, Yusuke Nakagawa, and Christopher T. Reinhard. 2018. 'Effects of primitive photosynthesis on Earth's early climate system.' *Nature Geoscience* 11, no. 1 (January): 55–59.

Palin, Richard M., and M. Santosh. 2021. 'Plate tectonics: What, where, why, and when?' *Gondwana Research* 100 (December): 3–24.

Pavlov, A.A., and J.F. Kasting. 2002. 'Mass-Independent Fractionation of Sulfur Isotopes in Archean Sediments: Strong Evidence for an Anoxic Archean Atmosphere.' *Astrobiology* 2, no. 1 (March): 27–41.

Payne, Rebecca C., Don Brownlee, and James F. Kasting. 2020. 'Oxidized micrometeorites suggest either high pCO2 or low pN2 during the Neoarchean.' *Proceedings of the National Academy of Sciences* 117, no. 3 (January): 1360–1366.

Peacock, Sarah, Travis Barman, Evgenya L. Shkolnik, Peter H. Hauschildt, and E. Baron. 2019. 'Predicting the Extreme Ultraviolet Radiation Environment of Exoplanets around Low-mass Stars: The TRAPPIST-1 System.' *The Astrophysical Journal* 871, no. 2 (February): 235.

Pecaut, Mark J., and Eric E. Mamajek. 2013. 'INTRINSIC COLORS, TEMPERATURES, AND BOLOMETRIC CORRECTIONS OF PRE-MAIN-SEQUENCE STARS.' *The Astrophysical Journal Supplement Series* 208, no. 1 (September): 9.

Peng, Jingping, Xiaohua Hu, and Paul Marshall. 1999. 'Experimental and ab Initio Investigations of the Kinetics of the Reaction of H Atoms with H2S.' *The Journal of Physical Chemistry A* 103, no. 27 (July): 5307–5311.

Penn, James, and Geoffrey K Vallis. 2018. 'Atmospheric Circulation and Thermal Phase-curve Offset of Tidally and Nontidally Locked Terrestrial Exoplanets.' *Astrophysical Journal* 868, no. 2 (December): 147.

Pierrehumbert, R. T. 2011. 'A PALETTE OF CLIMATES FOR GLIESE 581g.' *The Astrophysical Journal* 726, no. 1 (January): L8.

Pierrehumbert, Raymond T, and Mark Hammond. 2019. 'Atmospheric Circulation of Tide-Locked Exoplanets.' *Annual Review of Fluid Mechanics* 51 (1): 275–303.

Pierrehumbert, Raymond T. 2010. *Principles of Planetary Climate.* Cambridge University Press, December.

Pinto, Joseph P., G. Randall Gladstone, and Yuk Ling Yung. 1980. 'Photochemical Production of Formaldehyde in Earth's Primitive Atmosphere.' *Science* 210, no. 4466 (October): 183–185.

Planavsky, Noah J., Dan Asael, Axel Hofmann, et al. 2014. 'Evidence for oxygenic photosynthesis half a billion years before the Great Oxidation Event.' *Nature Geoscience* 7, no. 4 (April): 283–286.

Polyansky, Oleg L, Aleksandra A Kyuberis, Nikolai F Zobov, et al. 2018. 'ExoMol molecular line lists XXX: a complete high-accuracy line list for water.' *Monthly Notices of the Royal Astronomical Society* 480, no. 2 (April): 2597–2608.

Pope, Emily C., Dennis K. Bird, and Minik T. Rosing. 2012. 'Isotope composition and volume of Earth's early oceans.' *Proceedings of the National Academy of Sciences* 109, no. 12 (March): 4371–4376.

Poulsen, C J, and R L Jacob. 2004. 'Factors that inhibit snowball Earth simulation.' *Paleoceanography* 19 (4).

Quanz, S. P., M. Ottiger, E. Fontanet, et al. 2022. 'Large Interferometer For Exoplanets (LIFE).' *Astronomy & Astrophysics* 664 (August): A21.

Rajpurohit, A. S., C. Reylé, F. Allard, et al. 2013. 'The effective temperature scale of M dwarfs.' *Astronomy & Astrophysics* 556 (August): A15.

Ramirez, Ramses M., and Lisa Kaltenegger. 2014. 'THE HABITABLE ZONES OF PRE-MAIN-SEQUENCE STARS.' *The Astrophysical Journal* 797, no. 2 (December): L25.

Ranjan, S., E. W. Schwieterman, M. Leung, C. E. Harman, and R. Hu. 2023. 'A Re-Appraisal of CO/O2 Runaway on Habitable Planets Orbiting Low-Mass Stars.' *Submitted to AAS Journals.*

Ranjan, Sukrit, Edward W. Schwieterman, Chester Harman, et al. 2020. 'Photochemistry of Anoxic Abiotic Habitable Planet Atmospheres: Impact of New H2O Cross Sections.' *The Astrophysical Journal* 896, no. 2 (June): 148.

Rasmussen, Birger, and Roger Buick. 1999. 'Redox state of the Archean atmosphere: Evidence from detrital heavy minerals in ca. 3250–2750 Ma sandstones from the Pilbara Craton, Australia.' *Geology* 27 (2): 115.

Redfield, A. C. 1934. 'On the Proportions of Organic Derivatives in Sea Water and Their Relation to the Composition of Plankton.' *James Johnstone Memorial Volume,* 176–192.

Rein, Hanno, Yuka Fujii, and David S. Spiegel. 2014. 'Some inconvenient truths about biosignatures involving two chemical species on Earth-like exoplanets.' *Proceedings of the National Academy of Sciences* 111, no. 19 (May): 6871–6875.

Ridgway, R. 2023. 'Simulating the impact of stellar flares on the climate and habitability of terrestrial Earth–like exoplanets.' PhD diss., University of Exeter.

Ridgway, R J, M Zamyatina, N J Mayne, et al. 2022. '3D modelling of the impact of stellar activity on tidally locked terrestrial exoplanets: atmospheric composition and habitability.' *Monthly Notices of the Royal Astronomical Society* 518, no. 2 (November): 2472–2496.

Riding, Robert, Philip Fralick, and Liyuan Liang. 2014. 'Identification of an Archean marine oxygen oasis.' *Precambrian Research* 251 (September): 232–237.

Rimmer, P B, O Shorttle, and S Rugheimer. 2019. 'Oxidised micrometeorites as evidence for low atmospheric pressure on the early Earth.' *Geochemical perspectives letters* 9:38–42.

Rimmer, Paul B., Jianfeng Xu, Samantha J. Thompson, et al. 2018. 'The origin of RNA precursors on exoplanets.' *Science Advances* 4, no. 8 (August).

Roberts, Nick M. W., and Christopher J. Spencer. 2015. 'The zircon archive of continent formation through time.' *Geological Society, London, Special Publications* 389, no. 1 (January): 197–225.

Rose, Brian E J, Timothy W Cronin, and Cecilia M Bitz. 2017. 'Ice Caps and Ice Belts: The Effects of Obliquity on Ice-Albedo Feedback.' *The Astrophysical Journal* 846, no. 1 (August): 28.

Rosing, Minik T. 1999. '13C-Depleted Carbon Microparticles in 3700-Ma Sea-Floor Sedimentary Rocks from West Greenland.' *Science* 283, no. 5402 (January): 674–676.

Rosing, Minik T., Dennis K. Bird, Norman H. Sleep, and Christian J. Bjerrum. 2010. 'No climate paradox under the faint early Sun.' *Nature* 464, no. 7289 (April): 744–747.

Rothman, L S, I E Gordon, Y Babikov, et al. 2013. 'The HITRAN2012 molecular spectroscopic database.' *Journal of Quantitative Spectroscopy and Radiative Transfer* 130:4–50.

Rushby, Andrew J, Aomawa L Shields, and Manoj Joshi. 2019. 'The Effect of Land Fraction and Host Star Spectral Energy Distribution on the Planetary Albedo of Terrestrial Worlds.' *Astrophysical Journal* 887, no. 1 (December): 29.

Rustamkulov, Z., D. K. Sing, S. Mukherjee, et al. 2023. 'Early Release Science of the exoplanet WASP-39b with JWST NIRSpec PRISM.' *Nature* 614, no. 7949 (February): 659–663.

Sagan, Carl, and George Mullen. 1972. 'Earth and Mars: Evolution of Atmospheres and Surface Temperatures.' *Science* 177, no. 4043 (July): 52–56.

Sainsbury-Martinez, F, P Wang, S Fromang, et al. 2019. 'Idealised simulations of the deep atmosphere of hot Jupiters. Deep, hot adiabats as a robust solution to the radius inflation problem.' *Astronomy & Astrophysics* 632 (December): A114.

Sander, S. P., J. Abbatt, J. R. Barker, et al. 2011. *"Chemical Kinetics and Photochemical Data for Use in Atmospheric Studies, Evaluation No. 17," JPL Publication 10-6.* Technical report. Pasadena: Jet Propulsion Laboratory.

Sardeshmukh, Prashant D., and Brian J. Hoskins. 1988. 'The Generation of Global Rotational Flow by Steady Idealized Tropical Divergence.' *Journal of the Atmospheric Sciences* 45, no. 7 (April): 1228–1251.

Sauterey, Boris, Benjamin Charnay, Antonin Affholder, Stéphane Mazevet, and Régis Ferrière. 2020. 'Co-evolution of primitive methane-cycling ecosystems and early Earth's atmosphere and climate.' *Nature Communications* 11, no. 1 (June): 2705.

Schlaufman, K. C., and G. Laughlin. 2010. 'A physically-motivated photometric calibration of M dwarf metallicity.' *Astronomy and Astrophysics* 519 (September): A105.

Schofield, Keith. 1973. 'Evaluated Chemical Kinetic Rate Constants for Various Gas Phase Reactions.' *Journal of Physical and Chemical Reference Data* 2, no. 1 (January): 25–84.

Schonheit, Peter, Johanna Moll, and Rudolf K. Thauer. 1980. 'Growth parameters (K s, ?max, Y s) of Methanobacterium thermoautotrophicum.' *Archives of Microbiology* 127, no. 1 (August): 59–65.

Schopf, J. William, Kouki Kitajima, Michael J. Spicuzza, Anatoliy B. Kudryavtsev, and John W. Valley. 2018. 'SIMS analyses of the oldest known assemblage of microfossils document their taxon-correlated carbon isotope compositions.' *Proceedings of the National Academy of Sciences* 115, no. 1 (January): 53–58.

Schwieterman, Edward W., Nancy Y. Kiang, Mary N. Parenteau, et al. 2018. 'Exoplanet Biosignatures: A Review of Remotely Detectable Signs of Life.' *Astrobiology* 18, no. 6 (June): 663–708.

Schwieterman, Edward W., Christopher T. Reinhard, Stephanie L. Olson, et al. 2019. 'Rethinking CO Antibiosignatures in the Search for Life Beyond the Solar System.' *The Astrophysical Journal* 874, no. 1 (March): 9.

Seager, S., W. Bains, and R. Hu. 2013. 'A BIOMASS-BASED MODEL TO ESTIMATE THE PLAUSIBILITY OF EXOPLANET BIOSIGNATURE GASES.' *The Astrophysical Journal* 775, no. 2 (September): 104.

Seager, S., E.L. Turner, J. Schafer, and E.B. Ford. 2005. 'Vegetation's Red Edge: A Possible Spectroscopic Biosignature of Extraterrestrial Plants.' *Astrobiology* 5, no. 3 (June): 372–390.

Segura, Antígona, James F. Kasting, Victoria Meadows, et al. 2005. 'Biosignatures from Earth-Like Planets Around M Dwarfs.' *Astrobiology* 5, no. 6 (December): 706–725.

Sellar, Alistair A, Colin G Jones, Jane P Mulcahy, et al. 2019. 'UKESM1: Description and Evaluation of the U.K. Earth System Model.' *Journal of Advances in Modeling Earth Systems* 11 (12): 4513–4558.

Sergeev, D. E., and M Zamyatina. 2022. *aeolus.*

Sergeev, Denis E, Thomas J Fauchez, Martin Turbet, et al. 2021. *The TRAPPIST-1 Habitable Atmosphere Intercomparison (THAI). Part II: Moist Cases – The Two Waterworlds.*

Sergeev, Denis E., Thomas J. Fauchez, Martin Turbet, et al. 2022a. 'The TRAPPIST-1 Habitable Atmosphere Intercomparison (THAI). II. Moist Cases—The Two Waterworlds.' *The Planetary Science Journal* 3, no. 9 (September): 212.

Sergeev, Denis E., F. Hugo Lambert, Nathan J. Mayne, et al. 2020. 'Atmospheric Convection Plays a Key Role in the Climate of Tidally Locked Terrestrial Exoplanets: Insights from High-resolution Simulations.' *The Astrophysical Journal* 894, no. 2 (May): 84.

Sergeev, Denis E., Neil T. Lewis, F. Hugo Lambert, et al. 2022b. 'Bistability of the Atmospheric Circulation on TRAPPIST-1e.' *The Planetary Science Journal* 3, no. 9 (September): 214.

Sheldon, Nathan D. 2006. 'Precambrian paleosols and atmospheric CO2 levels.' *Precambrian Research* 147 (1): 148–155.

Shields, Aomawa L, Cecilia M Bitz, and Igor Palubski. 2019. 'Energy Budgets for Terrestrial Extrasolar Planets.' *Astrophysical Journal* 884, no. 1 (October): L2.

Shields, Aomawa L., Sarah Ballard, and John Asher Johnson. 2016. 'The habitability of planets orbiting M-dwarf stars.' *Physics Reports* 663 (December): 1–38.

Shields, Aomawa L., Victoria S. Meadows, Cecilia M. Bitz, et al. 2013. 'The Effect of Host Star Spectral Energy Distribution and Ice-Albedo Feedback on the Climate of Extrasolar Planets.' *Astrobiology* 13, no. 8 (August): 715–739.

Showman, Adam P, Robin D Wordsworth, Timothy M Merlis, Yohai Kaspi, and Renée Dotson. 2013. 'Atmospheric Circulation of Terrestrial Exoplanets.' In *Comparative Climatology of Terrestrial Planets*, edited by Stephen J Mackwell, Amy A Simon-Miller, Jerald W Harder, and Mark A Bullock, 277–326. University of Arizona Press.

Showman, Adam P., Jonathan J. Fortney, Yuan Lian, et al. 2009. 'ATMOSPHERIC CIRCULATION OF HOT JUPITERS: COUPLED RADIATIVE-DYNAMICAL GENERAL CIRCULATION MODEL SIMULATIONS OF HD 189733b and HD 209458b.' *The Astrophysical Journal* 699, no. 1 (July): 564–584.

Showman, Adam P., and Lorenzo M. Polvani. 2010. 'The Matsuno-Gill model and equatorial superrotation.' *Geophysical Research Letters* 37, no. 18 (September): n/a–n/a.

———. 2011. 'EQUATORIAL SUPERROTATION ON TIDALLY LOCKED EXOPLANETS.' *The Astrophysical Journal* 738, no. 1 (September): 71.

Showman, Adam P., Xianyu Tan, and Vivien Parmentier. 2020. 'Atmospheric Dynamics of Hot Giant Planets and Brown Dwarfs.' *Space Science Reviews* 216, no. 8 (December): 139.

Singleton, D. L., and R. J. Cvetanović. 1988. 'Evaluated Chemical Kinetic Data for the Reactions of Atomic Oxygen O(3P) with Sulfur Containing Compounds.' *Journal of Physical and Chemical Reference Data* 17, no. 4 (October): 1377–1437.

Slanger, Tom G., Bernard J. Wood, and Graham Black. 1972. 'Kinetics of O(3P) +CO +M Recombination.' *The Journal of Chemical Physics* 57, no. 1 (July): 233–238.

Sleep, Norman H., and Kevin Zahnle. 2001. 'Carbon dioxide cycling and implications for climate on ancient Earth.' *Journal of Geophysical Research: Planets* 106, no. E1 (January): 1373–1399.

Snyder, W C, Z Wan, Y Zhang, and Y.-Z. Feng. 1998. 'Classification-based emissivity for land surface temperature measurement from space.' *International Journal of Remote Sensing* 19 (14): 2753–2774.

Solomatov, V. S. 1995. 'Scaling of temperature- and stress-dependent viscosity convection.' *Physics of Fluids* 7, no. 2 (February): 266–274.

Som, Sanjoy M, Roger Buick, James W Hagadorn, et al. 2016. 'Earth's air pressure 2.7 billion years ago constrained to less than half of modern levels.' *Nature Geoscience* 9 (6): 448–451.

Som, Sanjoy M, David C Catling, Jelte P Harnmeijer, Peter M Polivka, and Roger Buick. 2012. 'Air density 2.7 billion years ago limited to less than twice modern levels by fossil raindrop imprints.' *Nature* 484 (7394): 359–362.

Stachnik, R. A., and M. J. Molina. 1987. 'Kinetics of the reactions of mercapto radicals with nitrogen dioxide and oxygen.' *The Journal of Physical Chemistry* 91, no. 17 (August): 4603–4606.

Stüeken, Eva E., and Roger Buick. 2018. 'Environmental control on microbial diversification and methane production in the Mesoarchean.' *Precambrian Research* 304 (January): 64–72.

Stüeken, Eva E., Michael A. Kipp, Matthew C. Koehler, and Roger Buick. 2016. 'The evolution of Earth's biogeochemical nitrogen cycle.' *Earth-Science Reviews* 160 (September): 220–239.

Tashkun, S A, and V I Perevalov. 2011. 'CDSD-4000: High-resolution, high-temperature carbon dioxide spectroscopic databank.' *Journal of Quantitative Spectroscopy and Radiative Transfer* 112 (9): 1403–1410.

Teal, D. J., Eliza M.-R. Kempton, Sandra Bastelberger, Allison Youngblood, and Giada Arney. 2022. 'Effects of UV Stellar Spectral Uncertainty on the Chemistry of Terrestrial Atmospheres.' *The Astrophysical Journal* 927, no. 1 (March): 90.

Teitler, Yoram, Guillaume Le Hir, Frédéric Fluteau, Pascal Philippot, and Yannick Donnadieu. 2014. 'Investigating the Paleoproterozoic glaciations with 3-D climate modeling.' *Earth and Planetary Science Letters* 395:71–80.

Tennyson, Jonathan, Sergei N Yurchenko, Ahmed F Al-Refaie, et al. 2016. 'The ExoMol database: Molecular line lists for exoplanet and other hot atmospheres.' *Journal of Molecular Spectroscopy* 327:73–94.

Thiemens, Maxwell M., Peter Sprung, Raúl O. C. Fonseca, Felipe P. Leitzke, and Carsten Münker. 2019. 'Early Moon formation inferred from hafnium–tungsten systematics.' *Nature Geoscience* 12, no. 9 (September): 696–700.

Thiesemann, Holger, John MacNamara, and Craig A. Taatjes. 1997. 'Deuterium Kinetic Isotope Effect and Temperature Dependence in the Reactions of CH[2Π] with Methane and Acetylene.' *The Journal of Physical Chemistry A* 101, no. 10 (March): 1881–1886.

Thompson, Maggie A., Joshua Krissansen-Totton, Nicholas Wogan, Myriam Telus, and Jonathan J. Fortney. 2022. 'The case and context for atmospheric methane as an exoplanet biosignature.' *Proceedings of the National Academy of Sciences* 119, no. 14 (April).

Thomson, Stephen I, and Geoffrey K Vallis. 2019. 'The effects of gravity on the climate and circulation of a terrestrial planet.' *Quarterly Journal of the Royal Meteorological Society* 145 (723): 2627–2640.

Tian, Feng, Kevin France, Jeffrey L. Linsky, Pablo J.D. Mauas, and Mariela C. Vieytes. 2014. 'High stellar FUV/NUV ratio and oxygen contents in the atmospheres of potentially habitable planets.' *Earth and Planetary Science Letters* 385 (January): 22–27.

Tian, Feng, J.F. Kasting, and K. Zahnle. 2011. 'Revisiting HCN formation in Earth's early atmosphere.' *Earth and Planetary Science Letters* 308, nos. 3-4 (August): 417–423.

Tiee, J.J., F.B. Wampler, R.C. Oldenborg, and W.W. Rice. 1981. 'Spectroscopy and reaction kinetics of HS radicals.' *Chemical Physics Letters* 82, no. 1 (August): 80–84.

Tilley, Matt A., Antígona Segura, Victoria Meadows, Suzanne Hawley, and James Davenport. 2019. 'Modeling Repeated M Dwarf Flaring at an Earth-like Planet in the Habitable Zone: Atmospheric Effects for an Unmagnetized Planet.' *Astrobiology* 19, no. 1 (January): 64–86.

Tomkins, Andrew G, Lara Bowlt, Matthew Genge, et al. 2016. 'Ancient micrometeorites suggestive of an oxygen-rich Archaean upper atmosphere.' *Nature* 533 (7602): 235–238.

Toon, Owen B., James F. Kasting, Richard P. Turco, and May S. Liu. 1987. 'The sulfur cycle in the marine atmosphere.' *Journal of Geophysical Research* 92 (D1): 943.

Trail, Dustin, E. Bruce Watson, and Nicholas D. Tailby. 2011. 'The oxidation state of Hadean magmas and implications for early Earth's atmosphere.' *Nature* 480, no. 7375 (December): 79–82.

Trainer, Melissa G, Alexander A Pavlov, H Langley DeWitt, et al. 2006. 'Organic haze on Titan and the early Earth.' *Proceedings of the National Academy of Sciences* 103 (48): 18035–18042.

Tremblin, P, G Chabrier, N. J. Mayne, et al. 2017. 'Advection of Potential Temperature in the Atmosphere of Irradiated Exoplanets: A Robust Mechanism to Explain Radius Inflation.' *Astrophysical Journal* 841, no. 1 (May): 30.

Troe, J. 1983. 'Theory of Thermal Unimolecular Reactions in the Fall-off Range. I. Strong Collision Rate Constants.' *Berichte der Bunsengesellschaft für physikalische Chemie* 87, no. 2 (February): 161–169.

Tsai, Shang-Min, Elspeth K. H. Lee, Diana Powell, et al. 2023. 'Photochemically produced SO2 in the atmosphere of WASP-39b.' *Nature* 617, no. 7961 (May): 483–487.

Tsang, W., and R. F. Hampson. 1986. 'Chemical Kinetic Data Base for Combustion Chemistry. Part I. Methane and Related Compounds.' *Journal of Physical and Chemical Reference Data* 15, no. 3 (July): 1087–1279.

Tsang, Wing, and John T. Herron. 1991. 'Chemical Kinetic Data Base for Propellant Combustion I. Reactions Involving NO, NO2, HNO, HNO2, HCN and N2O.' *Journal of Physical and Chemical Reference Data* 20, no. 4 (July): 609–663.

Turbet, Martin, Emeline Bolmont, Jeremy Leconte, et al. 2018. 'Modeling climate diversity, tidal dynamics and the fate of volatiles on TRAPPIST-1 planets.' *Astronomy & Astrophysics* 612:A86.

Turbet, Martin, Christian Boulet, and Tijs Karman. 2020. 'Measurements and semi-empirical calculations of CO2+CH4 and CO2+H2 collision-induced absorption across a wide range of wavelengths and temperatures. Application for the prediction of early Mars surface temperature.' *Icarus* 346:113762.

Turbet, Martin, Thomas J. Fauchez, Denis E. Sergeev, et al. 2022. 'The TRAPPIST-1 Habitable Atmosphere Intercomparison (THAI). I. Dry Cases—The Fellowship of the GCMs.' *The Planetary Science Journal* 3, no. 9 (September): 211.

Turbet, Martin, Jérémy Leconte, Franck Selsis, et al. 2016. 'The habitability of Proxima Centauri b - II. Possible climates and observability.' *Astronomy & Astrophysics* 596:A112.

Turco, R. P., R. C. Whitten, and O. B. Toon. 1982. 'Stratospheric aerosols: Observation and theory.' *Reviews of Geophysics* 20 (2): 233.

Vecchio, Antonio, Leonardo Primavera, Fabio Lepreti, Tommaso Alberti, and Vincenzo Carbone. 2020. 'Effect of Vegetation on the Temperatures of TRAPPIST-1 Planets.' *The Astrophysical Journal* 891 (1).

Villanueva, G.L., M.D. Smith, S. Protopapa, S. Faggi, and A.M. Mandell. 2018. 'Planetary Spectrum Generator: An accurate online radiative transfer suite for atmospheres, comets, small bodies and exoplanets.' *Journal of Quantitative Spectroscopy and Radiative Transfer* 217 (September): 86–104.

Wahr, J M. 1988. 'The Earth's Rotation.' *Annual Review of Earth and Planetary Sciences* 16, no. 1 (May): 231–249.

Walker, James C G. 1987. 'Was the Archaean biosphere upside down?' *Nature* 329 (6141): 710–712.

Walker, James C. G., P. B. Hays, and J. F. Kasting. 1981. 'A negative feedback mechanism for the long-term stabilization of Earth's surface temperature.' *Journal of Geophysical Research* 86 (C10): 9776.

Walters, D, A J Baran, I Boutle, et al. 2019. 'The Met Office Unified Model Global Atmosphere 7.0/7.1 and JULES Global Land 7.0 configurations.' *Geoscientific Model Development* 12 (5): 1909–1963.

Ward, Lewis M., Birger Rasmussen, and Woodward W. Fischer. 2019. 'Primary Productivity Was Limited by Electron Donors Prior to the Advent of Oxygenic Photosynthesis.' *Journal of Geophysical Research: Biogeosciences* 124, no. 2 (February): 211–226.

Warke, Matthew R., Tommaso Di Rocco, Aubrey L. Zerkle, et al. 2020. 'The Great Oxidation Event preceded a Paleoproterozoic "snowball Earth".' *Proceedings of the National Academy of Sciences* 117, no. 24 (June): 13314–13320.

Watson, Andrew J. 2008. 'Implications of an Anthropic Model of Evolution for Emergence of Complex Life and Intelligence.' *Astrobiology* 8, no. 1 (February): 175–185.

Weiss, Madeline C., Filipa L. Sousa, Natalia Mrnjavac, et al. 2016. 'The physiology and habitat of the last universal common ancestor.' *Nature Microbiology* 1, no. 9 (July): 16116.

Williams, George E. 2000. 'Geological constraints on the Precambrian history of Earth's rotation and the Moon's orbit.' *Reviews of Geophysics* 38 (1): 37–59.

Wilson, Damian R, Andrew C Bushell, Amanda M Kerr-Munslow, Jeremy D Price, and Cyril J Morcrette. 2008. 'PC2: A prognostic cloud fraction and condensation scheme. I: Scheme description.' *Quarterly Journal of the Royal Meteorological Society* 134 (637): 2093–2107.

Wilson, Damian R., and Susan P. Ballard. 1999. 'A microphysically based precipitation scheme for the UK meteorological office unified model.' *Quarterly Journal of the Royal Meteorological Society* 125, no. 557 (July): 1607–1636.

Wilson, David J., Cynthia S. Froning, Girish M. Duvvuri, et al. 2021. 'The Mega-MUSCLES Spectral Energy Distribution of TRAPPIST-1.' *The Astrophysical Journal* 911, no. 1 (April): 18.

Wine, P. H., W. L. Chameides, and A. R. Ravishankara. 1981. 'Potential role of CS2 photooxidation in tropospheric sulfur chemistry.' *Geophysical Research Letters* 8, no. 5 (May): 543–546.

Wolf, E T, and O B Toon. 2013. 'Hospitable Archean Climates Simulated by a General Circulation Model.' *Astrobiology* 13 (7): 656–673.

———. 2014. 'Controls on the Archean Climate System Investigated with a Global Climate Model.' *Astrobiology* 14 (3): 241–253.

Wolf, Eric T., Aomawa L. Shields, Ravi K. Kopparapu, Jacob Haqq-Misra, and Owen B. Toon. 2017. 'Constraints on Climate and Habitability for Earth-like Exoplanets Determined from a General Circulation Model.' *The Astrophysical Journal* 837, no. 2 (March): 107.

Wolszczan, A., and D. A. Frail. 1992. 'A planetary system around the millisecond pulsar PSR1257 + 12.' *Nature* 355, no. 6356 (January): 145–147.

Wood, Bernard J., Michael J. Walter, and Jonathan Wade. 2006. 'Accretion of the Earth and segregation of its core.' *Nature* 441, no. 7095 (June): 825–833.

Wood, Nigel, Andrew Staniforth, Andy White, et al. 2014. 'An inherently mass-conserving semi-implicit semi-Lagrangian discretization of the deep-atmosphere global non-hydrostatic equations.' *Quarterly Journal of the Royal Meteorological Society* 140, no. 682 (July): 1505–1520.

World Meteorological Organisation. 1957. 'Meteorology: a three-dimensional science, second session of the commission for aerology.' *WMO Bulletin* 6 (4): 134–138.

Wunderlich, Fabian, Markus Scheucher, M. Godolt, et al. 2020. 'Distinguishing between Wet and Dry Atmospheres of TRAPPIST-1 e and f.' *The Astrophysical Journal* 901, no. 2 (September): 126.

Yang, Huanzhou, and Jun Yang. 2019. 'How do Planetary Radius and Gravity Influence the Surface Climate of Earth-like Planets?' *arXiv e-prints* (October): arXiv:1910.06479.

Yang, Jun, and Dorian S Abbot. 2014. 'A LOW-ORDER MODEL OF WATER VAPOR, CLOUDS, AND THERMAL EMISSION FOR TIDALLY LOCKED TERRESTRIAL PLANETS.' *Astrophysical Journal* 784, no. 2 (March): 155.

Yang, Jun, Dorian S Abbot, Daniel D B Koll, Yongyun Hu, and Adam P Showman. 2019a. 'Ocean Dynamics and the Inner Edge of the Habitable Zone for Tidally Locked Terrestrial Planets.' *Astrophysical Journal* 871, no. 1 (January): 29.

Yang, Jun, Nicolas B Cowan, and Dorian S Abbot. 2013. 'STABILIZING CLOUD FEEDBACK DRAMATICALLY EXPANDS THE HABITABLE ZONE OF TIDALLY LOCKED PLANETS.' *Astrophysical Journal* 771, no. 2 (June): L45.

Yang, Jun, Jérémy Leconte, Eric T Wolf, et al. 2019b. 'Simulations of Water Vapor and Clouds on Rapidly Rotating and Tidally Locked Planets: A 3D Model Intercomparison.' *The Astrophysical Journal* 875, no. 1 (April): 46.

Yates, Jack S., Paul I. Palmer, James Manners, et al. 2020. 'Ozone chemistry on tidally locked M dwarf planets.' *Monthly Notices of the Royal Astronomical Society* 492 (2).

Yung, Y. L., M. Allen, and J. P. Pinto. 1984. 'Photochemistry of the atmosphere of Titan - Comparison between model and observations.' *The Astrophysical Journal Supplement Series* 55 (July): 465.

Yung, Yuk L., and W.B. Demore. 1982. 'Photochemistry of the stratosphere of Venus: Implications for atmospheric evolution.' *Icarus* 51, no. 2 (August): 199–247.

Yurchenko, Sergei N, Ahmed F Al-Refaie, and Jonathan Tennyson. 2018. 'EXOCROSS: a general program for generating spectra from molecular line lists.' *Astronomy & Astrophysics* 614 (June): A131.

Yurchenko, Sergei N, and Jonathan Tennyson. 2014. 'ExoMol line lists – IV. The rotation–vibration spectrum of methane up to 1500 K.' *Monthly Notices of the Royal Astronomical Society* 440, no. 2 (April): 1649–1661.

Zabarnick, S., J. W. Fleming, and M. C. Lin. 1989. 'Kinetics of CH radical reactions with N2O, SO2, OCS, CS2, and SF6.' *International Journal of Chemical Kinetics* 21, no. 9 (September): 765–774.

Zahnle, K., M. Claire, and D. Catling. 2006. 'The loss of mass-independent fractionation in sulfur due to a Palaeoproterozoic collapse of atmospheric methane.' *Geobiology* 4, no. 4 (December): 271–283.

Zahnle, Kevin, and James C.G Walker. 1987. 'A constant daylength during the precambrian era?' *Precambrian Research* 37, no. 2 (September): 95–105.

Zahnle, Kevin J. 1986. 'Photochemistry of methane and the formation of hydrocyanic acid (HCN) in the Earth's early atmosphere.' *Journal of Geophysical Research: Atmospheres* 91 (D2): 2819–2834.

Zahnle, Kevin J., Marko Gacesa, and David C. Catling. 2019. 'Strange messenger: A new history of hydrogen on Earth, as told by Xenon.' *Geochimica et Cosmochimica Acta* 244 (January): 56–85.

Zellem, Robert T., Nikole K. Lewis, Heather A. Knutson, et al. 2014. 'THE 4.5 μm FULL-ORBIT PHASE CURVE OF THE HOT JUPITER HD 209458b.' *The Astrophysical Journal* 790, no. 1 (July): 53.

Zerkle, Aubrey L., Mark W. Claire, Shawn D. Domagal-Goldman, James Farquhar, and Simon W. Poulton. 2012. 'A bistable organic-rich atmosphere on the Neoarchaean Earth.' *Nature Geoscience* 5, no. 5 (May): 359–363.

Zieba, Sebastian, Laura Kreidberg, Elsa Ducrot, et al. 2023. 'No thick carbon dioxide atmosphere on the rocky exoplanet TRAPPIST-1c.' *Nature* (June).